INVESTIGATION OF MAGNETIC BEHAVIOR: THE TUNING OF SPIN-TRANSITIONS AND REDOX PROPERTIES IN PENTANUCLEAR CYANIDE ARCHITECTURES

A Dissertation

by

CODI ANNE SANDERS

Submitted to the Office of Graduate and Professional Studies of
Texas A&M University
in partial fulfillment of the requirements for the degree of

DOCTOR OF PHILOSOPHY

Chair of Committee,	Timothy R. Hughbanks
Co-Chair of Committee,	Kim R. Dunbar
Committee Members,	Marcetta Darensbourg
	Donald G. Naugle
Head of Department,	Simon W. North

August 2016

Major Subject: Chemistry

ABSTRACT

The critical need to miniaturize electronic devices has initiated a renaissance in the study of the electronic and magnetic properties of both discrete molecules and extended structures vis-à-vis their potential for high-density data storage devices, sensors, switches, displays and quantum computing. Researchers in molecular magnetism are focusing on the fundamental behavior of unusual paramagnetic molecules in an effort to rationally design those with improved properties which requires exquisite synthetic control. One strategy that is particularly successful is to use a linear bridging ligand, such as cyanide, that allows for predictive magnetic exchange between spin centers. The use of cyanometallates to bridge metal centers has led to interesting properties, including remnant magnetization above room temperature, spin-crossover (SCO), charge-transfer-induced-spin-transition (CTIST), photomagnetism and single molecule magnetic properties.

The research described in this dissertation focuses on the synthesis of $[Ru^{III}(CN)_6]^{3-}$ and $[Os^{III}(CN)_6]^{3-}$ and their incorporation into discrete, pentanuclear molecules, referred to as trigonal bipyramids (TBPs). TBPs are modeled after the well-studied Prussian blue and its analogs (PBAs) and has a general formula of $[M^{II}(tmphen)_2]_3[M'^{III}(CN)_6]_2$ ($M_3M'_2$), which allows for six equivalent exchange interactions. TBPs are the largest homologous family of cyanide materials reported in literature and have been shown to mimic the behaviors exhibited by

PBAs. The incorporation of the heavier Group VIII 4d and 5d hexacyanometallates into TBPs was undertaken to explore magnetic exchange through the CN^- bridges which had been found to lead to interesting magnetic phenomena for the Fe analogs.

The tools of IR spectroscopy, thermal gravimetric analysis, magnetometry, single X-ray crystallography and ^{57}Fe Mössbauer spectroscopy (when appropriate) have been used to characterize the TBPs discussed herein. The rich redox behavior in the new Co_3Ru_2 and Co_3Os_2 TBPs manifested itself in the irreversible metal-to-metal-charge-transfer event in the Co_3Ru_2 and the reversible CTIST in the Co_3Os_2 TBPs. The Co_3Os_2 TBP is one of a very small number of compounds to display CTIST and is only the second Co/Os cyanide compound to do so, preceded only by a Co_3Os_2 Prussian Blue analog from the Dunbar laboratories. A study of the first Fe/Ru cyanide compound to exhibit CTIST is discussed in regard to how the identity and amount of solvent in the Fe_3Ru_2 TBP effects the CTIST events. A final study was aimed at investigating how changes in the π-π stacking interactions in the Fe_3Co_2 TBP affects the SCO behavior of the equatorial Fe^{II} metal centers.

DEDICATION

I dedicate this work to my father who has supported, encouraged and loved me unconditionally. He has shown me the true meaning of hard work and perseverance. He has a fierce tenacity for never giving up and always fighting for what he wants. He has made many sacrifices for me and my siblings to ensure that we are happy, healthy and successful and still continues to do so even now that we are grown. Through his enduring battle against cancer, he has taught me that it is OK to go against the grain, to think for myself and to educate myself so that I don't become led astray by others who think that they know what is best for me. He truly is an inspiration to me and is the reason I strive to be the best person that I can be. I am eternally grateful for the life lessons and support he has given me as I would not be who I am or where I am today without his guidance. He will always be my superhero just as I will always be his little girl!

Figure 0-1. Picture of my Superdad!

"…fundamental understanding of the science is not a prerequisite for technological progress."

–JM Coey

ACKNOWLEDGEMENTS

So many people have been instrumental in making my dream a reality. As the saying goes, it takes a village to raise a child and I believe this rings true throughout life, as learning doesn't cease with adulthood. First and foremost, I'd like to extend my gratitude to my advisor Professor Kim R. Dunbar for being there for me and helping me grow, not only as a scientist, but as a person. Being under her tutelage has been vital in my development, as she makes every effort to ensure that we are given every opportunity to strive for excellence and expand our knowledge base. The experiences she has afforded me during my time in her group, both as an undergraduate and graduate student, are greatly appreciated and will remain cherished memories.

I would like to thank my committee members Dr. Tim Hughbanks, Dr. Marcetta Darensbourg and Dr. Donald Naugle, as well as my previous committee member, Dr. Hong-Cai Zhou, for their helpful discussions, suggestions, support and the time they have spent on this process for me throughout the years. A special thank you is extended to Dr. Hughbanks for accepting the task of becoming the chair of my committee so that I could still defend in time for an August graduation when Dr. Dunbar was understandably unable to be in town for my defense.

Research is often a group effort, and as such, I would like to thank my collaborators who have spent their time and effort on measuring samples for me.

Dr. Catalina Achim, Meimei Chen and Heather Stout at Carnegie Mellon were instrumental in collecting and analyzing ^{57}Fe Mössbauer data for the Fe_3Ru_2 TBP project. I thank them for all of the insightful suggestions and discussions over the years. I'd also like to thank Dr. Doros Petasis and Keiron Stoddart at Allegheny College for the measurement and analysis of EPR data for the Ru and Os starting materials, as well as the Fe_3Ru_2 TBP samples. Simon Teat and Kevin Gagnon at the "Advanced Light Source (ALS) at Lawrence Berkeley National Laboratory" were instrumental in helping me collect and solve many of the structures reported here and many more that are not. I appreciate their help and patience.

I am grateful for the friendships that have been forged within the Dunbar group. Dr. Amanda David has been a close friend of mine since we began our time together in the Dunbar group and has been very helpful and supportive during this journey. I appreciate her daily motivational calls to make sure I am staying focused and on task. Dr. Andrew Brown and Dr. Zhanyong Li are two more life-long friends that the Dunbar group has afforded me. I am grateful for their support and enjoyed the many adventures we've shared. I am also thankful to Dr. Bruno Peña and his wife Andrea, who became good friends of mine over the years. I would also like to thank Dr. Dawid Pinkowicz for his friendship and help. It was always a joy to be around him, as his ever-lasting enthusiasm for science was contagious. I look forward to the days ahead when we can all gather for a BBQ like we used to. I am grateful to have made Dr. Maryfer Ballesteros Rivas my close friend during our time in the group together. She continually supported and

encouraged me, in addition to volunteering on numerous occasions to stay working late in the lab with me just so I wouldn't have to work alone. I am thankful for all of the help she has given me. Dr. Silvia Gómez Coca has become a great friend in the year she has been here. She has been instrumental in my research this last year while having to suffer through all of my stupid questions. I am eternally grateful for all of her help and encouragement. I am also thankful for Toby Woods, as he has helped me on numerous occasions and has been a good friend throughout the years. I would also like to thank the rest of the Dunbar group members, both past and present, for any help they've given me and for providing a friendly work environment: Xuan Zhang, Jill Ellenbarger, David Kempe, Francisco Birk, Sayan Saha, Ryan Coll, Haomiao Xie, Kelsey Schulte, Carolyn Gunthardt, Agustin Millet, Zhe Shen, Ed Funck, Sarah Lane, Dr. Mohamed Saber, Dr. Matt Hilfiger, Dr. Carolina Avendaño, Dr. Ferdi Karadas, Dr. Ian Giles, Dr. Heather Southerland, Dr. Kristen Funck, Dr. Zhongyue Zhang, Dr. Hanhua Zhao, Dr. Helen Chifotides, Dr. Yuanzhu Zhang, Dr. Yue Ma, Dr. Brian Dolinar, Dr. Dimitrios Alexandropoulos, Mayela Canales, Angie Wilson and Andrezza Antonio.

Finally, I would not be where I am today without the love and support from my friends and family. Naquita Patterson has been my best friend for many years and is the one who convinced me to come to Texas in the first place. I am forever grateful for her support, friendship and my god children. Judy Reyes has been like a sister to me and I am grateful to have her in my life. My family is my most treasured possession and it is for them that I strive to succeed. My mother Jeanne,

father Rick, sister Jeannine, brother William and sister Jane have supported me in any way they could and continually encouraged me to push through. My brothers-in-law Ricardo Mejia (Jeannine) and Gerrett Burns (Jane) have been a part of this wild ride as well and I appreciate their love and support throughout it. It has been very difficult being so far away from my family and I thank them for everything from the bottom of my heart! I also thank my siblings and friends for having such beautiful children for me to enjoy, so I didn't have to have my own during this time. Seeing and talking to my nieces (Aurora, Ashlynn and Emma), nephews (Andrew, Logan and Parker), god-children (Olivia and Erin) and friends' children is always an uplifting experience for me.

NOMENCLATURE

4-dmbpy	4,4’-dimethyl-2,2’-bipyridine
5-dmbpy	5,5’-dimethyl-2,2’-bipyridine
ALS	Advanced Light Source
bpy	2,2’-bypyridine (A.K.A. 2,2’-dipyridyl)
$B_S(y)$	Brillouin function
C	Curie constant
CD_3OD	deuterated methanol
CTIST	charge-transfer induced spin transition
CV	cyclic voltammetry
D_2O	deuterated water
DCM	dichloromethane
DMF	N,N’-dimethylformamide
EA	elemental analysis
EPR	electron paramagnetic resonance
EtOH	ethanol
g_e	electronic g-factor (= 2.00232)
HS	high spin
IR	infrared (spectroscopy)
LBNL	Lawrence Berkeley National Laboratory
LIESST	light-induced excited spin state trapping

LS	low spin
m	magnetic (dipole) moment
M	magnetization
Me_4Bpy	4,4’,5,5’-tetramethyl-2,2’-bipyridine
MeCN	acetonitrile
MeOH	methanol
M–L	metal–Ligand
MMCT	metal-to-metal charge transfer
MPMS	magnetic property measurement system
N	Avogadro’s number
OECD	Organisation for Economic Co-operation and Development
OSHA	Occupational Safety and Health Administration
PB	Prussian blue
PBA	Prussian blue analog
PPh_3	triphenylphoshpine
PPN	bis(triphenylphosphine)iminium
SCO	spin-crossover
SMM	single molecule magnet
SQUID	superconducting quantum interference device
T	Tesla (magnetic field unit)
$T_{1/2}$	transition temperature
TBA	tetrabutylammonium

TBP	trigonal bipyramid
T_c	Curie temperature
TEA	tetraethylammonium
TGA	thermogravimetric analysis
THF	tetrahydrofuran
tmbpy	4,4’,5,5’-tetramethyl-2,2’-bipyridine
tmphen	3,4,7,8-tetramethyl-1,10-phenanthroline
T_N	Néel temperature
δ	isomer/chemical shift
ΔE_Q	quadrupole splitting
Δ_O	octahedral ligand field splitting energy
θ	Weiss constant
π	spin-pairing energy
χ	susceptibility
χ^0	susceptibility due to Pascal’s constants
χ^D	diamagnetic susceptibility
χ_m	molar susceptibility
χ^P	paramagnetic susceptibility
χT	susceptibility multiplied by temperature (temperature dependent susceptibility)

TABLE OF CONTENTS

Page

ABSTRACT ii

DEDICATION iv

ACKNOWLEDGEMENTS v

NOMENCLATURE ix

TABLE OF CONTENTS xii

LIST OF FIGURES xvi

LIST OF TABLES xxvii

LIST OF EQUATIONS xxxiii

CHAPTER I INTRODUCTION TO CYANIDE MOLECULAR MAGNETISM AND SPIN-CROSSOVER BEHAVIOR 1

Basic Magnetic Principles 3
Molecular Magnetism 16
Molecular Bistability 18
Spin-crossover (SCO) 19
SCO Characterization Methods 23
Influences on SCO Behavior 32
Charge-Transfer-Induced-Spin-Transition (CTIST) 35
Cyanide Chemistry and Prussian Blue Analogs 39
Trigonal Bipyramidal Molecules (TBPs) 41

CHAPTER II STRAIGHTFORWARD SYNTHETIC ROUTES TO PURE HEXACYANOMETALLATE ANION SALTS OF TRIVALENT RUTHENIUM AND OSMIUM 47

Background 47
Experimental Details 51
Materials 51
Syntheses 52
$K_4[Ru^{II}(CN)_6]\cdot nH_2O$ 52

$K_4[Os^{II}(CN)_6]\cdot nH_2O$ 54
Bis(triphenylphosphine)iminium Chloride (PPNCl) 58
$(PPN)_3[Ru^{III}(CN)_6]\cdot H_2O$ (1) 62
$(PPN)_3[Os^{III}(CN)_6]\cdot H_2O$ (2) 63
Results and Discussion 65
Synthesis and Characterization 65
$(PPN)_3[Ru^{III}(CN)_6]\cdot H_2O$ (1) 70
$(PPN)_3[Os^{III}(CN)_6]\cdot H_2O$ (2) 76
Single Crystal X-ray Diffraction 80
Magnetic Properties 85
Electron Paramagnetic Resonance Spectroscopy 89
Cyclic Voltammetry 92
Concluding Remarks 95

CHAPTER III MAGNETIC PROPERTIES OF NEW TRIGONAL BIPYRAMIDAL MOLECULES BASED ON RUTHENIUM AND OSMIUM HEXACYANOMETALLATES 97

Background 97
Experimental Details 99
Materials 99
Syntheses 100
$\{[Co(tmphen)_2]_3[Ru(CN)_6]_2\}\cdot$nSolv ($Co_3Ru_2$) (3) 100
$\{[Co(tmphen)_2]_3[Os(CN)_6]_2\}\cdot$nSolv ($Co_3Os_2$) (4) 101
$\{[Zn^{II}(tmphen)_2]_3[Os^{III}(CN)_6]_2\}\cdot$nSolv ($Zn_3Os_2$) (5) 102
$\{[M^{II}(tmphen)_2]_2[Ru^{II}(CN)_4(tmphen)]_2\}\cdot 2DMF\cdot 8H_2O$ (Mn_2Ru_2) (6) 103
Results and Discussion 104
Synthesis and Characterization 104
Co_3Ru_2 (3) and Co_3Os_2 (4) 104
Zn_3Os_2 (5) 106
$\{[M^{II}(tmphen)_2]_2[Ru^{II}(CN)_4(tmphen)]_2\}$ (Mn_2Ru_2) (6) 108
Single Crystal X-ray Diffraction 108
Co_3Ru_2 (3) and Co_3Os_2 (4) TBPs 111
Zn_3Os_2 TBP (5) 119
$\{[M^{II}(tmphen)_2]_2[Ru^{II}(CN)_4(tmphen)]_2\}$ (Mn_2Ru_2) (6) 124
Magnetic Properties 129
Co_3Ru_2 (3) and Co_3Os_2 (4) TBPs 129
Zn_3Os_2 (5) 136
Concluding Remarks 139

CHAPTER IV SPIN-TRANSITION AND CHARGE-TRANSFER PROPERTIES OF THE Fe_3Ru_2 TBP AS A CONSEQUENCE OF SOLVATION 141

Background 141
Experimental Details 143
Materials 143
Syntheses 144
$Fe^{II}_4Cl_8(THF)_6$ 144
$\{[Fe(tmphen)_2]_3[Ru(CN)_6]_2\}$ (Fe_3Ru_2) (7) 145
Fe_3Ru_2 — Solvated (7a) 146
Fe_3Ru_2 — Filtered (7b) 146
Fe_3Ru_2 — Evacuated 3 Hours (7c) 147
Fe_3Ru_2 — Evacuated 24 Hours (7d) 147
Fe_3Ru_2 — Humid (7e) 148
Results and Discussion 148
Synthesis and Characterization 148
Single Crystal X-ray Diffraction 154
Fe_3Ru_2 (7) 154
Fe_3Ru_2 Solvated (7a) 158
Fe_3Ru_2 24 Hours (7d) 170
Fe_3Ru_2 Humid (7e) 175
Magnetic Properties 188
Fe_3Ru_2 Solvated (7a) 191
Fe_3Ru_2 Filtered (7b) 194
Fe_3Ru_2 3 Hours (7c) 196
Fe_3Ru_2 24 Hours (7d) 197
Fe_3Ru_2 Humid (7e) 199
^{57}Fe Mössbauer Properties 203
Fe_3Ru_2 Solvated (7a) 204
Fe_3Ru_2 Filtered (7b) 209
Fe_3Ru_2 3 Hours (7c) 211
Fe_3Ru_2 24 Hours (7d) 214
Fe_3Ru_2 Humid (7e) 217
Concluding Remarks 222

CHAPTER V INVESTIGATION OF π-π STACKING INTERACTIONS IN SPIN CROSSOVER Fe_3Co_2 TRIGONAL BIPYRAMIDAL COMPLEXES 226

Background 226
Experimental Details 229
Materials 229
Syntheses 230

4,4’,5,5’-tetramethyl-2,2’-bipyridine (tmbpy or Me_4Bpy) 230
$(PPN)_3[Co^{III}(CN)_6]$ 231
$\{[Fe^{II}(tmphen)_2]_3[Co^{III}(CN)_6]_2\}\cdot nSolv$ (Fe_3Co_2) (8) 232
$\{[Fe^{II}(4dmbpy)_2]_3[Co^{III}(CN)_6]_2\}\cdot nSolv$ (Fe_3Co_2 4dmbpy) (9) 233
$\{[Fe^{II}(5dmbpy)_2]_3[Co^{III}(CN)_6]_2\}\cdot nSolv$ (Fe_3Co_2 5dmbpy) (10) 234
$\{[Fe^{II}(tmbpy)_2]_3[Co^{III}(CN)_6]_2\}\cdot nSolv$ (Fe_3Co_2 tmbpy) (11) 235
Results and Discussion 236
Synthesis and Characterization 236
Fe_3Co_2 tmphen (8) 236
Fe_3Co_2 4dmbpy (9) 237
Fe_3Co_2 5dmbpy (10) 238
Fe_3Co_2 tmbpy (11) 239
Single Crystal X-ray Diffraction 241
Fe_3Co_2 tmphen (8) 243
Fe_3Co_2 4dmbpy (9) 253
Fe_3Co_2 5dmbpy (10) 262
Fe_3Co_2 tmbpy (11) 268
Magnetic Properties 279
Fe_3Co_2 tmphen (8) 280
Fe_3Co_2 4dmbpy (9) 283
Fe_3Co_2 5dmbpy (10) 286
Fe_3Co_2 tmbpy (11) 288
Concluding Remarks 295

CHAPTER VI SUMMARY AND FUTURE OUTLOOK 296

REFERENCES 306

APPENDIX A 322

Instrumentation and Physical Methods 322
Magnetic Measurements 322
Infrared (IR) Spectroscopy 324
Thermogravimetric Analysis (TGA) 324
Elemental Analysis (EA) 325
Cyclic Voltammetry (CV) 325
Single Crystal X-Ray Diffractometry 325
Fe_3Ru_2 Solvated 7a 326
Fe_3Ru_2 24 Hours 7d 327
Fe_3Ru_2 Humid 7e 327
^{57}Fe Mössbauer 328

LIST OF FIGURES

Page

Figure 0-1. Picture of my Superdad! iv

Figure 1-1. Illustration of how the magnetic moments align in paramagnetic (random), antiferromagnetic (antiparallel), ferromagnetic (parallel) and ferrimagnetic (antiparallel with unequal magnitudes) materials. 10

Figure 1-2. Representation of the expected behavior of the susceptibility (top) and inverse susceptibility (bottom) of paramagnetic (green), ferromagnetic (blue) and antiferromagnetic (red) materials when plotted as a function of temperature. 11

Figure 1-3. Schematic of the behavior of the χT vs temperature curves for paramagnetic (green), ferromagnetic (blue), antiferromagnetic (red) and ferrimagnetic (purple) materials. 12

Figure 1-4. Theoretical magnetization curves (in Bohr magnetons) at 1.8 K for ground states of S = ½, S = 1 and S = ⅗ systems that follow a Brillouin function. 15

Figure 1-5. Schematic of the interplay between ligand field strength (Δ) and spin-pairing energy (π) on the spin state of an octahedral metal ion. 21

Figure 1-6. Depiction of the electron configuration for the LS and HS states of an Fe^{II} metal center in an octahedral coordination environment that undergoes SCO upon an external stimulus. 22

Figure 1-7. Types of SCO behavior categorized in terms of cooperativity: (a) gradual, (b) abrupt, (c) with hysteresis, (d) step-wise or muti-step and (e) incomplete. Plots are given as molar fractions of HS molecules γ_{HS} as a function of temperature. Reprinted with permission of Springer; copyright 2004, Springer Berlin Heidelberg. Adapted from reference 85. 25

Figure 1-8. Depiction of the change in the octahedral coordination sphere of an Fe^{II} metal center upon SCO. The compound in the LS state is usually more intensely colored as compared to the HS state. Reproduced with permission from reference 77; published by The Royal Society of Chemistry. 27

Figure 1-9. Depiction of vibrational components within the energy curves for the LS and HS states in a SCO system. 27

Figure 1-10. Schematic of the nuclear energy levels for the source and absorber illustrating the isomer shift and quadrupole splitting of the absorber. An example of the doublet that occurs due to quadrupole splitting in the absence of a magnetic field is shown. The splitting is equivalent to the energy difference between the excited m_I substates. 30

Figure 1-11. Schematic illustrating isomer shift and quadrupole splitting parameters for a Mössbauer spectrum. Adapted from lecture notes by Phillip Gütlich from the University of Mainz. 31

Figure 1-12. Schematic depiction of the conversion between paramagnetic (top) $^{LS}Fe^{III}$–CN–$^{HS}Co^{II}$ and diamagnetic $^{LS}Fe^{II}$–CN–$^{LS}Co^{III}$ electronic configurations due to CTIST triggered by thermal and/or photoirradiation. 36

Figure 1-13. 3D structure of Prussian blue. Color scheme: Cyan is Fe^{II}, green is Fe^{III}, gray is C, blue is N, red is O and white is H. 40

Figure 1-14. General reaction scheme for preparing TBPs. 42

Figure 1-15. Typical unit cell for TBPs that crystallize in the $P2_1/c$ space group. Colors correspond to symmetry elements within the space group. Green represents a 2_1 screw axis, orange represents inversion and pink represents glides. The gray TBP is the asymmetric unit. 44

Figure 2-1. Reaction setup for the synthesis of PPNCl. 61

Figure 2-2. Bis(triphenylphosphine)iminium chloride (PPNCl) 66

Figure 2-3a-h. Typical colors expected as the synthesis of 1 progresses. 71

Figure 2-4. Filtered solutions of the oxidation step in the synthesis of 1. Left: Expected color when there is no decomposition and right: color of the solution due to decomposition occurring 72

Figure 2-5. IR spectra of $(PPN)_3[Ru^{III}(CN)_6]$ (1) in Nujol oil. Inset is a close-up of the cyanide stretching peaks. 73

Figure 2-6. IR spectra of (1) contaminated with decomposition by-products. Inset is a close-up of the $\nu_{C\equiv N}$ peaks. 74

Figure 2-7. Thermogram of 1. The blue line represents mass loss (%) and is on the left y-axis. The pink line represents temperature in °C and pertains to the right y-axis. These two variables were plotted against minutes. 76

Figure 2-8. Typical color and consistency of (2) when it is free of decomposition by-products. 77

Figure 2-9. IR spectrum of $(PPN)_3[Os^{III}(CN)_6]$ (2) in Nujol oil. Product is free of decomposition contamination. 78

Figure 2-10. Thermogram of (2) up to 200 °C in a N_2 atmosphere. 80

Figure 2-11. Asymmetric unit of $(PPN)_3[M^{III}(CN)_6]$. Yellow atoms are phosphorous. M^{III} is Os or Ru. 83

Figure 2-12. Packing diagram of $(PPN)_3[M^{III}(CN)_6]$, where M^{III} is Ru/Os. View is looking down the c axis. Color scheme: Green is Ru/Os, yellow is P, blue is N, red is O, grey is C and white is H. 84

Figure 2-13. Temperature dependent susceptibility data for compounds 1 (a) and 2 (b). The susceptibility for both compounds exhibit Curie behavior with TIP (red and pink lines). Data was fit using C = 0.30, g = 1.79 and TIP = 875 x 10^{-6} emu·K/mol for compound 1 and C = 0.29, g = 1.76 and TIP = 395 x 10^{-6} emu·K/mol for compound 2. 87

Figure 2-14. Magnetization data for compounds 1 (a) and 2 (b) at 1.8 K. The data are fit with the Brillouin function (pink lines) using g = 1.77 for compound 1 and g = 1.74 for compound 2. 88

Figure 2-15. Variable temperature EPR data for 1 (top) and 2 (bottom). Compounds were measured in 1 mM MeCN solutions. 90

Figure 2-16. Variable temperature EPR data collected on solid samples of 1 (top) and 2 (bottom). 91

Figure 2-17. Voltammograms of compounds 1 (top) and 2 (bottom) in MeCN with a glassy carbon working electrode and a Ag/AgCl as the reference electrode. 94

Figure 3-1. Asymmetric unit of the Co_3Os_2 TBP. Co_3Ru_2 is isomorphic and not shown. Color scheme: Green is Os, cyan is Co, blue is N and white is C. Hydrogen atoms have been omitted for the sake of clarity. 113

Figure 3-2. Dimeric unit of the Co_3M_2 TBPs where M = Ru/Os. The purple planes highlight the intermolecular interaction between these molecules. Interaction referred to as inter-pp. Hydrogen atoms are omitted for the sake of clarity. 117

Figure 3-3. View of the Co_3M_2 TBP (where M = Ru/Os) looking down the axial Ru/Os positions. The green planes are symmetrically equivalent to one another just as the blue ones are. The intramolecular interactions that occur in these TBPs occur between the green plane and the blue plane. Interaction referred to as intra-gb. Hydrogen atoms omitted for the sake of clarity. 118

Figure 3-4. View of the Zn_3Os_2 TBP stacking in a dimeric unit. The purple and yellow planes highlight the rings within the tmphen ligands that are involved in the intermolecular π-π stacking interactions (inter-pp and inter-py). Color code: Zn is Yellow, Os is green, C is white and N is blue. Hydrogen atoms omitted for clarity. The pink tmphen ligand is coordinated to a Zn(3) center and the cyan tmphen ligand is its symmetrically equivalent (due to inversion) tmphen ligand coordinated to the Zn(3) center on the neighboring TBP. These two ligands are the ones involved in the π-π stacking interactions. 122

Figure 3-5. View of the Zn_3Os_2 TBP looking down the axial Os positions. The teal colored planes portray the intra-tt intramolecular interaction and the green planes depict the intra-gg intramolecular interaction. There is no intramolecular interaction between the tmphen ligands on the Zn(1) and Zn(3) centers, as indicated by the red arrow marked out. Hydrogen atoms have been omitted for clarity. 123

Figure 3-6. Asymmetric unit of Mn_2Ru_2. Thermal ellipsoids at 50% probability level. Hydrogen bonds are represented with dashed lines. Color scheme: Mn is pink, Ru is purple, N is blue, C is grey, O is red and H is white. Looking down the *a*-axis, approximately. 125

Figure 3-7. Packing diagram of Mn_2Ru_2 looking down the *a*-axis. Hydrogen atoms are omitted for the sake of clarity. Color

scheme: Mn is pink, Ru is purple, N is blue, C is grey and O is red. 126

Figure 3-8. Depiction of the π-π stacking interactions in the Mn_2Ru_2 compound. Rings of the same color are symmetrically equivalent. 128

Figure 3-9. Temperature-dependent susceptibility data for the Co_3Ru_2 (a) and Co_3Os_2 (b) TBPs. 133

Figure 3-10. Magnetization data at 1.8 K for the Co_3Ru_2 (a) and Co_3Os_2 (b) TBPs. The pink line represents a Brillouin function for an $S = {}^3/_2$ system with a g = 2.0. 134

Figure 3-11. Reduced magnetization data for the Co_3Ru_2 (a) and Co_3Os_2 (b) TBPs..... 135

Figure 3-12. (a) Temperature-dependent susceptibility data for the Zn_3Os_2 TBP. Solid lines are fit lines for Curie-Weiss behavior with C = 0.56 (2 S = ½ ions with g = 1.75), θ = 0.05 and TIP = 1200 x 10^{-6} emu·K/mol. (b) Magnetization data at 1.8 K. Solid line is the best-fit Brillouin function for 2 S = ½ ions with a g = 1.67..... 138

Figure 4-1. Scheme of sample preparation. Colors coincide with magnetic and ^{57}Fe Mössbauer data discussed later. 151

Figure 4-2. View of the Fe_3Ru_2 TBPs stacking in a dimeric unit due to the intermolecular π-π stacking interactions between neighboring TBP molecules. The purple and yellow planes highlight the rings within the tmphen ligands that have the intermolecular interactions. Color code: Fe is green, Ru is violet, C is gray and N is blue. Hydrogen and solvent have been omitted for clarity. 156

Figure 4-3. View of the Fe_3Ru_2 TBP looking down the apical hexacyanoruthenate centers. The turquoise and yellow planes coupled with the red arrows highlight the rings within the tmphen ligands that have intramolecular π-π stacking interactions within the TBP. Color code: Fe is green, Ru is violet, C is gray and N is blue. Hydrogen and solvent have been omitted for clarity. 157

Figure 4-4. Asymmetric unit of the solvated Fe_3Ru_2 TBP (7a) at 20 K. Pink circles highlight the disordered tmphen and MeCN

molecules within the crystal. Color code: Fe is green, Ru is violet, C is gray, N is blue and O is red. Oxygen atoms were refined without hydrogen in order to obtain convergence of the structure. Hydrogen from all other atoms have been omitted for the sake of clarity. 165

Figure 4-5. Simple packing diagram of the solvated Fe_3Ru_2 TBP (7a). Dimeric units of the TBPs are colored using the same color (three dimeric units shown – green, yellow and cyan). Two individual TBP molecules shown using the following color scheme: Fe is green, Ru is violet, C is gray, N is blue and O is red. Oxygen atoms were refined without hydrogen in order to obtain convergence of the structure. Hydrogen from all other atoms have been omitted for the sake of clarity. 166

Figure 4-6. Packing diagram of the 24 hour evacuated Fe_3Ru_2 TBP. Color code: Fe is green, Ru is violet, C is gray, N is blue and O is red. Oxygen atoms were refined without hydrogen in order to obtain convergence of the structure. Hydrogen from all other atoms have been omitted for the sake of clarity. 174

Figure 4-7. The asymmetric unit of the Fe_3Ru_2 TBP left in a humid environment for a day. The pink circle highlights the hydrogen bond to a terminal cyanide ligand. Color code: Fe is green, Ru is violet, C is gray, N is blue and O is red. The dashed lines represent hydrogen bonds. 180

Figure 4-8. Dimeric unit of 7e at 50 K. The orange and yellow tmphen ligands are on opposite Fe(3) centers involved in π-π stacking. Water forms a hydrogen bonding network with a cyanide ligand on the Ru(2) center. Color code: Fe is green, Ru is violet, C is gray, N is blue and O is red. The orange and yellow tmphen ligands are the ones involved in the intermolecular interactions in the dimeric unit. The dashed lines represent the hydrogen bonds. 181

Figure 4-9. Packing diagram of 7e looking down the b-axis. Color code: Fe is green, Ru is violet, C is gray, N is blue and O is red. The dashed lines represent the hydrogen bonds. 182

Figure 4-10. View of the humid Fe_3Ru_2 TBP (7e) at 20 K stacking in a dimeric unit due to the intermolecular π-π stacking interactions between neighboring TBP molecules. The purple and yellow planes highlight the rings within the tmphen ligands that are

common between all of the structures discussed. The maroon plane highlights the additional interaction found only in this solvation state at this temperature. Color code: Fe is green, Ru is violet, C is gray and N is blue. Hydrogen and solvent have been omitted for the sake of clarity. 183

Figure 4-11. Graph of average Fe–N bond lengths for all temperatures of 7a (blue markers and lines), 7d (green markers) and 7e (orange markers and lines). The triangles represent the Fe(1) centers, the circles represent the Fe(2) centers and the squares represent the Fe(3) centers for each compound. 187

Figure 4-12. Temperature-dependent susceptibility data for the Fe_3Ru_2 TBP measured under MeCN (7a). The inset is the reduced magnetization data. 192

Figure 4-13. Temperature dependence of χT for the solvated (7a – dark blue circles) and filtered (7b – light blue circles) Fe_3Ru_2 TBPs. This filtered sample is easily recognized as it is measured up to 350 K. The inset is the reduced magnetization for the filtered sample. 195

Figure 4-14. Temperature dependent susceptibility of the Fe_3Ru_2 TBP put under vacuum for three hours. Inset: reduced magnetization data for the sample. 197

Figure 4-15. Temperature dependent χT curve for the Fe_3Ru_2 TBP (7d) exposed to vacuum for 24 hours prior to measurement. Inset: reduced magnetization data for the compound. 198

Figure 4-16. Temperature dependent susceptibility of the water-containing Fe_3Ru_2 TBP (7e). The reduced magnetization for this humid sample can be found in the inset. 200

Figure 4-17. A comparison of spin-transition curves exhibited in the temperature dependent χT data of Fe_3Ru_2 TBPs with different levels of solvation. 202

Figure 4-18. ^{57}Fe Mössbauer data for the solvated crystals of Fe_3Ru_2 (7a) at 150 K (a) and 4.2 K (b). Spectra were obtained without an applied field. Orange line is the simulation using the parameters in Table 4-17. Percentages of iron used in simulation are displayed on each figure for convenience. 206

Figure 4-19. ^{57}Fe Mössbauer spectra for the filtered sample (7b) at 150 K (a) and 4.2 K (b). Measurements done in zero field. The red line represents the simulation of the data with the parameters in Table 4-18. Total iron percentages are displayed on the spectra for convenience. 210

Figure 4-20. ^{57}Fe Mössbauer spectra for 7c collected at 250 K (a) and 150 K (b) in zero field. The orange line is the simulation of the data with the parameters in Table 4-19. The iron percentage and type is displayed on the figure for convenience. 213

Figure 4-21. ^{57}Fe Mössbauer spectra for 7d at room temperature (a), 150 K (b) and 4.2 K (c) in zero field. The green lines are the simulation of the HS Fe^{II} doublets, the blue lines are the simulations for the LS Fe^{II}/HS Fe^{III} doublets and the red lines are the overall simulations with all parameters in Table 4-20 for each temperature. 215

Figure 4-22. ^{57}Fe Mössbauer spectra for 7e at 150 K (a) and 4.2 K (b). The lines simulate the parameters in Table 4-21. The red lines are for HS Fe^{II}, the green lines simulate LS Fe^{III}, the blue lines simulate the LS Fe^{II}/HS Fe^{III} doublet and the orange line represents the overall simulation with the indicated parameters. The percentages attributed to each type of iron is displayed on the spectra for convenience. 219

Figure 4-23. Comparison of the ^{57}Fe Mössbauer data at 150 K for all solvation states (7a-7e). The HS Fe^{II} doublets are circled in red. 221

Figure 5-1. ChemDraw structures of the bidentate ligands used to make the Fe_3Co_2 TBPs. The number in parenthesis following the abbreviation of the name in bold-type font corresponds to the number of the compound in which the ligand is used. 228

Figure 5-2. Asymmetric unit of the Fe_3Co_2 TBP looking down the axial metal centers. Color scheme: Co is cyan, Fe is green, N is blue and C is grey. Hydrogen atoms have been omitted for the sake of clarity. 246

Figure 5-3. View of the dimeric unit of the Fe_3Co_2 TBP with tmphen ligands (8). The purple and yellow colored planes are the rings within the tmphen ligands that are involved in the intermolecular interactions. 249

Figure 5-4. Depiction of the intramolecular interactions in the Fe_3Co_2 TBP with tmphen (8). Arrows indicate the interaction between the planes. 250

Figure 5-5. Packing diagram looking down the *a*-axis for compound 8. The colored planes offer perspective and help distinguish the packing of the dimeric unit. Color scheme: Co is cyan, Fe is green, N is blue and C is grey. Hydrogen atoms have been omitted for the sake of clarity. 252

Figure 5-6. Asymmetric unit of the Fe_3Co_2 TBP at 100 K with 4dmbpy coordinated to the equatorial Fe centers. Color scheme: Co is cyan, Fe is green, N is blue and C is grey. Hydrogen atoms have been omitted for the sake of clarity. 256

Figure 5-7. View of intermolecular π-π stacking interactions in the Fe_3Co_2 TBP with 4dmbpy (9). The purple and yellow planes portray the inter-py interaction. 258

Figure 5-8. View of the intramolecular interactions in the Fe_3Co_2 TBP with the 4dmbpy ligands. The teal colored planes denote the intra-tt interaction and the red colored planes portray the intra-rr interaction. 259

Figure 5-9. Packing diagram looking down the *a*-axis for compound 9. The colored planes offer perspective and help distinguish the packing of the dimeric unit. Color scheme: Co is cyan, Fe is green, N is blue and C is grey. Hydrogen atoms have been omitted for the sake of clarity. 261

Figure 5-10. Axial view of the asymmetric unit of the Fe_3Co_2 TBP with 5dmbpy ligands coordinated to the equatorial Fe centers. Color scheme: Co is cyan, Fe is green, N is blue and C is grey. Hydrogen atoms have been omitted for the sake of clarity. 264

Figure 5-11. View looking down the axial metal positions of the intramolecular interactions occurring in the Fe_3Co_2 5dmbpy TBP (10). The intra-gg interaction is indicated by the green planes and the intra-tt interaction is shown with the teal planes. This TBP does not exhibit the intra-rr interaction between the Fe(2) and Fe(3) centers. Color scheme: Co is cyan, Fe is green, N is blue and C is grey. Hydrogen atoms have been omitted for clarity. 266

Figure 5-12. Packing diagram of Fe_3Co_2 5dmbpy (10) looking down the *a*-axis. The planes indicating the intra-gg interaction offer perspective on the packing of the molecules. Color scheme: Co is cyan, Fe is green, N is blue and C is grey. Hydrogen atoms have been omitted for clarity 267

Figure 5-13. View of the asymmetric unit of Fe_3Co_2 tmbpy (11) looking down the axial Co metal centers. Color scheme: Co is cyan, Fe is green, N is blue and C is grey. Hydrogen atoms have been omitted for the sake of clarity. 270

Figure 5-14. Depiction of the intramolecular π-π stacking interaction in the Fe_3Co_2 tmbpy TBP (11). The green planes indicate the rings involved in the intramolecular interation. Color scheme: Co is cyan, Fe is green, N is blue and C is grey. Hydrogen atoms have been omitted for the sake of clarity. 273

Figure 5-15. Packing diagram of Fe_3Co_2 tmbpy (11) looking down the *a*-axis. Color scheme: Co is cyan, Fe is green, N is blue and C is grey. Hydrogen atoms have been omitted for the sake of clarity. 275

Figure 5-16. Comparison of how compounds 8-11 pack looking down the *a*-axis. The colored planes indicating the π-π stacking interactions for each TBP offer perspective on the orientation of the molecules. 278

Figure 5-17. Temperature dependent susceptibility data for Fe_3Co_2 with tmphen (8). The order of measurement follows the order of the legend where the orange circles were 1st, the yellow circles 2nd, the dark green circles 3rd and the light green circles are the 4th measurement. 283

Figure 5-18. Temperature dependent susceptibility data for Fe_3Co_2 with 4dmbpy (9). The order of measurement follows the order of the legend where the orange circles were 1st, the yellow circles 2nd, the dark green circles 3rd and the light green circles are the 4th measurement. 286

Figure 5-19. Temperature dependent susceptibility data for Fe_3Co_2 with 5dmbpy (10). The orange circles are the data for the sample as it was warmed from 2 K to 390 K for the 1st time and the light green circles are the data as the sample was cooled from 390 K to 2 K for the 2nd time. 288

Figure 5-20. Temperature dependent susceptibility data for Fe_3Co_2 with tmbpy (11). The order of measurement follows the order of the legend where the orange circles are 1st, the yellow circles 2nd, the dark green circles 3rd and the light green circles are the 4th measurement. 290

Figure 5-21. Comparison of the temperature dependent susceptibilities for compounds 8-11 before (top) and after (bottom) solvent is removed. 292

LIST OF TABLES

Page

Table 1-1. Experimental and theoretical ordering temperatures reported for PBAs where M = free metal ion and M' = hexacyanometallate. 41

Table 1-2. Table illustrating the homologous family of TBPs reported by the Dunbar group (denoted with a ✓). Highlighted boxes are the TBPs that are the focus of the work presented in this dissertation. 46

Table 2-1. Cyanide stretching frequencies for $(PPN)_3[M^{III}(CN)_6]$, (M = Fe, Ru and Os). 79

Table 2-2. Crystal data and refinement parameters for single crystals of 1 and 2. 82

Table 2-3. Pertinent bond lengths for compounds 1 and 2. 83

Table 2-4. Half potentials for the reduction of $(PPN)_3[M^{III}(CN)_6]$. 93

Table 3-1. Cyanide stretching frequencies for compounds 3 and 4 along with the $K_4[M^{II}(CN)_6]$ and $(PPN)_3[M^{III}(CN)_6]$ starting materials as references. 106

Table 3-2. Room temperature IR $\nu_{C\equiv N}$ for the Zn_3Os_2 TBP (5). 107

Table 3-3. SQUEEZE analysis and results for the Co_3Ru_2, Co_3Os_2 and Zn_3Os_2 TBPs. 109

Table 3-4. Structural data and refinement parameters for compounds 3 – 6. 110

Table 3-5. M–L bond lengths for the asymmetric units of the Co_3Ru_2 and Co_3Os_2 TBPs. 114

Table 3-6. Geometric parameters (centroid-centroid distances, shift distances and angles between planes) for the inter- and intramolecular π-π stacking interactions in the Co_3M_2 TBPs (3 and 4). 116

Table 3-7. M–L bond lengths (in Å) for the Zn_3Os_2 TBP (5). 120

Table 3-8. Geometric parameters (centroid-centroid distances, shift distances and angles between planes) for the inter- and intramolecular π-π stacking interactions in the Zn_3Os_2 TBP (5). 121

Table 3-9. M-L bond distances (in Å) for Mn_2Ru_2 (6). 126

Table 3-10. Geometric parameters (centroid-centroid distances, shift distances and angles between planes) for the inter- and intramolecular π-π stacking interactions in Mn_2Ru_2 (6). 128

Table 3-11. Possible spin-transitions for the Co_3Os_2 TBP and the $\Delta\chi T_{spin\text{-}only}$ values associated with those transitions. If the transition involves an electron transfer, the additional change in χT due to the Os contribution is in the last column. 132

Table 4-1. Cyanide stretching frequencies from IR spectroscopy. 152

Table 4-2. Interstitial solvent molecules in the Fe_3Ru_2 TBPs according to TGA data. 154

Table 4-3. Crystal structure data and refinement parameters for the solvated Fe_3Ru_2 TBP at multiple temperatures. 160

Table 4-4. Void space and residual electron density for the solvated Fe_3Ru_2 TBPs (7a), as calculated from SQUEEZE analysis. Interstitial solvent was calculated using the electron density and the solver add-in in Excel 2013. 161

Table 4-5. Metal–Ligand (M–L) bond lengths (in Å) for the solvated Fe_3Ru_2 TBP (7a). 163

Table 4-6. Geometric parameters (centroid-centroid distance, shift distance and angle) for the inter- and intramolecular π-π stacking interactions in the solvated Fe_3Ru_2 TBPs (7a). The average values (avg) and the differences between the minimum and maximum values (Δ) have been included. *Indicates symmetry equivalent metal center 169

Table 4-7. Crystal structure data and refinement parameters for the Fe_3Ru_2 TBP evacuated for 24 hours. 171

Table 4-8. Void space and residual electron density for the Fe_3Ru_2 TBPs exposed to vacuum for 24 hours (7d), as calculated from

SQUEEZE analysis. Interstitial solvent was calculated using the electron density. 171

Table 4-9. M–L bond lengths (in Å) for the Fe_3Ru_2 TBP under vacuum for 24 hours (7d). 172

Table 4-10. Geometric parameters (centroid-centroid distances, shift distances and angles) for the inter- and intramolecular π-π stacking interactions in the 24 hour evacuated Fe_3Ru_2 TBPs at 150 K. *Indicates symmetry equivalent metal center. 173

Table 4-11. Crystal structure data and refinement parameters for the humid Fe_3Ru_2 TBP at multiple temperatures. 176

Table 4-12. Void space and residual electron density for the humid Fe_3Ru_2 TBPs (7e), as calculated from SQUEEZE analysis. Interstitial solvent was calculated using the solver add-in in Excel 2013 by considering both the electron density and void space. Water was treated as occupying 40 Å. 177

Table 4-13. M–L bond distances (in Å) for the humid Fe_3Ru_2 TBP (7e). 179

Table 4-14. Geometric parameters (centroid-centroid distance, shift distance and angle) for the inter- and intramolecular π-π stacking interactions in the humid Fe_3Ru_2 TBPs (7e). The average values (avg) and the differences between the minimum and maximum values (Δ) have been included. *Indicates symmetry equivalent metal center..... 185

Table 4-15. Typical and spin-only χT values and electronic configurations of Fe and Ru. 190

Table 4-16. Types of spin-transitions possible in the Fe_3Ru_2 TBP. The spin-only values of χT are used for the Δ values. If a charge transfer (CT) is involved, then the ΔχT associated with the Ru is included in the last column. 191

Table 4-17. ^{57}Fe Mössbauer data collected with no applied field for 7a. 205

Table 4-18. ^{57}Fe Mössbauer data for 7b at 4.2 K and 150 K. 209

Table 4-19. ^{57}Fe Mössbauer parameters for 7c at 150 K and 250 K in zero field. 211

Table 4-20. ^{57}Fe Mössbauer data for 7d at 4.2 K, 250 K and room temperature. 214

Table 4-21. ^{57}Fe Mössbauer data for 7e at 4.2 and 150 K collected with zero field. 217

Table 5-1. The $\nu_{C\equiv N}$ and H_2O stretching/bending modes for compounds 8-11 and $(PPN)_3[Co^{III}(CN)_6]$ for comparison. 240

Table 5-2. SQUEEZE analysis and calculated interstitial solvent for compounds 8-11. 243

Table 5-3. Crystal structure data and refinement parameters for the Fe_3Co_2 TBP with tmphen (8). 245

Table 5-4. The M–L bond distances (in Å) for the Fe_3Co_2 TBP with tmphen (8). 247

Table 5-5. Geometric parameters (centroid-centroid distance, shift distance and angle) for the inter- and intramolecular π-π stacking interactions in the Fe_3Co_2 TBP with tmphen (8). The average values (avg) and the differences between the minimum and maximum values (Δ) have been included. *Indicates symmetry equivalent metal center 251

Table 5-6. Structural data and cell refinement parameters for compound 9 at variable temperatures. Structural data at 20 K is for a different crystal than the data at 100, 200 and 250 K which were obtained on the same crystal. 254

Table 5-7. The M–L bond distances (in Å) for the Fe_3Co_2 TBP with 4dmbpy (9) 255

Table 5-8. Geometric parameters (centroid-centroid distance, shift distance and angle) for the inter- and intramolecular π-π stacking interactions in the Fe_3Co_2 TBP with 4dmbpy (9). The average values (avg) and the differences between the minimum and maximum values (Δ) have been included. *Indicates symmetry equivalent metal center 260

Table 5-9. Crystal structure data and refinement parameters for the Fe_3Co_2 TBP with 5dmbpy (10). 263

Table 5-10. The M–L bond distances (in Å) for the Fe_3Co_2 TBP with 5dmbpy (10) 263

Table 5-11. Geometric parameters (centroid-centroid distance, shift distance and angle) for the intramolecular π-π stacking interactions in the Fe_3Co_2 TBP with 5dmbpy (10). 265

Table 5-12. Crystal structure data and refinement parameters for the Fe_3Co_2 TBP with tmbpy (11). 269

Table 5-13. The M–L bond distances (in Å) for the Fe_3Co_2 TBP with tmbpy (11)..... 271

Table 5-14. Geometric parameters (centroid-centroid distance, shift distance and angle) for the intramolecular π-π stacking interactions in the Fe_3Co_2 TBP with tmbpy (11). The average values (avg) and the differences between the minimum and maximum values (Δ) have been included. 274

Table 5-15. Number of π-π stacking interactions found by Olex2 in the Fe_3Co_2 TBPs with different capping ligands (8-11). *Indicates very weak interactions that could be considered irrelevant by literature standards. 277

Table 5-16. Temperatures where the χT = 4.0 emu·K/mol is observed for the samples before and after losing solvent. This χT value was chosen as a representative value for 1 HS Fe^{II} center based upon the maximum χT value reached for compound 8 at 390 K. 293

Table 5-17. Comparison of χT values (before solvent loss) for molecules 8-11 at 2 K, 300 K and 390 K..... 293

Table 5-18. Comparison of χT values for compounds 8-11 at 2 K and 300 K before losing solvent (initially) and after losing solvent (after warming). Solvent content was determined through a combination of the difference in mass of the sample before and after measurement in the SQUID and analysis of the sample with TGA after being measured in the SQUID. 294

Table 6-1. Summary of the transition events on the Fe centers in the Fe_3Ru_2 TBPs (7a-e). 300

Table 6-2. A summary of the electronic configurations that are observed for the TBPs discussed. * Indicates when the transition is not complete. The state that is given with the * is the majority of the spin state present. # Indicates an incomplete charge transfer process where the majority of the observed configuration is

given. Note that there is no change in electronic configuration of the Co_3Ru_2 TBP. 302

LIST OF EQUATIONS

Page

Equation 1-1 4
Equation 1-2 5
Equation 1-3 5
Equation 1-4 6
Equation 1-5 7
Equation 1-6 7
Equation 1-7 7
Equation 1-8 9
Equation 1-9 14
Equation 1-10 14
Equation 1-11 14
Equation 1-12 14
Equation A-1 322

CHAPTER I

INTRODUCTION TO CYANIDE MOLECULAR MAGNETISM AND SPIN-CROSSOVER BEHAVIOR

Magnetic materials are interesting topics of study for many interdisciplinary fields. Magnetism plays a crucial role in biology as well as human technology. For example it is known that some animals, especially those that are migratory in nature, use the earth's magnetic field for magnetic homing, or navigation.[1-4] The detection of a magnetic field by animals (magnetoreception) is rendered possible in two different ways: the animal contains magnetic nanoparticles (like in the abdomen of a honey bee[5]) able to respond to the geomagnetic field and/or chemical reactions that are influenced by magnetic fields occur within the animal.[6] Magnetoreception has been discovered in bacteria, mollusks, arthropods and in major taxonomic groups of vertebrates but not in humans. It is said that a cryptochrome (a flavoprotein sensitive to blue light) in the human eye could serve this purpose however.[7]

Magnetic materials have also been utilized throughout civilization as a way for humans to navigate, albeit externally instead of internally as in nature. At the turn of the second millennium, the Chinese carved lodestone (magnetite, or Fe_3O_4) into the shape of a spoon, mounted it on a base to align its handle with the Earth's magnetic field and called it a "South Pointer". In 1088 Shen Kuo described a navigational compass based on a steel needle magnetized in the Earth's field.

Reinvention of this compass in Europe a century later led to the discovery of Africa by Cheng Ho in 1433 and the Americas by Christopher Columbus in 1492. It wasn't long until some of the most brilliant minds of the past few centuries began to study magnets as a means for more than just their navigational ability and discovered the connection between electricity and magnetism. In Denmark in 1820 Hans-Christian Oersted stumbled across this connection by showing that a current-carrying wire produced a field capable of deflecting a compass needle. The electromagnetic revolution was launched a few weeks later when André-Marie Ampère, in Paris, wound wire into a coil and demonstrated that the current-carrying coil was equivalent to a magnet. In 1821 Michael Faraday discovered electromagnetic induction and used a steel magnet, a dish of mercury and a current-carrying wire to demonstrate the principle of the electric motor. In 1845 he discovered a connection between light and magnetism with the Faraday effect. All of this led to the formulation of a unified theory of electricity, magnetism and light by James Clerk Maxwell in 1864 which is the foundation of our classical understanding of these fields. These impressive discoveries and advancements in the early history of human civilization forever changed the world and all of this was before the electron was discovered in 1897, a true testament to the belief "that fundamental understanding of the science may not be a prerequisite for technological progress."[8] Today, technological progress has developed into a ubiquitous relationship between technology and magnets, as nearly all electronics, motors and generators require magnetic materials. The technological

industry is not alone in the utilization of magnetic materials, as the cosmetics, electronics, energy production, health and transportation industries (just to name a few) all use magnets as well. These latter industries rely on permanent magnets as they have become the basis of many devices in modern life.

Currently, there are four main types of permanent magnets commonly used: NdFeB and SmCo which are rare earth magnets used in motors, automobiles, telephones, monitors, audio systems, credit cards, imaging devices, etc and AlNiCo and ferrite which are cheaper, more brittle magnets that are used in many household products, DC motors, MRI machines, tools, etc.[9] The global permanent magnet industry is dominated by ferrite and AlNiCo as their raw materials are cheaper which leads to lower manufacturing costs. The magnetic materials market overall is expected to grow from a $13.4 billion industry (2015) to a $96 billion industry in 2020 with the growth being driven by the automotive industry, the modernization of infrastructure, and the development of innovative technologies.[10]

Basic Magnetic Principles

As amply demonstrated by the aforementioned discussion, magnetic materials play a crucial role in modern society and the advancement of various technologies. As such, a basic understanding of magnetism is a fundamental exercise in being educated as a scientist. A brief introduction of some pertinent concepts and equations necessary to understand the research presented herein

will be given.

Magnetism arises from two sources: electric current and magnetic moments of elementary particles, the latter of which will be the focus of this discussion. Magnetic moments result from intrinsic properties of the spin and electric charge of the particles. Due to the fact that magnetic moments of protons are thousands of times smaller than moments of electrons, they are considered negligible in the discussion of magnetization of materials. The electron is a charged particle that has both spin and orbital angular momentum. As the charged electron rotates due to these motions, it creates a magnetic dipole with magnetic poles of equal magnitude that are opposite in polarity, akin to a small bar magnet that has north and south poles. In simplest terms, this magnetic dipole moment, m, can be quantized with a value equal to:

$$m = g\frac{-e}{2m_e}L = -g\mu_B\frac{L}{\hbar} \qquad \textbf{Equation 1-1}$$

where g is a dimensionless quantity that relates the observed magnetic moment to its angular momentum and a unit of magnetic moment (like the Bohr magneton, μ_B, 9.27 x 10^{-24} $J \cdot T^{-1}$), e is the charge of an electron (1.6 x 10^{-19} C), m_e is the electron mass (9.109 x 10^{-31} AMU), L corresponds to angular momentum (due to spin and/or orbital contributions) and $\hbar$ is Planck's constant (1.054 x 10^{-34} J/s).

This value tends to reach unity when orbital angular momentum is ignored and $g_e \approx 2$. When orbital contribution can be ignored, or any other interactions, the effective magnetic moment has a magnitude dependent upon the spin, S:

$$m_{eff} = g_e S(S+1)\mu_B^2 \qquad \textbf{Equation 1-2}$$

Usually, materials have many magnetic moments and the magnetic moment per volume of sample is known as magnetization, M. Magnetization is proportional to an applied magnetic field (H) as expressed by:

$$\chi_m = {}^{M}/_{H} \qquad \textbf{Equation 1-3}$$

where χ_m is the molar susceptibility which indicates how responsive a material is to an applied magnetic field and χT (the susceptibility multiplied by temperature) is the value most often used in magnetic analysis. **Note: Any discussion of χ or χT in this dissertation refers to χ_m or $\chi_m T$.** Equation 1-3 is valid when large fields are applied or at low temperatures. When a magnetic field (H) is applied to the molecules, the magnetization can either be attracted to the field as is the case in

paramagnetic materials (those having unpaired electrons) or repelled by the field as is the case with diamagnetic materials (those having no unpaired electrons).

Diamagnetism is present in all molecules as it is intrinsic to all atoms and bonds but it is a minor effect in the scheme of things as it is much smaller than the paramagnetic form of magnetism. As it still contributes to the overall susceptibility of the material, it must be taken into account and corrected for so that the true paramagnetic susceptibility of the molecules can be obtained. This can be done using:

$$\chi = \chi^D + \chi^P \qquad \textbf{Equation 1-4}$$

where χ^D and χ^P represent the diamagnetic and paramagnetic susceptibilities, respectively. The former is negative and repelled by a field while the latter is positive and attracted by a field. The diamagnetic contribution is independent of temperature and applied field and includes diamagnetism that is intrinsic to the atoms and bonds within the material as well as any contribution to the susceptibility from solely diamagnetic molecules (ie: solvent). The intrinsic contribution can be calculated from known values called Pascal's constants (usually denoted as χ^0). A very nice paper from Gordon Bain and John Berry in the Journal of Education explains how to calculate these constants.[11]

Paramagnetism encompasses different behaviors: paramagnetism, ferromagnetism, antiferromagnetism and ferrimagnetism. When the magnetic moments are considered magnetically dilute, in other words there is no interaction between them, a material is considered to be paramagnetic throughout all temperatures. When a field is applied, magnetic moments tend to orient themselves toward the same direction of the magnetic field. However, in paramagnetic materials, the thermal energy is sufficient to lead to effective random orientations of the magnetic moments. What ensues is a magnetization that has an inverse dependency on temperature, known as the Curie law:

$$\chi_m = {}^{C}/_{T} \qquad \textbf{Equation 1-5}$$

$$C = \frac{N_A m^2}{3k_B} = \frac{N_A}{3k_B} g_e^2 S(S+1)\mu_B^2 \qquad \textbf{Equation 1-6}$$

$$\chi_m T = C \approx \frac{g^2 S(S+1)}{8} \qquad \textbf{Equation 1-7}$$

where C is the Curie constant and is characteristic of the atomic or molecular species concerned, N_A is Avogadro's number and k_B is the Boltzmann's constant (1.38×10^{-23} $J \cdot K^{-1}$). This is the simplest situation in magnetism when first-order

angular momentum effects can be neglected and a large separation in energy from the ground state to the first excited states exists so that there is no coupling between these states. The value of χT can then be calculated by solving for the Curie constant (Equation 1-7). Many paramagnetic materials do not obey Curie's law however, because interactions between moments cannot be neglected. When there is short or long range interaction between the magnetic moments of individual atoms or molecules ferromagnetism, antiferromagnetism or ferrimagnetism is usually observed. Like paramagnetic substances, the magnetic moments tend to align with a magnetic field but have an additional tendency to orient themselves to each other as well due to the intrinsic field generated by each moment. In ferromagnetic materials the moments align themselves parallel to each other so that the net magnetic response is greater than in a paramagnet below its Curie temperature, T_c, which is the temperature at which the material loses its permanent magnetic properties and thermal energy causes the magnetic moments to revert to a state of disorder. Below the T_c, the material retains its magnetization once the applied field is removed. Antiferromagnetic materials are similar to ferromagnetic materials except that the moments align antiparallel to one another below the Néel ordering temperature, T_N, resulting in a zero net magnetization. Ferrimagnetic behavior occurs from antiferromagnetic interactions of unequal magnitudes of the moments which results in a net magnetic moment that is retained below T_c once the applied magnetic field is removed. Most ferrites (such as magnetite) exhibit ferrimagnetic behavior. Figure 1- illustrates how the

magnetic moments align for each of these paramagnetic behaviors. In 1907, P. Weiss had postulated the existence of these internal interactions between localized moments, which he termed a “molecular field”, and revised the Curie law to explain the temperature dependence of the susceptibility exhibited by most paramagnetic materials to what is known as the Curie-Weiss law, given by:

$$\chi = \frac{C}{T - \theta} \qquad \textbf{Equation 1-8}$$

where θ indicates the strength and type of interaction and is known as the Weiss constant or Weiss temperature. Paramagnetic materials that strictly obey Curie’s law have a θ = 0 while ferromagnetic materials have a positive θ and ferri- and antiferromagnetic materials have a negative θ. Figure 1-2 is a schematic of the susceptibility (top) and inverse susceptibility (bottom) versus temperature for paramagnetic, ferromagnetic and antiferromagnetic materials. The χ vs T plot shows the expected behavior in χ above and below the spontaneous ordering that occurs at T_c for ferromagnetic materials or T_N for antiferromagnetic materials in comparison to a paramagnetic material. The χ^{-1} versus temperature plot (bottom of Figure 1-2) shows the expected response of the inverse susceptibility as a function of temperature for the different paramagnetic behaviors. The x-intercept of a linear fitting of the high temperature region where the material mostly obeys

the Curie law by acting as a paramagnet with no internal molecular interaction with neighboring moments gives the Weiss constants. Note the negative intercept of the fit line for an antiferromagnetic material that results in a negative Weiss constant. Ferrimagnetic materials behave similarly to ferromagnetic materials in these representations. As temperature dependent susceptibility (χT) is commonly plotted for magnetic materials, Figure 1-3 illustrates how the magnetic moments for these different paramagnetic behaviors respond to an applied field as a function of temperature.

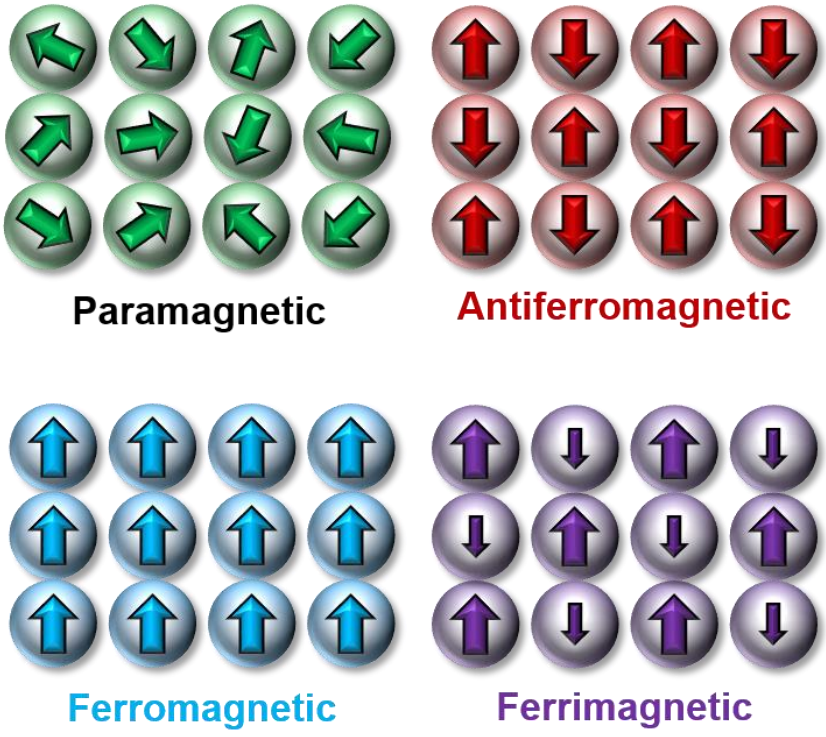

Figure 1-1. Illustration of how the magnetic moments align in paramagnetic (random), antiferromagnetic (antiparallel), ferromagnetic (parallel) and ferrimagnetic (antiparallel with unequal magnitudes) materials.

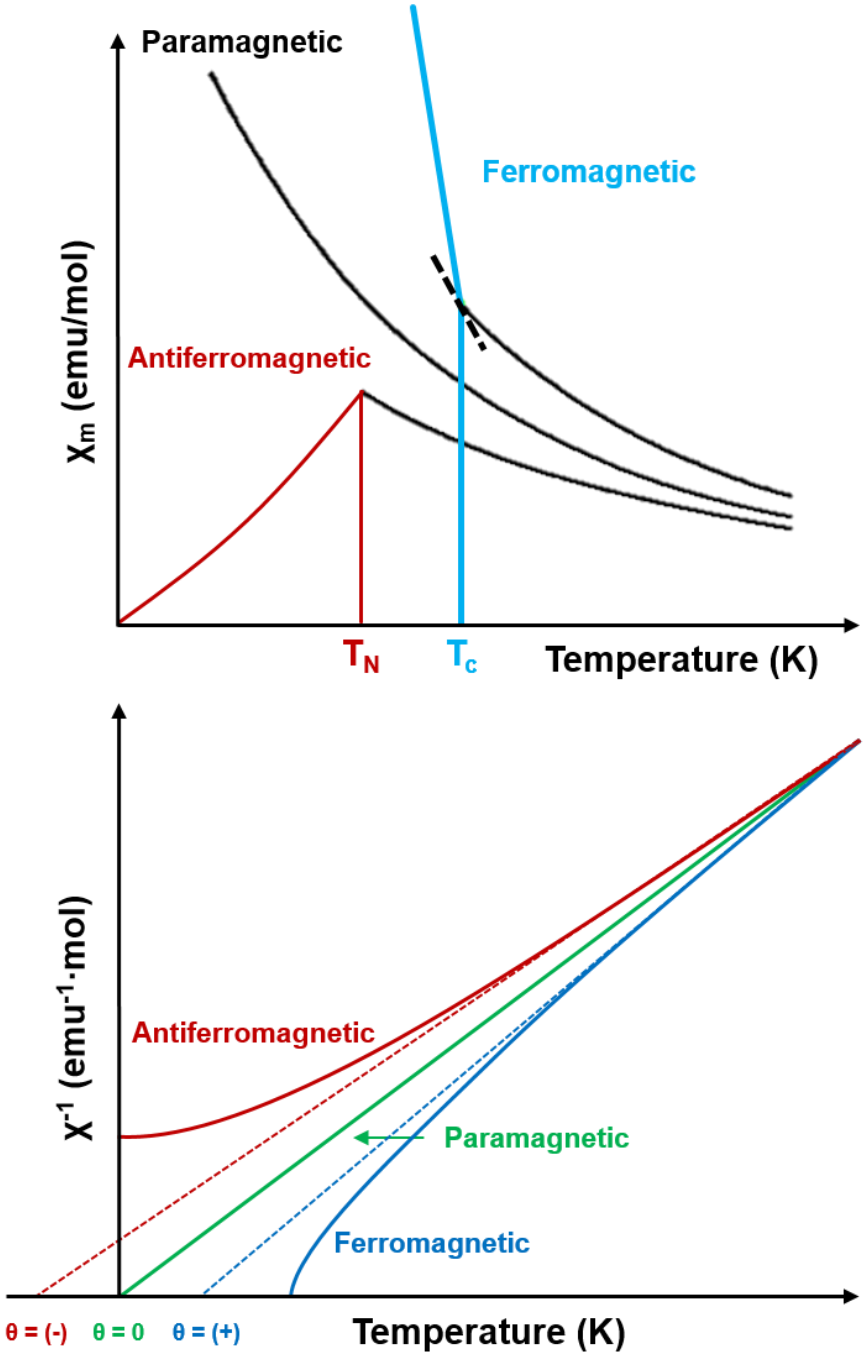

Figure 1-2. Representation of the expected behavior of the susceptibility (top) and inverse susceptibility (bottom) of paramagnetic (green), ferromagnetic (blue) and antiferromagnetic (red) materials when plotted as a function of temperature.

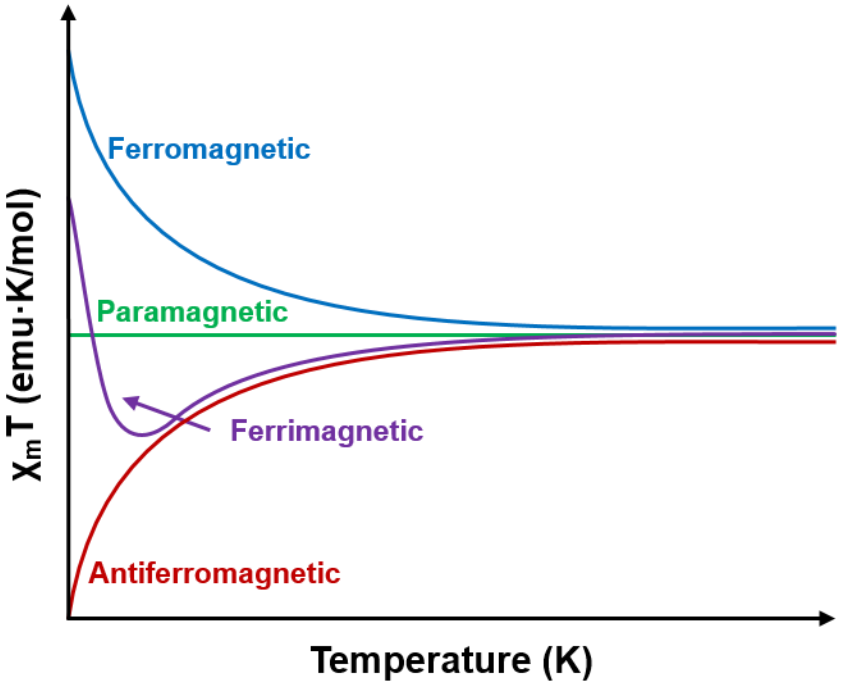

Figure 1-3. Schematic of the behavior of the χT vs temperature curves for paramagnetic (green), ferromagnetic (blue), antiferromagnetic (red) and ferrimagnetic (purple) materials.

Until now, compounds with thermally isolated ground states and void of orbital contributions have been considered. When considering a diamagnetic compound, the expected susceptibility in this case is zero. However, Van Vleck formulated that a paramagnetic contribution that is independent of temperature can arise if the ground state is mixed into excited states when a field is applied if the excited states are close in energy to the ground state. This contribution is known as temperature-independent paramagnetism (TIP) and like diamagnetism, is a property of all molecules. TIP is usually on the same order of magnitude as

diamagnetism (10^{-6}), but of opposite sign and is not restricted to materials with a diamagnetic ground state. TIP also occurs in paramagnetic materials when a magnetic ground state couples to non-thermally populated excited states.

Thus far, the classical magnetism discussed has been in the limit of considering angular momentum that arises from the spin of the electron while neglecting any orbital angular momentum. Often, the use of spin-only values (especially when considering some 3d metals) is a good approximation for most materials. However, orbital angular momentum cannot be ignored for some metal ions (particularly lanthanides), as the orbital momentum of the electrons is not quenched. This results in deviations of the χT values from the expected spin-only ones. These differences are expressed in the magnitude of the g-factor in Equation 1-7. An anisotropic value of g that deviates from the isotropic, spin-only $g_e = 2.00232$ is a direct indication of orbital angular contributions. Typically, transition metals with less than five electrons will have g values less than 2 while transition metals with more than 5 electrons typically have g values greater than 2.

As mentioned before, the susceptibility relates the magnetization with the applied field, as long as $H/k_BT \ll 1$. In magnetism, to determine the electronic ground state of a compound experimentally, a sample is measured at the lowest temperature possible (usually 1.8 K) to prevent the thermal population of excited states between fields of 0 – 7 Tesla (T). The molar magnetization can be calculated with the help of the Brillouin function:

$$M = N_A g \mu_B S B_s(y) \qquad \textbf{Equation 1-9}$$

$$y = \frac{g\mu_B SH}{k_B T} \qquad \textbf{Equation 1-10}$$

$$B_s(y) = \frac{2S+1}{2S}\coth\left(\frac{2S+1}{2S}y\right) - \frac{1}{2S}\coth\left(\frac{1}{2S}y\right) \qquad \textbf{Equation 1-11}$$

where $B_s(y)$ is the Brillouin function (Equation 1-11). When H/k_BT is small the Curie law holds and $\chi = M/H$. However, when H/k_BT becomes large (like it does during these experimental measurements as the field is increased while the temperature remains constant), $B_s(y)$ tends to unity and M tends to saturate at the M_s value:

$$M_s = N_A g \mu_B S \qquad \textbf{Equation 1-12}$$

In other words, assuming an isotropic g-factor, if there is one unpaired electron in the ground state, a saturation of the magnetization occurs near 1 μ_B. If there are two unpaired electrons in the ground state, then the magnetization occurs near 2 μ_B etc... Figure 1-4 shows a plot depicting magnetization at 1.8 K that follows a

Brillouin function with an isotropic g-factor for S = ½, S = 1 and S = ⅜ ground states. Deviations from this curve can be due to several factors, the simplest of which is the population of low lying excited states and dipolar interactions as well as anisotropic effects. For a more in-depth explanation of the basic magnetic concepts presented above as well as to gain a more comprehensive knowledge of magnetism, refer to several books cited here.[8,12-16]

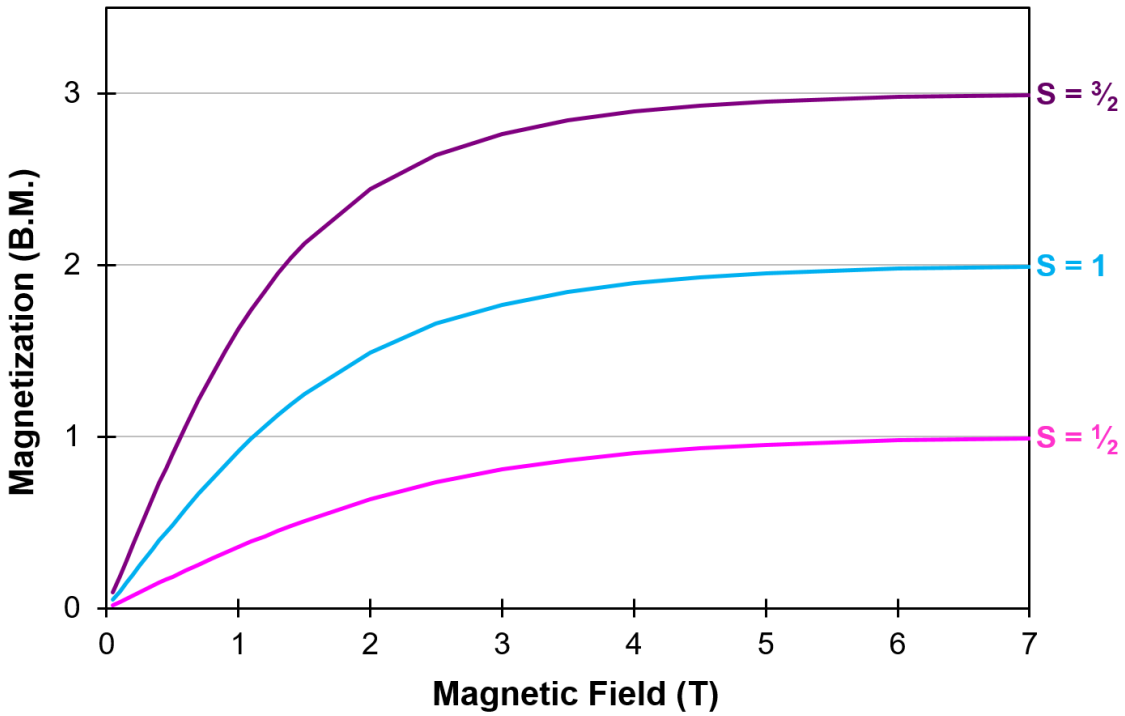

Figure 1-4. Theoretical magnetization curves (in Bohr magnetons) at 1.8 K for ground states of S = ½, S = 1 and S = ⅜ systems that follow a Brillouin function.

Molecular Magnetism

The previously discussed applications rely on classical, or bulk magnets that involve metals such as Fe, Co, Ni, rare earths (or a combination thereof) or metal oxides such as magnetite, Fe_3O_4. These metallic and ionic materials remain magnetized above room temperature after the magnetizing field has been removed, hence their status as permanent magnets. They are usually prepared by a method called Powder Metallurgy which involves pulverizing the materials into a fine powder, aligning the particles just before compacting them and then heating the powder in an induction melting furnace at high temperatures to cause densification through liquid phase sintering. In the case of the SmCo and Nd magnets, the pulverized powder must be protected from oxygen as it is chemically reactive and capable of igniting spontaneously in air.[17]

Since 1955, data storage devices have relied on a medium of iron oxide particles coated on a platter commonly made of aluminum or glass. Currently, they rely on a thin film of magnetic material made of a Co alloy. These materials are reaching a density limit and as technology advances, modern society requires high-density data storage devices capable of storing the massive amounts of data. To overcome these limitations a new approach to the design of low-dimensional magnetic materials that retain their magnetization above room temperature is required. This approach has helped usher in the transitioning from magnetochemistry (referred to by Carlin[12] as a branch of chemistry which uses physical measurements to obtain structural information on simple paramagnetic

systems with the use of magnetic techniques) to the recent field of study (early 1980s) in molecular magnetism (referred to by Kahn[15] as an interdisciplinary field driven by the collaboration of chemists and physicists to design, synthesize and model phenomenological properties of magnetic materials of increasing complexity).[16] The first step towards the realization of room temperature ordered materials in molecular magnetism was achieved by Kahn's and Verdaguer's groups when they reported the first molecular ferrimagnet based on Cu^{II}-Mn^{II} derivatives.[18] In 1991, Miller's group made the first major breakthrough in preparing high temperature (Tc = 350 K) magnets with the first room temperature ferrimagnet based on V^{II} with TCNE (TCNE = tetracyanoethylene) being isolated.[19]

Other than the obvious advantage of lower density in molecular over solid state materials, other advantages include easier synthetic processes as they are generally prepared at lower temperatures, they have higher solubility for processing into films or nanostructures and allow for easier synthetic tuning of their intrinsic properties. Discrete molecules are also advantageous because their size allows for a simplification of theoretical models which can guide synthetic chemists in the preparation of high temperature magnets.

Molecular magnetism has also been shown to have potential applications in spintronics. Since the invention of the silicon-based integrated circuits in 1959, the demand to miniaturize electronic devices has grown exponentially as well as the demand for smaller, high-density data storage devices. In 1965 Gordon Moore

made a 10-year prediction known as Moore's Law, that states the number of transistors in an integrated circuit should double every two years[20] This law has remained relevant and the minimum size of the transistor has decreased from 10,000 nm in 1971 with the Intel C4004 microprocessor to 14 nm in their current technology as of 2016.[21] However, the technological and physical limitations of the materials currently used in these devices are rapidly approaching.[22-24] Although main-stream devices based on molecular materials have not been realized yet, the field has demonstrated that molecular magnetic materials hold promise for the advancement of technology due to behaving as high temperature magnets,[25-28] molecular switches,[29-31] single molecule magnets (SMMs)[32-34] and molecular logic gates,[35,36] to name a few. These findings have led to additional goals for the field of molecular magnetism of preparing materials that exhibit other interesting magnetic and electrical phenomena that are not observed in classical magnets, such as spin-crossover (SCO), charge-transfer-induced-spin-transition (CTIST), photomagnetism and multifunctionality.[37]

Molecular Bistability

The underlying principle behind molecular magnetism for applications such as information storage and processing is molecular bistability which is the ability of a molecule to exhibit two stable states within a range of external perturbations (ie: temperature, pressure, light, magnetic field, etc…). In this respect, the discovery of the first SMM in 1991 (fully characterized and defined in 1993),

$[Mn_{12}O_{12}(O_2CCH_3)_{16}(H_2O)_4]\cdot 4H_2O\cdot 2CH_3CO_2H$,[38-40] brought a surge of renewed focus to the field of molecular magnetism due to the ability of SMMs to exhibit magnetic hysteresis of a molecular origin below a certain blocking temperature without requiring long-range ordering of the magnetic moments, unlike conventional and molecule-based magnets.[41] Currently, the highest blocking temperature achieved for SMMs is 20 K for a mononuclear Dy^{III} molecule in a trigonal bipyramidal geometry, $[Dy(Cy_3PO)_2(H_2O)_5]Br_3\cdot 2(Cy_3PO)\cdot 2H_2O\cdot 2EtOH$ (Cy_3PO = tricyclohexyl phosphine oxide) and was reported in 2016.[42] Previously, the record of 14 K was reported for a radical-bridged diterbium complex, $\{[(Me_3Si)_2N]_2(THF)Tb\}_2(\mu\ \eta^2{:}\eta^2\text{-}N_2)^-$, in 2011.[43] Although SMMs remain of great interest to the molecular magnetic community due to their interesting properties, their potential use in household devices will remain theoretical until the blocking temperatures can be increased to more practical temperatures. This is where materials that exhibit other forms of bistability may have an advantage over SMMs for data storage and spintronics as their switching behavior can occur closer to room temperature.[44]

Spin-crossover (SCO)

SCO is a thriving area of study in molecular magnetism with many subcategories of interest.[45-48] Active areas of SCO research include studies that aim to tune the transition temperature,[49,50] prepare guest-dependent SCO,[51-54] pressure-induced SCO[55-57] and multi-functional SCO compounds.[58-60] Much of the

focus in SCO revolves around preparing compounds that exhibit wide[61-63] and multi-step hysteresis loops[64] that span room temperature because these materials have the potential to be used in memory devices. Many books[65-69] and reviews[70-77] have been written about SCO since its discovery in 1931;[78] a testament to the importance of this phenomenon.[65,66] The design, rather than trial and error, of SCO materials that exhibit useful technological properties remains a challenge for researchers as SCO behavior is extremely sensitive to subtle changes. Prediction of SCO behavior through experimental and theoretical studies is a major goal in the field of SCO. Much of the work presented in this dissertation focuses on SCO and how chemical and physical perturbations affect the transition behavior in pentanuclear, cyanometallate-containing compounds.

SCO is a reversible electronic transition between a low-spin (LS) electronic state and a high-spin (HS) electronic state due to application of an external stimulus such as heat, light and/or pressure. SCO typically occurs in 3d transition metals in an octahedral coordination environment with 4 to 7 electrons and is dependent upon the interplay between the strength of the ligand field (Δ) and the spin pairing energy (π) of the electrons. If the strength of the ligand field is less than the pairing energy ($\Delta \ll \pi$), then it is energetically favorable to comply with Hund's rule and the configuration with the most unpaired electrons will result, known as the HS state. If the strength of the ligand field is more than the pairing energy ($\Delta \gg \pi$), then it is energetically favorable for the electrons to pair so that

the least number of unpaired electrons results, known as the LS state. Figure 1-5 illustrates the interplay between Δ and π and Figure 1-6 illustrates the change in electronic configuration for the SCO in an octahedral Fe^{II} metal ion. When Δ and π have similar values that allow for SCO, the difference in energy between the LS and HS states is of the order of magnitude of the thermal energy (k_BT). During the transition, the pairing energy changes very little unlike the splitting energy of the ligand field. The strength of the ligand field varies for several reasons with the main one being the identity of the ligands. The spectrochemical series gives insight into the strength of the ligand field and whether or not SCO behavior is expected. With regards to some of the main ligands in the series:

Weak-field Ligands

$I^- < Br^- < S^{2-} < SCN^- < Cl^- < NO_3^- < F^- < OH^- < O^{2-} < H_2O < NCS^- < CH_3CN$

$< NH_3 \approx$ pyridine < bipyridine < phenanthroline < NO_2^- < PPh_3 < $CN^- \approx CO$

Strong-field Ligands

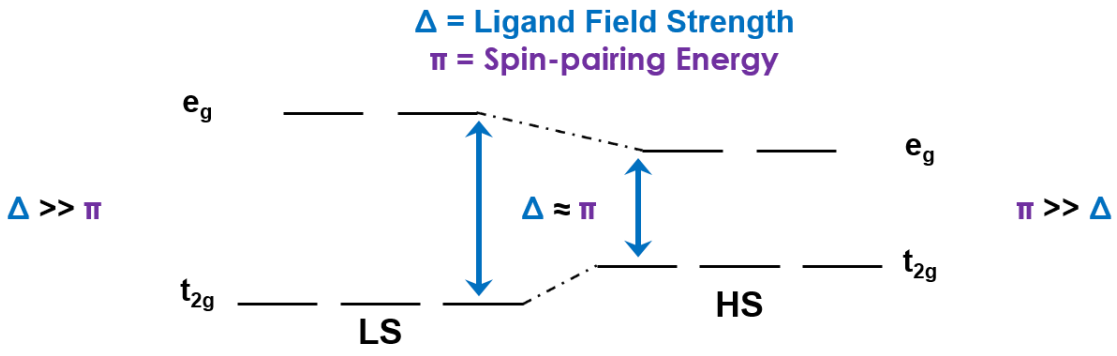

Figure 1-5. Schematic of the interplay between ligand field strength (Δ) and spin-pairing energy (π) on the spin state of an octahedral metal ion.

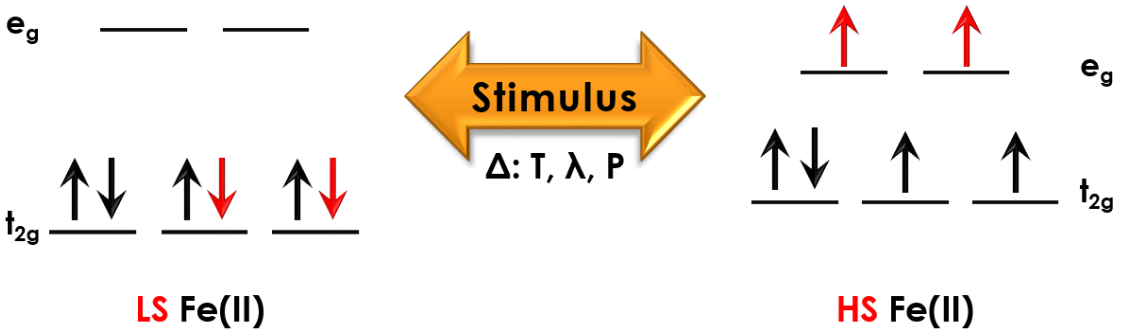

Figure 1-6. Depiction of the electron configuration for the LS and HS states of an Fe^{II} metal center in an octahedral coordination environment that undergoes SCO upon an external stimulus.

Ligand field strength also increases with increasing oxidation number (~700 – 3000 cm^{-1} for divalent species and 1200 – 3500 cm^{-1} for trivalent species) and upon moving down a group in the periodic table (~50% from 3d to 4d and ~25% from 4d to 5d metals).[79] The latter fact, in conjunction with the fact that spin pairing energies decrease for 4d and 5d metals is why SCO is not observed for 4d and 5d transition metal complexes. The former fact in addition to the requirement of needing a d^4 to d^7 electronic configuration is why SCO is only observed in divalent and trivalent metal centers. The most studied metal ion in SCO is Fe^{II} as it not only has the most favorable ligand field for SCO when surrounded by a nitrogen coordination environment, but it also undergoes the most drastic change in electronic configuration. The LS Fe^{II} ($t_{2g}^6 \rightarrow {}^1A_{1g}$, S = 0) is diamagnetic and acts as an "off" state whereas the HS Fe^{II} ($t_{2g}^4e_g^2 \rightarrow {}^5T_{2g}$, S = 2) is paramagnetic and acts as an "on" state, in terms of technological applications. Other metals that

commonly exhibit SCO include Fe^{III} and Co^{II}. To a lesser extent Cr^{II}, Mn^{II} and Mn^{III} compounds have shown thermal SCO in a few cases but most exist in the HS state.[80] Even fewer examples of SCO exist in Co^{III} complexes as only one type of Co^{III} complex based on two tridentate oxygen tripod ligands has been shown to be capable of SCO.[81] Other Co^{III} compounds exist solely as either LS or HS depending on the ligands' position in the spectrochemical series.

SCO Characterization Methods

Some of the physical methods that can be utilized to characterize SCO species are: SQUID magnetometry due to the change in magnetic moment, X-ray crystallography to monitor the change in M–L bond lengths, ^{57}Fe Mössbauer to probe the spin and oxidation states of Fe-containing compounds, differential scanning calorimetry (DSC) due to the evolution of heat, electronic absorption spectroscopy due to color changes and EPR spectroscopy. The dielectric constant and electrical resistance of the compound is also affected by the LS ↔ HS transition in SCO materials. For the sake of brevity, only the techniques discussed in the chapters of this dissertation will be discussed in detail. There are several reviews and books already referenced that lend insight into the myriad of changes that occur at the metal center with SCO and the techniques used to probe these changes.

SQUID Magnetometry

Several changes to the metal center occur as a result of SCO and are monitored by different characterization methods. Due to the changes in the number of unpaired electrons, the most common technique utilized to monitor thermal SCO behavior is magnetometry and the use of a Superconducting Quantum Interference Device (SQUID). A SQUID contained within a magnetic property measurement system (MPMS) allows for the measurement of magnetic materials between 1.8 – 400 K (most common temperature range) and in applied fields between 0 – 7 Tesla. SCO behavior is generally categorized by the type of cooperativity as depicted in Figure 1-7, ie: (a) gradual, (b) abrupt, (c) with hysteresis, (d) step-wise or multi-step and (e) incomplete.[68] The plots are given in terms of the molar fractions of HS molecules γ_{HS} as a function of temperature. The point where half of the molecule exists in the LS and HS states is marked by $T_{1/2}$ and is known as the transition temperature. More commonly, SCO behavior is represented with χT vs T plots as the expected value of χT can be estimated according to Equation 1-7. The shapes of the χT vs T plots are similar to the curves shown in Figure 1-7 for the same degree of cooperativity. Extrapolating molar fractions can be difficult for gradual or incomplete SCO so the data are usually displayed at χT vs T.

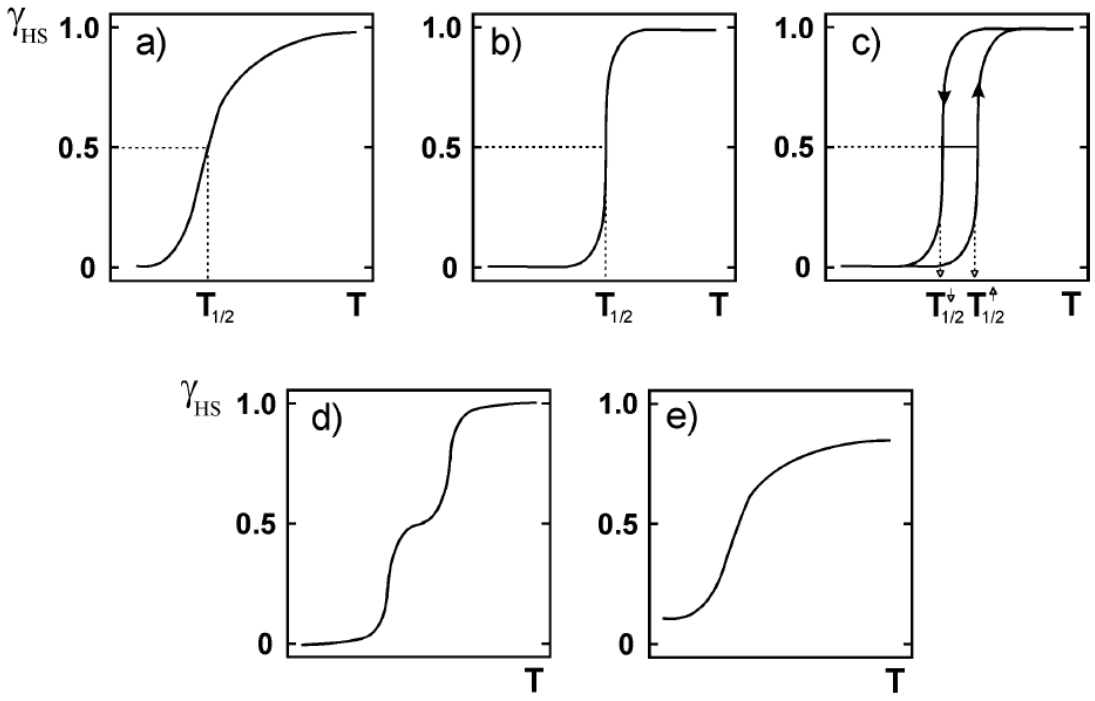

Figure 1-7. Types of SCO behavior categorized in terms of cooperativity: (a) gradual, (b) abrupt, (c) with hysteresis, (d) step-wise or muti-step and (e) incomplete. Plots are given as molar fractions of HS molecules γ_{HS} as a function of temperature. Reprinted with permission of Springer; copyright 2004, Springer Berlin Heidelberg. Adapted from reference 85.

X-ray Crystallography

Another common technique used to monitor the SCO event in compounds is temperature dependent X-ray crystallography due to the characteristic lengthening of the M–L bonds as the metal transitions from the LS to the HS state which results in an expansion of the octahedral coordination sphere as depicted in Figure 1-8. These changes are expected as there is a greater population of electrons in the antibonding e_g* orbitals when in the HS state. This effect is more

apparent for the Fe^{II} compounds coordinated to N in an octahedral environment ($\Delta S = 2$). The LS state has Fe^{II}–N bond lengths (~1.8 – 2.0 Å) that are usually ~10% shorter than in the HS state (~2.0 – 2.2 Å) which typically results in a change of bond lengths in the range of ~0.14 - 0.24 Å.[79,82] The typical range is ~0.11 – 0.15 Å for Fe^{III} ($\Delta S = 2$) and ~0.09 – 1.1 Å for Co^{II} ($\Delta S = 1$).[79] This effect can be seen with the diagram in Figure 1-9. At low temperatures the metal center is in the LS state, but increasing temperature leads to the population of excited vibrational levels up to the crossing point of the LS and HS energy curves where the geometry of both metal states are the same. The enthalpy gap that exists between the stronger M–L bonds (shorter) in the LS state and the weaker M–L bonds (longer) in the HS form must be overcome by the entropy of the system ($\Delta E < T\Delta S$) for SCO to occur.[79]

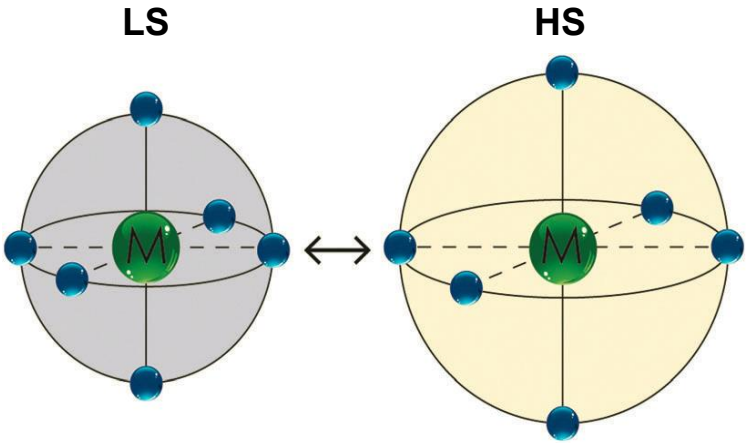

Figure 1-8. Depiction of the change in the octahedral coordination sphere of an Fe^{II} metal center upon SCO. The compound in the LS state is usually more intensely colored as compared to the HS state. Reproduced from reference 77; published by The Royal Society of Chemistry.

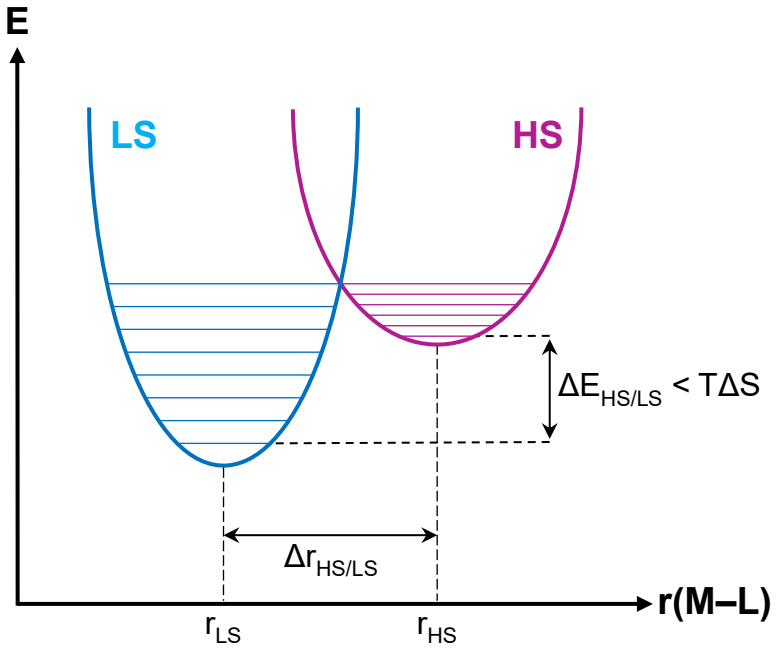

Figure 1-9. Depiction of vibrational components within the energy curves for the LS and HS states in a SCO system.

^{57}Fe Mössbauer Spectroscopy

^{57}Fe Mössbauer spectroscopy is a powerful tool for characterizing compounds containing iron and is particularly useful when there are different spin or oxidation states of Fe present within one compound. Ultimately, electron density at the nucleus differs for the LS and HS states of Fe and two of the most important parameters derived from a Mössbauer spectrum (isomer shift, δ, and quadrupole splitting, ΔE_Q) differ significantly between the LS and HS states of Fe^{II}.[83] The isomer shift results from electric monopole interactions (Coulomb interactions) due to differences in the s-electron environment between the source (usually ^{57}Co embedded in Rh metal) and the absorber (sample being measured).[84] The shift in the resonance energy of the transition that is produced can be either positive or negative and is quoted relative to a known absorber, like alpha-iron at room temperature. The isomer shift is particularly useful for determining oxidation states due to the different s-electron density at the nucleus because of the screening effects of the d-electrons.[85] For example, Fe^{II} has less s-electron density at the nucleus which results in a larger positive isomer shift than Fe^{III} ions.[83] Figure 1-10 depicts an isomer shift between the source and absorber. Electric quadrupole interaction results if at least one of the nuclear states involved

has a non-zero quadrupole moment, (a non-symmetric charge distribution as is the case for nuclei with spin I > ½ as in the case of ^{57}Fe), and if the electric field at the nucleus is inhomogeneous (non-cubic valence electron distribution).[86] Electric quadrupole interaction in the absence of magnetic dipole interaction (no magnetic field present) produces a doublet where the separation of the two resonance lines are equal to the energy of the quadrupole interaction (ΔE_Q) which is proportional to the electric field gradient and the quadrupole moment. The splitting gives useful information about the oxidation state, spin state and local symmetry of the atom.[87] Figure 1-10 shows this effect for the I = ⅜ excited state of ^{57}Fe and the splitting of the resonance that is observed in the spectrum. Figure 1-11 illustrates isomer shift and quadrupole splitting parameters as observed in a spectrum.

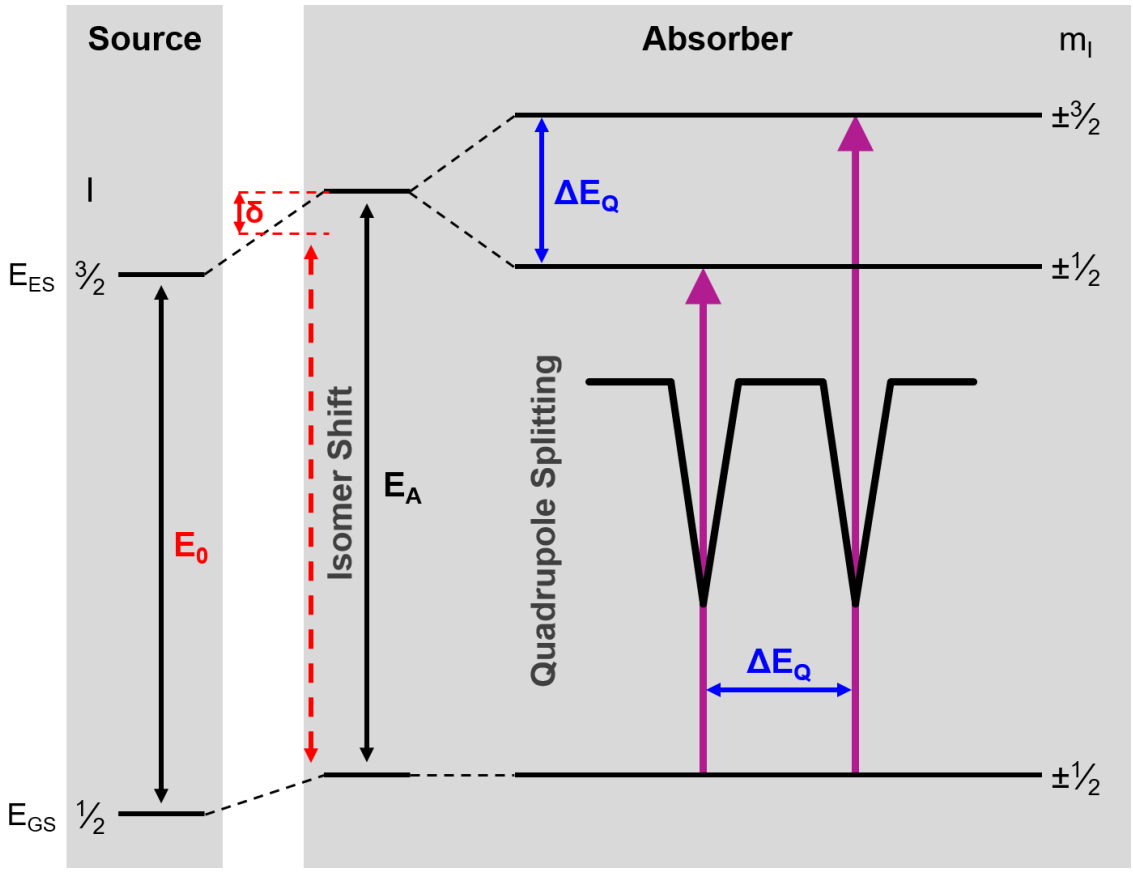

Figure 1-10. Schematic of the nuclear energy levels for the source and absorber illustrating the isomer shift and quadrupole splitting of the absorber. An example of the doublet that occurs due to quadrupole splitting in the absence of a magnetic field is shown. The splitting is equivalent to the energy difference between the excited m_I substates.

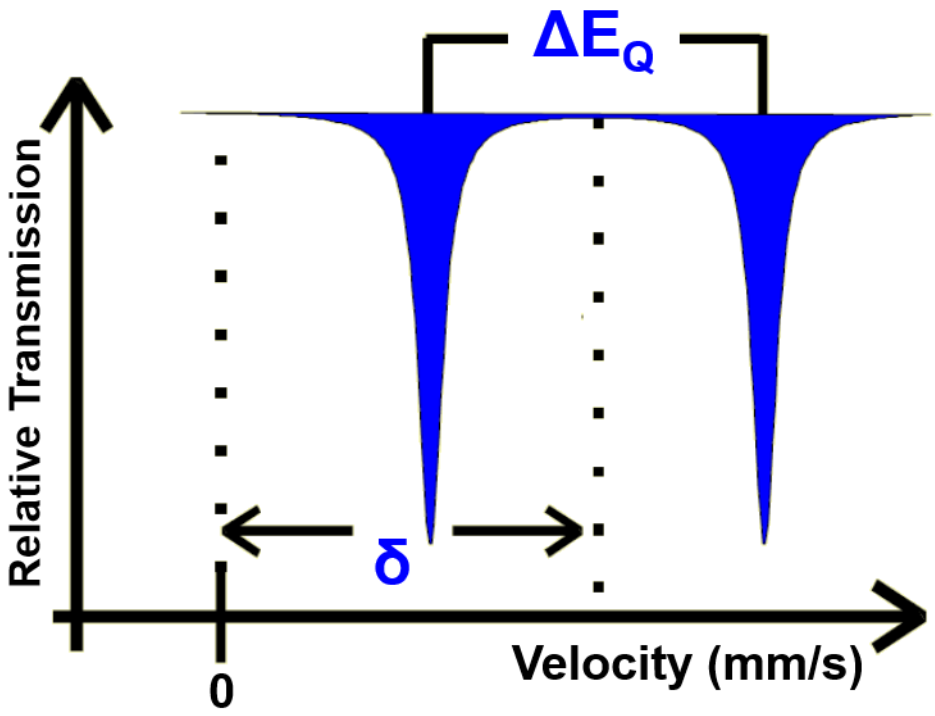

Figure 1-11. Schematic illustrating isomer shift and quadrupole splitting parameters for a Mössbauer spectrum. Adapted from lecture notes by Phillip Gütlich from the University of Mainz.

Vibrational Spectroscopy

Upon transition from HS to LS, there is an electron redistribution that occurs from the antibonding e_g orbitals to the slightly bonding t_{2g} orbitals. Consequently, a strengthening of the M–L bonds occurs which results in higher vibrational energy in the bond. This can be observed in the vibrational spectrum between ~250 – 500 cm^{-1} where the M–L stretching frequencies of transition metals typically appear. Reporter ligands, such as CN^- (where the N end is coordinated), have also been shown to be susceptible to changes in spin state of the metal atom and

allow for easier assignment of the spin-state since these peaks appear in an uncluttered region of most spectra. As expected, the LS form exhibits an increase of the cyanide stretching frequency (~2100 – 2140 cm^{-1}) as compared to the HS form (~2060 – 2090 cm^{-1}).[77,85] This technique is particularly useful when samples are measured as the temperature is varied. This results in intensity changes of the vibrational bands associated with the LS and HS species which could allow for a spin-transition curve as a function of molar fraction and temperature to be derived.[88]

Influences on SCO Behavior

One of the multiple challenges of crystal engineering in the SCO field is having a detailed understanding of how the strength and dimensionality of intermolecular interactions in a crystal control the phase transition in SCO compounds. This is complicated by the fact that generalizations about the structure-function relationship can rarely be made due to the many subtle interactions that can occur within these compounds and influence the transition behavior in different ways. This facet is a testament as to why a phenomenon that was discovered over 80 years ago is still intensely studied to this day. Fundamental studies are needed to gain a better understanding of the underlying factors that influence SCO so compounds that exhibit enhanced properties can be rationally designed for the advancement of technology. Discussion of the factors that influence SCO will be very limited here as a comprehensive coverage

of the topic is not feasible for a dissertation. Specifically, pressure and light effects will not be discussed.

The most obvious way to influence SCO is by altering the strength of the ligand field which can be achieved through ligand exchange and ligand substituent effects.[88] Ligand substitution is one of the many ways researchers have altered SCO behavior. Both steric and electronic effects from ligand substituents have been shown to alter or suppress the SCO in many mononuclear Fe^{II} compounds with substituted bipyridine and phenanthroline ligands. Generally, it appears that adding substituents to adjacent positions of the donor atoms results in a steric destabilization of the LS state to the point where the singlet state is no longer accessible if electron-withdrawing groups are adjacent to the donor atoms. This effect was observed for $[Fe^{II}(phen)_3]^{2+}$ which does not exhibit SCO until a methyl group is incorporated into the 2-position of the phenanthroline ligand. The LS state became completely inaccessible, however, upon incorporation of an electron-withdrawing chloro substituent. Studies that evaluate the addition of substituents of the phenanthroline ring in positions further from the donor N atoms show very little change in SCO behavior most likely as a result of little to no steric barrier to coordination.[85]

Anion,[89-91] guest species[51,52,54] and solvate effects[50,63,92-96] are more subtle influences that have been shown to alter SCO behavior. These changes have resulted in variations of transition temperature and complete suppression of the transition. The effects of these perturbations are not consistent from one system

to another though and are not easily predicted. Modification of the transition is expected upon replacement of anions, solvent and guest species however as they modify the crystal packing geometry and the strength of the intermolecular forces. One generalization that is usually made is that incorporation of a hydrogen bonding network will increase the transition temperature due to the stabilization of the LS state and that cooperativity generally increases as an effective network of hydrogen bonding allows for better communication between spin centers throughout the lattice.

Metal dilution studies have also been shown to influence the cooperativity of SCO compounds where an increase in dilution tends to suppress the cooperativity of the transition indicating the importance of cooperative elastic interactions between spin centers. Usually, the most cooperative spin-transitions occur when the structural changes at the molecular level are effectively transmitted between spin centers in the bulk material.[97] Crystal packing and π-π stacking interactions play an important role in this regard.[98-100]

In general, cooperative spin transitions are usually associated with large structural changes between LS and HS states of a compound. This is elegantly demonstrated by the fact that cooperative transitions are reasonably common for Fe^{II} compounds, rare in Fe^{III} compounds and relatively unknown for compounds containing other metal centers capable of SCO.[101] Overall, the backdrop of extensive fundamental studies over the course of several decades has led to the realization that cooperative interactions between spin centers are of utmost

importance for the SCO behavior in solid compounds. Three synthetic strategies have been devised to engender and strengthen cooperativity within SCO compounds: i) incorporation of hydrogen bonding networks, ii) incorporation of moieties capable of π-π stacking interactions and iii) coordination of bridging ligands (to increase nuclearity).[83]

Charge-Transfer-Induced-Spin-Transition (CTIST)

CTIST couples an electron transfer with a SCO event and has only recently been discovered in materials as a purely metal-based phenomenon. About 30 years ago, a change in oxidation state of Co^{II} to Co^{III} due to an electron charge transfer between the metal and the complexed radical dbSq (dbSq = 3,5-di-tertbutylsemiquinonate) was followed by a change in spin state as well. The paramagnetic HS Co^{II} ion (S = 3/2) became a diamagnetic LS Co^{III} ion (S = 0) as a function of decreased temperature.[102] This phenomenon was classified as a CTIST and is the result of the interaction between a radical ligand and the metal however. The first purely metal-based CTIST was not known until 1996 when Hashimoto and coworkers reported this behavior for a Prussian blue type compound, $K_{0.2}Co_{1.4}[Fe(CN)_6]\cdot 6.9H_2O$.[103,104] The behavior was a result of the conversion of a diamagnetic LS–Co^{III}/LS–Fe^{II} pair to a HS–Co^{II}/LS–Fe^{II} pair (illustrated in Figure 1-12). It was found that CTIST in this compound could be reversibly triggered with both temperature and light.

This finding spurred interest in finding new compounds that could exhibit

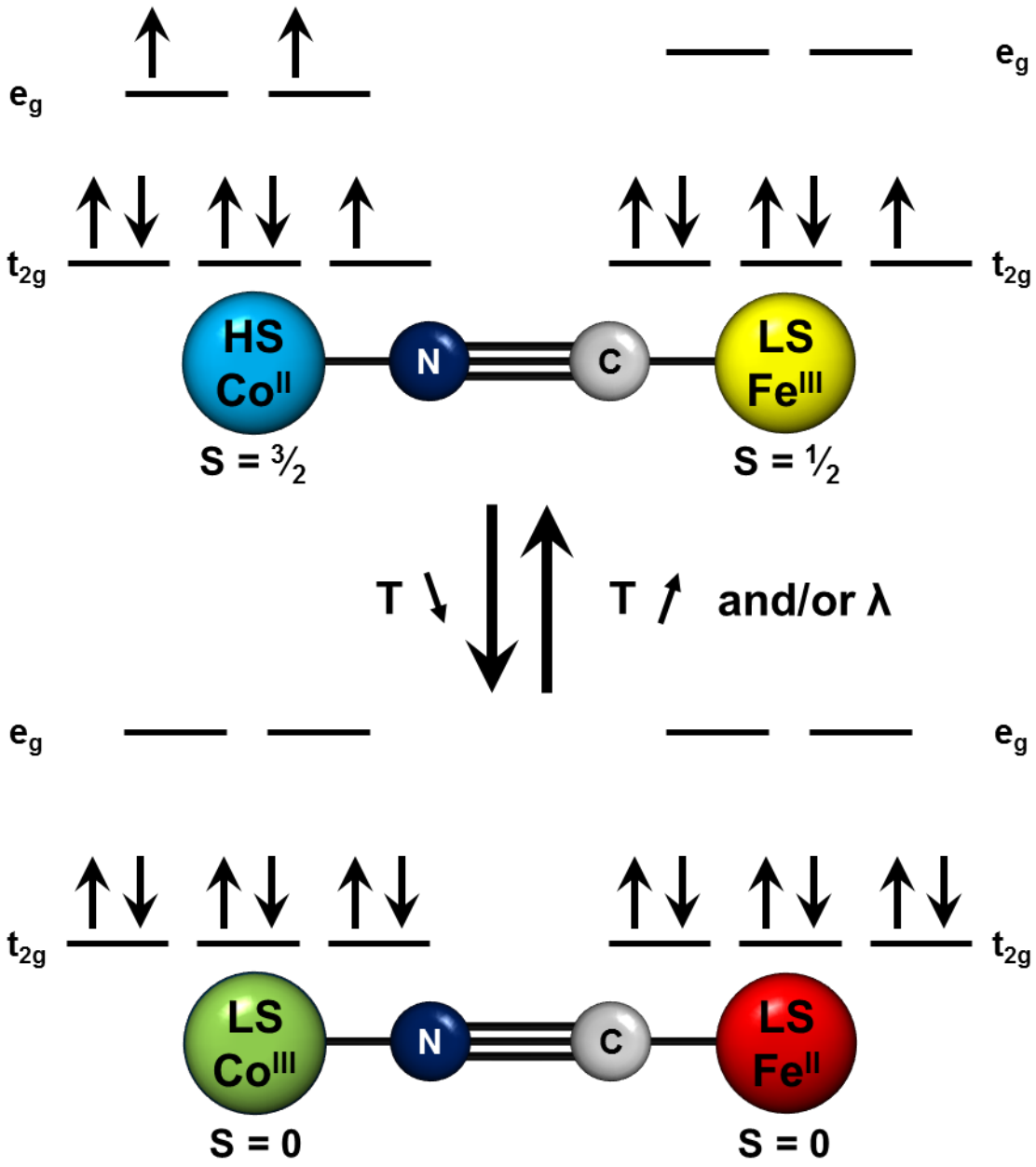

Figure 1-12. Schematic depiction of the conversion between paramagnetic (top) $^{LS}Fe^{III}$–CN–$^{HS}Co^{II}$ and diamagnetic $^{LS}Fe^{II}$–CN–$^{LS}Co^{III}$ electronic configurations due to CTIST triggered by thermal and/or photoirradiation.

this type of switchable redox isomerism and made cyanometallate-containing compounds a prime candidate. Since this discovery in 1996, several other Co/Fe cyanometallate compounds (both discrete molecules and extended networks) have been shown to exhibit this behavior and comprise the majority of research in this field.[70,105-114] Other metal combinations that have been reported to undergo CTIST in cyanometallate-based compounds where the M' in M/M' refers to the cyanometallate are: Co/Os,[115] Fe/Os,[116] Co/W[117-119] and FeCo/W.[120,121] From these few compounds that exhibit metal-to-metal charge transfer (MMCT) coupled with a spin state transition, it is clear that the Co^{II}/Co^{III} couple dominates and is by far the most prevalent in CTIST compounds. The only other metal to undergo a spin-transition concomitantly with a MMCT in cyanometallate-containing compounds is Fe^{II}/Fe^{III}

Many of the physical methods discussed for SCO are valid techniques for characterizing CTIST compounds as well. The spin and oxidation states of compounds can usually be discerned by examining a combination of the crystal structures, magnetism, IR and Mössbauer spectra (where applicable) as a function of temperature and light irradiation. X-ray crystallography remains a useful tool in determining M–L bond lengths which gives insight into the spin state of the transition metal. There is no significant change in bond length attributed to a change in oxidation state, however. For example, LS Fe^{II} has very similar Fe-N bond distance as LS Fe^{III} and the same can be said for the HS forms of these oxidation states as well. That being said, crystallography alone cannot

conclusively determine whether a metal center is undergoing a spin-transition due to SCO or a CTIST event. This is where a chemist must reach into their toolbox to find another tool that can do the job, such as SQUID magnetometry or ^{57}Fe Mössbauer, if applicable. SQUID magnetometry is no different for the characterization of CTIST compounds but again, cannot always determine whether a SCO or CTIST occurs due to the phenomena having very similar χT values in some compounds as a consequence of orbital contributions. ^{57}Fe Mössbauer is particularly useful in this regard when Fe is present in the sample for reasons discussed earlier. A very useful technique used in deciphering oxidation states of cyanometallates is IR spectroscopy because cyanide stretching frequencies ($\nu_{C\equiv N}$) are governed by the i) electronegativity, ii) oxidation state and iii) coordination number of the complexed metal.[122] The sensitivity of the $\nu_{C\equiv N}$ to oxidation state is primarily derived from the σ-donating and π-accepting nature of CN^-. Upon increasing the valency of the metal coordinated to CN^-, σ-donation of the CN^- increases and the π-backbonding of the metal decreases. The increased σ-donation removes electrons from the 5σ orbital of CN^- (which is weakly anti-bonding) resulting in higher $\nu_{C\equiv N}$. Also, a decrease in backbonding corresponds to weaker M–C bonds and a decrease of electrons in the antibonding π* orbitals of the CN^-. While the M–C bond becomes weaker with higher oxidation states, the C≡N bonds become stronger which results in higher $\nu_{C\equiv N}$.[123]

Cyanide Chemistry and Prussian Blue Analogs

Prussian blue analogs have been briefly mentioned above as they have exhibited many of the magnetic phenomena discussed already but have not been discussed in any detail. Historically, the Berlin artist Diesbach had accidentally prepared an insoluble dark blue solid during his efforts to prepare a red dye in 1703 by mixing soluble salts of Fe^{III} and $[Fe^{II}(CN)_6]^{4-}$.[124,125] This resulted in the first coordination compound, $Fe^{III}_4[Fe^{II}(CN)_6]_3 \cdot 14H_2O$, which came to be known as Prussian blue (PB) (Figure 1-13) and was used as a paint pigment initially.[126] Today, Prussian blue (and its analogs) have an extensive list of applications that range from technological devices[26,27] discussed earlier to MRI contrast agents[127] to the first FDA approved treatment of internal radioactive contamination (Cs or Tl) as a countermeasure to "dirty" or radioactive bombs.[128-130]

It wasn't until over 250 years after its first discovery that Bell Labs (1956) found PB orders ferromagnetically at a T_c of 5.6 K.[131] Finding that the paramagnetic Fe^{III} centers participate in magnetic exchange through the 10.28 Å diamagnetic $–N{\equiv}C–Fe^{II}–C{\equiv}N–$ bridge ushered in a new era for the study of magnetic materials. This study showed that a linear, diamagnetic bridge could effectively allow magnetic exchange interactions between metal centers through valence delocalization in the ground state between the Fe^{II} and Fe^{III} sites.[132] Cyanometallate-containing magnetic materials has been widely studied since 1956 and several Prussian blue analogs (PBA) have been found to be high temperature magnets. A few of these PBAs and their ordering temperatures can

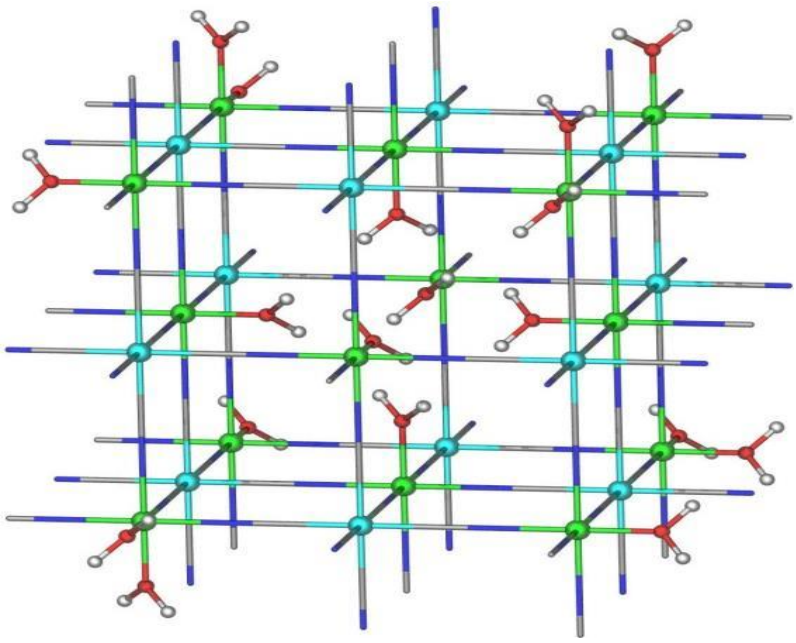

Figure 1-13. 3D structure of Prussian blue. Color scheme: Cyan is Fe^{II}, green is Fe^{III}, gray is C, blue is N, red is O and white is H.

be found in Table 1-1. Theorists have studied PBAs also and have made predictions about their potential ordering temperatures and exchange interactions which can guide synthetic chemists to experimentally realizing a new high temperature magnet. These predictions are summarized in Table 1-1. In addition to being new high temperature magnets, PBAs have exhibited magnetic bistability with magnetic phenomena such as SCO, CTIST and photomagnetic behavior as discussed earlier. The rich chemistry exhibited by Prussian blue analogs has been an inspiration for chemists in the field of cyanide molecular magnetism in their quest for designing discrete molecules that show interesting magnetic behavior.

Table 1-1. Experimental and theoretical ordering temperatures reported for PBAs where M = free metal ion and M' = hexacyanometallate.

Experimental				Theoretical	
MM'	Compound	T_c (K)	Reference	MM'	T_c (K)
$V^{II}Cr^{III}$	$KV[Cr(CN)_6]\cdot 2H_2O$	376	133	$Mn^{III}V^{II}$	480
$V^{II}/V^{III}Cr^{III}$	$K_{0.058}V[Cr(CN)_6]_{0.79}(SO_4)_{0.058}$	372	134	$Mo^{III}V^{II}$	552
	$K_{0.50}V[Cr(CN)_6]_{0.95}\cdot 1.7H_2O$	350	134	$Cr^{III}Mo^{II}$	355
	$V[Cr(CN)6]_{0.86}\cdot 2.8H_2O$	315	27	$V^{III}V^{II}$	344
	$V[Cr(CN)_6]_{0.69}(SO_4)_{0.23}\cdot 3H_2O$	315	135	$Cr^{III}V^{II}$	315
$Cr^{II}Cr^{III}$	$[Cr_5(CN)_{12}]\cdot 10H_2O$	240	26	$Cr^{III}Mo^{II}$	185
$Mn^{II}V^{II}$	$(Et_4N)_{0.5}Mn_{1.25}[V(CN)_5]\cdot 2H_2O$	230	136	$Mo^{III}Cr^{II}$	308
				$Mn^{III}Cr^{II}$	147
				$Cr^{III}Cr^{II}$	116

Trigonal Bipyramidal Molecules (TBPs)

A set of discrete polynuclear molecules with trigonal bipyramidal (TBP) geometries have been prepared over the years in the Dunbar laboratories to mimic the behavior of PBAs including strong exchange interactions, SCO, CTIST, linkage isomerism and photomagnetic behavior (Figure 1-, on right). TBPs have been of considerable interest to theorists due to their small size and high symmetry which allows for a simplification of calculations.[137-142] The general formula of TBPs is $[M^{II}(tmphen)_2]_3[M'^{III}(CN)_6]_2$ (hereafter denoted as $M_3M'_2$ or MM'; tmphen = 3,4,7,8-tetramethyl-1,10-phenanthroline) with three divalent metal ions in the equatorial positions and two trivalent hexacyanometallate ions in the axial,

or apical, positions which results in a neutral, pentanuclear molecule with six identical exchange interactions. This geometry can engender strong magnetic anisotropy as evidenced by the Mn_3Mn_2 TBP which was the first cyanide molecule to exhibit SMM behavior.[137,138,143] Among these molecules is also the remarkable $V^{II}_3Mo^{III}_2$ TBP reported in 2014 which holds the record for antiferromagnetic coupling in a 3d/4d cyanide-bridged compound (J = -114 cm^{-1}: the previous record was -61 cm^{-1} for a $V^{II}_4Mo^{III}$ molecule).[144] Many of the TBPs exhibit thermal or photo-induced magnetic bistability as a result of SCO[111,145,146] or CTIST.[111,116,146-148] The TBPs that have been reported in the literature by the Dunbar group to display these bistable behaviors contain either Fe or Co in the equatorial positions and Co, Fe or Os hexacyanometallates in the apical positions.

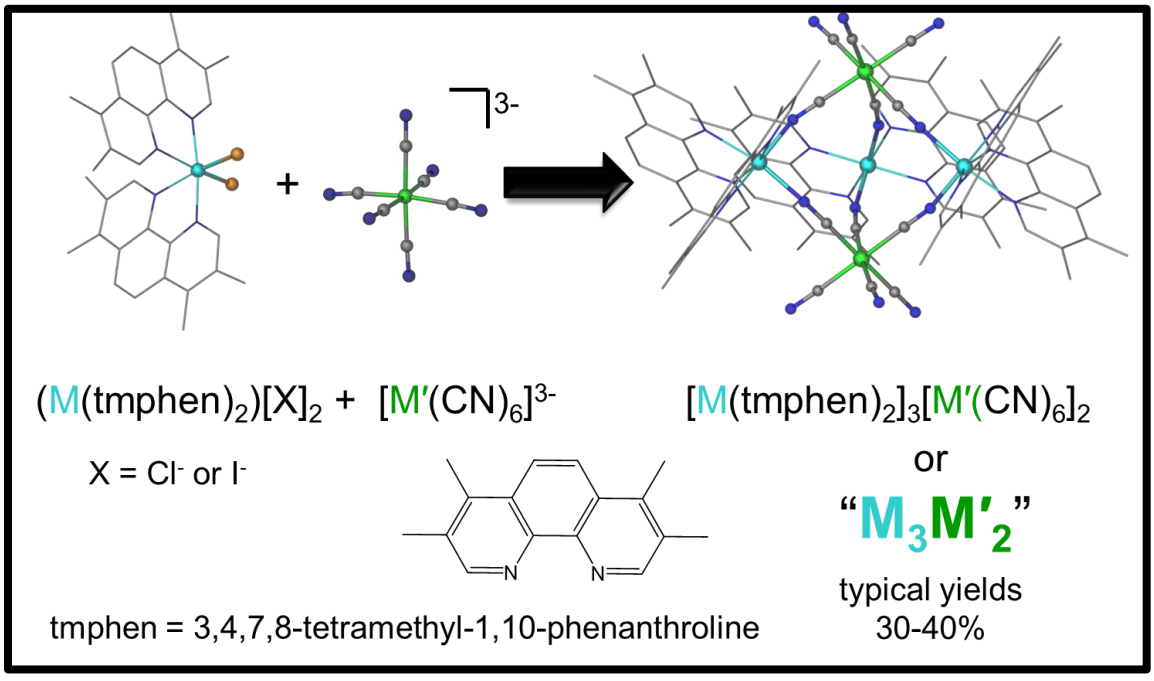

Figure 1-14. General reaction scheme for preparing TBPs.

Most of the TBP syntheses are conducted by a general procedure of preparing the equatorial precursor *in situ* by mixing a divalent chloride salt with two equivalents of 3,4,7,8-tetramethyl-1,10-phenanthroline (tmphen) in acetonitrile and combining this solution in a 1:1 ratio with an acetonitrile solution of the hexacyanometallate (Figure 1-). Most TBPs crystallize in the monoclinic $P2_1/c$ space group wherein a dimeric unit of two TBPs form through the π-π stacking of symmetry equivalent tmphen ligands. Figure 1-15 is a typical unit cell for a TBP in the $P2_1/c$ space group which highlights the symmetry elements and how the TBP forms the dimeric unit. The gray TBP is the asymmetric unit. The green lines represent the 2_1 screw axes, the orange dots represent inversion centers and the pink planes represent glide planes. The orange TBP is equivalent to the gray one by inversion, as the green is equivalent by a 2_1 screw rotation and the purple one is related by a glide.

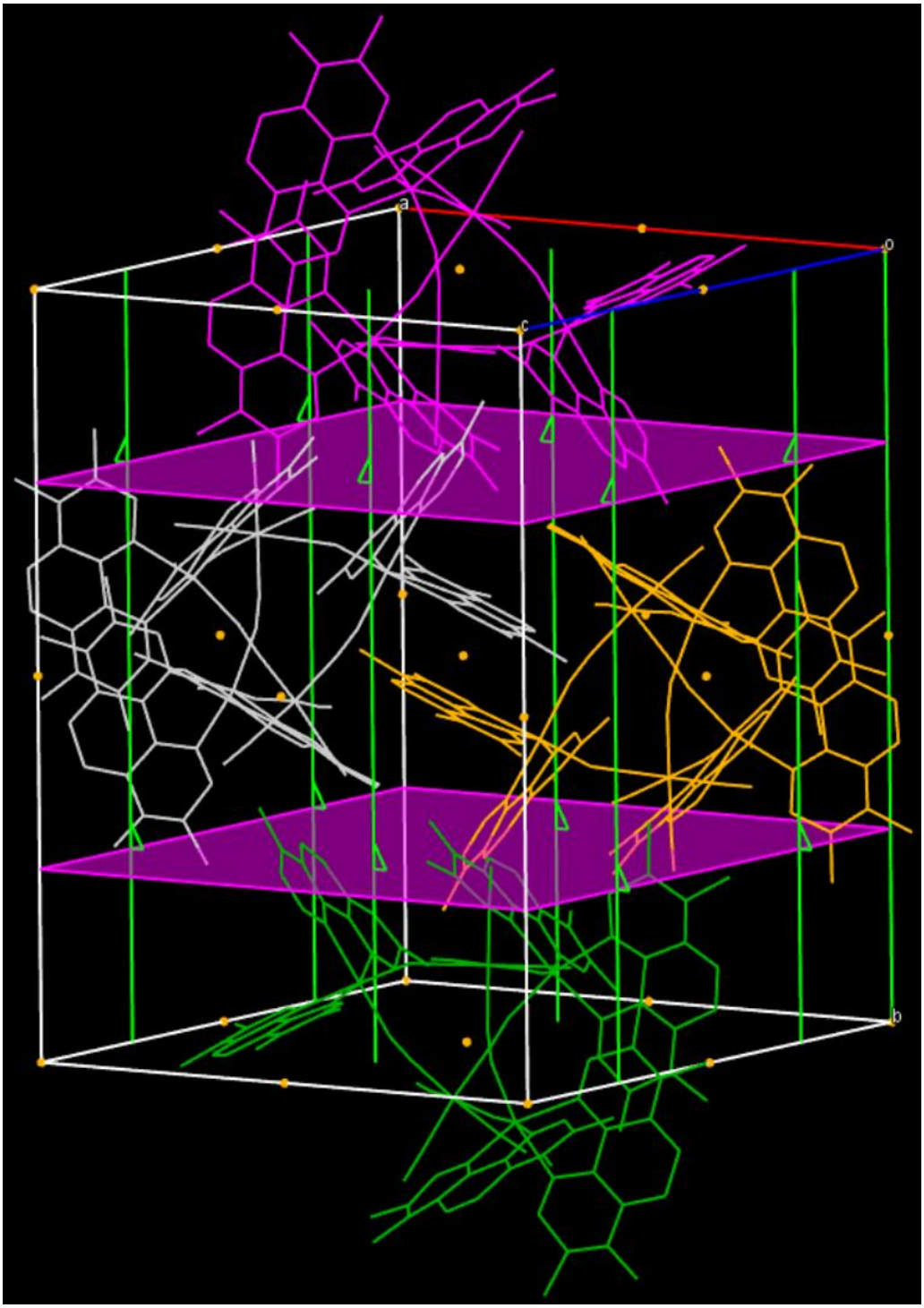

Figure 1-15. Typical unit cell for TBPs that crystallize in the $P2_1/c$ space group. Colors correspond to symmetry elements within the space group. Green represents a 2_1 screw axis, orange represents inversion and pink represents glides. The gray TBP is the asymmetric unit.

The study of TBPs by the Dunbar group constitutes the largest body of work for a homologous family of cyanide compounds known in the literature (Table 1-2). The boxes that contain a checkmark are the TBPs that have been reported in literature to date. The highlighted boxes are metal combinations that are the focus of this dissertation. It is a goal for our group to continue the extensive study on TBPs as we strive to prepare other metal combinations guided by theoretical predictions. The incorporation of $[Ru^{III}(CN)_6]^{3-}$ and $[Os^{III}(CN)_6]^{3-}$ into TBPs along with the study of their magnetic behavior is one of the main focuses of the research presented here. TBPs offer a great scaffold for fundamental studies of the effect of chemical and/or physical perturbations on magnetic behavior. The influence of solvation and π-π stacking interactions on the SCO and CTIST events in the Fe_3Ru_2 and Fe_3Co_2 TBPs is another focus point of the research presented here.

Table 1-2. Table illustrating the homologous family of TBPs reported by the Dunbar group (denoted with a ✓). Highlighted boxes are the TBPs that are the focus of the work presented in this dissertation.

		$[M^{III}(CN)_6]^{3-}$								
		Ti^{III}	V^{III}	Cr^{III}	Mn^{III}	Fe^{III}	Co^{III}	Mo^{III}	Ru^{III}	Os^{III}
$[M^{II}(tmphen)_2]^{2-}$	Ti^{II}									
	V^{II}							✓		
	Cr^{II}			✓						
	Mn^{II}			✓	✓	✓	✓			
	Fe^{II}			✓		✓	✓			✓
	Co^{II}			✓		✓	✓	✓		
	Ni^{II}			✓		✓	✓	✓		✓
	Zn^{II}			✓		✓	✓			
	Ru^{II}									
	Os^{II}									

CHAPTER II

STRAIGHTFORWARD SYNTHETIC ROUTES TO PURE HEXACYANOMETALLATE ANION SALTS OF TRIVALENT RUTHENIUM AND OSMIUM

Background

Cyanide chemistry has a very rich history beginning with the synthesis of the very first coordination compound Prussian blue $Fe^{III}_4[Fe^{II}(CN)_6]_3 \cdot xH_2O$ (x = 14-16) by Dippel and Diesbach in 1703.[124] The discovery of magnetic exchange occurring in this extended network[149] launched later studies aimed at incorporating other cyanometallates into molecular magnetic materials. First row transition cyanometallates have been widely studied, the most prolific of these being based on ferrocyanide, $[Fe^{III}(CN)_6]^{3-}$.[150,151] Hexacyanoferrate(III) is easily prepared and is well documented to be highly stable.[152-155] To date, there are relatively few investigations of homoleptic 4d and 5d cyanometallates owing to synthetic difficulties and generally lower stabilities. Heavier transition metal cyanide building blocks reported are usually seven-, or eight-coordinate owing to the tendency of these metals to exist in higher oxidation states which supports the presence of additional cyanide ligands. Studies support the presence of increased orbital overlap between cyanide ligands and 4d/5d metals due to increasing orbital diffuseness which leads to enhanced magnetic exchange interactions as compared to 3d transition metals[156]. In addition to enhanced magnetic exchange,

heavier elements have increased anisotropy due to larger spin-orbit coupling constants. For example, spin-orbit coupling constants (λ) for Fe, Ru and Os are reported as 460 cm^{-1} for Fe[157], 880 and 1180 cm^{-1} for Ru[12,157,158] and 3000 cm^{-1} for Os.[12,159] Their intrinsic properties of larger, more diffuse orbitals and increased anisotropy make 4d and 5d cyanometallates attractive targets for their potential to enhance magnetic exchange interactions.[160] High yield syntheses of 4d/5d congeners of 3d cyanometallates are therefore of high priority in the cyanide magnetic community so that families of related compounds can be prepared and their properties compared. One of the most appealing groups in the periodic table to offer this comparison is Group 8 because both divalent and trivalent hexacyanometallates of Fe, Ru and Os are known to exist. Unlike $[Fe^{III}(CN)_6]^{3-}$, which is well studied and incorporated into a multitude of compounds, there are only a few compounds that incorporate the Ru and Os congeners although they have been known for decades.[161,162] A perusal of the literature makes it clear that this situation is due to the synthetic challenges presented by their instability in aqueous media.[161] These trivalent precursors are usually obtained through the oxidation of the divalent, alkali metal analog which makes the oxidation of the divalent Ru and Os hexacyanometallates difficult to conduct in non-aqueous media. The first isolation of a $[Ru^{III}(CN)_6]^{3-}$ salt was reported in 1990 by Fischer using both tetrabutylammonium $(TBA)^+$ and tetraethylammonium $(TEA)^+$ as cations,[163] thirty-two years after the first isolation of the $(TBA)_3[Os^{III}(CN)_6]$ salt. This fact speaks to the increased difficulty in obtaining a stable trivalent

hexacyanoruthenate salt as compared to its Os cousin. In fact, several studies focused on the difficulty in oxidizing ruthenocyanide and the likely decomposition products of the cyanometallate upon oxidation.[161,164]

Although the first isolation of a $[Os^{III}(CN)_6]^{3-}$ salt was in 1968, the incorporation of the anion into a molecular compound did not occur until 2008, when our group reported the Ni_3Os_2 TBP and Prussian blue phase, which exhibit enhanced anisotropic magnetic exchange.[141,165] The next molecular compounds to include this anion were in 2010 and by the Dunbar group as well, namely the Fe_3Os_2, TBP[116] which exhibits CTIST, and the Co_3Os_2 Prussian blue analog,[115] also reported to exhibit CTIST and photomagnetic behavior. That same year, a linear, trinuclear compound of formula $(Net_4)[Mn^{III}_2$(5-Brsalen$)_2(MeOH)_2Os^{III}(CN)_6]$ (Net_4 = tetraethylammonium and 5-Brsalen = *N,N'*-ethylenebis(5-bromosalicylidene-iminate) was reported to exhibit single molecule magnetic behavior (SMM) by Bendix and coworkers.[159] Since then, a $[Mn^{III}_6Os^{III}](ClO_4)_3$ complex with a triplesalen ligand,[166] a $(Ph_4P)_2[Mn^{III}$(acacen$)Os^{III}(CN)_6](H_2O)_{1.5}(C_3H_7O)_{0.7}$ chain[167] and a (PPN){$[Mn^{III}$(salphen)$(MeOH)]_2[Os^{III}(CN)_6]$ trinuclear compound[168] have emerged, all showing SMM behavior. This situation is in stark contrast to the incorporation of the $[Ru^{III}(CN)_6]^{3-}$ anion into molecular materials. Although it was first isolated in 1990, the first report of its incorporation into a compound was in 2011 by Bendix and coworkers who demonstrated that the $(Net_4)[Mn^{III}_2$(5-Brsalen$)_2(MeOH)_2Ru^{III}(CN)_6]$ trinuclear molecule exhibits SMM behavior.[158] The

next time the $[Ru^{III}(CN)_6]^{3-}$ anion was reported in a compound was in 2015 by the Dunbar group, which is when they reported the family of linear, trinuclear compounds of formula $(PPN)\{[Mn^{III}(salphen)(MeOH)]_2[M^{III}(CN)_6]$ where M = Fe, Ru, Os and Co, all of which (with the exception of the Co congener) are SMMs.[168]

The relative lack of molecular magnets containing $[Ru^{III}(CN)_6]^{3-}$ is a consequence of its facile redox chemistry and the difficulty in preparing the anion. Since its isolation in 1990, several papers on the topic of the synthesis of the anion have been published[163,169,170] with all of the authors claiming that the initial synthesis was unreliable and led to green decomposition products. The work conducted during the course of the research in this chapter verified these conclusions, despite claims made by the authors to have made stable, pure precursors with no sign of decomposition.

In this chapter, a straightforward method to the isolation of pure crystals of $(PPN)_3[Ru^{III}(CN)_6]$ and $(PPN)_3[Os^{III}(CN)_6]$ (PPN = bis(triphenylphosphine)iminium chloride) are reported from oxidation of $K_4[M^{II}(CN)_6]$ (M = Ru, Os) with $Ce^{IV}(SO_4)_2$ in aqueous media. The detailed procedure discussed herein affords crystalline material of both the Ru and Os trivalent cyanometallates that are soluble in organic media. The procedure is carried out under very mild conditions within 1-2 hours of bench work, unlike previously reported procedures. The characterization and magnetic properties will be discussed in addition to the first structural characterization of these trivalent $(PPN)^+$ salts.

Experimental Details

Materials

All chemicals and solvents were of ACS reagent grade or higher and used as received. ***Reagents for the synthesis of bis(triphenylphosphine)iminium chloride (PPNCl):*** triphenylphosphine (PPh_3, flake, 99%, Alfa Aesar), chlorine (Cl_2, gas, 99.5%, Sigma Aldrich), hydroxylamine hydrochloride ($NH_2OH{\cdot}HCl$, hygroscopic powder, 96%, Alfa Aesar), 1,1,2,2-tetrachloroethane ($C_2H_2Cl_4$, liquid, 98.5%, Acros Organics) and potassium hydroxide (KOH, hygroscopic pellets, 85+%, EMD Millipore). ***Reagents for the synthesis of $K_4[M^{II}(CN)_6]$ where M^{II} = Ru, Os:*** potassium hydroxide (KOH, hygroscopic pellets, 85+%, EMD Millipore), potassium cyanide (KCN, hygroscopic powder, 97+%, Alfa Aesar), ruthenium(III) trichloride trihydrate ($Ru^{III}Cl_3{\cdot}3H_2O$, hygroscopic powder, 40% metal, Pressure Chemical Company) and osmium(VIII) tetroxide ($Os^{VIII}O_4$, volatile solid, 75% metal, Pressure Chemical Company). ***Reagents for the synthesis of $(PPN)_3[M^{III}(CN)_6]$ where M^{III} = Ru, Os:*** cerium(IV) sulfate anhydrous ($Ce^{IV}(SO_4)_2$, powder, 97%, Alfa Aesar). ***Solvents used:*** propyl alcohol (Macron Fine Chemicals), acetone (EMD Millipore), ethyl acetate (Macron Fine Chemicals), N,N-dimethylformamide (DMF) (EMD Millipore), acetonitrile (MeCN) (Fisher Scientific), tetrahydrofuran (THF) (EMD Millipore) and diethyl ether (EMD Millipore) were used as received from Texas A&M University's chemistry stockroom. All water used was distilled by Texas A&M University. All reactions

were performed in an aerobic environment in the fume hood, unless otherwise noted.

Syntheses

$K_4[Ru^{II}(CN)_6]\cdot nH_2O$

CAUTION: This reaction uses KCN which can react with water to form HCN gas. According to OSHA (Occupational Safety and Health Administration), exposure times in air to concentrations of 109 ppm (119.2 mg/m^3) for one hour, 182 ppm (200.2 mg/m^3) for 10 minutes or 364 ppm (400.4 mg/m^3) for 2 minutes, are fatal.[171] *KCN should be opened in a fume hood so that any $HCN_{(g)}$ that has collected in the container can be liberated safely. Cyanide can be absorbed through the skin with similar adverse health effects so it is prudent that proper safety attire is worn and that WORK IS CONDUCTED IN AN EFFICIENT CERTIFIED FUME HOOD ONLY!*

The compound *$K_4[Ru^{II}(CN)_6]$* was prepared similarly to reported procedures.[172,173] In a 125 mL Erlenmeyer flask outfitted with a long, rod-shaped stir bar, $RuCl_3\cdot 3H_2O$ (1 g, 3.9 mmol) was dissolved in water (~50 mL). A large excess of KOH (2 g, 35.6 mmol) was added to the dark-brown solution and after five minutes of stirring, KCN (6 g, 92.8 mmol) was added to the dark-brown/black solution. The solution was gently heated to dryness. **NOTE: Heating to excessive temperatures will cause white, water-insoluble by-products, so care should be taken to heat the solution just to the point that the water evaporates.* During the

heating process, the reaction changed colors from dark brown, to black, to dark brown again, to dark green and then to maroon. Once the water has evaporated and the solid continues to bake on the hot plate, the color of the solid gradually lightens and becomes white. As the color of the dry solid changed from maroon to white, small amounts of water were added to the flask and boiled off several times until the solid is entirely white in color. The white solid was dissolved in water (~50 mL) and the solution was allowed to cool to room temperature. Any insoluble white particles were removed by gravity filtration to give a clear, colorless solution. The product was precipitated with the addition of methanol (~75 mL), collected by filtration on a medium (M) frit and washed with methanol (30 mL x 3). The recovered product was re-dissolved in water (~50 mL), gravity filtered to remove more water-insoluble impurities and re-precipitated with methanol (~75 mL) at least two more times. The final product was recovered and rinsed in the same manner as before, but with an additional rinse of diethyl ether (30 mL x 3). The product was dried in air with an aspirator for approximately 10 minutes; typical yield is 1.4 g (79%). Infrared spectroscopy (IR) reveals cyanide stretching frequencies, v(C≡N), at 2110 (w, sp), 2084 (s, sp), 2075 (m, sp), 2052 (vs, b), and 2038 cm^{-1} (vs, b) where w = weak, m = medium, s = strong, vs = very strong, b = broad and sp = sharp. Below 75 °C, thermogravimetric analyses (TGA) exhibit ranges of mass losses from 0 - 11.2% which corresponds to 0 - 52.3 g/mol of solvent loss. This mass loss can be attributed to up to three water molecules. TGA confirms that all solvent can be removed from the product if it is placed in an oven

for several hours. R*efer to page twenty-three in notebook three for a representative, in-depth description of the procedure and detailed observations for the synthesis*.

$K_4[Os^{II}(CN)_6]\cdot nH_2O$

CAUTION: OsO_4 is VERY TOXIC, especially to the lungs and nervous system! It is extremely hazardous if ingested or inhaled, can permeate skin and cause blindness.[174] The acute toxicity, or the adverse health effects a substance imposes within 14 days due to either a single exposure or repeated exposure within 24 hours,[175] has been determined to have an oral LD_{50} of 162 mg/kg of body weight in mice.[174] The LD_{50} is the amount of a substance determined to be lethal to 50% of the test subjects. According to the Organisation for Economic Co-operation and Development (OECD), the LD_{50} limit guidelines rank OsO_4 as harmful with an LD_{50} falling within the range of 50 – 500 mg/kg.[176] OsO_4 purchased from Pressure Chemicals Inc. is sold in 1g ampules and is a volatile solid, which will sublime in air when the ampule is opened. WORK WITH THIS IN A FUME HOOD ONLY! As with the synthesis of $K_4[Ru^{II}(CN)_6]$, this reaction utilizes KCN and the same concerns and practices are valid. The LD_{50} for inhalation of HCN is 100-300 ppm and will result in death within 10-60 minutes, while the LD_{50} for ingestion is 1-3 mg/kg of body weight.[171]

The $K_4[Os^{II}(CN)_6]$ salt can be prepared in an analogous manner to the $K_4[Ru^{II}(CN)_6]$ congener but here we discuss a slightly different method that was

found to result in higher yields than the method previously reported.[172]

Into a 125 mL Erlenmeyer flask outfitted with a large rod-shaped stir bar, KOH (2.9 g, 51.1 mmol) was added to 50 mL of water. The solution was stirred slowly to dissolve the KOH completely. In the hood, the ampule containing the OsO_4 (1.0 g, 3.934 mmol) was broken open inside the tissue paper it was wrapped in from the manufacturer. The entire ampule was then immediately put into the flask containing the clear, colorless, aqueous KOH solution. The color of the clear, colorless solution changed to yellow and then to dark orange. After 15 minutes of stirring, KCN (13.3 g, 204.3 mmol) was *SLOWLY* added to the solution. The KCN was added scoop by scoop; each scoop was added only when the previous scoop of KCN had dissolved completely. Upon addition of the KCN, the solution immediately became a clear, dark-reddish-orange-brown color. The pieces of the ampule were fished out with a scoopula and rinsed with water into the reaction flask to ensure all of the brown solution was out of the ampule. *The ampule was placed back into the plastic container it was shipped in, capped and then disposed of into a solid waste container.* The reaction flask was heated to a gentle boil while stirring slowly. Within one hour, the solution changed to a clear, dark-green/black color. A small amount of white water-insoluble particles had precipitated. After two additional hours, the solution changed to a clear, dark-brown color with the insoluble particles still present. Once the solution had been concentrated to about 30 mL, a recrystallization dish was used to cover the flask in order to keep the reaction from going to dryness. After three additional hours of heating and stirring,

the solution color was a lighter brown with a greater amount of precipitate present. Water was added until the solution reached ~50 mL in total volume in order to redissolve most of the solid. Gentle heating continued until the solution color was light brown. Additional KCN (5.0 g) and KOH (1.1 g) was added to the heating reaction. The volume of the solution was kept at ~50 mL with continued heating for another hour with the vessel still being covered. After this time, the flask was uncovered and the solution was heated to dryness with stirring until a sludge remained, after which time stirring was ceased and heating continued. Small amounts of water were added to the dry, light-tan solid and then allowed to bake off again until the dry solid that remained was a white powder. Once the reaction had become a homogenous white solid, the flask was removed from heat and allowed to cool completely. Water (~60 mL) was added to the cooled flask and the solution was stirred briefly. The light-blue solution was filtered to remove the white insoluble impurities and then heated again to dryness. Once the solution had gone to dryness, it was removed from heat and allowed to cool again. The minimum amount of water required to dissolve most of the white solid (~50 mL) was added to the flask again. The light-blue solution was filtered once more to remove insoluble impurities. Methanol was added to the filtrate until a precipitate had begun to form causing the solution to be slightly murky. The flask was covered and put into a freezer maintained at -2 °C for 90 minutes. The blue-gray, block-shaped crystals that had formed were collected by filtration, washed with copious amounts of methanol, rinsed with ~15 mL of diethyl ether three times and left

under aspiration for about ten to fifteen minutes before being put into a vial. The resulting product is a very faint blue-gray microcrystalline powder (1.2 g). Additional methanol was added to the mostly clear and colorless filtrate until the solution became murky. The flask was covered and returned to the freezer. After several hours in the freezer, a very fine microcrystalline solid precipitated from the solution. The product (a finer microcrystalline solid and lighter in color than the first fraction of product collected) was recovered using filtration. The product was rinsed with copious amounts of methanol and then with approximately 15 mL of diethyl ether three times. The solid was dried with an aspirator for about 10 minutes and then put into a vial (0.6 g). In total, this synthesis yielded 1.8 g of product (91% yield), in contrast to the previous synthetic method yielding a highly impure sample before recrystallizations due to water-insoluble impurities and 75% after multiple recrystallizations. IR, v(C≡N): 2112 (m, sp), 2079 (vs, sp), 2068 (vs, sp), 2039 (vs, vb) and 2021 cm^{-1} (vs, b) where m = medium, vs = very strong, sp = sharp, b = broad and vb = very broad. In contrast to the previous synthetic method used to obtain the product, IR spectroscopy of the product prepared by the procedure above exhibits well resolved cyanide stretching frequencies and a lack of significant peaks at 1646 cm^{-1}, 1617 cm^{-1} and around 1057 cm^{-1} (broad) attributed to impurities that plague both the $K_4[Ru^{II}(CN)_6]$ and $K_4[Os^{II}(CN)_6]$ salts. TGA analysis of the product prepared using the above method confirms the product is completely dry and does not decompose below 450 °C (the analysis was stopped after this temperature). *Refer to page eleven in notebook six for an*

in-depth description of the procedure and detailed observations for this synthesis.

Bis(triphenylphosphine)iminium Chloride (PPNCl)

CAUTION: This reaction should be performed in a working fume hood as hydrogen chloride gas is liberated during the reaction. Limit the amount of exposed metal in the hood to prevent corrosion of the metal. NO GREASE should be used because Cl_2 gas reacts with hydrocarbons. All joints should be wrapped with Teflon tape or covered with Teflon sleeves. Inhalation, ingestion and eye contact with 1,1,2,2-tetrachloroethane are very hazardous. This substance has been determined to be carcinogenic by OSHA and has an acute oral toxicity LD_{50} of 250 mg/kg in rats.[177] *This substance is toxic to the liver, kidneys, blood and nervous system and prolonged exposure can produce target organ damage.*

This procedure is a modified version of a previously reported method.[178] This reaction was carried out under N_2 gas on a Schlenk line. A very large egg-shaped stir bar was put into a 2 L three-necked round-bottomed flask. A water condenser outfitted with a gas inlet adapter connected to the Schlenk line was placed into the middle neck of the flask while another gas inlet adapter with a Teflon stopcock and a gas outlet adapter were secured onto the remaining two necks of the flask. The gas inlet adapter with the Teflon stopcock was connected to a large, clean, oil bubbler which was connected to a lecture bottle of Cl_2 gas. Tygon tubing was used to join the lecture bottle and oil bubbler to the gas inlet adapter and also the gas outlet adapter to an oil bubbler containing silicon oil.

Refer to Figure 2-1 for a picture of the reaction setup. With the use of a funnel, PPh_3 (786 g, 3.0 mol) and 1 L of 1,1,2,2-tetrachloroethane were added to the 3-necked flask. The reagents were stirred together under N_2 until all of the PPh_3 dissolved, leaving a clear and colorless solution. The solution was submerged into a dry ice/isopropanol bath between -20 °C and -30 °C and stirring continued as chlorine gas was added to the reaction. A large oil bubbler was used to condense Cl_2 (~91 mL, 2 mol). This was achieved by marking the bubbler to denote 91 mL of volume and then the bubbler was submerged in a Dewar containing a dry ice/acetone mixture (~77 °C). The lecture bottle (connected to a needle valve for better control) was slowly opened and then closed once condensed chlorine reached the line marked on the bubbler. The oil bubbler was slowly removed from the Dewar in a step-wise fashion in order to allow the chlorine to slowly evaporate into the 3-necked flask. Stirring of the solution became impeded due to the viscosity. Once all chlorine had been added, the gas inlet adapter was removed, hydroxylamine hydrochloride ($NH_2OH{\cdot}HCl$, 69.0 g, 0.99 mol) was added to the now yellow solution and a stopper replaced the gas inlet adapter. The 3-necked flask was removed from the Dewar and warmed to room temperature slowly, resulting in an off-white suspension. The flask was placed in a heating mantle and refluxed until the pH of the outgas from the small oil bubbler was neutral (about 8-9 hours), indicating that no more HCl was being liberated. The reaction was cooled to room temperature. Ethyl acetate (2 L) was added to a large 3-necked round-bottomed flask. Half of the reaction was slowly added to the 3-necked flask

containing the ethyl acetate and then 2 L of ethyl acetate was added to the remaining solution in the original reaction flask. White solid had precipitated in both flasks. More product crystallized in both flasks upon standing overnight. The product was collected by filtration and the filtrate was treated with more ethyl acetate and left to stand overnight. This process was repeated several times until the filtrate was mostly clear and colorless instead of light-yellow in color. The crude product was recrystallized from boiling water (~1 L of water for every 100 g of product) yielding 286 g (50%). *Refer to page sixty-two in notebook four for a detailed description of the procedure and observations for the synthesis of PPNCl and to page one hundred in notebook four for a detailed description of the procedure and observations for the recrystallization of crude PPNCl.*

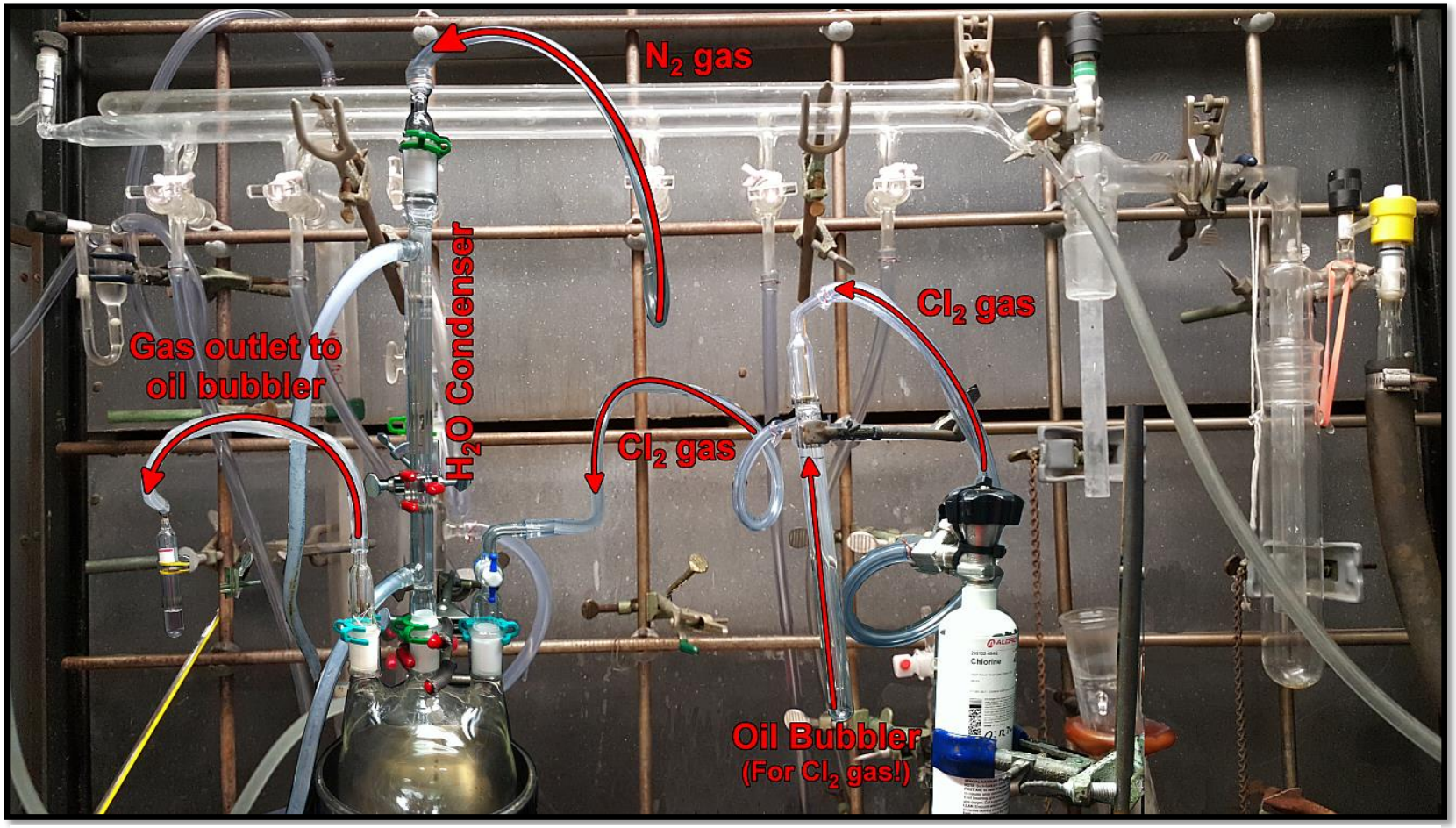

Figure 2-1. Reaction setup for the synthesis of PPNCl.

$(PPN)_3[Ru^{III}(CN)_6]\cdot H_2O$ (1)

This procedure is a modified version of previously reported methods.[169,172] A slight excess of PPNCl (3.3 g, 5.7 mmol) was added to 125 mL of H_2O in a 250 mL Erlenmeyer flask. The solution was warmed just enough to dissolve the PPNCl (~40-45 °C). The starting material, $K_4[Ru^{II}(CN)_6]$ (0.75 g, 1.8 mmol), was dissolved in ~60 mL of water in a 125 mL Erlenmeyer flask. The largest volume of DMF (~20 mL) that could be added without precipitating the reagent from the water, was added to the clear, colorless, aqueous solution of $K_4[Ru^{II}(CN)_6]$. The solution was then stirred over excess $Ce^{IV}(SO_4)_2$ (~0.7 g, ~2 mmol) until the solution was a golden yellow color (approximately 30 – 45 minutes). The golden yellow solution of $K_3[Ru^{III}(CN)_6]$ was gravity filtered into the clear, colorless, aqueous solution of PPNCl while the reaction was stirred and gently heated until the filtration was complete. The product was collected immediately by filtration. The filtrate was a clear, light-green color due to the decomposition products being soluble in DMF. The product is a wet, yellow powder. The product was dissolved in the minimal amount of MeCN (~5 – 10 mL). THF was added to the clear, golden yellow solution to the point just before precipitate formed (~75 - 100 mL). Several aliquots of 10-20 mL of diethyl ether were added to the solution. For the first few additions of diethyl ether, the solution was swirled to dissipate any yellow precipitate that had formed and then the solution was left undisturbed for 10 – 15 minutes between each addition. Yellow, needle-shaped crystals formed with each addition of diethyl ether. Additions continued in this manner until the solution

became nearly colorless, leaving only yellow crystals which were collected by filtration and rinsed with diethyl ether (15 mL x 3). The product was dried in air with an aspirator for approximately 10 minutes with typical yields being 2.2 g (55%). IR, v(C≡N): 2094 (m, sp) and 2085 (m, sp) cm^{-1} where m = medium and sp = sharp. Below 50 °C, TGA thermograms exhibit very small mass losses (-0.46% on average) indicating the product has less than one water molecule (0.7) per formula unit, or the presence of surface solvent. Elemental analysis (EA): Calculated for $(PPN)_3[Ru^{III}(CN)_6]\cdot H_2O$, ($C_{114}H_{92}N_9P_6ORu$) (%): C, 72.41; N, 6.66; H, 4.90. Average found (%): C, 72.19; N, 6.66; H, 5.04. Difference (%): C, -0.3; N, 0.0; H, 2.7. *NOTE: The clean oxidation from Ru^{II} to Ru^{III} is challenging as the product can easily turn green from the formation of divalent, decomposition products. Several factors influence the increase in the formation of decomposition. Too much time over $Ce^{IV}(SO_4)$ is just one of these factors so care should be taken to ensure the reaction does not stay in contact with the oxidant for more than one hour. Most importantly, decomposition is facile if the solution is too hot. Special care is necessary to ensure the aqueous PPNCl solution does not rise above 40 °C, otherwise the product rapidly decomposes. Refer to page thirty-two in notebook six for a representative, detailed accounting of the procedure and observation for the synthesis of $(PPN)_3[Ru^{III}(CN)_6]$ (1).*

$(PPN)_3[Os^{III}(CN)_6]\cdot H_2O$ (2)

This procedure is a modified version of previously reported methods[172,179]

and is analogous to that of its ruthenium congener, $(PPN)_3[Ru^{III}(CN)_6]$. This salt is also susceptible to the formation of dark-green, divalent-osmium decomposition products, but slightly less so than the ruthenium analog.

A slight excess of PPNCl (5.5 g, 9.6 mmol) in 125 mL of H_2O was gently warmed (<50 °C) in a 250 mL Erlenmeyer flask while the solution was being stirred. In a 125 mL Erlenmeyer flask, water (60 mL) and DMF (20 mL) were used to dissolve $K_4[Os^{II}(CN)_6]$ (1.5 g, 3.0 mmol). An excess of $Ce^{IV}(SO_4)_2$ (1.2 g, 3.6 g mmol) was added to the clear, colorless osmium-containing solution. The solution instantaneously turned a very bright yellow-green color and was stirred over the oxidizer for about 30 minutes. The bright, neon green solution was gravity filtered into the PPNCl solution with continued heating and stirring. In order to keep excess PPNCl from precipitating, the bright green product was collected while the solution was still warm. The powder was rinsed three times with 30 mL aliquots of diethyl ether. The product was recrystallized from MeCN and THF in the same manner as $(PPN)_3[Ru^{III}(CN)_6]$. The product is a light-neon-green microcrystalline solid. Average yield is 4.2 g (70% yield). IR, ν(C≡N): 2083 (m, sp) and 2076 (s, sp) cm^{-1} where m = medium, s = strong and sp = sharp. Below 50 °C, TGA thermograms exhibit very small mass losses (0.54% on average), indicating the product has less than one water molecule (0.6) per formula unit, or the presence of surface solvent. Elemental analysis (EA): Calculated for $(PPN)_3[Os^{III}(CN)_6]\cdot H_2O$, ($C_{114}H_{92}N_9P_6ORu$) (%): C, 69.15; N, 6.36; H, 4.68. Average found (%): C, 68.65; N, 6.43; H, 4.86. Difference (%): C, 0.7; N, 1.1;

H, 3.8. *Refer to page sixty-seven in notebook five for a representative accounting of the synthetic details and observations for the preparation of* $(PPN)_3[Os^{III}(CN)_6]$ *(2).*

Results and Discussion

Synthesis and Characterization

Several aspects of the synthetic procedure for the trivalent, hexacyanometallate $(PPN)^+$ salts of Ru and Os warrant discussion. Most of this discussion will focus on the synthesis of $(PPN)_3[Ru^{III}(CN)_6]$ as it was found to be the most challenging, but the same issues apply to the synthesis of $(PPN)_3[Os^{III}(CN)_6]$.

First, the choice in cation should be discussed. The $(PPN)^+$ cation (Figure 2-2) has been successfully used in the preparation of several hexacyanometallate salts, including the divalent Ru species.[180,181] The cation is good for stabilizing air-sensitive anions when other cations proved to be unsuccessful which has led to their extensive use in metal carbonyl chemistry.[182] Organometallic chemists have found the cation to be useful in stabilizing large anionic complexes due to its bulkiness and low tendency to engage in interactions which can enhance the nucleophilic tendencies of the anion.[180] The cation is not hygroscopic and is soluble in organic media which allows for a wide array of solvent choice for reactions other than the usual water or MeOH solutions used in cyanometallate chemistry. Common reagents such as alkali metal ions, encapsulated in crown

ethers and tetraalkylammonium, phosphoium and arsonium cations have several disadvantages compared to $(PPN)^+$: they can be more difficult to prepare, are generally less soluble, tend to be more hygroscopic, can catalyze oxidation reactions and are more expensive.[183] The $(PPN)^+$ cation is air stable and can easily be purified from boiling water.[178] The solubility of the $(PPN)^+$ salt in warm water makes metathesis reactions with the alkali cyanometallates a fast and easy synthetic process with no need for complicated or time-consuming extractions as reported for other synthetic methods of the $(PPN)_3[Ru^{III}(CN)_6]$ precursor.[170] For the reasons stated above, our group has chosen PPNCl as a counter cation in preparing many of the cyanometallates we use. It is readily available to purchase or can be made as explained in the experimental section.

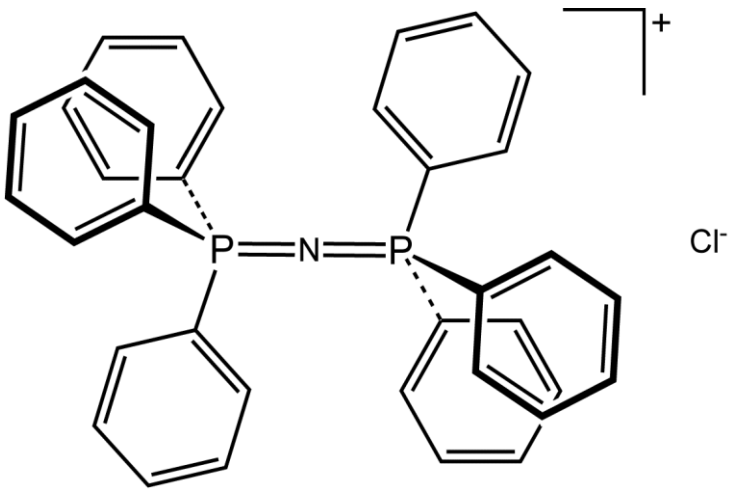

Figure 2-2. Bis(triphenylphosphine)iminium chloride (PPNCl)

A second point is that decomposition during the oxidation process has been a major hurdle for many groups undertaking the preparation of these trivalent Ru and Os cyanometallates. Reports of decomposition are more prevalent in the preparation of the Ru congener but this problem exists for Os analog as well, albeit to a lesser extent. Early work described the formation of divalent green solutions or powders during the oxidation process.[161,164] Crean and Schug suggested that the oxidation of $K_4[Ru^{II}(CN)_6]$ with strong oxidizers such as Ce^{IV} in aqueous media is unstable if the concentration of the Ru salt is greater than 1 mM, the pH is too acidic or if an excess of the oxidant is present.[164] They claim that aquation, dimerization and redox reactions all contribute to the spontaneous decomposition. The current work with these precursors in aqueous solutions has confirmed that decomposition to divalent green species readily occurs in aqueous media with $Ce(SO_4)_2$. Previous synthetic reports indicate that the divalent alkali cyanometallates of Ru and Os are rapidly and completely oxidized by stirring in air in the presence of DMF or H_2O_2.[163] This approach has not proven to be successful in our laboratories or others'.[170] A previous group member, Dr. Matthew Hilfiger, attempted to prepare $(PPN)_3[Ru^{III}(CN)_6]$ using different methods, both aerobic and anaerobic, but found the easiest method to be the common method with $Ce(SO_4)_2$ in aqueous media. His synthetic method to slow the rate of decomposition in these $(PPN)_3[Ru^{III}(CN)_6]$ and $(PPN)_3[Os^{III}(CN)_6]$ precursors was to add MeCN or MeOH to the aqueous solution during the oxidation process.[172] Unfortunately, this approach still led to an undesirable level of impurity due to

decomposition. In the current syntheses of the $(PPN)_3[Ru^{III}(CN)_6]$ and $(PPN)_3[Os^{III}(CN)_6]$, a mixture of water and DMF was used during the oxidation process with $Ce(SO_4)_2$ in an attempt to stabilize the oxidized product as Fischer *et. al* had reported that the oxidation of $(R_4N)[Ru^{II}(CN)_6]$ was readily carried out in air if the solvent was DMF and the cation was tetrabutylammonium. This change in organic media during the oxidation process proved to be very fruitful as the reaction solution no longer turned green within a short period of time. It became evident however that the longer the $[Ru(CN)_6]^{4-/3-}$ solution was kept in contact with $Ce(SO_4)_2$, the more decomposition occurred. The solutions should not be stored over $Ce(SO_4)_2$ for more than one hour. The DMF is also a valuable component of the reaction once the product has begun to form. The use of MeCN during the oxidation process did not help with co-precipitation as the decomposition by-products are not sufficiently soluble in the MeCN/water mixture. The DMF/water mixture allows for any small amount of decomposition product(s) to stay in the filtrate. Although the formation of the decomposition by-products during the oxidation step had been resolved, it was found that the degradation during the metathesis step was still possible with too much heating. It was found that these reactions are extremely heat sensitive and that decomposition is rapidly accelerated with increasing temperatures. Considering the aqueous solution containing the PPNCl must be heated slightly to dissolve the PPNCl, care must be taken to ensure the temperature of the solution is just hot enough to dissolve the reagent which usually occurs at mild temperatures around 40 – 50 °C. If

decomposition still occurs one can purify the product by recrystallization from an MeCN/THF/diethyl ether solution. As stated earlier, the decomposition by-product is not very soluble in MeCN. By dissolving the product in a minimal volume of MeCN the insoluble green particles can be removed by filtration through Celite. To re-precipitate the product, THF was found to be very useful as the addition of just diethyl ether to the concentrated MeCN solutions results in an emulsion that requires vigorous stirring in copius amounts of diethyl either in order to obtain a very wet powder. The addition of THF before diethyl ether however, prevents the formation of an emulsion due to the sparingly soluble nature of $(PPN)^+$ salts in THF. Upon addition of enough diethyl ether into the MeCN/THF solution, small crystals precipitate from solution leading to a pure, microcrystalline product.

The method described above and in the experimental section have several advantages over previously reported methods. Other methods reported the use of harsh chemicals such as HCl which is not the safest option for a reagent in a reaction using cyanide. The same method using HCl is also reported to take several days to prepare, whereas the current method can take approximately 1-2 hours to complete. Other reported methods similar to the method discussed in this chapter have been unreliable and the product is invariably highly contaminated with decomposition by-products. All of the structures reported for the $[Ru^{III}(CN)_6]^{3-}$ and $[Os^{III}(CN)_6]^{3-}$ contain at least two water molecules per formula unit. The crystallization of the product with two water molecules holds true for the $(PPN)_3[Mn^{III}(CN)_6]$ and $(PPN)_3[Fe^{III}(CN)_6]$ precursors previously reported as

well.[180,181] The use of THF as a recrystallization solvent limits the amount of water in the product for both the Ru and Os salts to less than one molecule per formula unit. This makes the use of these precursors in a water- and oxygen free environment more successful. These precursors have also been found to remain stable in air as a solid or organic solution, contrary to the products reported previously.[169]

$(PPN)_3[Ru^{III}(CN)_6]\cdot H_2O$ (1)

In **Figure 2-3**, one can see the typical colors expected during the synthesis of **1** as it progresses without decomposition. Figure 2-4 is a comparison of what the oxidized solution should look like without decomposition present (a) and what the color of the solution is when decomposition is prevalent. The reaction steps in Figure 2-3: a and b) The water/DMF mixtures containing $K_4[Ru^{II}(CN)_6]$ and $Ce(SO_4)_2$ as time progresses, c) the metathesis step, d) the product that precipitates as a powder from the metathesis step, e) the filtrate, after the product is collected, with evidence of decomposition f and g) recrystallization from MeCN, THF and diethyl ether as time progresses and h) the microcrystalline product of **1**. The left picture in Figure 2-4 is of a filtered solution of the oxidized reaction before the metathesis step and is what the color should look like if the synthesis is progressing well. The picture on the right, however, is what the solution looks like if decomposition occurred during the oxidation step.

Figure 2-3a-h. Typical colors expected as the synthesis of 1 progresses.

Figure 2-4. Filtered solutions of the oxidation step in the synthesis of 1. Left: Expected color when there is no decomposition and right: color of the solution due to decomposition occurring

IR spectroscopy of cyanometallate compounds can be very revealing as to the oxidation state of the product. Trivalent hexacyanoruthenate species exhibit characteristic $\nu_{C\equiv N}$ at ~2090 wavenumbers[163,169] while the divalent species move to lower frequencies at ~2050 wavenumbers[184] due to the increased π-backbonding and decreased σ-donation with the metal. This large separation in frequency renders assignment of the peaks to the correct oxidation state of the metal relatively easy. The IR spectra in Figure 2-5 is typical for $(PPN)_3[Ru^{III}(CN)_6]$ and has $\nu_{C\equiv N}$ peaks at 2094 and 2085 cm^{-1} which correspond well to literature values and is consistent with the expected decrease in π-backbonding. Figure 2-6 is IR spectra for (1) contaminated with the green decomposition by-product as the emergence of the new $\nu_{C\equiv N}$ peak at 2048 cm^{-1} clearly indicates. The decomposition by-product is consistent with a divalent Ru-CN bridged species as Crean and Schug suggested many years ago.[164]

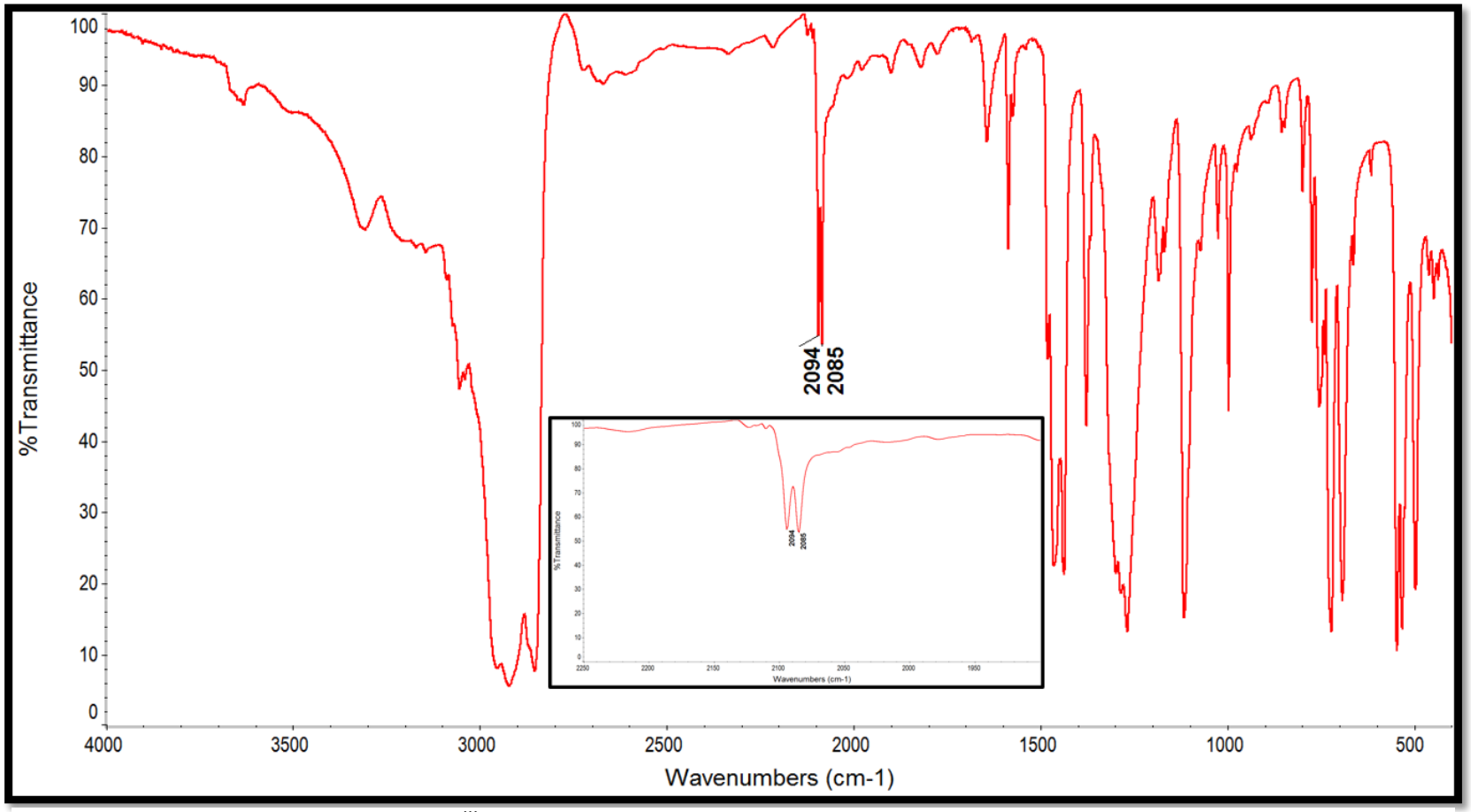

Figure 2-5. IR spectra of $(PPN)_3[Ru^{III}(CN)_6]$ (1) in Nujol oil. Inset is a close-up of the cyanide stretching peaks.

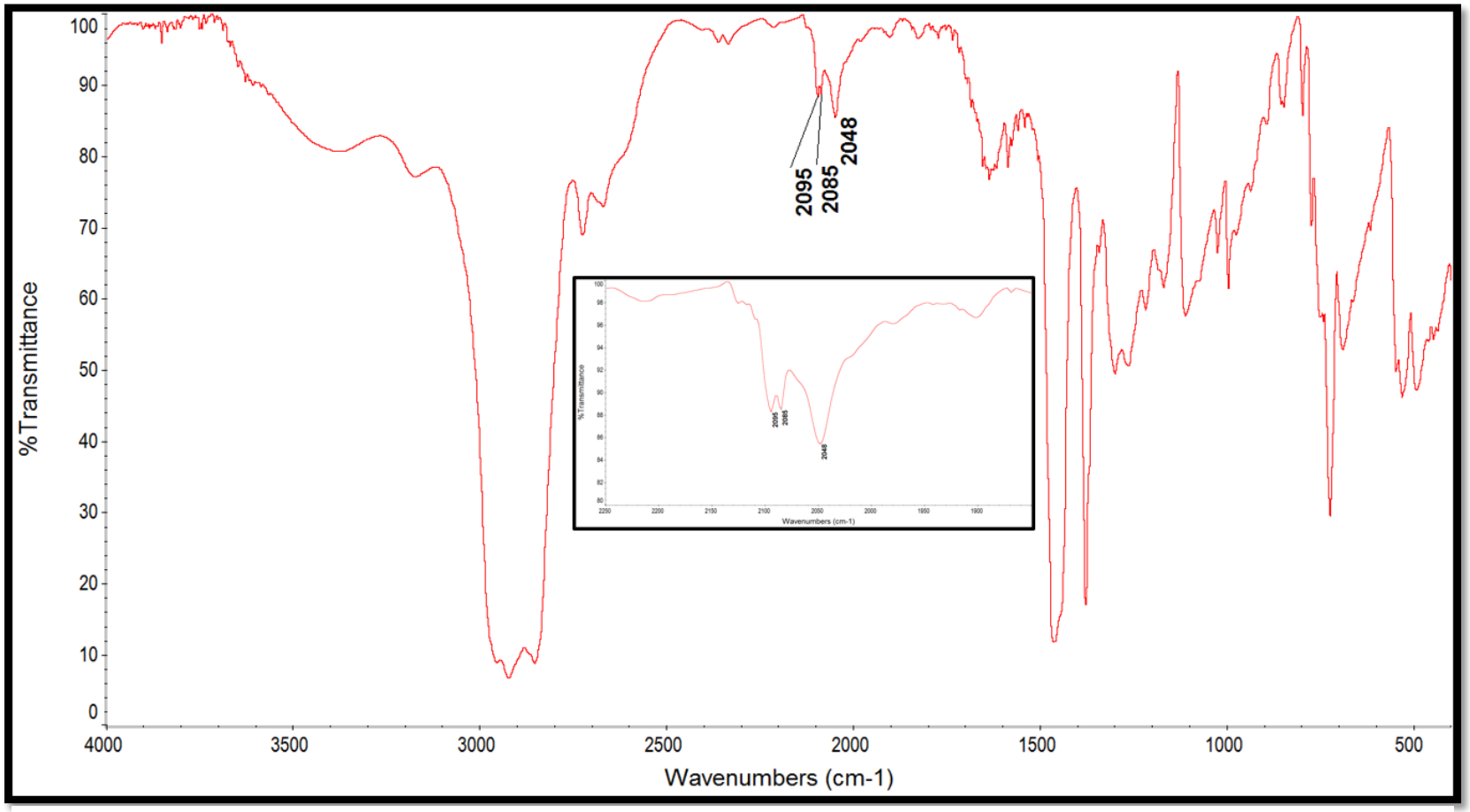

Figure 2-6. IR spectra of (1) contaminated with decomposition by-products. Inset is a close-up of the $\nu_{C\equiv N}$ peaks.

TGA performed on (1) (Figure 2-7) in a N_2 atmosphere suggests the presence of ~ 1 (0.9) H_2O molecules per $(PPN)_3[Ru^{III}(CN)_6]$ and demonstrates the thermal stability of $(PPN)_3[Ru^{III}(CN)_6]$. The TGA was only performed up to 250 °C but the sample maintained its composition throughout the analysis. The temperature was held at 70°C for 30 minutes during the measurement in an effort to distinguish surface solvent from coordinated water. The bump in the data as temperature begins to increase again after the 30 minute hold-time is most likely due to a combination of buoyancy (the temperature of the gas is in advance of the sample itself which causes the buoyancy of the gas to decrease, resulting in an artificial increase in the sample mass) and gas displacement effects. These effects are most prevalent at the start of the experiment and tails off at higher temperatures once the sample and gas are at similar temperatures.

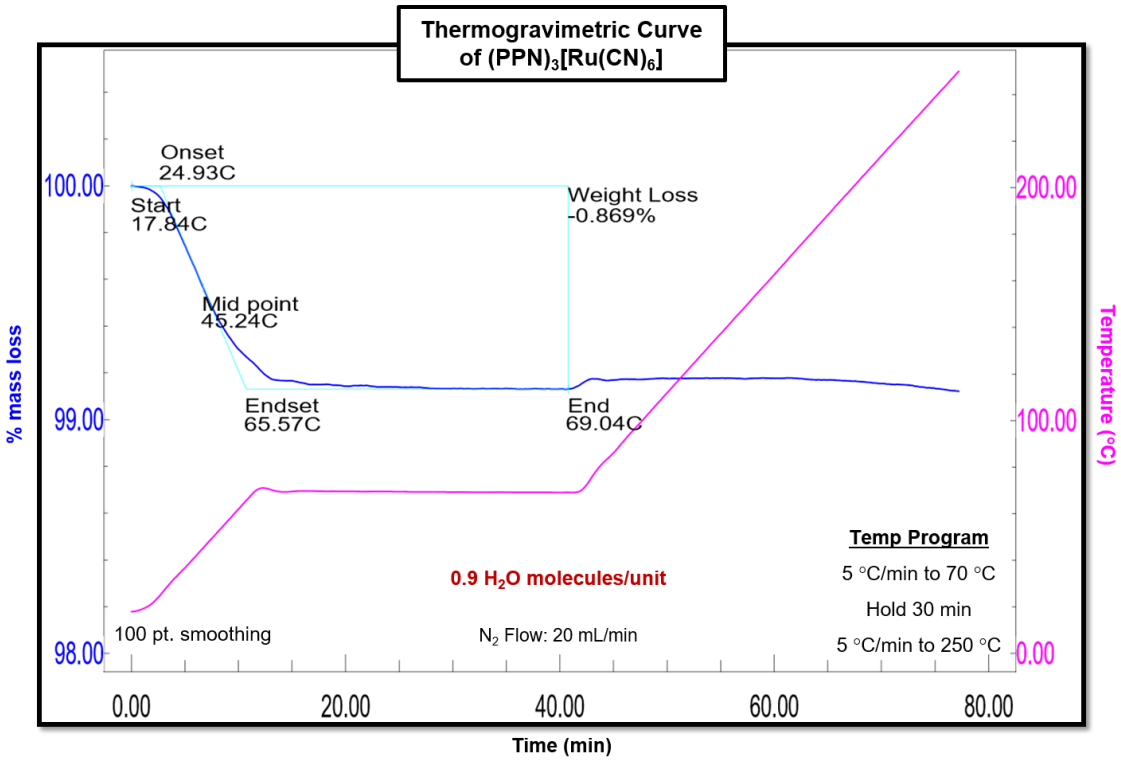

Figure 2-7. Thermogram of 1. The blue line represents mass loss (%) and is on the left y-axis. The pink line represents temperature in °C and pertains to the right y-axis. These two variables were plotted against minutes.

$(PPN)_3[Os^{III}(CN)_6]\cdot H_2O$ (2)

As stated above, the oxidation process to obtain $[Os^{III}(CN)_6]^{3-}$ is still susceptible to spontaneously decomposing in aqueous media and co-precipitating divalent by-products, but not as readily as is $[Ru^{III}(CN)_6]^{3-}$. The synthetic method described in this chapter works well for the $(PPN)_3[Os^{III}(CN)_6]$ congener and results in very similar observations but instead of a golden yellow color, the solutions and product are more of a neon yellow/green color (Figure 2-8).

Figure 2-8. Typical color and consistency of (2) when it is free of decomposition by-products.

Typical $\nu_{C\equiv N}$ frequencies have been reported at ~2070 wavenumbers[170] for $[Os^{III}(CN)_6]^{3-}$ anions and ~2030 wavenumbers[184,185] for $[Os^{II}(CN)_6]^{4-}$ species. Again, this large difference in frequency allows for easy assignment of the oxidation states of the precursor and can easily give insight into whether the product is contaminated with decomposition by-products. It should be noted, however, that the use of KBr pellets for collecting IR spectra can lead to cation exchange[180] or reduction of the cyanometallate[163] resulting in different $\nu_{C\equiv N}$ frequencies, so mineral oil or Nujol mulls can be employed. The IR spectrum in Figure 2-9 exhibits $\nu_{C\equiv N}$ frequencies at 2083 and 2086 cm^{-1} which is in good agreement with values reported in literature. The reduced $\nu_{C\equiv N}$ frequencies in comparison to the $(PPN)_3[Ru^{III}(CN)_6]$ precursor is consistent with the increase in π-backbonding strength as is expected from the more diffuse 5d orbitals of Os.

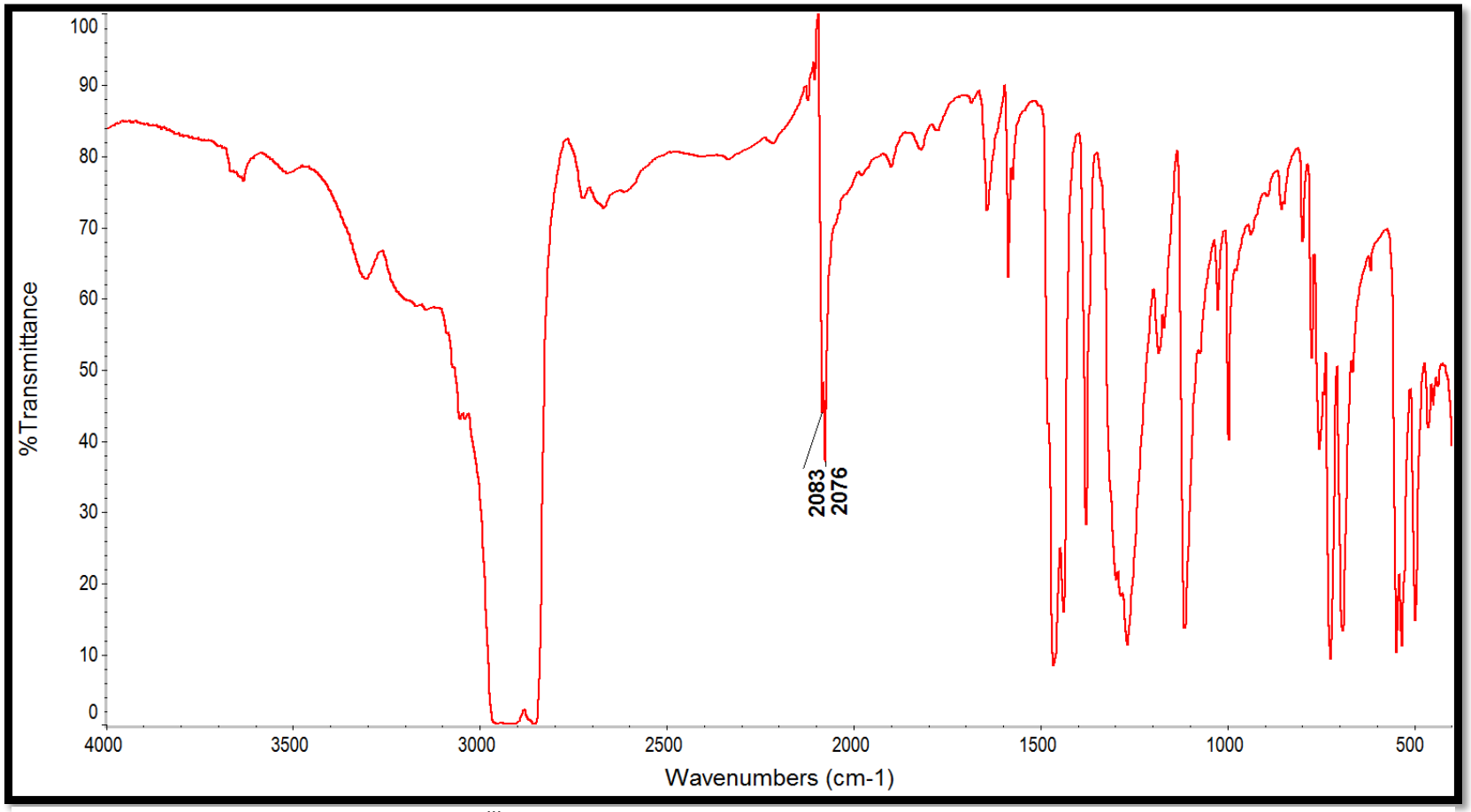

Figure 2-9. IR spectrum of $(PPN)_3[Os^{III}(CN)_6]$ (2) in Nujol oil. Product is free of decomposition contamination.

The cyanide stretching frequencies for both $(PPN)_3[Ru^{III}(CN)_6]$ and $(PPN)_3[Os^{III}(CN)_6]$ are in good agreement with those reported for the $(PPN)_3[Fe^{III}(CN)_6]$ congener (2104, 2099 and 2093 cm^{-1}).[180] The increase in frequencies for the Fe salt follows the trend expected with a decrease in backbonding as the heavier transition metals are replaced with lighter ones. The cyanide stretching frequencies for the Fe, Ru and Os salts are in Table 2-1.

Table 2-1. Cyanide stretching frequencies for $(PPN)_3[M^{III}(CN)_6]$, (M = Fe, Ru and Os).

Compound	$\nu_{C\equiv N}$ (cm^{-1})		
$(PPN)_3[Fe^{III}(CN)_6]$	2104	2099	2093
$(PPN)_3[Ru^{III}(CN)_6]$	—	2094	2085
$(PPN)_3[Os^{III}(CN)_6]$	—	2083	2076

Thermogravimetric analysis of $(PPN)_3[Os^{III}(CN)_6]$ in a N_2 atmosphere (Figure 2-10) suggests there are ~0.6 interstitial H_2O molecules per cyanometallate. As with the Ru congener, this is less interstitial water as compared to previous reports in the literature. The TGA was performed up to 200 °C. The compound exhibited thermal stability throughout the temperature range. The initial increase in mass at low temperatures is usually an effect of buoyancy.

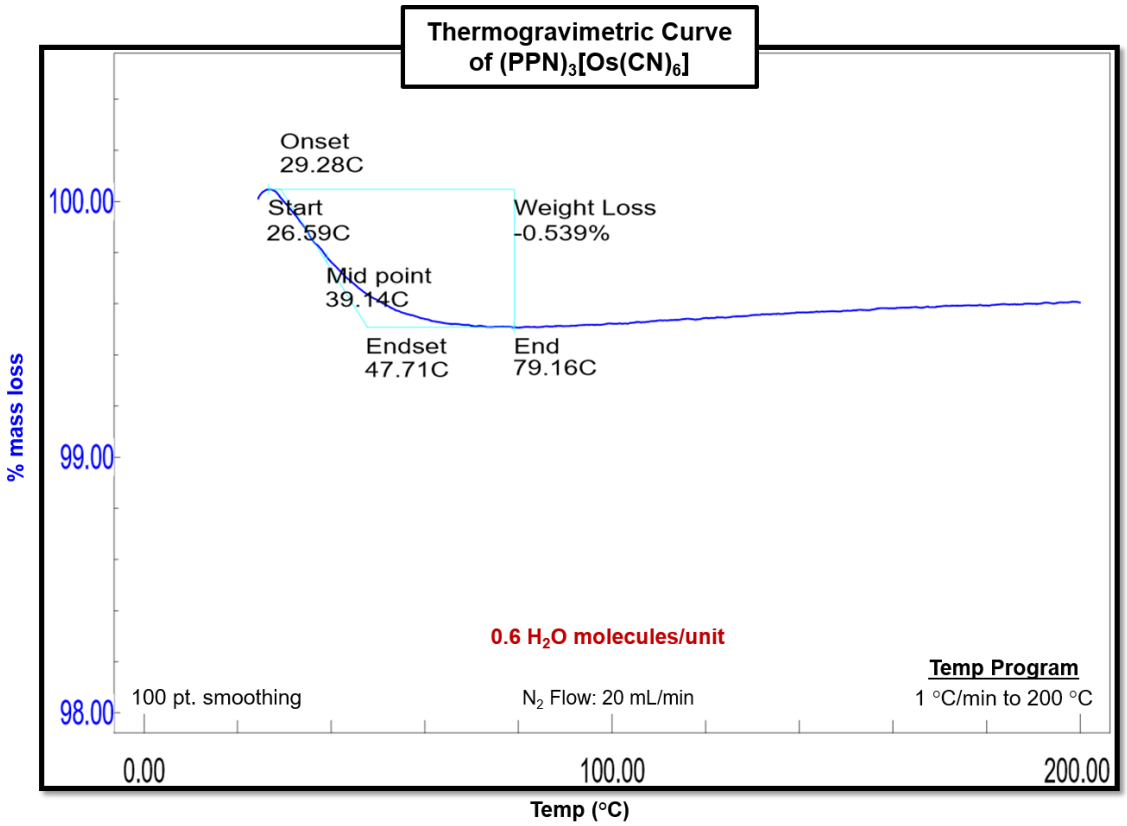

Figure 2-10. Thermogram of (2) up to 200 °C in a N_2 atmosphere.

Single Crystal X-ray Diffraction

The structures of **1** and **2** were collected on the Texas A&M University APEXII instruments at 110 K. Details can be found in Appendix A. By using the synthetic method described above, X-ray quality crystals of these precursors were obtained for the first time. As expected, the structures were found to crystallize in the same space group as each other (orthorhombic Pbcn). They both contain two crystallographically independent $(PPN)^+$ cations. One of the cations occupies a

general position whereas the nitrogen atom of the other resides on a two-fold rotation axis resulting in one half of the cation being crystallographically independent. The metal of the anion also resides on 2-fold rotation axis resulting in only half of the anion being crystallographically independent. The relevant structural data and refinement parameters for compounds **1** and **2** are listed in Table 2-2. The asymmetric units were determined to contain ~0.3 H_2O molecules for $(PPN)_3[Ru^{III}(CN)_6]$ and ~0.7 H_2O molecules for $(PPN)_3[Os^{III}(CN)_6]$. The water molecules were modeled anisotropically with hydrogen atoms and exhibit hydrogen bonding to one of the cyanide ligands. Pertinent M–C bond lengths for each structure as well as the O–N bond length are in Table 2-3. The M–C and C≡N bond lengths are very similar to each other and are consistent with the previously reported salts of these trivalent hexacyanometallates. The average M–C bond lengths (2.06 Å) are slightly elongated in comparison to the $(PPN)_3[Fe^{III}(CN)_6]$ analog reported (1.94 Å).[180] The errors on the cyanide bond lengths are too large in both these structures and those reported in literature to draw any correlation. The general structure of compound 2 is depicted in Figure 2-11. Compound 1 is isomorphous to 2 and is not shown. Figure 2-12 is a packing diagram of 2 looking down the c axis.

Table 2-2. Crystal data and refinement parameters for single crystals of 1 and 2**.**

Formula	**$C_{114}H_{90}N_9P_6Ru\cdot0.3H_2O$**	**$C_{114}H_{90}N_9P_6Os\cdot0.7H_2O$**
Space Group	Pbcn	Pbcn
a/ Å	23.839(3)	23.80(6)
b/ Å	20.368(2)	20.467(5)
c/ Å	19.348(2)	19.353(5)
α = γ = β/ °	90	90
Volume/ $Å^3$	9394.3(18)	9430(4)
Temperature	110 K	110 K
μ/ mm^{-1}	0.326	1.511
2Θ Range for Data Collection/ °	3.368 to 52.232	2.624 to 49.468
Crystal Description Crystal Size/ mm^3	Yellow block 0.10 x 0.09 x 0.05	Green block 0.09 x 0.09 x 0.08
Independent Reflections	9327 R_{int} = 0.0723 R_{sigma} = 0.0636	8024 R_{int} = 0.0613 R_{sigma} = 0.0341
Data/Restraints/ Parameters	9327/0/600	8024/0/602
[a]GooF on F^2	1.011	1.041
[b,c]Final R Indexes [I>=2σ (I)]	R_1 = 0.0421 wR_2 = 0.0.0867	R_1 = 0.0298 wR_2 = 0.0.0604
[b,c]Final R Indexes [all data]	R_1 = 0.0.0704 wR_2 = 0.0.0976	R_1 = 0.0.0465 wR_2 = 0.0.0697
Largest Diff. Peak/Hole/ e $Å^{-3}$	0.55 / -0.73	0.56 / -0.60

Radiation = MoKα (λ = 0.71073), α = γ = 90°, Z = 4, [a]GooF: Goodness-of-fit = $\{\sum[w(F_o^2 - F_c^2)^2]/(n-p)\}^{1/2}$, where *n* is the number of reflections and *p* is the total number of parameters refined. [b]$R = \sum||F_o|-|F_c||/\sum|F_o|$. [c]$wR = \{\sum[w(F_o^2 - F_c^2)^2]/\sum w(F_o^2)^2]\}^{1/2}$.

Table 2-3. Pertinent bond lengths for compounds 1 and 2.

		$(PPN)_3[Ru^{III}(CN)_6]$		$(PPN)_3[Os^{III}(CN)_6]$	
Bond Lengths	Angles	Bond Lengths (Å)	Angles (°)	Bond Lengths (Å)	Angles (°)
M–C(1)	C(1)–M–C(2)	2.065(3)	89.77(10)	2.067(4)	90.85(12)
M–C(2)	C(2)–M–C(3)	2.063(3)	89.19(10)	2.063(4)	89.91(13)
M–C(3)	C(1)–M–C(3)	2.054(3)	178.25(11)	2.060(4)	178.48(13)
Avg M–C	—	**2.061(3)**	—	**2.063(4)**	—
C(1)≡N(1)	—	1.158(3)	—	1.153(4)	—
C(2)≡N(2)	—	1.152(3)	—	1.159(4)	—
C(3)≡N(3)	—	1.157(3)	—	1.150(4)	—
Avg C≡N	—	**1.156(3)**	—	**1.154(4)**	—
O–N	—	**2.861(16)**	—	**2.852(9)**	—

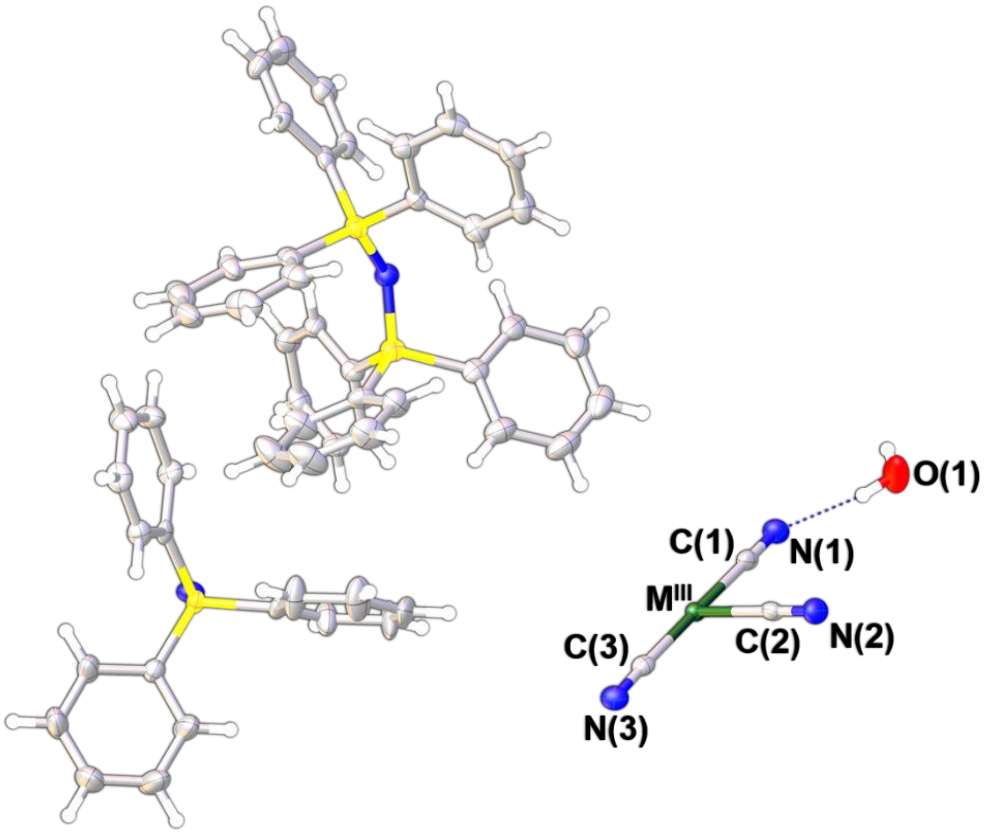

Figure 2-11. Asymmetric unit of $(PPN)_3[M^{III}(CN)_6]$. Yellow atoms are phosphorous. M^{III} is Os or Ru.

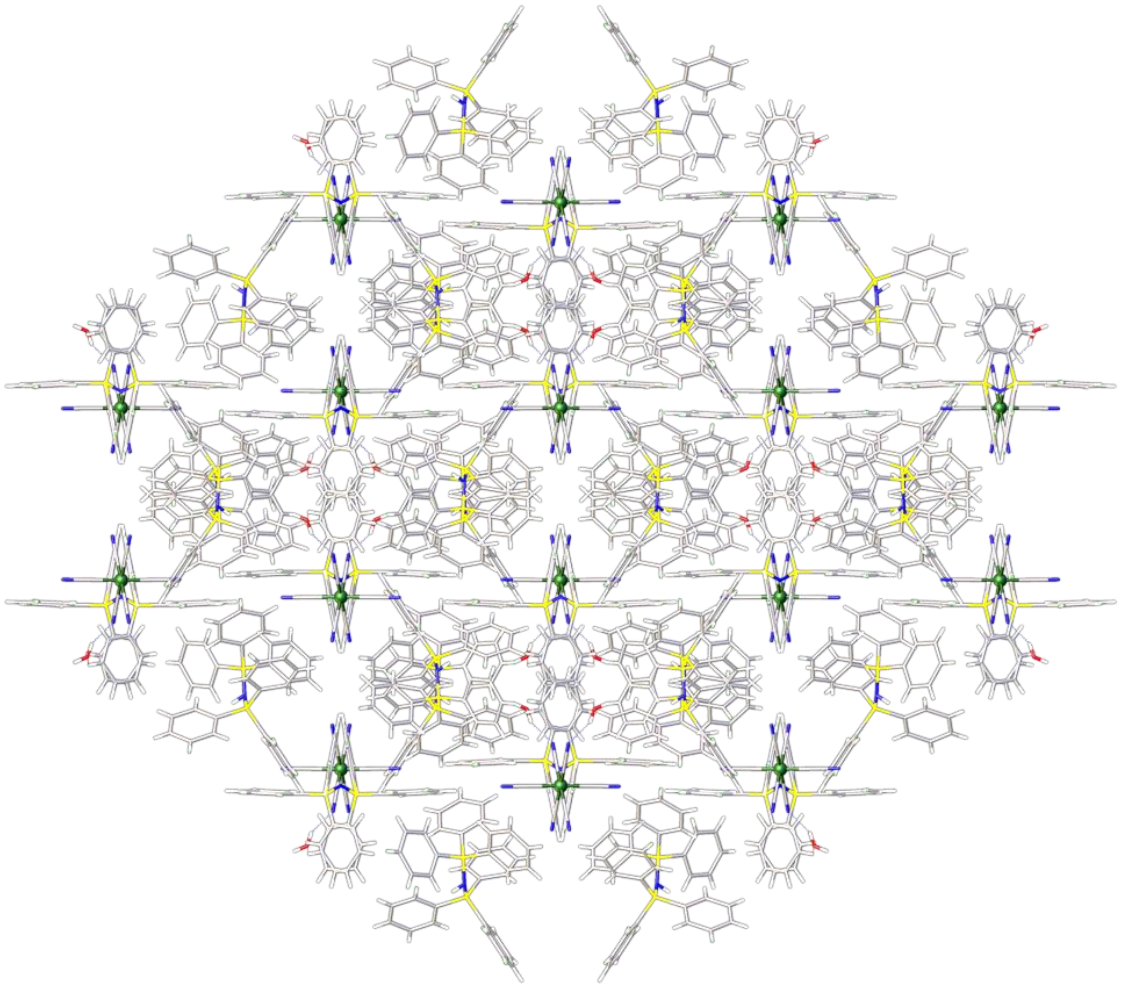

Figure 2-12. Packing diagram of $(PPN)_3[M^{III}(CN)_6]$, where M^{III} is Ru/Os. View is looking down the c axis. Color scheme: Green is Ru/Os, yellow is P, blue is N, red is O, grey is C and white is H.

Magnetic Properties

Both $(PPN)_3[Ru^{III}(CN)_6]$ and $(PPN)_3[Os^{III}(CN)_6]$ are S = ½ systems and, in the absence of any anisotropic effects, are expected to follow Curie law. As shown in Figure 2-13, Curie behavior is indeed exhibited for both $(PPN)_3[Ru^{III}(CN)_6]$ (Figure 2-13a) and $(PPN)_3[Os^{III}(CN)_6]$ (Figure 2-13b). For spin-only S = ½ systems, one would expect a χT value of 0.375 emu·K/mol. As can be seen from the data in Figure 2-13, both precursors have a value at 2 K slightly below what is expected for a spin-only value of χT. $(PPN)_3[Ru^{III}(CN)_6]$ exhibits a value of 0.30 emu·K/mol at 2 K while the Os congener has a χT value of 0.29 emu·K/mol. As temperature is increased, both compounds exhibit temperature induced paramagnetism (TIP). The pink and red lines in Figure 2-13 represent values expected for a Curie paramagnet with C = 0.30 and C = 0.29 emu·K/mol for the Ru and Os congeners, respectively. For the Ru compound, the 2 K data were fit using g = 1.79 and the room temperature data were fit by including a TIP value of 875×10^{-6} emu·K/mol. In order to fit $(PPN)_3[Os^{III}(CN)_6]$ to the Curie law, a g = 1.76 and TIP = 395×10^{-6} emu·K/mol were used. The fit lines modeled the experimental data best when no Weiss constant (θ) was taken into account. Magnetization data at 1.8 K (Figure 2-14) for both compounds are consistent with a S = ½ system as the data saturates near 1 B.M. The data were fit with the Brillouin function (pink line in Figure 2-14) using S = ½ for both compounds, with g = 1.77 for $(PPN)_3[Ru^{III}(CN)_6]$ and g = 1.74 for $(PPN)_3[Os^{III}(CN)_6]$.

According to Figgis and Hitchman,[186] the free ions of Ru^{3+} and Os^{3+} with

ground state terms of $^2T_{2g}$ should not deviate much from the spin-only values for these S = ½ ions. By taking λ and the orbital angular momentum reduction factor (k) into account, Figgis predicts that as temperature is reduced from 300 K, Ru^{3+} should vary in χT by ~47% and Os^{3+} should vary by ~21% as a function of kT/|λ|, where k and λ are held constant. For free ions, the value of k is unity as there is no delocalization of electrons from the t_{2g} orbitals of the ions onto the donor atoms of the ligands. When delocalization does occur, the value of k decreases and corresponds to an additional quenching of the orbital angular momentum which usually brings the magnetic moment closer to the spin-only value. As delocalization of the electrons is expected for the $(PPN)_3[Ru^{III}(CN)_6]$ and $(PPN)_3[Os^{III}(CN)_6]$ starting materials, the variance in the χT values and the deviation of the values from the spin-only ones are not in accord with the predictions made by Figgis for these $^2T_{2g}$ compounds. Between 2 and 300 K, the values of χT vary 77% and 41% for the Ru^{III} and Os^{III} hexacyanometallates, respectively. However, cases have been known for T terms in which an interaction with a nearby higher configuration results in an effective value of k that is greater than unity and would result in greater deviations from the spin-only values of χT. Essentially, these precursors seem to exhibit more orbital contribution to the magnetic properties than Figgis and Hitchman predicted.

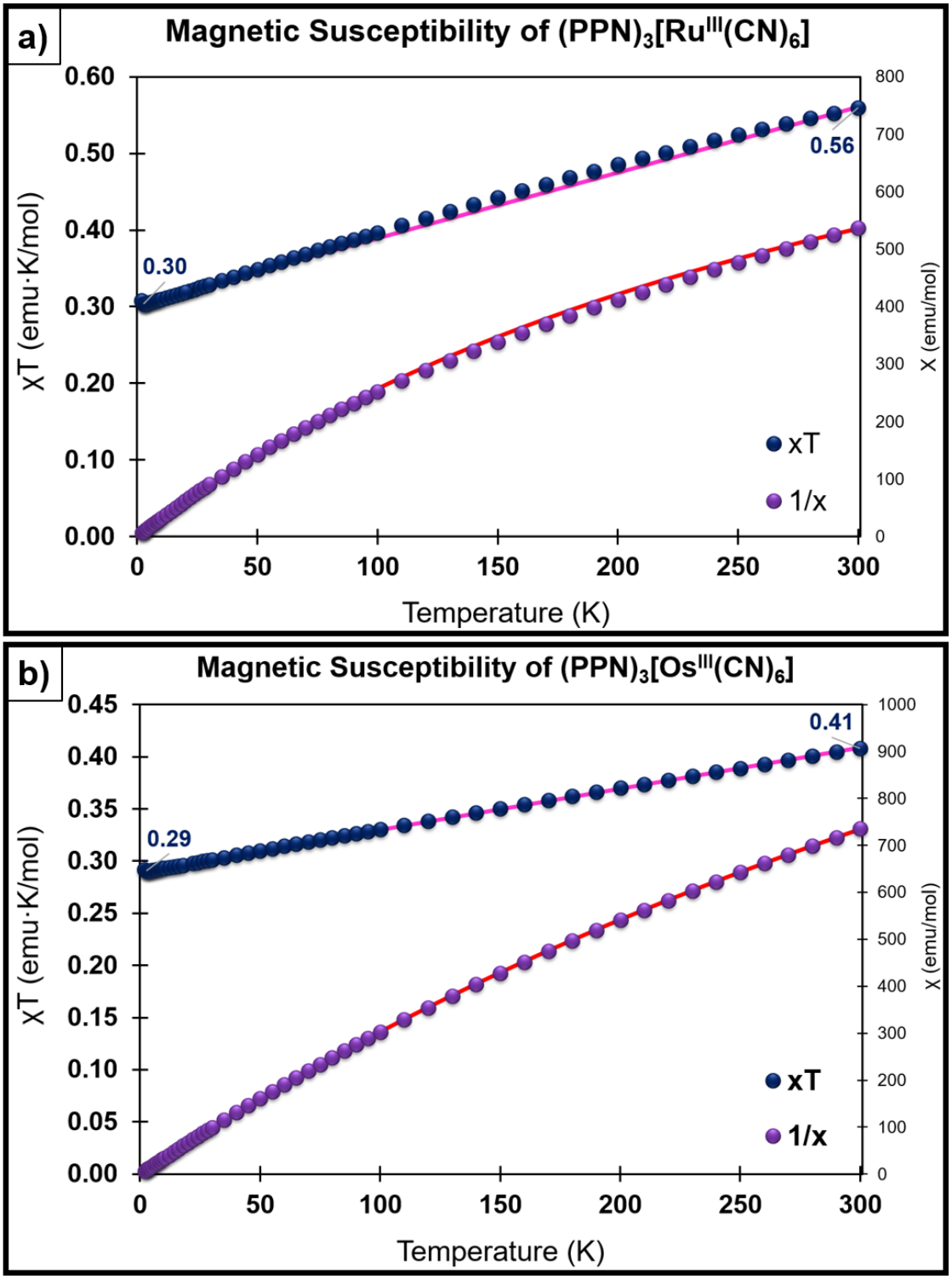

Figure 2-13. Temperature dependent susceptibility data for compounds 1 (a) and 2 (b). The susceptibility for both compounds exhibit Curie behavior with TIP (red and pink lines). Data was fit using C = 0.30, g = 1.79 and TIP = 875 x 10^{-6} emu·K/mol for compound 1 and C = 0.29, g = 1.76 and TIP = 395 x 10^{-6} emu·K/mol for compound 2.

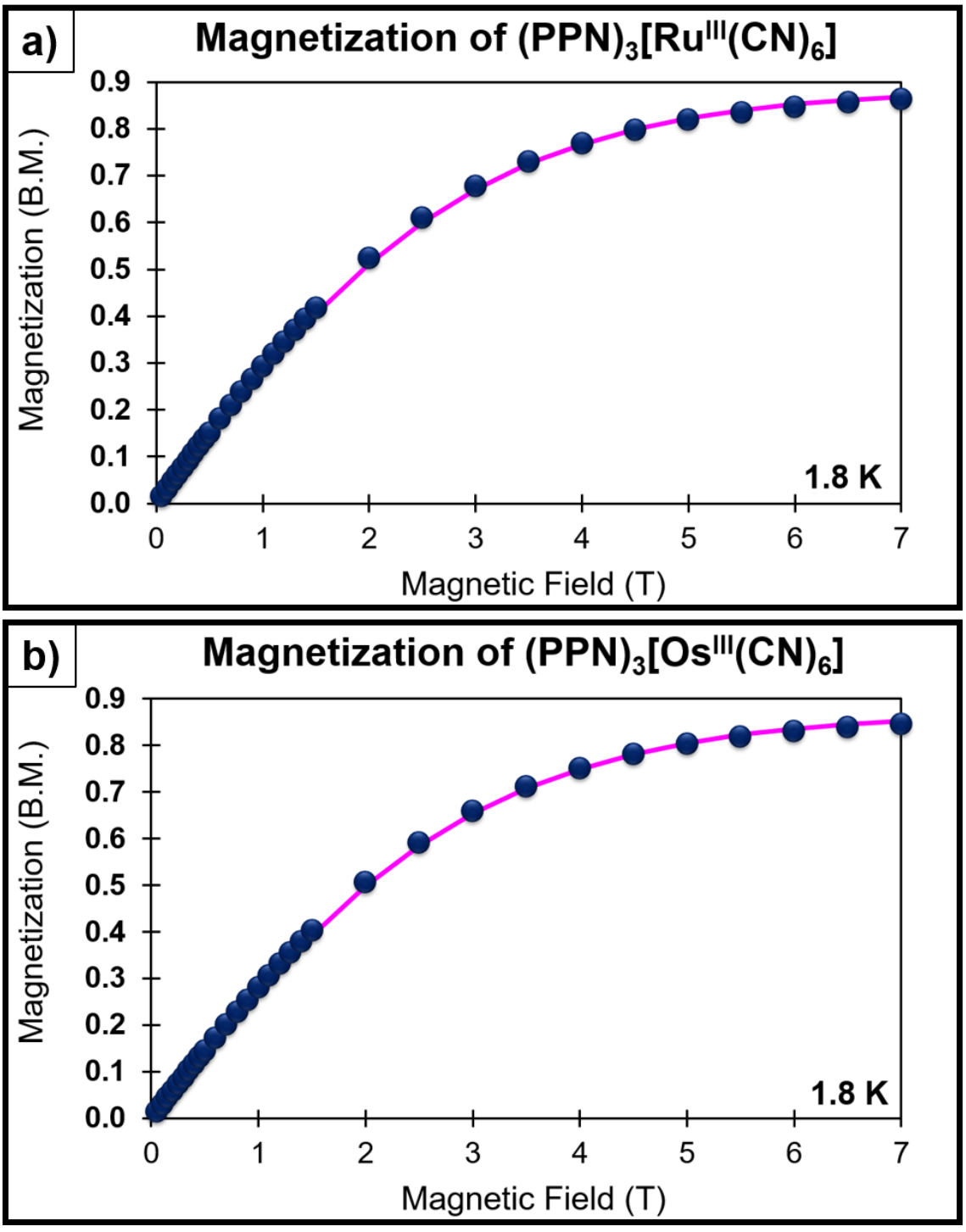

Figure 2-14. Magnetization data for compounds 1 (a) and 2 (b) at 1.8 K. The data are fit with the Brillouin function (pink lines) using g = 1.77 for compound 1 and g = 1.74 for compound 2.

Electron Paramagnetic Resonance Spectroscopy

Variable temperature electron paramagnetic resonance (EPR) data were collected by our collaborators, Dr. Doros Petasis and his student Keiron Stoddard at Allegheny College in Pennsylvania. Data were measured on solid samples of compounds 1 and 2 and also on 1 mM MeCN solution of both compounds. The spectra obtained for the compounds in MeCN (Figure 2-15) are broad and do not give much information. The intensities of the peaks decrease with increasing temperature until they are no longer observed above 100 K. The broad peaks are centered around a g ~ 2 for $(PPN)_3[Ru^{III}(CN)_6]$ and g ~ 1.8 for $(PPN)_3[Os^{III}(CN)_6]$. Spectra obtained on solid samples of 1 and 2 (Figure 2-16) exhibit multiple line structures centered around g ~ 1.8 for both samples, indicative of some unresolved hyperfine coupling. Literature reports of g values for Ru^{III} have been calculated or estimated to be 1.88[168] and 1.9.[158,187] EPR data at 78 K on a frozen methanol solution of $(K@18\text{-crown-6})_3[Ru^{III}(CN)_6]$ was reported to exhibit a single, broad resonance at 1.85.[170] The same group reported a g = 1.8 for the Os congener measured in the same manner[170] whereas another group obtained a g = 1.82 on a frozen water solution of $(Ph_4P)_3[Os^{III}(CN)_6]\cdot 6H_2O$.[179] Several g values for Os^{III} have been calculated or estimated in the literature recently: 1.75,[168] 1.79[179] and 1.8.[159,187] These values are in good agreement with the EPR data for the new $(PPN)^+$ salts and follow a trend of lower g values for Os^{III} as compared to Ru^{III}. In similar compounds, effective g values for $[Fe^{III}(CN)_6]^{3-}$ anions have been estimated to be 2.01[188] and 1.98.[168]

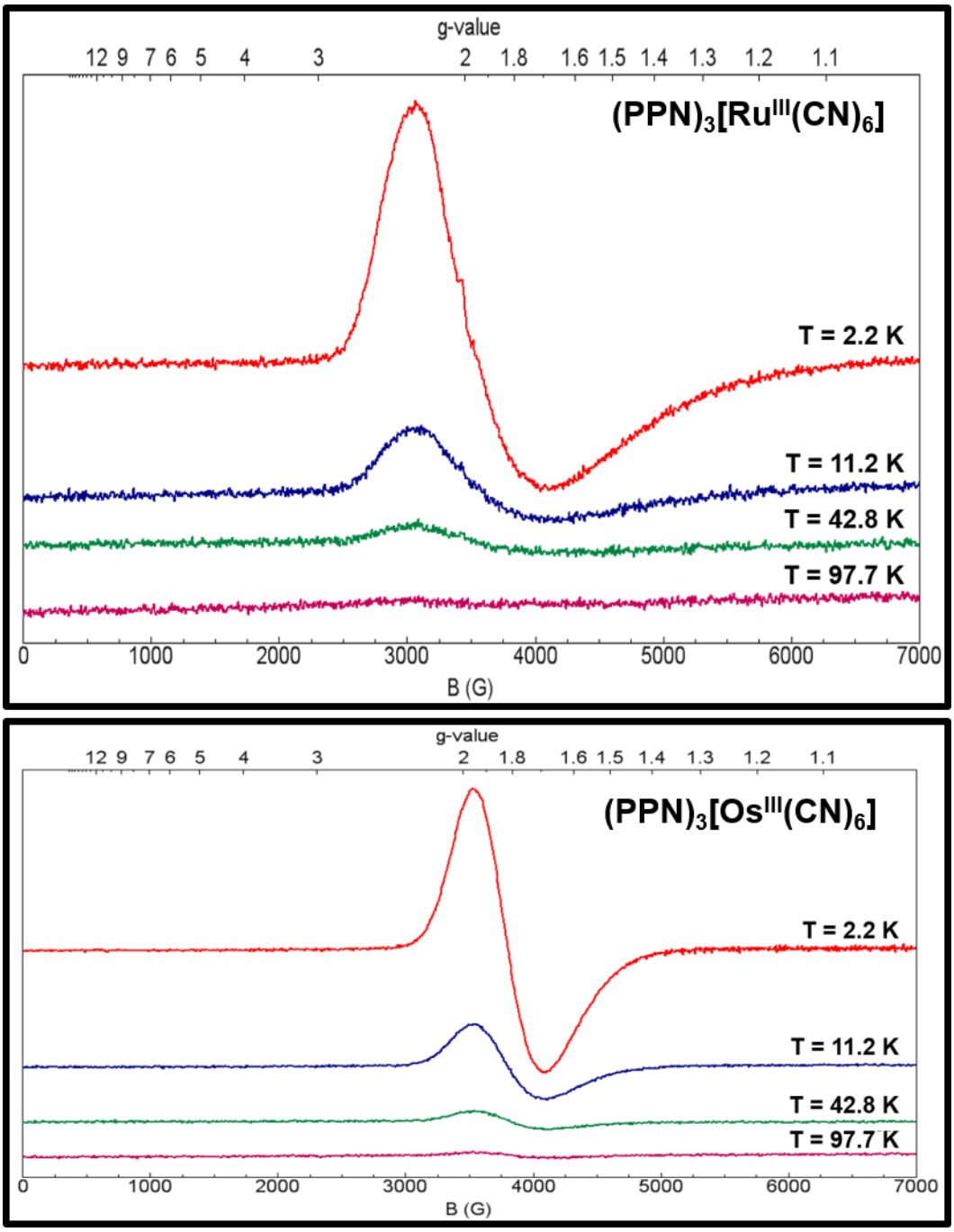

Figure 2-15. Variable temperature EPR data for 1 (top) and 2 (bottom). Compounds were measured in 1 mM MeCN solutions.

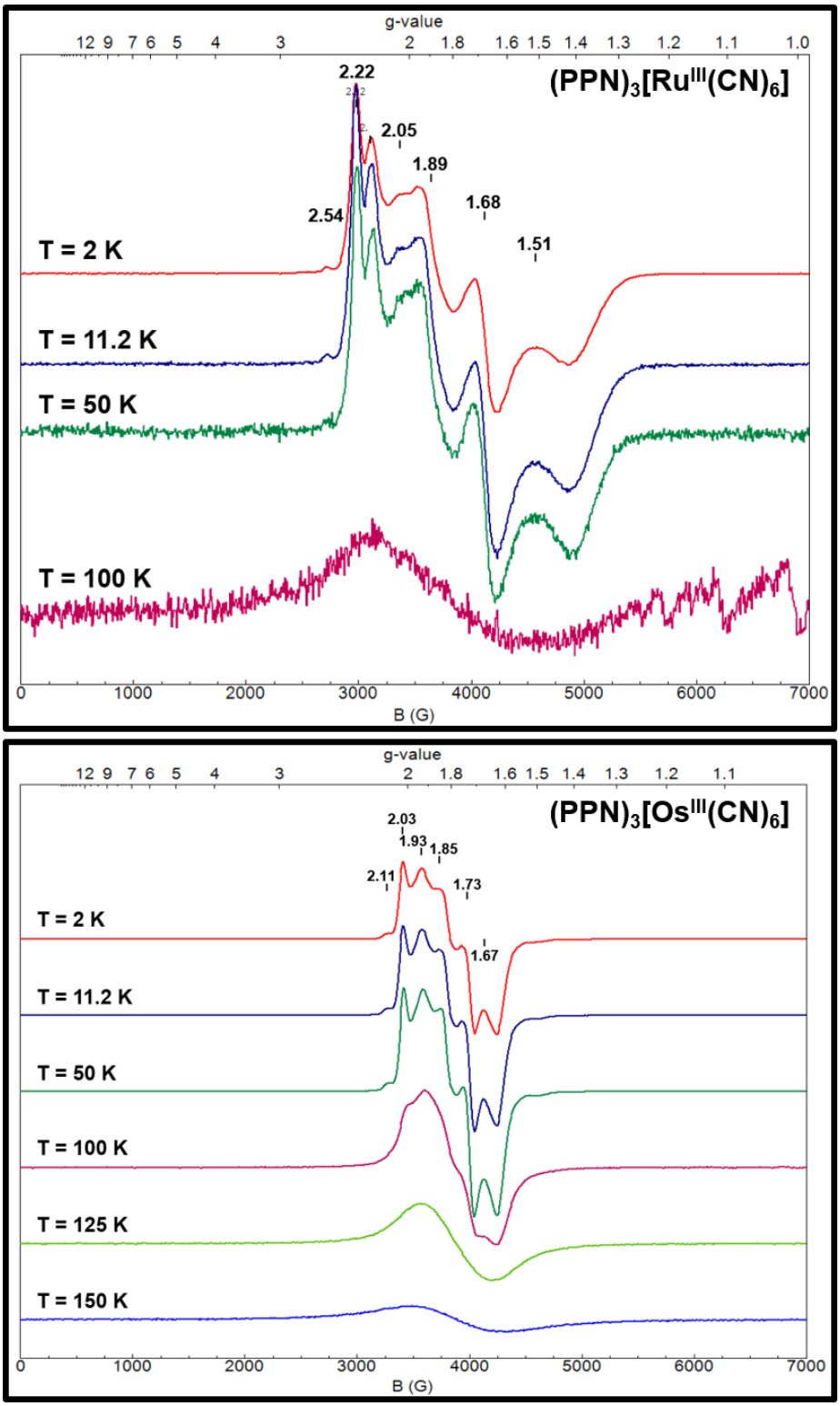

Figure 2-16. Variable temperature EPR data collected on solid samples of 1 (top) and 2 (bottom).

Cyclic Voltammetry

The ability of cyanometallates to be reversibly reduced or oxidized is an interesting facet of their magnetism. The redox properties of the hexacyanometallates incorporated into molecular cyanide materials have been widely studied for interesting magnetic phenomena such as charge-transfer-induced-spin-transition (CTIST). The $[Fe(CN)_6]^{3-/4-}$ redox properties have been rigorously studied and it is known that the reduction potential varies depending on several factors including the cation, solvent, electrolyte and working electrode. When the CV's of $(PPN)_3[Ru^{III}(CN)_6]$ and $(PPN)_3[Os^{III}(CN)_6]$ were attempted with a platinum working electrode, no redox couples were observed so a glassy carbon electrode was used for CV characterization. Experimental details can be found in Appendix A. During electrochemical studies of $(PPN)_3[Fe^{III}(CN)_6]$, Cauzzi and coworkers suggested that the non-electroactive $(PPN)^+$ cation is responsible for the lack of an electrochemical response with Pt and Au working electrodes due to adsorption phenomena.[180] They found that $(PPN)_3[Fe^{III}(CN)_6]$ exhibits a quasi-reversible reduction couple at -0.92 V (Table 2-4) with a ΔE separation of 0.1 V when using a glassy carbon electrode and a scan rate of 0.2 V/s.[180] Figure 2-17 shows the voltammograms for compounds 1 (top) and 2 (bottom) collected between a potential of +2 to -2 V. The compounds were scanned in the negative direction starting at an initial potential of 0 V. The reduction couple of $M^{III/II}$ (Table 2-4) occurs at -0.425 V for $(PPN)_3[Ru^{III}(CN)_6]$ and -0.70 V for $(PPN)_3[Os^{III}(CN)_6]$ referenced against Ag/AgCl with ΔE separations of 0.072 V for Ru and 0.078 V

for Os. The couples are assigned to the reduction of these trivalent compounds to their divalent counterparts, $[M^{III}(CN)_6]^{3-} \rightarrow [M^{II}(CN)_6]^{4-}$ The half potential for the reduction of $(PPN)_3[Ru^{III}(CN)_6]$ occurs at less negative potentials (~0.28 V and ~0.42 V less) in comparison to the $(PPN)_3[Os^{III}(CN)_6]$ and $(PPN)_3[Fe^{III}(CN)_6]$ compounds, respectively. As the potential is scanned in a more positive direction than the reduction couple, $(PPN)_3[Ru^{III}(CN)_6]$ exhibits two irreversible oxidations at +0.98 V and +1.78 V and $(PPN)_3[Os^{III}(CN)_6]$ exhibits a single irreversible wave at +0.85 V. Upon scanning back in the negative direction after this event, the original reduction events are no longer reversible as expected if the original species at the electrode surface has decomposed.

Table 2-4. Half potentials for the reduction of $(PPN)_3[M^{III}(CN)_6]$.

Compound	$E_{½}$ ($M^{III/II}$)
$(PPN)_3[Fe^{III}(CN)_6]$	-0.92 V
$(PPN)_3[Ru^{III}(CN)_6]$	-0.43 V
$(PPN)_3[Os^{III}(CN)_6]$	-0.70 V

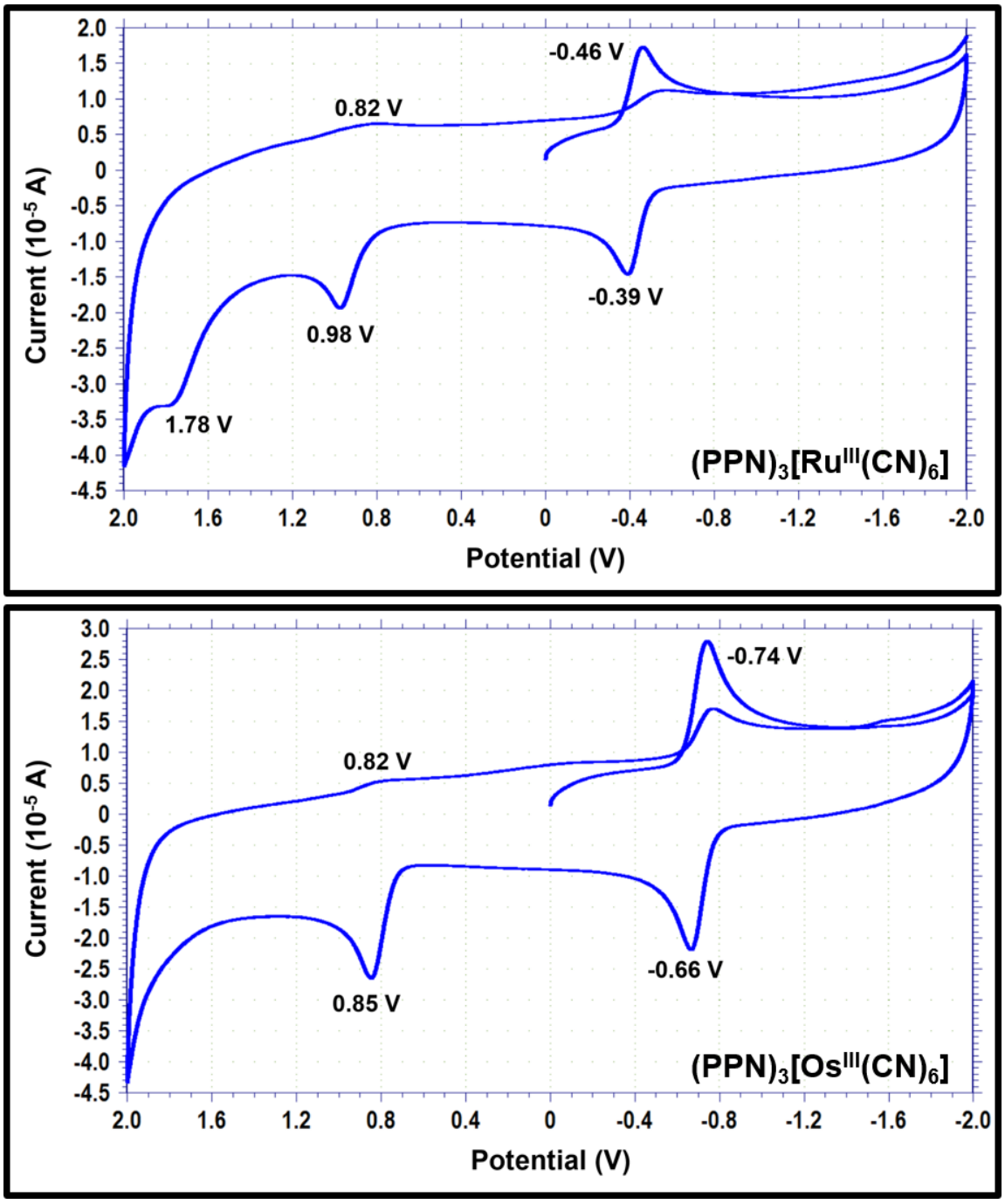

Figure 2-17. Voltammograms of compounds 1 (top) and 2 (bottom) in MeCN with a glassy carbon working electrode and a Ag/AgCl as the reference electrode.

Concluding Remarks

Access to pure precursors for their use as building blocks in coordination complexes is an important task of a synthetic inorganic chemist working in molecular magnetism. In the fast-paced field of magnetic cyanometallate chemistry, there are numerous groups competing to push back the frontiers by designing new heavy cyanometallates and probing how their magnetic properties differ from their 3d-transition-metal analogs and developing such methods is crucial. Although salts of $[Ru^{III}(CN)_6]^{3-}$ and $[Os^{III}(CN)_6]^{3-}$ have been reported in the literature previously, the methods led to products highly contaminated with divalent decomposition by-products. Not only were these previous methods unreliable, but they were also time consuming and used expensive organic cations as the counterions. In this work, the syntheses of these trivalent precursors has been vastly improved by using mild reagents/conditions that require only about one hour to complete. These new trivalent cyanometallate salts of $(PPN)^+$ were characterized structurally for the first time and found to crystallize in the orthorhombic Pbcn space group with less water than previous salts. Their $\nu_{C\equiv N}$ stretching frequencies and magnetic properties are consistent with the previously reported salts. The EPR data were also obtained to support the g values estimated from the susceptibility and magnetization data. The redox properties of these $(PPN)^+$ salts were studied for the first time with the results indicating that the reduction of these trivalent species is readily achieved. As expected, the results shown here demonstrate the similarity in behavior for the

Group VIII $[M^{III}(CN)_6]^{3-}$ anions and support the idea of Os having more intrinsic anisotropy than its 4d and 3d counterparts.

CHAPTER III

MAGNETIC PROPERTIES OF NEW TRIGONAL BIPYRAMIDAL MOLECULES BASED ON RUTHENIUM AND OSMIUM HEXACYANOMETALLATES

Background

As discussed in the introduction to the previous chapter, magnetic materials containing 3d transition metals have received most of the attention in magnetism research as they are easier to handle both experimentally and theoretically as compared to their 4d and 5d counterparts. Incorporation of 4d and 5d transition metals into molecular magnetic compounds offer several advantages over their 3d transition metal counterparts however. Specific differences between the first row metal ions and their heavier congeners are that the heavier metal ions (i) have more diffuse orbitals with the trend being 5d > 4d ≫ 3d,[156,160] (ii) possess larger intrinsic spin-orbit coupling (SOC) resulting in increased orbital contributions[15,157] (iii) are found in a variety of oxidation states, (iv) have redox properties that can be triggered with external stimulus and (v) can exhibit higher coordination numbers.[189] These advantages have been found to lead to new and enhanced magnetic behavior when these metal ions are incorporated into compounds. As stated in the last chapter, hexacyanoruthenate and hexacyanoosmate are similar to hexacyanoferrate in that they exist in both the divalent and trivalent oxidation states with six coordinated cyanide ligands. This situation allows for direct comparison of magnetic behaviors upon exchanging

hexacyanoferrate for the heavier, more anisotropic Group VIII metal ions and provides insight into the effects of increased magnetic exchange in cyanide bridged compounds. To date, very few compounds incorporating these heavier hexacyanometallate precursors have been reported. The first magnetic materials to incorporate one of these heavier Group VIII metals were the Ni_3Os_2 TBP and Prussian blue analog reported in 2008,[165] followed by the Fe_3Os_2 TBP[116] and the Co_3Os_2 Prussian blue analog[115] in 2010, all reported by our group. As discussed in the last chapter, enhanced magnetic properties were generally observed by incorporating the heavier Os metal ion into these compounds. A few compounds containing $[Ru^{III}(CN)_6]^{3-}$ and $[Os^{III}(CN)_6]^{3-}$ have been reported since 2010 and exhibit either SMM or SCM behavior.[158,159,166-168,187]

Our group's large study on TBP molecules presents itself as a powerful scaffold for probing how exchanging 3d hexacyanometallates for second and third row transition metals affects the magnetic properties of cyanide-bridged materials. A former group member worked on incorporating $[Ru^{III}(CN)_6]^{3-}$ and $[Os^{III}(CN)_6]^{3-}$ anions into the TBP framework but he was not able to obtain the elusive Co_3Ru_2 and Co_3Os_2 TBPs despite continued efforts, nor was he able to obtain structural data for the Mn_3Ru_2 TBP.[172] These homologous TBPs are highly sought by our group considering the interesting magnetic behavior shown by their 3d metal ion counterparts. The Co_3Fe_2 TBP can exist in different electronic isomeric forms depending on the amount and identity of interstitial solvent molecules – $[Co^{III}_2Co^{II}Fe^{II}_2]$, $[Co^{II}_2Co^{III}Fe^{III}Fe^{II}]$, $[Co^{II}_3Fe^{III}_2]$ – and can undergo charge-

transfer-induced-spin-transition behavior (CTIST) with both temperature and light irradiation.[111,142,148] Although both the Mn_3Fe_2[146] and Mn_3Os_2 analogs exhibited antiferromagnetic coupling, only the Mn_3Os_2 TBP exhibited SMM behavior.[172]

This chapter describes the Co_3Ru_2 and Co_3Os_2 TBPs and their structural and magnetic properties with details about the synthetic methods required to obtain them. This chapter will also describe the synthetic challenges involved to obtaining crystals of the Mn_3Ru_2 TBP and will introduce the Zn_3Os_2 TBP for the first time.

Experimental Details

Materials

All chemicals and solvents were of ACS reagent grade or higher and used as received, unless stated otherwise. ***Reagents for the synthesis of {[M^{II}(tmphen)$_2$]$_3$[M^{III}(CN)$_6$]$_2$}·nSolv:*** cobalt (II) iodide anhydrous (CoI_2 anhydrous, light sensitive and hygroscopic powder, 99.5%, Alfa Aesar), zinc (II) chloride ($ZnCl_2$, powder, 98+%, Sigma Aldrich), 3,4,7,8-tetramethyl-1,10-phenanthroline (**tmphen**) ($C_{16}H_{16}N_2$, crystalline powder that varies in color from pinkish to off-white, 98+%, Alfa Aesar). The CoI_2 anhydrous was stored in an oxygen- and water-free glove box with a nitrogen atmosphere. ***Reagents for the synthesis of {[M^{II}(tmphen)$_2$]$_2$[Ru^{II}(CN)$_4$(tmphen)]$_2$}·nSolv:*** manganese (II) chloride

anhydrous ($MnCl_2$, anhydrous, hygroscopic flakes, 96.8%, Alfa Aesar) and 3,4,7,8-tetramethyl-1,10-phenanthroline (**tmphen**) ($C_{16}H_{16}N_2$, crystalline powder that varies in color from pinkish to off-white, 98+%, Alfa Aesar). ***Solvents used:*** methanol (MeOH) (EMD) and acetonitrile (MeCN) (Fisher Scientific) were used as received from Texas A&M University's chemistry stockroom. N,N-dimethylformamide, anhydrous (DMF) (hygroscopic, 99.8%, Alfa Aesar, packed under Argon in a resealable ChemSeal™ bottle), was purchased and pumped into an oxygen- and water-free glove box with a nitrogen atmosphere before being opened. Once opened, DMF was stored in the glove box. Acetonitrile purchased from the stockroom was also pre-dried for two weeks over 3 Å molecular sieves (hygroscopic 3-5 mm beads, Alfa Aesar), refluxed over 3 Å molecular sieves and then distilled before being stored in the glove box.

Syntheses

$\{[Co(tmphen)_2]_3[Ru(CN)_6]_2\}\cdot nSolv$ (Co_3Ru_2) (3)

This reaction was carried out in an oxygen- and water-free glove box with a N_2 atmosphere and can be scaled up with minimal yield loss. A sample of CoI_2 (0.059 g, 0.189 mmol) was added to a 20 mL vial. MeCN (~12 mL) was added to the vial and the green mixture was stirred. The addition of DMF (~5-7 mL) to this solution that contained some CoI_2 undissolved turned the solution a light pink color. Slightly less than 2 equivalents of tmphen (0.078 g, 0.330 mmol) was added to the murky, light pink solution and stirred for about ten minutes - resulting in a

cloudy, yellow solution. A sample of $(PPN)_3[Ru^{III}(CN)_6]$ (0.214 g, 0.114 mmol) was dissolved in MeCN (~17 mL) in a different 20 mL vial to give a clear, golden-yellow-colored solution. The Co-containing solution was divided equally into two 20 mL vials and then half of the $(PPN)_3[Ru^{III}(CN)_6]$ solution was poured into each vial, resulting in dark blue/green solutions. Within five days, large, dark blue, block-shaped crystals formed in both vials, leaving a light yellow solution. Typical yields are 30-40%. IR, ν(C≡N): 2139 (vw, sp), 2101 (w, sp) and 2059 (m, b) cm^{-1} where vw = very weak, w = weak, m = medium, sp = sharp and b = broad. TGA thermograms exhibit mass losses between 10 and 12.5% up to 200 °C which correspond to ~5.7 to 7.4 molecules of acetonitrile per TBP molecule. *Refer to page eighty-three in notebook number three for a detailed description of the procedure and observations for the synthesis of the Co_3Ru_2 TBP (3).*

$\{[Co(tmphen)_2]_3[Os(CN)_6]_2\}\cdot$nSolv ($Co_3Os_2$) (4)

This reaction was also carried out in an oxygen- and water-free glove box with a N_2 atmosphere in an analogous manner to the Co_3Ru_2 congener and can be scaled up with minimal yield loss. A sample of CoI_2 (0.053 g, 0.177 mmol) was dissolved in MeCN (~12 mL) and DMF (~5-7 mL). Less than two equivalents of tmphen (0.077 g, 0.326 mmol) were stirred into the light, pink solution for approximately ten minutes (turning the solution yellow) before being divided equally into two 20 mL vials. A 20 mL, neon-green, MeCN solution of $(PPN)_3[Os^{III}(CN)_6]$ (0.246 g, 0.125 mmol) was divided equally and each half was

used to layer onto the cobalt-containing solution in each vial which resulted in powder formation and a dark blue/green solution at the interface. Large, dark blue, block-shaped crystals had formed within five days and the intensity of the solution had lightened. The vials were swirled to kick up any unwanted powder. The solvent and powder were decanted and the solvent was replaced with fresh MeCN. The samples were left under fresh MeCN for several hours before this purification step was repeated. This process is repeated as many times as necessary to obtain a solution free of powder and color. Once the MeCN remained clear and colorless with time, the crystals were collected by filtration. Typical yields range from 30-40% for TBPs. IR, ν(C≡N): 2142 (w, sp), 2095 (m, sh) and 2052 cm^{-1} (vs) where w = weak, m = medium, sp = sharp and sh = shoulder. TGA thermograms exhibit mass losses up to 200 °C that range between 7 and 20%, which corresponds to ~4 – 14 molecules of acetonitrile per TBP molecule depending on the batch. *Refer to page twenty-one in notebook four for a detailed description of the procedure and synthesis for the Co_3Os_2 TBP (4).*

{[Zn^{II}(tmphen)$_2$]$_3$[Os^{III}(CN)$_6$]$_2$}·nSolv (Zn_3Os_2) (5)

A light, neon-green-colored solution of $(PPN)_3[Os^{III}(CN)_6]$ (0.20 g, 0.102 mmol) was prepared with MeCN (20 mL) in a 40 mL vial. A stoichiometric shortage of tmphen (0.0592 g, 0.251 mmol) was added to a 20 mL MeCN solution of $ZnCl_2$ (0.0279 g, 0.205 mmol) and then MeOH (8 mL) was added before stirring the reaction for about five minutes. The zinc-containing solution was gravity

filtered directly into the osmium containing solution in the 40 mL vial. Small, yellow needles formed from the yellow reaction mixture within 30 minutes. After this time, powder may be present. When this occurred, the solvent and powder were decanted as soon as powder began to form. The solvent was replaced with fresh MeCN and the solution was decanted again. A crop of crystals was collected resulting in a ~36% yield. IR, v(C≡N): 2150 (w, sp), a doublet at 2133 and 2125 (w), 2099 (m, b), 2073 (w, sh) and 2051 (w, b) cm^{-1} where w = weak, m = medium, b = broad and sh = shoulder. Below 150 °C, TGA thermograms exhibit a continuous, gradual mass loss which corresponds to varying amounts of interstitial solvent present from sample to sample. The compound is thermally stable up to ~270 °C. *Refer to page ninety-seven in notebook six for a detailed description of the procedure and observations for the synthesis of the Zn_3Os_2 TBP (5).*

{[M^{II}(tmphen)$_2$]$_2$[Ru^{II}(CN)$_4$(tmphen)]$_2$}·2DMF·8H_2O (Mn_2Ru_2) (6)

Methanol (20 mL) was added to $MnCl_2$ anhydrous (0.0162 g, 0.129 mmol) in air and the mixture was stirred. DMF (20 mL) was added to aid in the dissolution of anhydrous $MnCl_2$. The reaction was stirred for 20 minutes after which time tmphen (0.0668 g, 0.283 mmol) was added to the solution. A MeOH solution (40 mL) of $(PPN)_3[Ru^{III}(CN)_6]$ (0.217 g, 0.116 mmol) was prepared. Thin tubes were used to layer the yellow solution of $(PPN)_3[Ru^{III}(CN)_6]$ onto the light yellow solution of the Mn solution. A small amount of yellow powder formed at the dark

brown solvent interface. The tubes were covered with Parafilm® M and left undisturbed. Small, yellow, rod-shaped crystals formed between 2 and 6 months. No characterization data was obtained except for the crystal structure. *Refer to page thirty-four in notebook six for a detailed description of the procedure and synthesis for the Mn_2Ru_2 square (6).*

Results and Discussion

Synthesis and Characterization

Co_3Ru_2 (3) and Co_3Os_2 (4)

Several attempts to prepare these TBP analogs were made before finding the right combination of solvent and starting materials that would result in the formation of crystals. Conventional methods used to prepare TBP molecules (combining MeCN or MeOH solutions of the $[M^{II}(tmphen)_2]Cl_2$ and $[M^{III}(CN)_6]^{3-}$ precursors) did not suffice and generally resulted in the crystallization of $[Co^{II}(tmphen)_3]Cl_2$. Multiple solvent combinations and layering techniques were tried but none were found to work until two concomitant changes were made. By changing the starting material from $CoCl_2$ to CoI_2 and adding DMF to the MeCN solution containing the divalent halide salt and tmphen, crystals of both the Co_3Ru_2 and Co_3Os_2 analogs were obtained. The addition of DMF proved useful during the oxidation of the divalent hexacyanometallates to the trivalent species and it was thought that the addition of DMF during the formation of the TBP would help stabilize the reaction.

Although these compounds were first prepared under anaerobic conditions, it was found that they can be prepared in air as well. The anaerobic preparation of the TBPs allows for some control of interstitial solvent and better reproducibility of the compounds' properties as it has been shown that TBPs are very susceptible to solvent exchange with water which usually affects the magnetic properties of them. It was also found that these TBPs can be prepared in a bulk manner when the synthetic conditions discussed here are met, similarly to most other TBPs made by our group.

IR stretching frequencies of the terminal and bridging cyanide ligands for both compounds are listed in Table 3-1. The higher frequency values are consistent with bridging cyanide ligands while the frequencies at 2059 cm^{-1} and 2052 cm^{-1} are in accord with terminal cyanide ligands coordinated to Ru^{II} and Os^{II}, respectively. The room temperature IR spectra indicate that the Ru^{III} precursor has been reduced to Ru^{II}, most likely from a charge-transfer (CT) event between Co^{II} and Ru^{III}. As there are no $\nu_{C\equiv N}$ modes that correspond to frequencies exhibited by the $[Ru^{III}(CN)_6]^{3-}$ starting material, it is believed that two CT events occurred and the TBP exists as $[Co^{II}Co^{III}_2Ru^{II}_2]$ at room temperature. The IR spectrum for Co_3Os_2 is very similar to that of Co_3Ru_2 and suggests that two CT events occurred resulting in a room temperature configuration of $[Co^{II}Co^{III}_2Os^{II}_2]$, which is in contrast to the room temperature magnetic data (vide infra).

Table 3-1. Cyanide stretching frequencies for compounds 3 and 4 along with the $K_4[M^{II}(CN)_6]$ and $(PPN)_3[M^{III}(CN)_6]$ starting materials as references.

Compound	Bridging (cm^{-1})	Terminal (cm^{-1})
Co_3Ru_2 (3)	**2139, 2101**	**2059**
$K_4[Ru^{II}(CN)_6]$	—	2052, 2038
$(PPN)_3[Ru^{III}(CN)_6]$	—	2094, 2085
Co_3Os_2 (4)	**2142, 2095**	**2052**
$K_4[Os^{II}(CN)_6]$	—	2068, 2039
$(PPN)_3[Os^{III}(CN)_6]$	—	2083, 2076

TGA data demonstrate that the ability of TBPs to contain varied amounts of solvent in the interstices is not different for these congeners and underscores the importance of characterizing samples used for magnetic measurements by TGA. Crystal data alone is not sufficient for determining interstitial solvent molecules for the diamagnetic correction of magnetic data, making TGA a necessary characterization method for TBPs. Co_3Ru_2 and Co_3Os_2 were found to be thermally stable throughout the analyses, which were carried out until 200 °C.

Zn_3Os_2 (5)

The crystallization of the Zn_3Os_2 TBP requires specific conditions, similar to the other TBPs mentioned here. The synthesis of this TBP only works when MeOH is added to the MeCN solution of $ZnCl_2$ and tmphen before mixing it with the MeCN solution of $(PPN)_3[Os^{III}(CN)_6]$. If the MeOH is not included, crystals will not form and powder will precipitate within twenty minutes. This still occurs even

if MeOH is added after the two solutions are mixed but before the powder precipitates. The yield of the reaction is dependent upon the rate at which the solutions are mixed. Layering the two solutions results in very few crystals forming along with the yellow powder. However, quickly mixing the two solutions together leads to the formation of the crystalline product.

The IR spectra exhibit six different peaks in the cyanide stretching frequency region (refer to Table 3-2). As with other TBPs and cyanometallate compounds, the three higher frequency peaks are attributed to the bridging cyanide ligands while the two lowest frequency peaks are most likely due to the terminal cyanide ligands as they resemble the stretching frequencies exhibited by the $(PPN)_3[Os^{III}(CN)_6]$ precursor. The stretch at 2099 cm^{-1} is the most dominate of the peaks and is assigned to a terminal stretching frequency and is 26 cm^{-1} lower than the three peaks attributed to the bridging cyanide and 26 cm^{-1} higher than the typical values for $[Os^{III}(CN)_6]^{3-}$ salts.

Table 3-2. Room temperature IR $\nu_{C\equiv N}$ for the Zn_3Os_2 TBP (5).

	Bridging (cm^{-1})	**Terminal (cm^{-1})**
Zn_3Os_2 TBP (5)	2150, 2133, 2125	2099, 2073, 2051

As with most TBPs studied, analysis of the TGA thermograms for the Zn_3Os_2 TBP reveal that the amount of solvent in these compounds vary. Typical

thermograms exhibit an immediate but gradual mass loss between room temperature and 150 °C which typically corresponds to ~4 – 10% mass loss. The Zn_3Os_2 TBP was determined to be thermally stable up to 270 °C before decomposition began. Analysis of the thermogram that was performed on the Zn_3Os_2 sample measured in the SQUID revealed the TBP lost 5.6% of its mass due to solvent loss, which corresponds to ~7.6 H_2O molecules per TBP.

{[M^{II}(tmphen)$_2$]$_2$[Ru^{II}(CN)$_4$(tmphen)]$_2$} (Mn_2Ru_2) (6)

The formation of this molecule was not intentional and was the result of one of many attempts to crystallize the Mn_3Ru_2 TBP. By layering MeOH/DMF solutions of the usual starting materials for the synthesis of TBPs, in conjunction with being left undisturbed for a significant amount of time (> 2 months), yellow rod-shaped crystals formed among yellow powder. Due to the small amount of crystallized product, no characterization techniques other than single X-ray crystallography could be done on this compound.

Single Crystal X-ray Diffraction

Relevant crystal structure data and refinement parameters for the compounds discussed in this chapter are listed in Table 3-4. Details on the methods used to collect the structural data for the compounds can be found in Appendix A. For compounds 3 and 4, both MeCN and water molecules were determined to be in the void spaces while trying to model the disordered Q-peaks.

The Zn_3Os_2 TBP (5) was determined to contain only water in the void space as the electron densities were not consistent for MeCN. The SQUEEZE program[190] within PLATON was used to analyze the void spaces and the amount of electron density for molecule 3 – 5 (Table 3-3). With the use of Solver (a built in Excel add-in), both the calculated electron density and void space were used to solve for the approximate amount of MeCN and/or water molecules for each TBP. The increase in electron density found in the Co_3Os_2 TBP at 20 K as compared to 100 K is most likely the result of ice formation on the crystal or could possibly be due to the crystal absorbing atmospheric water during data collection. The solvent in the Mn_2Ru_2 compound (6) was modeled so the use of SQUEEZE was not needed.

Table 3-3. SQUEEZE analysis and results for the Co_3Ru_2, Co_3Os_2 and Zn_3Os_2 TBPs.

TBP Temp	**Void Space (Å)**	**Number of Electrons**	**% Void Space**	**H_2O/TBP**	**MeCN/TBP**
Co_3Ru_2 110 K	4151.0	2012	40.0	24.0	4.5
Co_3Os_2 20 K	4180.0	2498	40.2	27.8	3.7
Co_3Os_2 100 K	4223.8	866	40.2	20.6	3.2
Zn_3Os_2 100 K	3156.0	873	26.5	21.8	0

Table 3-4. Structural data and refinement parameters for compounds 3 – 6.

Compound	**Co_3Ru_2 (3)** 110 K	**Co_3Os_2 (4)** 20 K	**Co_3Os_2 (4)** 100 K	**Zn_3Os_2 (5)** 100 K	**Mn_2Ru_2 (6)** 100 K
Space Group	*P*3_221	*P*3_221	*P*3_221	*P*2_1/c	*P*-1
a/ Å	24.552(4)	24.5892(15)	24.646(10)	19.8681(14)	15.6277(7)
b/ Å	24.552(4)	24.5892(15)	24.646(10)	25.0997(17)	18.4130(8)
c/ Å	19.857(3)	19.7803(14)	19.830(8)	24.1240(17)	20.8511(9)
α/ °	90	90	90	90	80.533(3)
β/ °	90	90	90	98.781(5)	79.169(3)
γ/ °	120	120	120	90	69.601(3)
Volume/ $Å^3$	10366(3)	10357.4(15)	10431(10)	11889.2(14)	5491.5(4)
Z	3	3	3	4	2
[a]Interstitial Solvent	2 MeCN, 23 H_2O	3 MeCN, 23 H_2O	4 MeCN, 21 H_2O	22 H_2O	2 DMF, 8 H_2O
μ/ mm^{-1}	0.61	2.23	2.215	3.359	6.389
Crystal Habitat	Dark Blue Block	Dark Blue Block	Dark Blue Block	Yellow Needle	Yellow Rod
Crystal Size/ mm^3	0.22 x 0.27 x 0.36	N/A	N/A	0.12 × 0.11 × 0.02	0.028 × 0.019 × 0.019
λ	MoKα 0.71073	MoKα 0.71073	MoKα 0.71073	Sync. 0.7749	Sync. 0.7749
2Θ Range for Data Collection/ °	2.806 to 54.96	3.826 to 61.424	8.862 to 61.612	4.124 to 46.078	4.328 to 48.296
Independent Reflections	13069 R_{int} = 0.0556 R_{sigma} = 0.0702	21403 R_{int} = 0.1849 R_{sigma} = 0.1169	21647 R_{int} = 0.2275 R_{sigma} = 0.1907	12800 R_{int} = 0.1339 R_{sigma} = 0.0954	13487 R_{int} = 0.1241 R_{sigma} = 0.0999
Data/Restraints/Parameters.	13069/0/629	21403/153/631	21647/153/631	12800/456/1256	13487/0/1367
[b]GooF on F^2	0.931	1.03	0.983	1.066	1.021
[c,d]Final R Indexes [I>=2σ (I)]	R_1 = 0.0362 wR_2 = 0.0875	R_1 = 0.0655 wR_2 = 0.1273	R_1 = 0.0753 wR_2 = 0.1506	R_1 = 0.0897 wR_2 = 0.2601	R_1 = 0.0580 wR_2 = 0.1468
[c,d]Final R Indexes [all data]	R_1 = 0.0544 wR_2 =0.0970	R_1 = 0.1628 wR_2 = 0.1704	R_1 = 0.2045 wR_2 = 0.2096	R_1 = 0.1389 wR_2 = 0.2998	R_1 = 0.1064 wR_2 = 0.1695
Largest Diff. Peak / Hole/ e $Å^{-3}$	0.29 / -0.22	1.73 / -0.85	1.42 / -0.82	1.95 / -1.05	1.67 / -.60

[a]*Calculated from SQUEEZE data.* [b]GooF: Goodness-of-fit = $\{\sum[w(F_o^2 - F_c^2)^2]/(n-p)\}^{1/2}$, where *n* is the number of reflections and *p* is the total number of parameters refined. [c]$R = \sum||F_o|-|F_c||/\sum|F_o|$. [d]*w*R = $\{\sum[w(F_o^2 - F_c^2)^2]/\sum w(F_o^2)^2]\}^{1/2}$.

Co_3Ru_2 (3) and Co_3Os_2 (4) TBPs

Whereas most TBPs studied by our group (including the Co_3Fe_2 TBP) crystallize in the $P2_1/c$ space group, the Co_3Ru_2 and Co_3Os_2 TBPs crystallize in the enantiomorphic, more symmetrical $P3_221$ space group. This results in the equatorial Co ions having near perfect three-fold rotation when looking down the axial positions of the TBP and the asymmetric unit being only half of the TBP (Figure 3-1). The metal–ligand (M–L) bond lengths for the Co_3Ru_2 and Co_3Os_2 TBPs can be found in Table 3-5. Variable temperature studies were tried for the Co_3Os_2 TBP as magnetic behavior (vida infra) warranted it. Unfortunately, the Co_3Os_2 TBP rapidly desolvates so room temperature data were not obtained. Data collected above 100 K on multiple crystals could not be well resolved and will not be discussed. The M–C bond lengths for these TBPs are similar between them (~2.02 Å) and give no indication of the oxidation state of the metal. Due to the symmetry of the TBP, only one axial metal position (M–C) is crystallographically unique. The symmetry of these TBPs results in one and one-half of the equatorial cobalt centers being crystallographically unique as well. In these structures, the Co(1) centers are symmetrically equivalent and make up 2/3 of the equatorial metal sites. Typical bond lengths for a $Co–N_6$ coordination environment generally follow the trend: LS Co^{III} (~1.9 Å) < LS Co^{II} (~2.0 Å) < HS Co^{II} (~2.1 Å).[191-195] A HS electronic configuration of Co^{III} is very unlikely as the only known examples of this situation are for $[CoF_6]^{3-}$, $[CoF_3(OH_2)_3]$ and Klaui complexes.[81,196-199] The Co_3Ru_2 TBP at 110 K and the Co_3Os_2 TBP at both 20 K

and 100 K have similar metrical parameters. All have one cobalt center (Co(2)) with an average Co–N bond length of ~1.9 Å and two symmetrically equivalent cobalt centers (Co(1)) with an average Co–N bond length of ~2.0 Å. The average Co–N bond lengths for the Co(2) centers are consistent with literature values for a LS Co^{III} center and the Co(1) centers have typical bond lengths characteristic of a LS Co^{II}–N_6 configuration. These data suggest that both the Co_3Ru_2 and Co_3Os_2 TBPs are in a $[(LS\text{-}Co^{II})_2(LS\text{-}Co^{III})M^{II}M^{III}]$ (M = Ru or Os) electronic configuration. However, as these TBPs are more symmetrical than usual, the actual bond lengths of the Co(1) centers could be different from one another and the values obtained could be spatial averages of the two centers throughout the lattice. If this is the case, then one of the Co(1) centers could actually have an average Co–N bond length closer to 1.9 Å (for a LS Co^{III} center) while the other Co(1) center has Co–N bond lengths closer to 2.1 Å (typical for a HS Co^{II} center). Knowing this, the possibility of a $[(HS\text{-}Co^{II})(LS\text{-}Co^{III})_2M^{II}_2]$ (M = Ru or Os) configuration cannot be precluded as a possibility and is actually the case for the water containing Co_3Fe_2 congener that crystallizes in the less symmetric $P2_1/c$.[147,148]

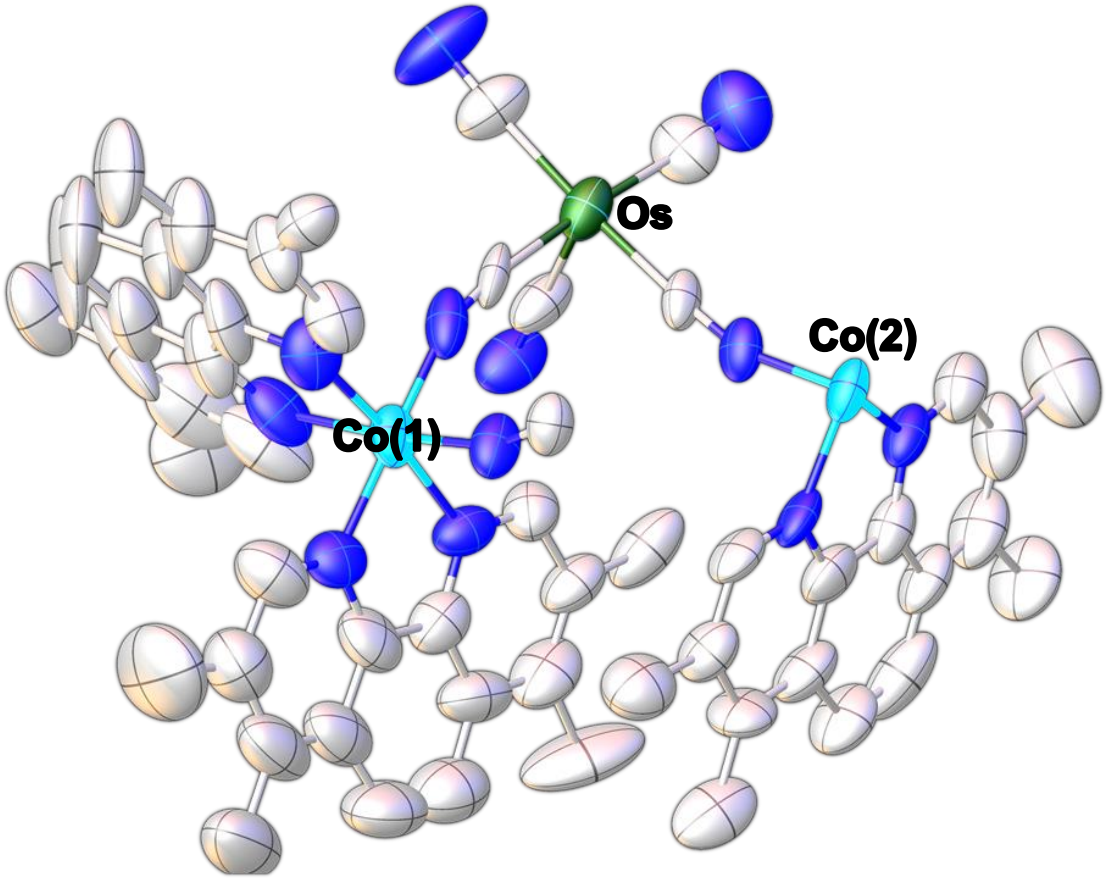

Figure 3-1. Asymmetric unit of the Co_3Os_2 TBP. Co_3Ru_2 is isomorphic and not shown. Color scheme: Green is Os, cyan is Co, blue is N and white is C. Hydrogen atoms have been omitted for the sake of clarity.

Table 3-5. M–L bond lengths for the asymmetric units of the Co_3Ru_2 and Co_3Os_2 TBPs.

Co_3Ru_2 (3)	Co(1)–N	Co(2)–N	Ru(1)–C
110 K	1.948(6)	1.894(4)	1.971(6)
	1.958(4)	1.945(5)	2.005(5)
	2.025(5)	1.962(4)	2.021(5)
	2.030(5)		2.050(5)
	2.032(6)		2.059(6)
	2.046(7)		2.068(7)
Avg M–L	**2.006(5)**	**1.934(4)**	**2.029(6)**
Co_3Os_2 (4)	Co(1)–N	Co(2)–N	Os(1)–C
20 K	1.954(10)	1.902(09)	1.965(11)
	1.954(14)	1.933(11)	1.998(15)
	2.034(11)	1.960(09)	2.007(12)
	2.043(11)		2.041(14)
	2.068(10)		2.047(18)
	2.078(13)		2.069(13)
Avg M–L	**2.022(11)**	**1.932(10)**	**2.021(14)**
100 K	1.952(12)	1.885(12)	1.952(14)
	1.954(17)	1.916(12)	2.001(18)
	2.014(13)	1.946(11)	2.020(15)
	2.023(13)		2.024(20)
	2.061(14)		2.041(17)
	2.061(11)		2.058(16)
Avg M–L	**2.011(13)**	**1.916(12)**	**2.016(17)**

Upon investigating the π-π stacking interactions within the Co_3Ru_2 and Co_3Os_2 TBPs using the Olex2 structure solution program[200], it was found that these molecules have one intermolecular interaction (Figure 3-2) and one intramolecular interaction (Figure 3-3). The parameters Olex2 uses to detect intermolecular interactions is a centroid-centroid distance less than 4 Å between

planes formed by NC_5 or C_6 rings and a shift distance between centroids that is less than 3 Å. A 4 Å distance for the centroid-centroid distance is considered to be slightly long for π-π stacking interactions, as discussed by Janiak.[201] Strong π-π interactions are considered to be at a distance ~3.3 Å with weaker interactions ~3.6 – 3.8 Å. The distance of 3.8 Å is generally considered the maximum distance for which π-π interactions are acknowledged, which is in accordance with the sum of Van der Waals radii's (with 1.77 Å the proposed radii for C).[202] Figure 3-2 highlights the intermolecular interaction (purple plane in the figure) between the carbon ring in one tmphen ligand with its symmetrically equivalent self in the other TBP. This interaction, being a consequence of these TBPs stacking in a dimeric unit due to symmetry, is the stronger of the two π-π stacking interactions as indicated by the smaller centroid-centroid distance (Table 3-6). Figure 3-3 highlights the intramolecular interactions (blue and green planes in the figure) between tmphen ligands on the Co(1) and Co(2) centers and is the weaker of the two molecular interactions, having centroid-centroid distances of ~3.96 Å. This interaction is very weak and the centroid-centroid distance can be considered as being too long for an interaction to be relevant (according to Janiak), but for the purpose of comparisons, the distance of 4.0 Å that Olex2 uses to define an interaction will be used throughout this dissertation. Despite the structure having nearly three-fold symmetry when looking down the axial metal positions, there is no intramolecular interaction between the tmphen ligands coordinated to the two Co(1) centers (centroid-centroid distances just slightly over 4 Å), just like in the

TBPs that crystallize in $P2_1/c$. When comparing the π-π interactions (Table 3-6) between the Co_3Ru_2 and Co_3Os_2 TBPs, it appears that they are slightly slipped (as indicated by the increase in shift distances) for the Co_3Ru_2 congener with the most noticeable difference between the two TBPs being the intramolecular interaction.

Table 3-6. Geometric parameters (centroid-centroid distances, shift distances and angles between planes) for the inter- and intramolecular π-π stacking interactions in the Co_3M_2 TBPs (3 and 4).

Interaction-Plane	TBP	Temperature	Centroid-Centroid Distance (Å)	Shift Distance (Å)	Angle (º)
inter-pp	Co_3Ru_2	110 K	3.700	1.313	2.598
	Co_3Os_2	20 K	3.652	1.220	3.206
		100 K	3.653	1.250	3.127
intra-gb	Co_3Ru_2	110 K	3.964	1.597	12.268
	Co_3Os_2	20 K	3.949	1.324	11.180
		100 K	3.970	1.366	10.257

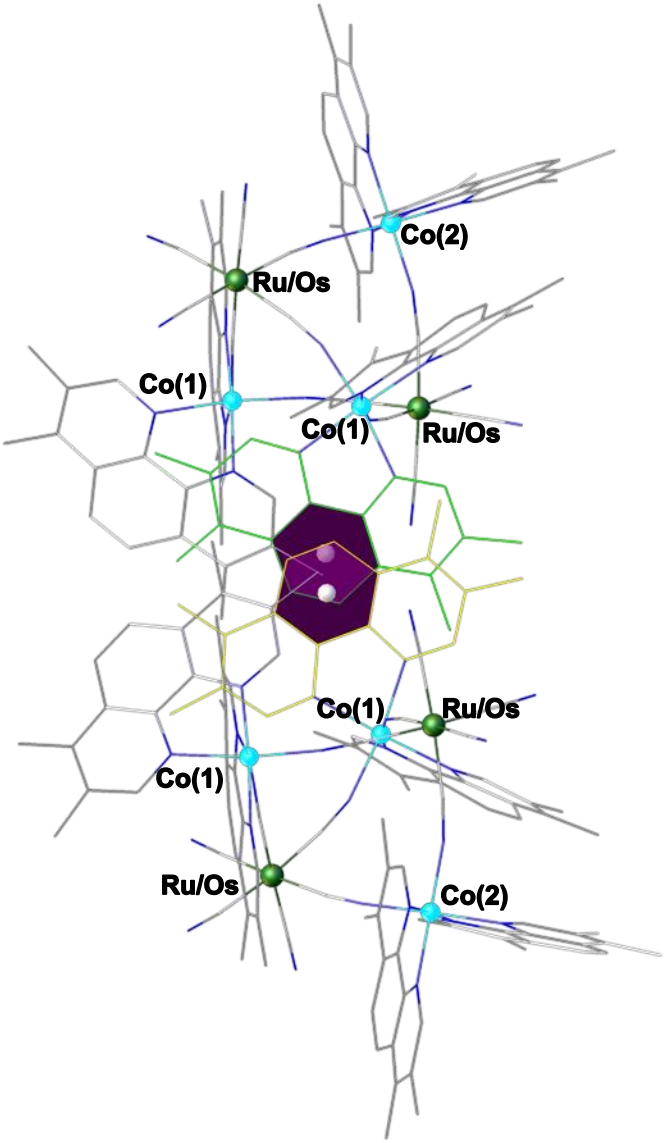

Figure 3-2. Dimeric unit of the Co_3M_2 TBPs where M = Ru/Os. The purple planes highlight the intermolecular interaction between these molecules. Interaction referred to as inter-pp. Hydrogen atoms are omitted for the sake of clarity.

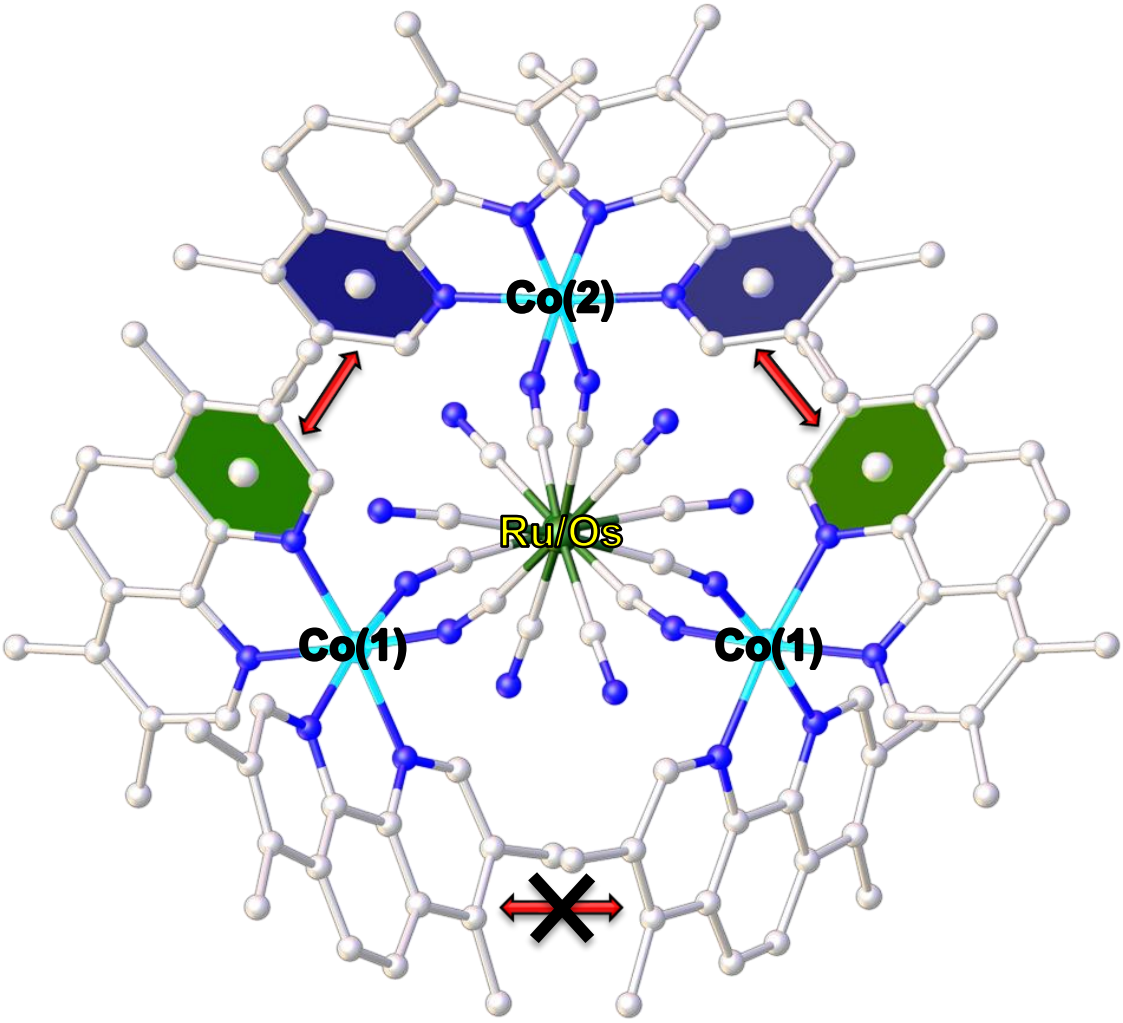

Figure 3-3. View of the Co_3M_2 TBP (where M = Ru/Os) looking down the axial Ru/Os positions. The green planes are symmetrically equivalent to one another just as the blue ones are. The intramolecular interactions that occur in these TBPs occur between the green plane and the blue plane. Interaction referred to as intra-gb. Hydrogen atoms omitted for the sake of clarity.

Zn_3Os_2 TBP (5)

The Zn_3Os_2 TBP crystallizes in the $P2_1/c$ space group, similarly to most of the TBPs prepared by our group. The structural data and refinement parameters are listed in Table 3-4 and the M-L bond lengths can be found in Table 3-7. It is not possible that a Zn^{II} ion (d^{10}) will undergo a charge transfer with the Os^{III} metal center so there is no ambiguity concerning oxidation states of the metal centers in this TBP. There is also no uncertainty of the spin state of the Zn^{II} metal center as it cannot undergo a SCO owing to its $t_{2g}^6e_g^4$ electronic configuration. This makes the assignment of the electronic structure of this TBP straightforward and is assigned as $Zn^{II}_3Os^{II}_2$. At 100 K the average Zn^{II}–N bond distances are ~2.14 Å for all three Zn^{II} centers and correspond well to the average Zn^{II}–N bond distances of ~2.15 Å in the Zn_3Fe_2 TBP at 150 K.[145] The average Os^{III}–C bond distances are 2.05(3) Å and 2.03(3) Å for the Os(1) and Os(2) centers, respectively. As expected, due to the larger radius for 5d metals as compared to 3d metals, the Os^{III}–C bond lengths of ~2.0 Å in the Zn_3Os_2 TBP are slightly longer than the Fe^{III}–C bond lengths of ~1.9 Å for both the Zn_3Fe_2 and Co_3Fe_2 TBPs.[145,148]

Table 3-7. M–L bond lengths (in Å) for the Zn_3Os_2 TBP (5).

Temperature	Zn(1)–N	Zn(2)–N	Zn(3)–N	Os(1)–C	Os(2)–C
100 K	2.01 (2)	2.05 (2)	2.02 (2)	1.97 (3)	1.96 (4)
	2.14 (2)	2.05 (3)	2.05 (2)	2.03 (2)	1.96 (3)
	2.14 (2)	2.18 (2)	2.14 (2)	2.05 (3)	2.06 (3)
	2.17 (2)	2.20 (2)	2.14 (2)	2.07 (2)	2.07 (3)
	2.19 (2)	2.20 (2)	2.25 (2)	2.07 (3)	2.07 (5)
	2.22 (2)	2.22 (2)	2.26 (2)	2.08 (3)	2.08 (3)
Avg M–L	**2.14 (2)**	**2.15 (2)**	**2.14 (2)**	**2.05 (3)**	**2.03 (3)**

Similarly to the other TBPs that crystallize in the *P*2_1/*c* space group, the Zn_3Os_2 TBP stacks in a dimeric unit with two intermolecular interactions between two tmphen ligands coordinated to the Zn(3) centers in neighboring TBP molecules and two intramolecular interactions between tmphen ligands on the Zn(1) and Zn(2) metal centers and the Zn(2) and Zn(3) centers. The purple and yellow planes in Figure 3-4 depict the intermolecular interactions due to the π-π stacking between TBPs in the dimeric unit. Table 3-8 contains the pertinent centroid-centroid and shift distances as well as the angles between the planes. The interactions are labeled according to the color used for each plane: purple (p), yellow (y), teal (t) and whether it is an inter- (inter) or intramolecular (intra) interaction occurring between planes. The inter-pp and inter-py interactions (Figure 3-4) are the strongest of the π-π stacking interactions in the Zn_3Os_2 TBP with centroid-centroid distances of ~3.6 Å but are still considered relatively weak as far as π-π stacking interactions are concerned. The intra-tt interaction involving the Zn(1) and Zn(2) metal centers and the intra-gg interaction involving the Zn(2)

and Zn(3) metal centers are the weakest of the π-π stacking interactions in this TBP (Figure 3-5). Overall, the Zn(3) center has one tmphen ligand involved in two intermolecular interactions and the other tmphen ligand involved in an intramolecular interaction (3 interactions total) whereas the Zn(2) center is involved in two very weak intramolecular interactions and the Zn(1) center is involved in one very weak intramolecular interaction.

Table 3-8. Geometric parameters (centroid-centroid distances, shift distances and angles between planes) for the inter- and intramolecular π-π stacking interactions in the Zn_3Os_2 TBP (5).

Interaction-Plane	Centroid-Centroid Distance (Å)	Shift Distance (Å)	Angle (º)
inter-pp	3.652	1.163	0
inter-py	3.672	1.326	1.545
intra-tt	3.939	1.491	8.237
intra-gg	3.895	1.178	6.526

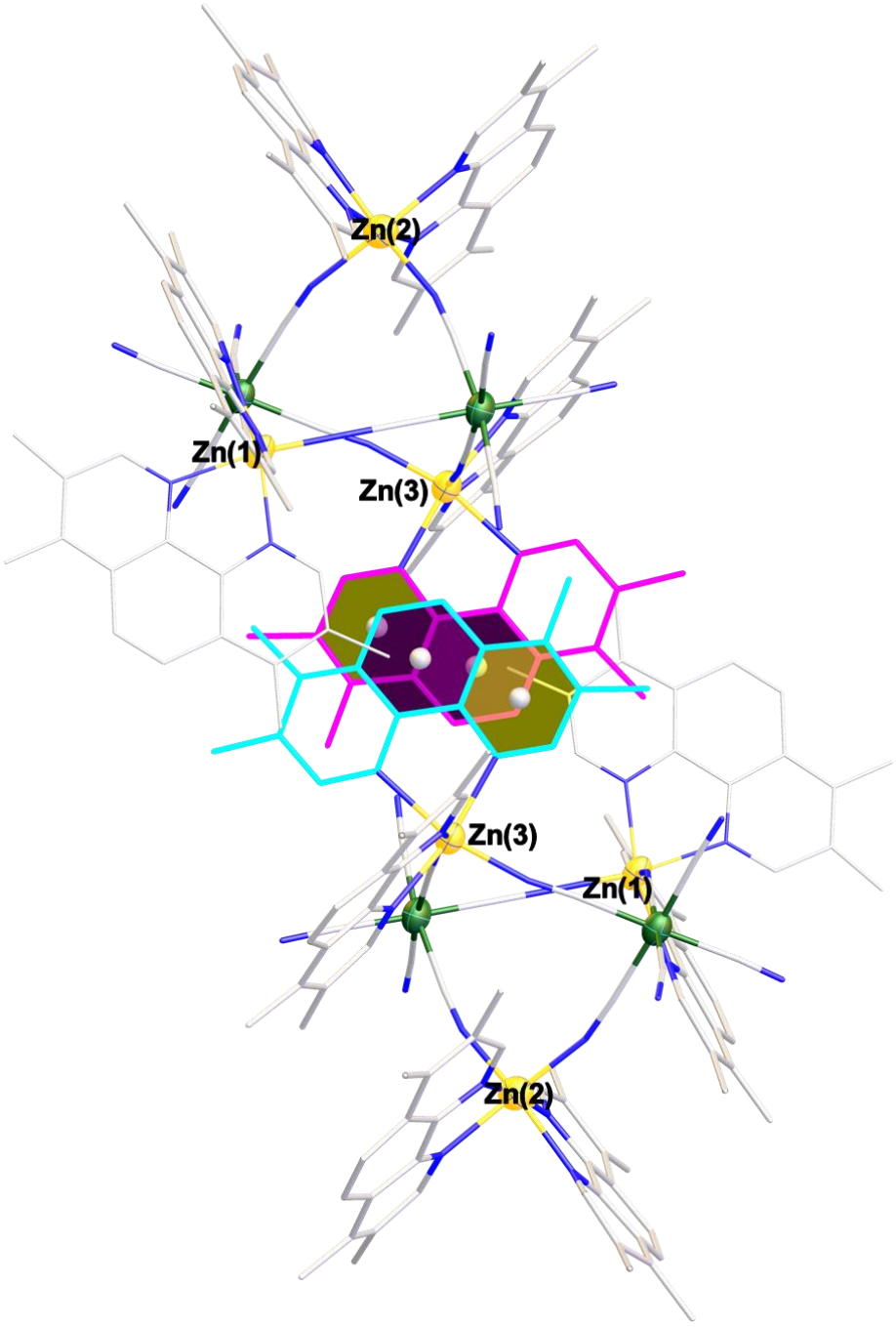

Figure 3-4. View of the Zn_3Os_2 TBP stacking in a dimeric unit. The purple and yellow planes highlight the rings within the tmphen ligands that are involved in the intermolecular π-π stacking interactions (inter-pp and inter-py). Color code: Zn is Yellow, Os is green, C is white and N is blue. Hydrogen atoms omitted for clarity. The pink tmphen ligand is coordinated to a Zn(3) center and the cyan tmphen ligand is its symmetrically equivalent (due to inversion) tmphen ligand coordinated to the Zn(3) center on the neighboring TBP. These two ligands are the ones involved in the π-π stacking interactions.

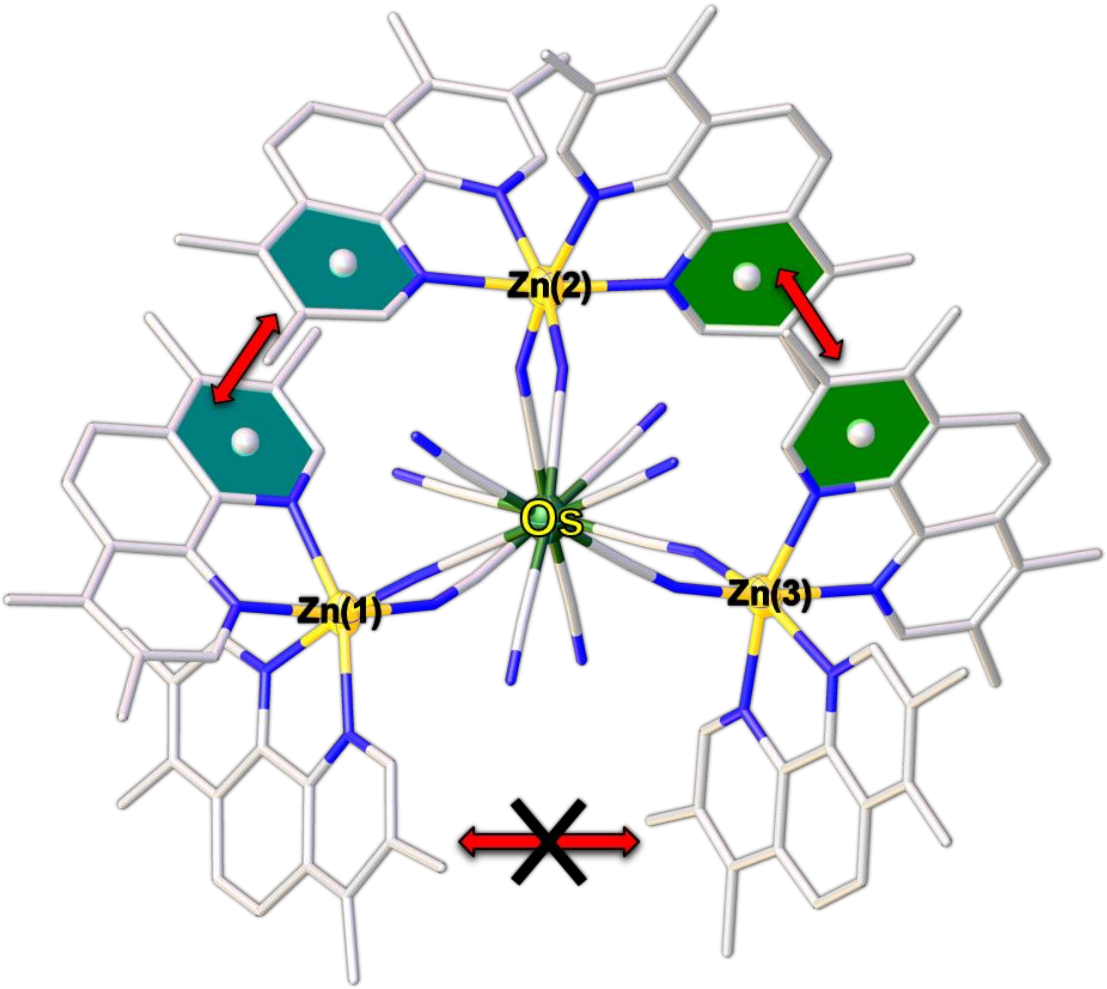

Figure 3-5. View of the Zn_3Os_2 TBP looking down the axial Os positions. The teal colored planes portray the intra-tt intramolecular interaction and the green planes depict the intra-gg intramolecular interaction. There is no intramolecular interaction between the tmphen ligands on the Zn(1) and Zn(3) centers, as indicated by the red arrow marked out. Hydrogen atoms have been omitted for clarity.

{[M^{II}(tmphen)$_2$]$_2$[Ru^{II}(CN)$_4$(tmphen)]$_2$} (Mn_2Ru_2) (6)

This molecule is a tetranuclear compound consisting of two divalent Mn ions and two divalent Ru ions that crystallizes in *P*-1, having an inversion center as its only symmetry element. In order for the molecule to be charge-balanced, the $[Ru^{III}(CN)_6]^{3-}$ starting material must have been reduced to $[Ru^{II}(CN)_6]^{4-}$ moieties. Two of the cyanide ligands from each of the reduced $[Ru^{III}(CN)_6]^{3-}$ units were replaced with a tmphen molecule, which magnifies the underlying concept of the $[Ru^{III}(CN)_6]^{3-}$ moiety not being stable. Not only was the Ru^{III} reduced to Ru^{II} but the cyanide ligands have become labile in solution. The metal centers form a distorted square-type geometry wherein both Ru^{II} ions are bridged to the Mn^{II} centers in a Ru^{II}–C≡N–Mn^{II} fashion. The ruthenium atoms do not bridge each other nor do the manganese centers. The molecule crystallizes with 8 H_2O and two DMF molecules that participate in hydrogen bonding with all of the terminal cyanide ligands as shown in Figure 3-6. Figure 3-7 is a packing diagram of the molecule looking down the *a*-axis. The structural data and refinement parameters for the molecule at 100 K are in Table 3-4 and the M-L bond lengths are in Table 3-9. Both Mn^{II} centers have average Mn^{II}–N bond lengths of ~2.23 Å, which matches the average Mn^{II}–N bond lengths in the Mn_3Fe_2 TBP.[203] The Ru^{II} ion is in a different octahedral coordination environment from the usual TBP configuration. Now the Ru^{II} metal centers have only four cyanide ligands coordinated to them (two of them are terminal and the other two are bridging the Mn^{II} centers) whereas the other two coordination sites are occupied by nitrogen

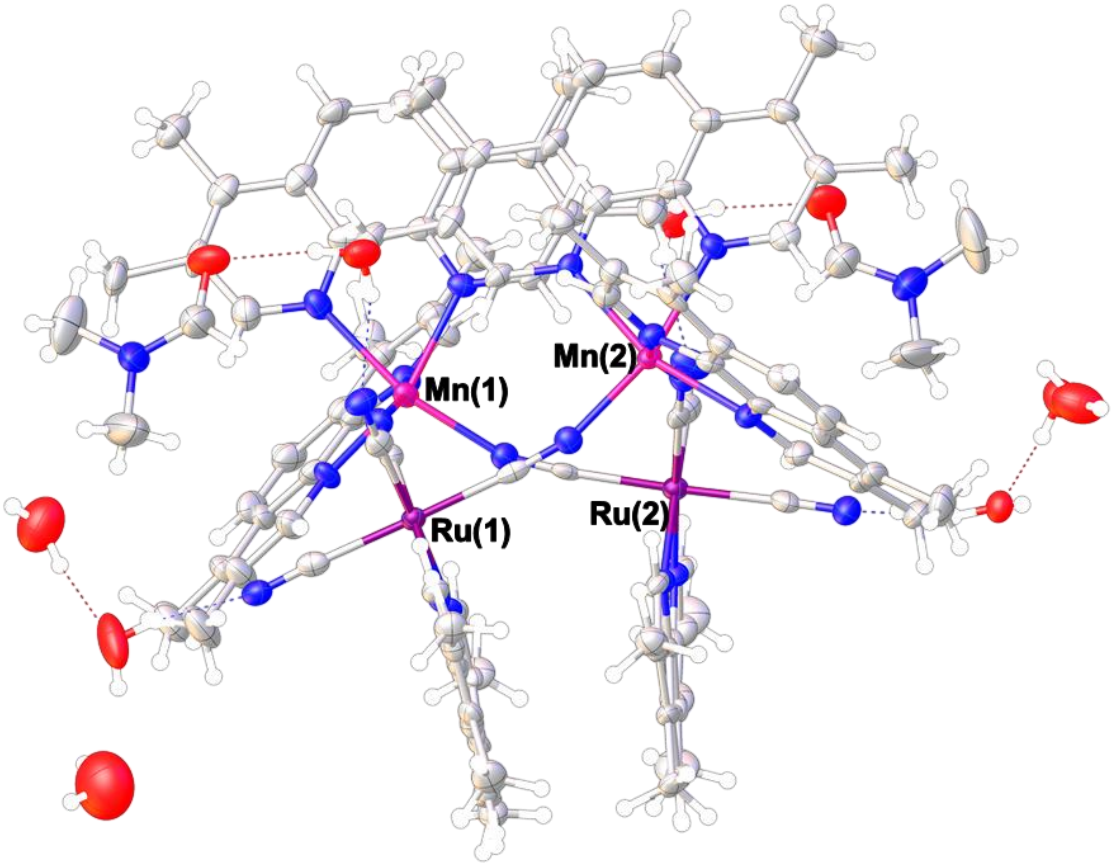

Figure 3-6. Asymmetric unit of Mn_2Ru_2. Thermal ellipsoids at 50% probability level. Hydrogen bonds are represented with dashed lines. Color scheme: Mn is pink, Ru is purple, N is blue, C is grey, O is red and H is white. Looking down the *a*-axis, approximately.

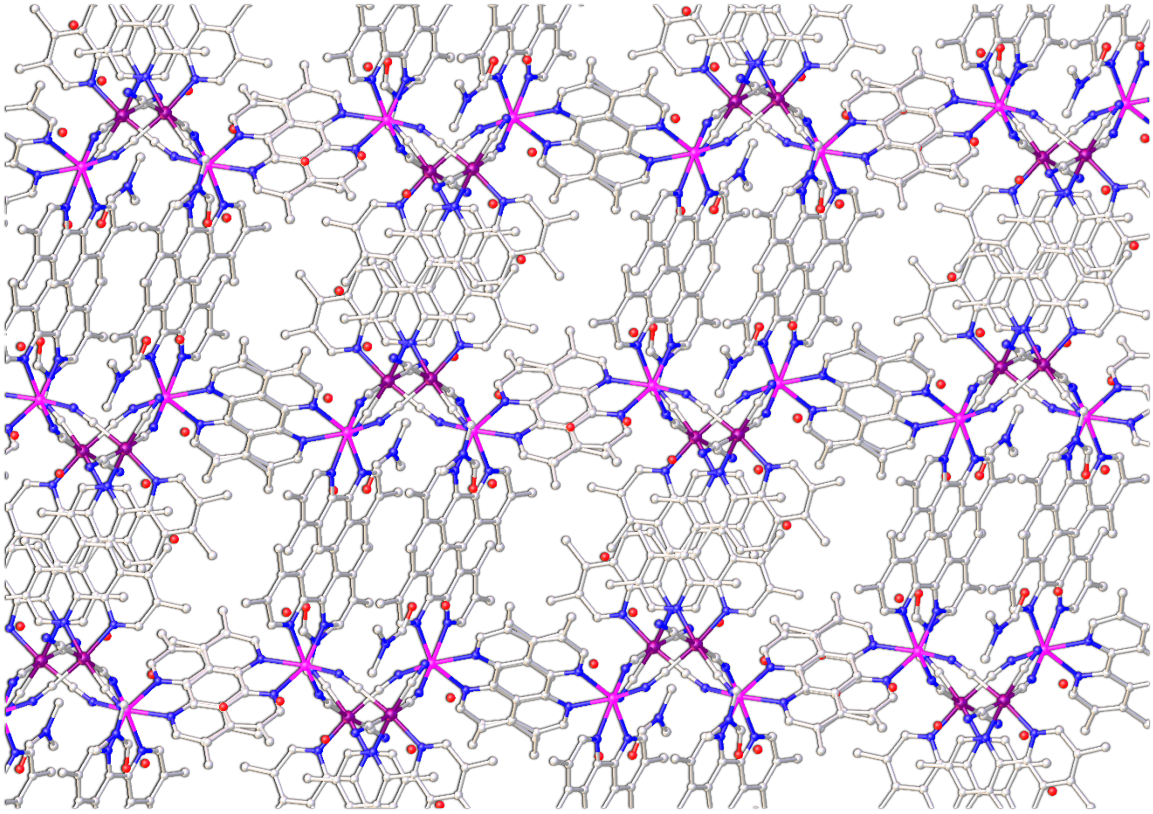

Figure 3-7. Packing diagram of Mn_2Ru_2 looking down the *a*-axis. Hydrogen atoms are omitted for the sake of clarity. Color scheme: Mn is pink, Ru is purple, N is blue, C is grey and O is red.

Table 3-9. M-L bond distances (in Å) for Mn_2Ru_2 (6).

Temperature	Mn(1)–N	Mn(2)–N	Ru(1)–C	Ru(1)–N	Ru(2)–C	Ru(2)–N
100 K	2.118 (7)	2.114 (7)	1.971 (9)	2.109 (6)	1.951 (09)	2.107 (6)
	2.142 (7)	2.145 (7)	1.995 (9)	2.119 (6)	1.995 (09)	2.117 (6)
	2.249 (6)	2.248 (6)	2.036 (9)		2.024 (10)	
	2.262 (7)	2.264 (6)	2.042 (9)		2.031 (10)	
	2.269 (6)	2.322 (7)				
	2.355 (6)	2.325 (7)				
Avg M–L	**2.233 (7)**	**2.236 (7)**	**2.011 (9)**	**2.114 (6)**	**2.000 (9)**	**2.112 (6)**

atoms from the coordinated tmphen molecule. The average Ru^{II}–C bond lengths for each center are ~2.0 Å and the average Ru^{II}–N bond lengths are ~2.1 Å for each Ru^{II} center. Analysis of the π-π stacking interactions with Olex2 reveals that the molecule has intermolecular interactions with three other adjacent molecules and two intramolecular interactions. All of the rings in the tmphen ligand that are involved in the π-π stacking interactions are colored in Figure 3-8 and the corresponding geometric parameters are in Table 3-10. In the table, the interactions are labeled according to plane color: purple (p), yellow (y), teal (t), maroon (m), blue (b), red (r), green (g) and grey and also whether it is an inter- (inter) or intramolecular (intra) interaction occurring between planes. Planes of the same color are symmetrically equivalent. Except for the inter-gg interaction, the intermolecular interactions are weaker than the intramolecular interactions, which is in contrast to the TBP molecules. All of the π-π stacking interactions are considered to be weak and three of the four intermolecular interactions could be considered irrelevant according to literature standards.

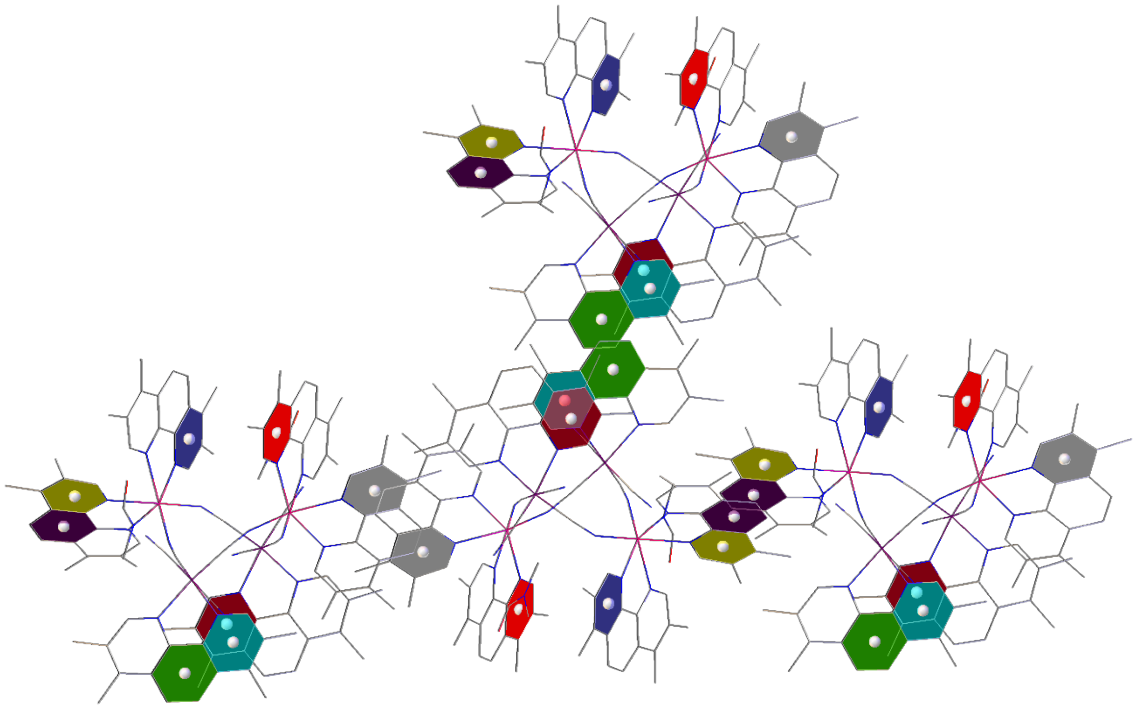

Figure 3-8. Depiction of the π-π stacking interactions in the Mn_2Ru_2 compound. Rings of the same color are symmetrically equivalent.

Table 3-10. Geometric parameters (centroid-centroid distances, shift distances and angles between planes) for the inter- and intramolecular π-π stacking interactions in Mn_2Ru_2 (6).

Plane	Centroid-Centroid Distance (Å)	Shift Distance (Å)	Angle (º)
inter-py	3.930	2.057	3.354
inter-gg	3.697	1.358	0
inter-yy	3.939	1.922	0
inter-grey	3.948	1.857	0
intra-mt	3.804	1.223	6.903
intra-rb	3.732	1.372	3.278

Magnetic Properties

Co_3Ru_2 (3) and Co_3Os_2 (4) TBPs

Although the Co_3Ru_2 and Co_3Os_2 TBPs have very similar structural properties, their magnetic behavior is quite different. As shown in Figure 3-9, the temperature dependent susceptibility data varies between the two congeners, from the Co_3Ru_2 TBP being a paramagnet to the Co_3Os_2 exhibiting some form of spin-transition behavior. The room temperature susceptibility data for the Co_3Ru_2 TBP Figure 3-9a) is ~2.7 emu·K/mol which corresponds to a $[(HS\text{-}Co^{II})(LS\text{-}Co^{III})_2Ru^{III}_2]$. The only paramagnetic center contributing to the magnetic moment in this configuration is the HS Co^{II} center, which has a spin-only value of 1.875 emu·K/mol but is typically observed to be 2.0 – 3.2 emu·K/mol due to orbital contributions.[195,204,205] The only other electronic combination that would come close to a χT value of ~2.7 is $[(LS\text{-}Co^{II})_3Ru^{III}_2]$ (spin-only value of 1.875 emu·K/mol) but this does not account for the difference in the Co–N bond lengths (~2.0 and ~1.9 Å), nor does it account for the sharp decrease in the χT data below 100 K to 1.7 emu·K/mol which is attributed to decreasing orbital contributions and zero field splitting effects. The saturation of the magnetization data (Figure 3-10a) at 2.1 μ_B instead of 3 μ_B is also typical for a HS Co^{II} ion with significant orbital contributions in an O_h coordination environment.[15,206,207] In the Co_3Fe_2 TBP, simulation of EPR spectra gives g-values for the HS Co^{II} site as $g_1 = 2.53$, $g_2 = 2.42$, $g_3 = 2.02$, resulting in a $g_{eff} \cong 2.39$ indicating an important orbital contribution.[148] Splitting of the isofield lines in the reduced magnetization

data (**Figure 3-11a**) is not observed.

In contrast to the Co_3Ru_2 TBP, the Co_3Os_2 TBP exhibits reversible redox properties between 2 K and 300 K. The χT value of 8.2 emu·K/mol (Figure 3-9b) at 350 K renders the assignment of the TBP electronic configuration relatively easy when any configuration depending on a HS Co^{III} ion is not considered. The only reasonable electronic configuration for the TBP above room temperature then becomes analogous to anhydrous crystals of the Co_3Fe_2 congener and is $[(HS\text{-}Co^{II})_3Os^{III}_2]$. The spin-only value for this configuration is ~6.4 emu·K/mol, but due to significant orbital contributions from HS Co^{II}, it is reasonable that χT is much higher. As the temperature is lowered, an immediate decrease in the susceptibility data is observed ($\Delta \cong 5.5$ emu·K/mol) until the decrease becomes more gradual between 200 and 70 K ($\Delta \sim 1$ emu·K/mol). Below 70 K, χT decreases by ~1.6 emu·K/mol as it reaches 2.1 emu·K/mol at 2 K. The overall curve shape is indicative of a gradual spin-transition that lacks cooperativity and occurs over the entire temperature range of 2 – 350 K with a total change of 6.1 emu·K/mol in the susceptibility data. Table 3-11 lists the possible spin-transitions for the equatorial Co sites and the expected changes in the χT values (spin-only model) associated with each transition. If an electron transfer is involved in the spin-transition, then the additional change in χT expected for the contribution of the Os is also included. In order to induce a change of 6.1 emu·K/mol, one of a few possible spin-transition scenarios must occur as the temperature is decreased to 2 K: (1) a total of 3 SCO events from HS $Co^{II} \rightarrow$

LS Co^{II} ($\Delta\chi T_{spin\text{-}only}$ = 4.5 emu·K/mol), (2) 2 CTIST events from HS $Co^{II} \rightarrow$ LS Co^{III} ($\Delta\chi T_{spin\text{-}only}$ = 4.5 emu·K/mol) or (3) 2 CTIST events from HS $Co^{II} \rightarrow$ LS Co^{III} coupled with a SCO from HS $Co^{II} \rightarrow$ LS Co^{II} ($\Delta\chi T_{spin\text{-}only}$ = 6 emu·K/mol). However, susceptibility data alone does not allow for definitive assignment of the spin-transitions occurring as the temperature changes, especially when significant spin-orbit coupling is involved. Magnetization data at 1.8 K, however (Figure 3-10b), begins to saturate near 3 μ_B at 7 T which is indicative of an electronic configuration with 3 unpaired electrons. Scenario 1 would result in a TBP configuration of [(LS-Co^{II})$_3$$Os^{III}_2$] at 1.8 K and 5 unpaired electrons. Scenario 2 would lead to a [(HS-Co^{II})(LS-Co^{III})$_2$$Os^{II}_2$] configuration with 3 unpaired electrons at 1.8 K and scenario 3 would cause a configuration of [(LS-Co^{II})(LS-Co^{III})$_2$$Os^{II}_2$] which would have 1 unpaired electron at 1.8 K. Magnetization data suggests that the TBP undergoes the transitions in scenario 2 (2 CTIST events) as temperature is decreased to obtain the same electronic configuration as the Co_3Ru_2 TBP at 1.8 K, which is [(HS-Co^{II})(LS-Co^{III})$_2$$Os^{II}_2$]. Reduced magnetization data for the Co_3Os_2 TBP (Figure 3-11b) exhibit more splitting between the iso-field lines than the Co_3Ru_2 congener. Preliminary photomagnetic studies were pursued for these TBPs but no change in magnetic moment was observed at 10 K with white light irradiation for a few hours.

Table 3-11. Possible spin-transitions for the Co_3Os_2 TBP and the $\Delta\chi T_{spin\text{-}only}$ values associated with those transitions. If the transition involves an electron transfer, the additional change in χT due to the Os contribution is in the last column.

Possible Electronic Transitions	Type of Transition	ΔχT (Co Only) (emu·K/mol)	Total ΔχT (Os Included) (emu·K/mol)
LS Co^{II} ↔ HS Co^{II}	SCO	1.5	1.5
LS Co^{II} ↔ LS Co^{III}	CT	0.375	0.750
HS Co^{II} ↔ LS Co^{III}	CTIST	1.875	2.250

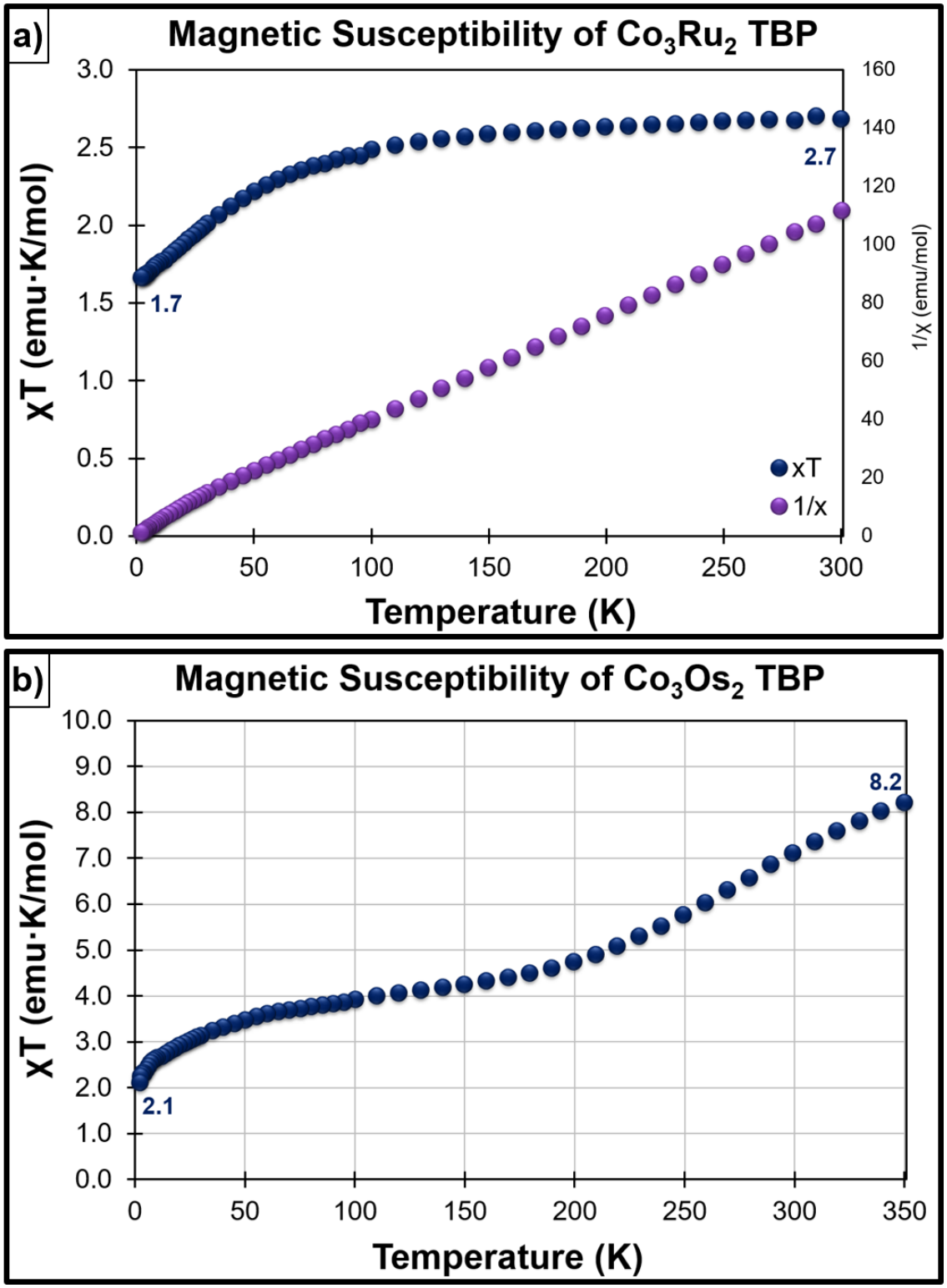

Figure 3-9. Temperature-dependent susceptibility data for the Co_3Ru_2 (a) and Co_3Os_2 (b) TBPs.

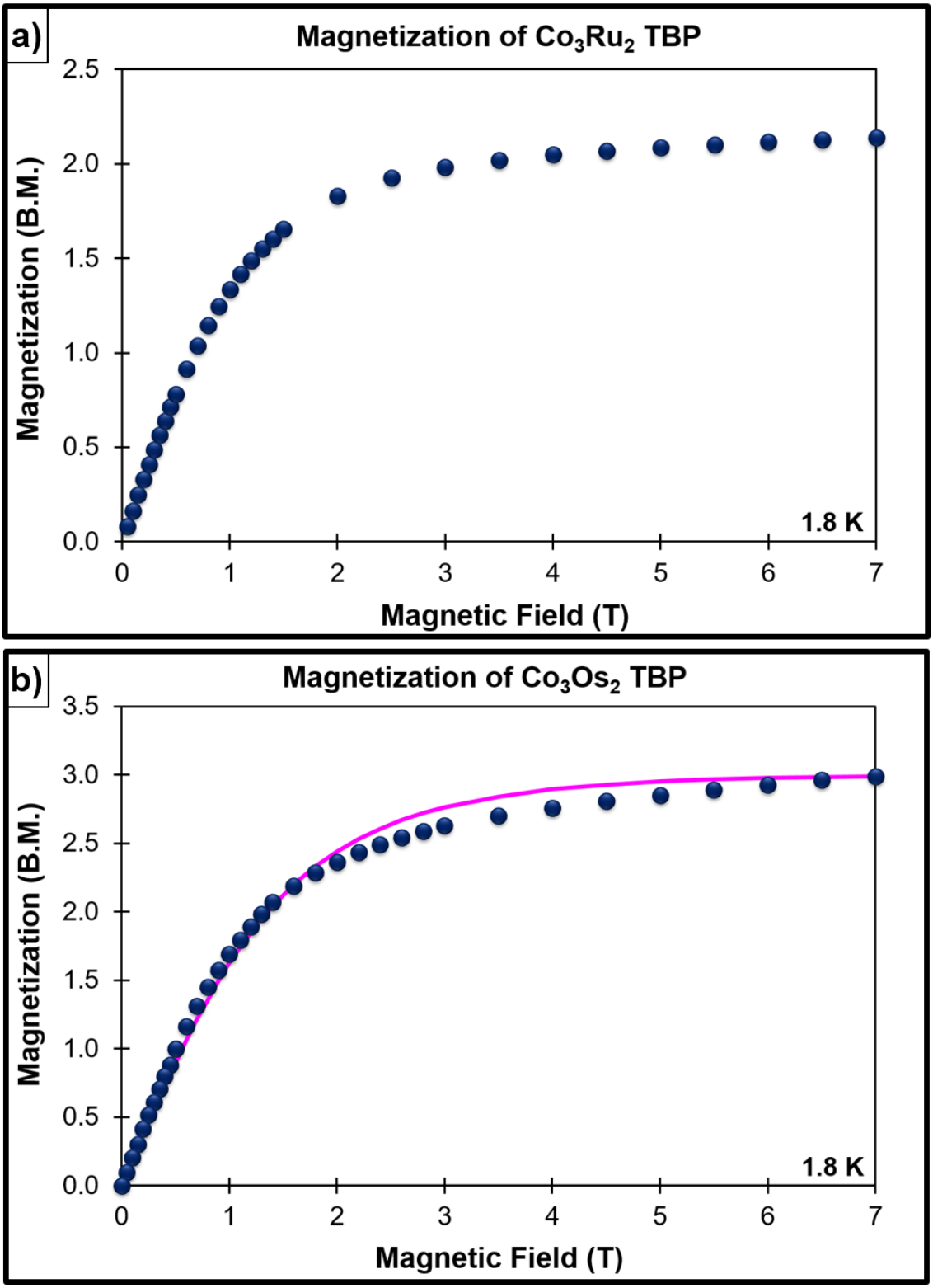

Figure 3-10. Magnetization data at 1.8 K for the Co_3Ru_2 (a) and Co_3Os_2 (b) TBPs. The pink line represents a Brillouin function for an S = $^3/_2$ system with a g = 2.0.

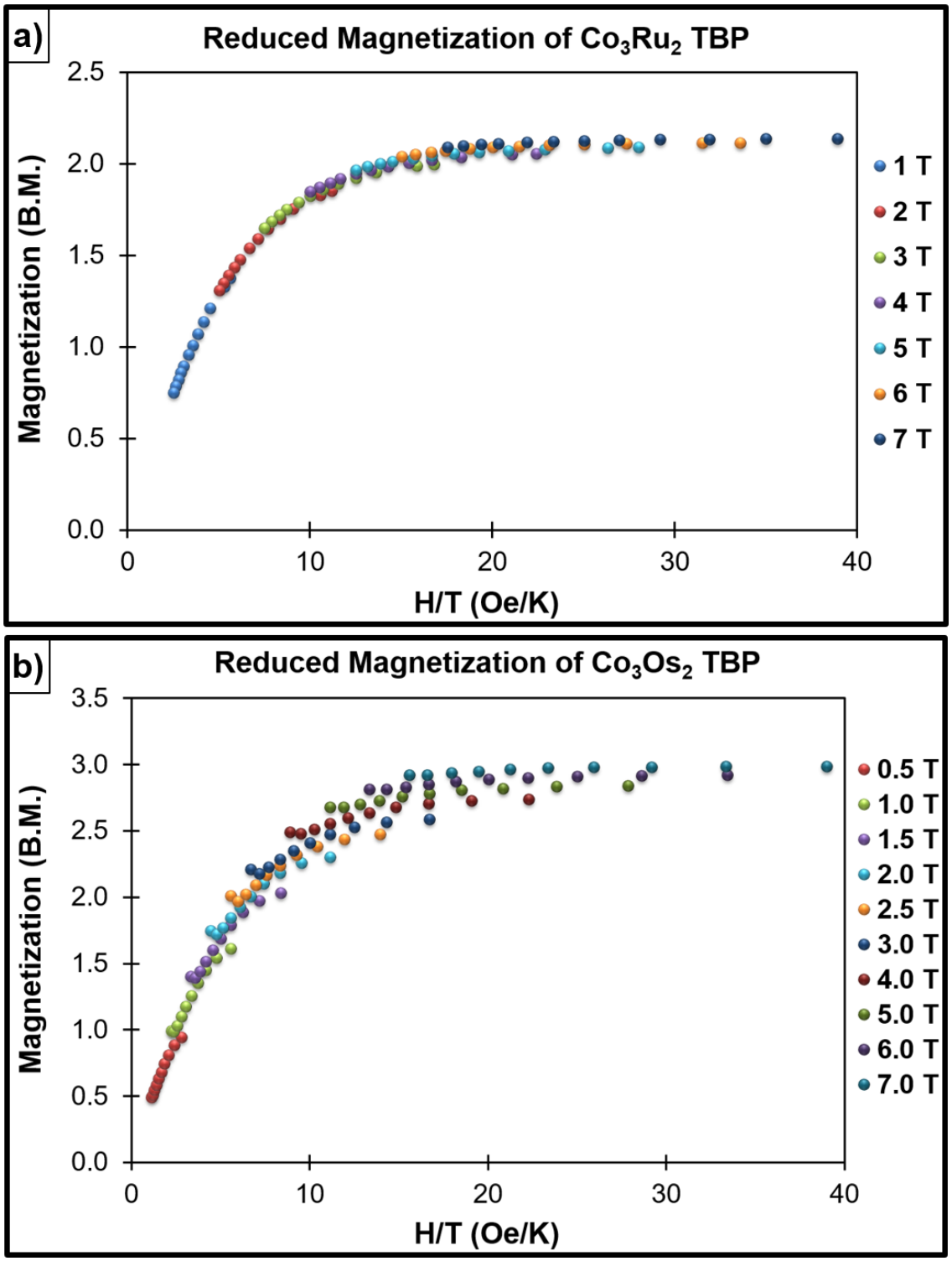

Figure 3-11. Reduced magnetization data for the Co_3Ru_2 (a) and Co_3Os_2 (b) TBPs.

Upon comparing magnetic behavior, the Ru^{III} metal ions in the Co_3Ru_2 TBP undergo an irreversible electron transfer with the Co^{II} centers which then behaves as an isolated HS Co^{II} paramagnet while the Co_3Os_2 TBP has rich redox properties that allow for two reversible CTIST events as temperature changes. Both of these TBPs differ from the spin-transitions observed in the three different solvation states of the Co_3Fe_2 TBP. The Co_3Fe_2 TBP exists as a blue solid when prepared in air, a red solid when a sample prepared in air is subjected to a vacuum and as red crystals when prepared in an anhydrous environment using MeCN. As temperature is increased from 2 to 300 K, the blue solid remains mostly in the $[(HS\text{-}Co^{II})(LS\text{-}Co^{III})_2Fe^{II}_2]$ state but appears to begin a spin-transition near 300 K (similar to the Co_3Ru_2 TBP except for the appearance of a spin-transition near 300 K), the red solid remains as $[(HS\text{-}Co^{II})_3Fe^{III}_2]$ and the red crystals begin as $[(HS\text{-}Co^{II})(LS\text{-}Co^{II})(LS\text{-}Co^{III})Fe^{III}Fe^{II}]$ before undergoing one CTIST event which leads to the same configuration as the red solid (similar to the Co_3Os_2 TBP but has only one CTIST event instead of two).[147,148] The blue solid form of the Co_3Fe_2 TBP is also photomagnetic, capable of converting ~36% of the diamagnetic Co^{III}–Fe^{II} pairs to HS-Co^{II}–Fe^{III} pairs with 1 hour of irradiation with white light at 10 K.[111]

Zn_3Os_2 (5)

The purpose of preparing and measuring the Zn_3M_2 TBPs was to obtain model compounds in order to determine the magnetic contribution of the axial

metal centers to the TBP. One does not expect any exchange interactions between the two axial metal centers through the long, diamagnetic –C≡N–Zn^{II}–N≡C– bridge. The temperature-dependent magnetic susceptibility data of Zn_3Os_2 (Figure 3-12a) was fit to Curie-Weiss behavior with a Curie constant (C) of ~0.58 emu·K/mol, a Weiss constant (θ) of 0.05 and a TIP = 1200 x 10^{-6} emu·K/mol. The Curie constant was obtained using S = ½ and g = 1.75 for each Os^{III} center. The Weiss constant of 0.05 indicates very weak ferromagnetic coupling between the axial Os^{III} centers through the long, diamagnetic –C≡N–Zn^{II}–N≡C– linkage. Magnetization data at 1.8 K (Figure 3-12b) was modeled with a Brillouin function for two S = ½ ions with g = 1.67. The Zn_3Fe_2 TBP exhibits similar magnetization and χT values but does not exhibit the small upturn in the curve below 10 K as the Zn_3Os_2 TBP does[145,203] indicating that the Os centers possibly have stronger magnetic exchange through the diamagnetic bridge than its Fe counterpart.

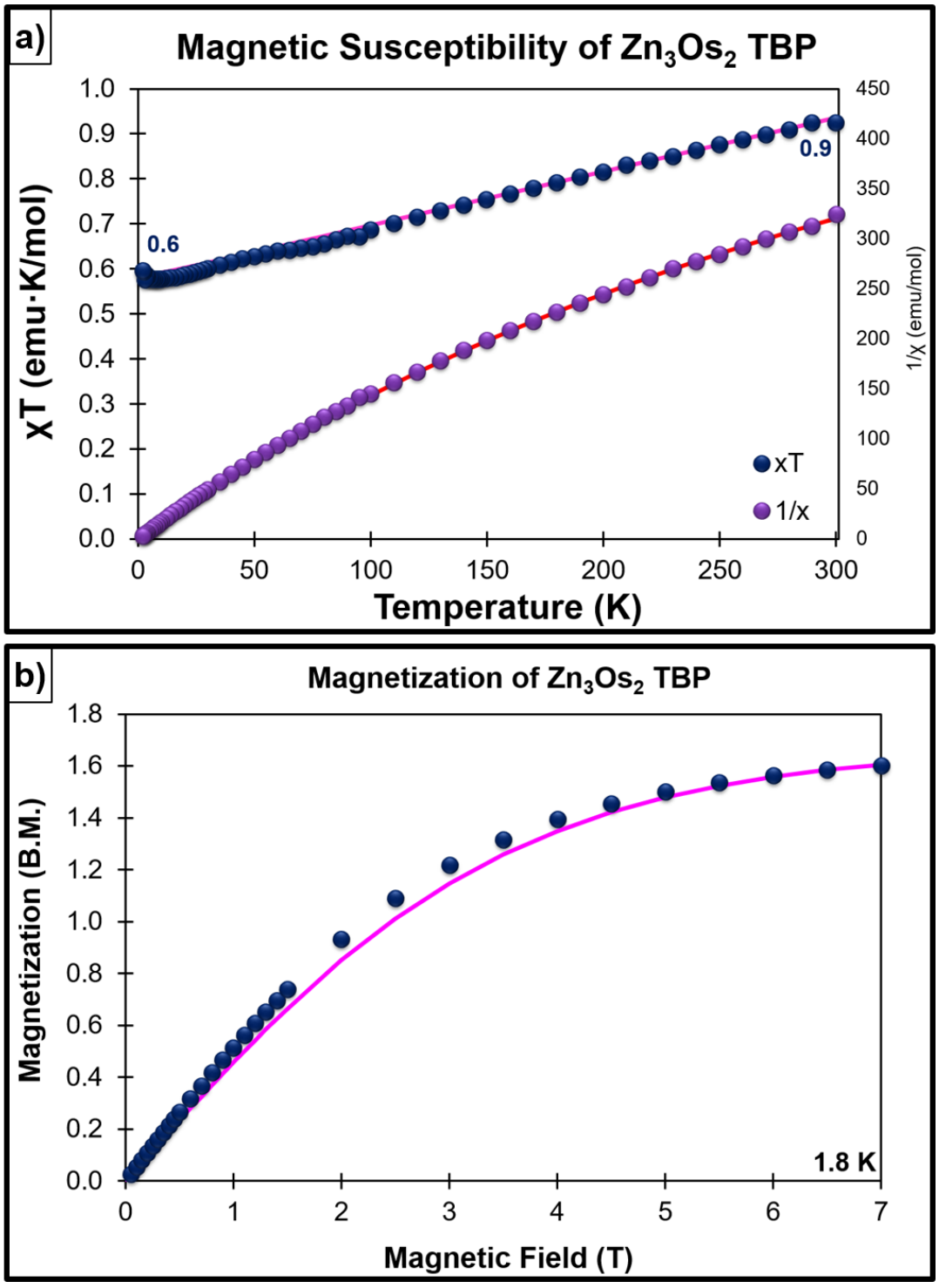

Figure 3-12. (a) Temperature-dependent susceptibility data for the Zn_3Os_2 TBP. Solid lines are fit lines for Curie-Weiss behavior with C = 0.56 (2 S = ½ ions with g = 1.75), θ = 0.05 and TIP = 1200 x 10^{-6} emu·K/mol. (b) Magnetization data at 1.8 K. Solid line is the best-fit Brillouin function for 2 S = ½ ions with a g = 1.67.

Concluding Remarks

Three new TBPs were prepared and characterized both structurally and magnetically. These new TBPs are interesting additions to the large homologous family of TBPs studied by the Dunbar group. The Co_3Ru_2 and Co_3Os_2 TBPs were successfully prepared after attempts by former group members by changing from $CoCl_2$ to CoI_2 and adding a small volume of DMF. The Co_3Ru_2 TBP exhibits irreversible electron transfers from two of the $[Co^{II}(tmphen)]^{2+}$ precursors to the two $[Ru^{III}(CN)_6]^{3-}$ moieties while the Co_3Os_2 TBP displays reversible redox behavior and undergoes two CTIST events as temperature changes, adding to the small number of compounds that exhibit this type of behavior. The Co_3Fe_2 TBP demonstrates different magnetic behavior from both the Co_3Ru_2 and Co_3Os_2 TBPs. Although the Co_3Fe_2 TBP exhibits photomagnetic properties when irradiated with white light for an hour at 10 K, no photomagnetic behavior was observed in the Co_3Ru_2 and Co_3Os_2 congeners under the same conditions. Diffuse reflectance and additional photomagnetic studies should be investigated as these preliminary measurements do not exclude the possibility that these Co_3Fe_2 congeners can exhibit photomagnetic behavior, especially given their facile redox capabilities. The model compound Zn_3Os_2 was prepared and characterized and found to display enhanced magnetic exchange as compared to its Zn_3Fe_2 cousin as evidenced by the Weiss constant of 0.05 indicating the presence of very weak ferromagnetic interactions between axial Os^{III} centers through the long diamagnetic bridge. Although the Mn_3Ru_2 TBP was not obtained

in crystalline form, a Mn_2Ru_2 compound was formed instead. The lability of the cyanide in this compound exemplifies the synthetic challenges in preparing the $[Ru^{III}(CN)_6]^{3-}$ starting material as discussed in the last chapter. This facile labilization of the cyanide ligands is likely to be the fact that crystallization of the Mn_3Ru_2 TBP has evaded previous group members. Three differently colored powders (yellow, green and orange) were obtained during the synthesis of the Mn_3Ru_2 TBP and they all exhibit magnetic data consistent with possible electronic configurations of the TBP but without structural data, this TBP will remain to be fully determined.

CHAPTER IV

SPIN-TRANSITION AND CHARGE-TRANSFER PROPERTIES OF THE Fe_3Ru_2 TBP AS A CONSEQUENCE OF SOLVATION

Background

Spin-crossover (SCO) is an active field of study in molecular magnetism because compounds that exhibit bistable states with vastly different electronic and magnetic properties have applications in technological and medical fields such as sensors, displays, data storage devices and contrast agents to name a few.[47,65,66,208] The majority of compounds studied (~90%) contain Fe^{II} and are soluble salts that are usually mononuclear.[82,209] In recent years, more dinuclear and polynuclear compounds are being studied in an effort to probe the effects of polynuclearity on the cooperativity of SCO complexes.[210-213] Additionally, several studies have been reported recently with the purpose of studying the role of solvent.[51,95,96] A less common phenomenon related to SCO that has emerged in the last decade is charge-transfer-induced-spin-transition (CTIST).[111,116,214,215] Compounds exhibiting this type of behavior also have bistable states with most of the compounds reported being cyanometallate-based and often contain iron and cobalt.[109,147,148,151,214,216] It should be noted that two of the reported compounds in the literature are Co_3Fe_2 and Fe_3Os_2 TBP molecules from the Dunbar group. Single crystal X-ray crystallography, SQUID magnetometry and ^{57}Fe Mössbauer spectroscopy measurements showed that the CTIST events in the Co_3Fe_2 TBP

are dependent upon solvation environment, varying from one to two reversible CTIST events based on solvent content. The Fe_3Os_2 TBP exhibits two reversible CTIST events between 2 K and 350 K.[116,145] In comparison, the Fe_3Fe_2 TBP does not exhibit CTIST but was found to undergo a spin-transition at two of the Fe centers due solely to SCO.

With this information, it is not an unreasonable assumption to expect the Fe_3Ru_2 TBP compound to exhibit some form of spin-transition as well, whether it be from SCO or CTIST. Preliminary studies on the Fe_3Ru_2 TBP by a former group member (Dr. Matthew Hilfiger)[172] confirmed that this metal combination does exhibit spin-transition behavior but that it is more complex in nature than its congeners. It was found through the current research in this dissertation that the reason for the complexity in the spin-transition behavior is related to the interstitial solvent in the void spaces of the crystals. Herein, a detailed study of the Fe_3Ru_2 TBP in five different solvation environments is reported and compared to the isostructural Fe_3Fe_2 and Fe_3Os_2 TBPs reported previously by our group.[116,145] This chapter discusses the syntheses, characterization, structures and magnetic properties that differ from the isostructural congeners as a consequence of substitution of the apical Fe and Os metal centers for Ru and also as a consequence of the amount and identity of solvent contained within the crystals.

Experimental Details

Materials

All chemicals and solvents were of ACS reagent grade or higher, were dried (if necessary) and stored in an oxygen- and water-free glove box with a nitrogen atmosphere, unless stated otherwise. ***Reagents for the synthesis of*** $\boldsymbol{Fe^{II}_4Cl_8(THF)_6}$***:*** iron(II) chloride, anhydrous ($FeCl_2$, air-sensitive, hygroscopic powder, 98%, Strem Chemicals). Anhydrous $FeCl_2$ was stored in an oxygen- and water-free glove box with a nitrogen atmosphere. ***Reagents for the synthesis of*** $\boldsymbol{\{[Fe(tmphen)_2]_3[Ru(CN)_6]_2\}\cdot nSolv}$***:*** 3,4,7,8-tetramethyl-1,10-phenanthroline (**tmphen**) ($C_{16}H_{16}N_2$, crystalline powder that varies in color from pinkish to off-white, 98+%, Alfa Aesar). ***Solvents used:*** tetrahydrofuran, anhydrous (THF) (Sigma Aldrich, ≥99.9%, contains 250 ppm butylated hydroxytoluene as an inhibitor, packed under Argon in a Sure/Seal™ bottle) was purchased and pumped into a N_2 atmosphere glove box where it remained once opened. Diethyl ether (EMD Millipore) was purchased from the Texas A&M University's chemistry stockroom and then purified with an MBRAUN Solvent Purification System (MB-SPS). Acetonitrile (MeCN) (Fisher Scientific) was bought from the department's stockroom, pre-dried for two weeks over 3 Å molecular sieves (hygroscopic 3-5 mm beads, Alfa Aesar), refluxed over 3 Å sieves and then distilled before being stored in a N_2 atmosphere glove box. All water used was distilled by Texas A&M University. All reactions and sample preparations for the various characterization techniques utilized were done in an anaerobic manner using an

oxygen- and water-free glove box with a nitrogen atmosphere or a Schlenk line, unless noted otherwise.

Syntheses

$Fe^{II}_4Cl_8(THF)_6$

CAUTION: $FeCl_2$ is classified as a hazardous material that can cause severe skin burns and eye damage, is toxic if swallowed and is suspected of causing genetic defects. This chemical should be handled under inert gas as it is air-sensitive and will readily oxidize to Fe(III).

The product is very sensitive to moisture and will turn brown immediately upon exposure to moisture (or within minutes upon exposure to a humid atmosphere) due to the oxidation of the iron so this reaction must be done using anaerobic methods. The synthesis was done according to literature methods.[217]

In a N_2 atmosphere glove box, $FeCl_2$ (6.54 g, 51.6 mmol, the amount is trivial) was added to a Schlenk flask. THF was added to the flask to give about a ½" layer of solvent above the solid. The mixture was refluxed for one day on a Schlenk line and then returned to the glove box where the orange solution was filtered to collect the off-white product. The finely divided powder was rinsed with copious volumes of THF until the washings were colorless. A total of 10.8 g was retrieved, giving a yield of 89.2%. *Refer to page fifty-eight in notebook three for a detailed description of the procedure and observations for the preparation of $Fe^{II}_4Cl_8(THF)_6$.*

{[Fe(tmphen)$_2$]$_3$[Ru(CN)$_6$]$_2$} (Fe_3Ru_2) (7)

In order to obtain sufficient sample to subject it to five different levels of solvation and to carry out all of the characterization methods, five batches were prepared and combined.

In a glove box with a N_2 atmosphere, $Fe_4Cl_8(THF)_6$ (0.168 g, 0.060 mmol) was dissolved in MeCN (~75 mL) to give a clear, colorless solution before tmphen (0.35 g, 0.062 mmol) was added. The red solution was stirred for fifteen minutes before it was poured into a 250 mL screw-cap jar containing $(PPN)_3[Ru^{III}(CN)_6]$ (0.89 g, 0.059 mmol) dissolved in MeCN (~75 mL). The combination of these two solutions resulted in a dark brown/blue color and the precipitation of a dark blue/purple powder. The jar was capped and within eight hours, needle-like crystals had formed on the sides of the jar. After several days, the color of the solution turned dark green and many more dark-colored crystals had formed from solution. The jar was swirled to suspend any remaining powder in the solvent and then the solvent and powder were decanted. Fresh MeCN was added and after several hours, the solvent was decanted once again. This process continued until the MeCN remained colorless after sitting over the crystals for several hours. Several crystals were set aside in the mother liquor for structural analysis. The remaining crystals were collected by vacuum filtration but extreme care was taken to ensure that the vacuum was broken as soon as the MeCN had passed through the frit so as not to remove interstitial solvent molecules from the crystals. The crystals were transferred to a mortar and pestle where they were ground to a very

fine solid. The product was divided into five vials, each containing at least 200 mg of product, to be subjected to different solvation states as described below. The crystals set aside for crystal structure analysis (solvated, 24 hours and humid samples) were prepared before data collection in the same manner as described below. *Refer to page ten in notebook four for an in-depth description of the procedure and observations for the synthesis of the Fe_3Ru_2 TBP (7).*

Fe_3Ru_2 — Solvated (7a)

The crushed crystals in this vial from above, were stored under fresh MeCN for one day before magnetic measurements were performed in order to allow the crystals to reabsorb any solvent they may have lost during the sample preparation. IR, ν(C≡N): 2247 (w, sp), 2121 (w, sp), 2087 (s) and 2006 cm^{-1} (vs, b) where w = weak, s = strong, vs = very strong, sp = sharp and b = broad. TGA data were collected up to 150 °C with continuous mass loss being observed beginning from room temperature for a total loss of 13.7%. This result is attributed to 8.1 interstitial MeCN molecules per TBP, which is most likely less than the actual value due to the necessary step of removing excess solvent from the sample before running TGA on it.

Fe_3Ru_2 — Filtered (7b)

This sample is the crystals put into a vial after being crushed with a mortar and pestle. IR, ν(C≡N): 2248 (m, sp), 2123 (m, sp), 2085 (vs), 2039 (vs, sh) and

2010 cm^{-1} (vs, b) where m = medium, vs = very strong, sp = sharp, sh = shoulder and b = broad. TGA analysis exhibits a 14.6% continuous mass loss between room temperature and about 160 °C before the mass begins to rise again, resulting in 8.8 interstitial MeCN molecules per TBP.

Fe_3Ru_2 — Evacuated 3 Hours (7c)

Aluminum foil, with holes poked through it, was used to cover the vial containing the crushed crystals. The vial was then loaded into an Abderhalden drying apparatus and put under vacuum for three hours on the Schlenk line before being pumped back into the glove box to be prepared for characterization methods. IR, v(C≡N): 2118 (vw, sp), 2084 (m) and 2016 cm^{-1} (s, b) where vw = very weak, m = medium, s = strong, sp = sharp and b = broad. TGA exhibits a 10.1% continuous mass loss between room temperature and ~130 °C, which is attributed to 5.7 interstitial MeCN molecules per TBP.

Fe_3Ru_2 — Evacuated 24 Hours (7d)

As in the case of the three hour sample, the crushed crystals for this sample were loaded into an Abderhalden drying apparatus and subjected to vacuum for twenty-four hours on a Schlenk line before being pumped back into the glove box to be prepared for several characterization techniques. IR, v(C≡N): 2248 (vw, sp), 2118 (w, sp), 2086 (s, sp), 2017 (s, sh) and 2002 cm^{-1} (s, sh) where vw = very weak, s = strong, vs = very strong, sp = sharp and b = broad. A TGA thermogram

exhibits a 7.8% continuous mass loss between room temperature and 150 °C when the heating had stopped. This is attributed to 4.3 interstitial MeCN molecules per TBP.

Fe_3Ru_2 — Humid (7e)

The vial containing the crushed crystals for this sample was removed from the glove box and left open in air, inside of a beaker that contained a small amount of distilled water and a wet paper towel wrapped around the inside of the beaker. The beaker was covered with Parafilm® M and the sample was left in this humid environment for one day before being prepared for various characterization techniques. IR, ν(C≡N): 2126 (w, sp), 2080 (s, sp), 2046 (s, sh) and 2017 cm^{-1} (vs, b) where w = weak, s = strong, vs = very strong, sp = sharp, sh = shoulder and b = broad. A TGA thermogram exhibits a 17.1% continuous mass loss between room temperature and 140 °C, which is attributed to 24.0 interstitial water molecules per TBP.

Results and Discussion

Synthesis and Characterization

The synthesis of the Fe_3Ru_2 TBP is similar to other homologous TBPs studied by our group since 2002.[143,218] The formation of the Fe_3Ru_2 TBPs does not require an anaerobic atmosphere as they have been isolated both in air and from an inert atmosphere preparation. Once formed, the TBPs are stable but the

magnetic properties vary according to the amount and type of solvent present in the interstices of these crystals. It is for this reason, that the Fe_3Ru_2 TBP has been studied in various states of solvation: under MeCN (solvated) (7a), freshly filtered (filtered) (7b), exposed to vacuum for 3 hours (3 hrs) (7c), exposed to vacuum for 24 hours (24 hrs) (7d) and exposed to a humid environment (humid) (7e). For the sake of reproducibility and to determine the underlying reason for the change in electronic configuration of the metals, the synthesis of the Fe_3Ru_2 TBPs presented herein was conducted with a strict adherence to maintaining an anhydrous, anaerobic environment from beginning to end, except for the sample that was purposely subjected to a humid atmosphere after it had been synthesized in an anhydrous, inert environment. The synthesis was repeated five times on the same day and after several days of crystal growth, all of the batches were combined and worked up together in order to rule out variations due to different batches. Although this reaction can be scaled up, it precipitates less powder and yields more crystals when the reaction solution is more dilute (~4 mM). The $Fe_4Cl_8(THF)_6$ used for this synthesis was found to be a much cleaner source of iron(II) than $FeCl_2$ typically is. Iron dichloride does not readily dissolve in MeCN and leaves behind undissolved material which contaminates the TBP reaction if not removed by filtration first. In contrast, $Fe_4Cl_8(THF)_6$ readily dissolves in MeCN and reacts with tmphen to form the $[Fe(tmphen)_2]^{2+}$ precursor in situ. MeCN is used as a solvent as it is readily stored in the glove box under a N_2 environment, is relatively easy to dry and is chemically unreactive in these reactions. Once combined, the

$[Fe(tmphen)_2]^{2+}$ and $[Ru^{III}(CN)_6]^{3-}$ solutions precipitate a dark blue or purple powder. The color of the solution can vary between brown, purple and blue. After a few days, needle-like crystals that are dark in color (generally a red/purple) form among the powder. The color of the solution generally changes or lightens as more product forms. The powder that forms can easily be separated from the crystalline product by swirling the jar which leads to a suspension of the powder in solution with the crystals remaining on the bottom of the jar. The powder and mother liquor are then readily decanted from the crystals. If crystals have formed that are not the desired TBP, (generally a salt of some nature that contains $[Fe(tmphen)_3]^{2+}$), these by-products can be re-dissolved in fresh MeCN. Fresh MeCN is added to the jar and allowed to sit over the crystals for several hours at a time. Once the MeCN remains clear and colorless with time, the crystals are ready to be characterized. The yield is generally 30-40%.

Although the sample work-up described in the experimental section is conducted precisely, slight variations in samples are unavoidable due to the large void spaces in the crystals that lead to small changes in solvent content distributed over all of the samples; combinations of batches leads to averaging of the variability. A schematic of the sample preparation is provided in Figure 4-1. Sample preparation for magnetic and ^{57}Fe Mössbauer measurements were carried out under an inert atmosphere for all but the humid sample (7e). It is important to note that the glove box was purged immediately before sample preparations to ensure that the inert atmosphere was free from any solvent. This

was particularly important when preparing the samples that had been exposed to vacuum. Details on how the samples were prepared and measured can be found in Appendix A.

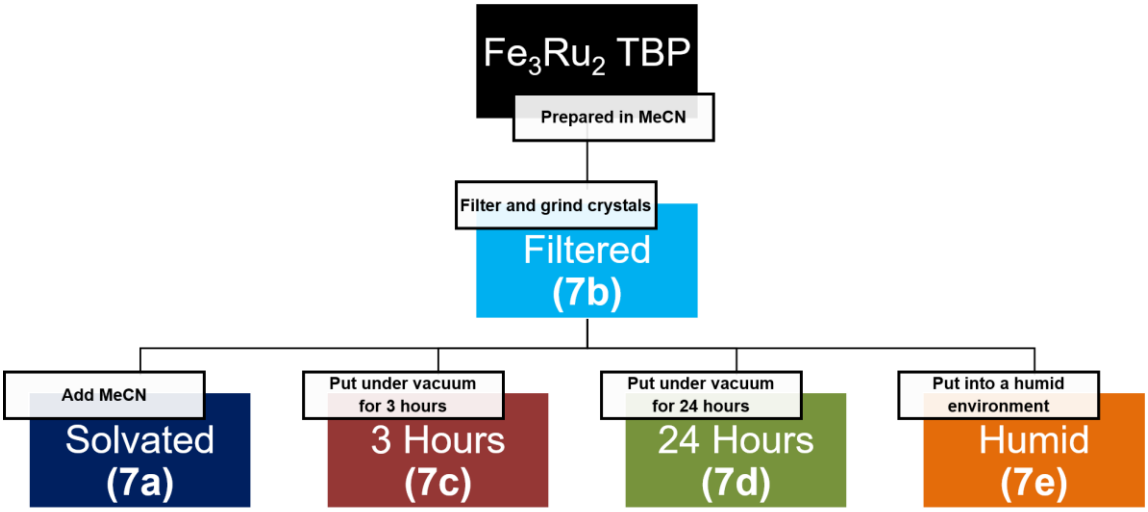

Figure 4-1. Scheme of sample preparation. Colors coincide with magnetic and ^{57}Fe Mössbauer data discussed later.

Both IR spectroscopy and TGA characterizations were performed in air and care was taken to minimize the amount of time the samples were exposed to air before and during the characterization. Both characterization techniques were performed in air and on the same samples that were measured in the SQUID. Table 4-1 lists the $\nu_{C\equiv N}$ for compounds 7a-7e, as well as $K_4[Ru^{II}(CN)_6]$ and $(PPN)_3[Ru^{III}(CN)_6]$ for reference. The spectra obtained at room temperature for all of the Fe_3Ru_2 TBPs exhibit $\nu_{C\equiv N}$ modes (~2006 – 2046 cm^{-1}) reminiscent of the

Table 4-1. Cyanide stretching frequencies from IR spectroscopy.

Compound	Bridging (cm^{-1})		Terminal (cm^{-1})	
7a - Solvated	2121 (w, sp)	2087 (s, sp)	—	2006 (vs, b)
7b - Filtered	2123 (m, sp)	2085 (vs, sp)	2039 (vs, sh)	2010 (vs, b)
7c - 3 Hours	2118 (vw, sp)	2084 (m, sp)	—	2016 (s, b)
7d - 24 Hours	2118 (w, sp)	2086 (m, sp)	2017 (s, sp)	2002 (s, sp)
7e - Humid	2126 (w, sp)	2080 (s, sp)	2046 (s, sh)	2017 (vs, b)
$K_4[Ru^{II}(CN)_6]$	—	—	2051 (s, sp)	2039 (m, sp)
$(PPN)_3[Ru^{III}(CN)_6]$	—	—	2094 (m, sp)	2085 (m, sp)

$\nu_{C\equiv N}$ stretches in $K_4[Ru^{II}(CN)_6]$ (2039 and 2046 cm^{-1}). These frequencies are assigned to the terminal cyanide groups in the TBPs and indicate the presence of divalent ruthenium at room temperature in all samples. Similarly to Prussian blue analogs,[115,219,220] the higher vibrational frequencies are assigned to the bridging cyanide groups within the TBP. Several factors are responsible for this; the kinematic effect, bonding effects due to electron-density redistribution, vibronic effects and charge effects are all reasons why the vibrational frequencies of $\nu_{C\equiv N}$ increase upon bridging.[221] Some of the modes (~2084 cm^{-1}) assigned as bridging cyanide are very close to the cyanide stretching frequencies in the $(PPN)_3[Ru^{III}(CN)_6]$ starting material. These modes could also be assigned as terminal modes for trivalent ruthenium as well, but are most likely due to bridging cyanide between Ru^{II} and Fe^{III} as evidenced by the ^{57}Fe Mössbauer and magnetic data (vide infra).

TGA studies were performed immediately after opening the NMR tube

containing the samples used for magnetic measurements. The solvated sample (7a) was placed under vacuum briefly to remove excess solvent immediately before TGA was performed. Although necessary, this step leads to a minor loss of interstitial solvent molecules and is reflected in the analysis. The filtered sample appears to contain more molecules of MeCN per TBP (8.8) as compared to the solvent sample (8.1). All solvent in the solvated sample was accounted for and used to correct the magnetic data. The intensity and gradual nature of the mass losses in the TGA data are very similar for all of the solvation states of the TBP. Due to the ambiguity of the thermograms and the relatively similar temperatures at which the mass loss is centered, the mass loss was attributed to the loss of acetonitrile for the solvated, filtered, 3 hour and 24 hour samples. This is more of a convenient assumption since they were prepared and handled in an anaerobic environment up until the time the TGA was performed in a furnace with a N_2 flow of 20 mL/min. The samples were only exposed to air long enough to put the sample in the cell, the cell onto the hanging pan and to raise the furnace (typically takes less than two minutes). The humid sample was assumed to contain only water when the TGA was performed. Table 4-2 lists the number of interstitial solvent molecules attributed to the mass loss obtained from the thermograms for all five stages of solvation of the Fe_3Ru_2 TBPs .

Table 4-2. Interstitial solvent molecules in the Fe_3Ru_2 TBPs according to TGA data.

Interstitial Solvent	7a Solvated	7b Filtered	7c 3 Hours	7d 24 Hours	7e Humid
MeCN	8.1	8.8	5.7	4.3	—
H_2O	—	—	—	—	24.0

Single Crystal X-ray Diffraction

Fe_3Ru_2 (7)

Like most other TBPs studied in this group, the Fe_3Ru_2 TBP is isostructural with the Fe_3Fe_2 and Fe_3Os_2 congeners, as well as several other metal combinations. Being from the same group however, the Fe_3Fe_2 and Fe_3Os_2 TBPs can offer a direct comparison of the effects of traversing down a group. As expected from the Fe and Os hexacyanometallate-containing analogs, the Fe_3Ru_2 TBP crystallizes in the monoclinic $P2_1/c$ space group and contains a racemic mixture of two optical isomers – the homochiral (each center is either Δ, Δ, Δ or Λ, Λ, Λ) of the equatorial $[Fe(tmphen)_2]^{2/3+}$ sites. As described in the main introduction for other homologous TBPs reported by our group,[146] the Fe_3Ru_2 TBPs pack as dimers due to the π-π stacking interactions between tmphen ligands on one TBP molecule with the tmphen ligands coordinated to a TBP related by inversion. These interactions were analyzed using Olex2 which uses a centroid-centroid distance and shift distance less than 4 and 3 Å, respectively, to detect intermolecular interactions. The nature of both the inter- and intramolecular π-π stacking interactions are depicted in Figure 4-2 and Figure 4-3, respectively.

The TBP has a total of two inter- and two intramolecular interactions. The dimeric unit has two intermolecular interactions resulting from π-π stacking between symmetry equivalent tmphen ligands coordinated to the Fe(3) centers. Two of the rings of the tmphen ligand (the center ring denoted by the purple plane in Figure 4-2 and one of the pyridine rings denoted by the yellow plane in Figure 4-2) π-π stack with each other. The center ring in the tmphen ligand interacts with both its symmetry equivalent ring (interaction designated as inter-pp – purple ring interacting with a purple ring, pp) and the pyridine ring in the neighboring tmphen ligand (interaction referred to as inter-py – purple and yellow rings interacting, py). For the intramolecular interactions, one of the pyridine rings in the tmphen ligand on the Fe(1) center π-π stacks with one of the pyridine rings in the tmphen ligand on the Fe(2) center (these rings are denoted by the turquoise planes in Figure 4-3 – interaction referred to as intra-tt). The other tmphen ligand on the Fe(2) center also has the same type of intramolecular interaction with a tmphen ligand on the Fe(3) center (these rings are colored in yellow in Figure 4-3, interaction designated as intra-yy). The Fe(1) and Fe(3) centers do not engage in an intramolecular interaction, however, owing to the much longer average Fe(1)–Fe(3) distance of 10.0603 Å when compared to the average Fe(1)–Fe(2) distance of 6.4119 Å and the average Fe(2)-Fe(3) distance of 6.3213 Å. These are the average Fe–Fe distances found for the solvated (7a), 24hr (7d) and humid (7e) samples collected at various temperatures. The ranges for all thirteen structures used in the averages are 0.1392 Å, 0.2227 Å and

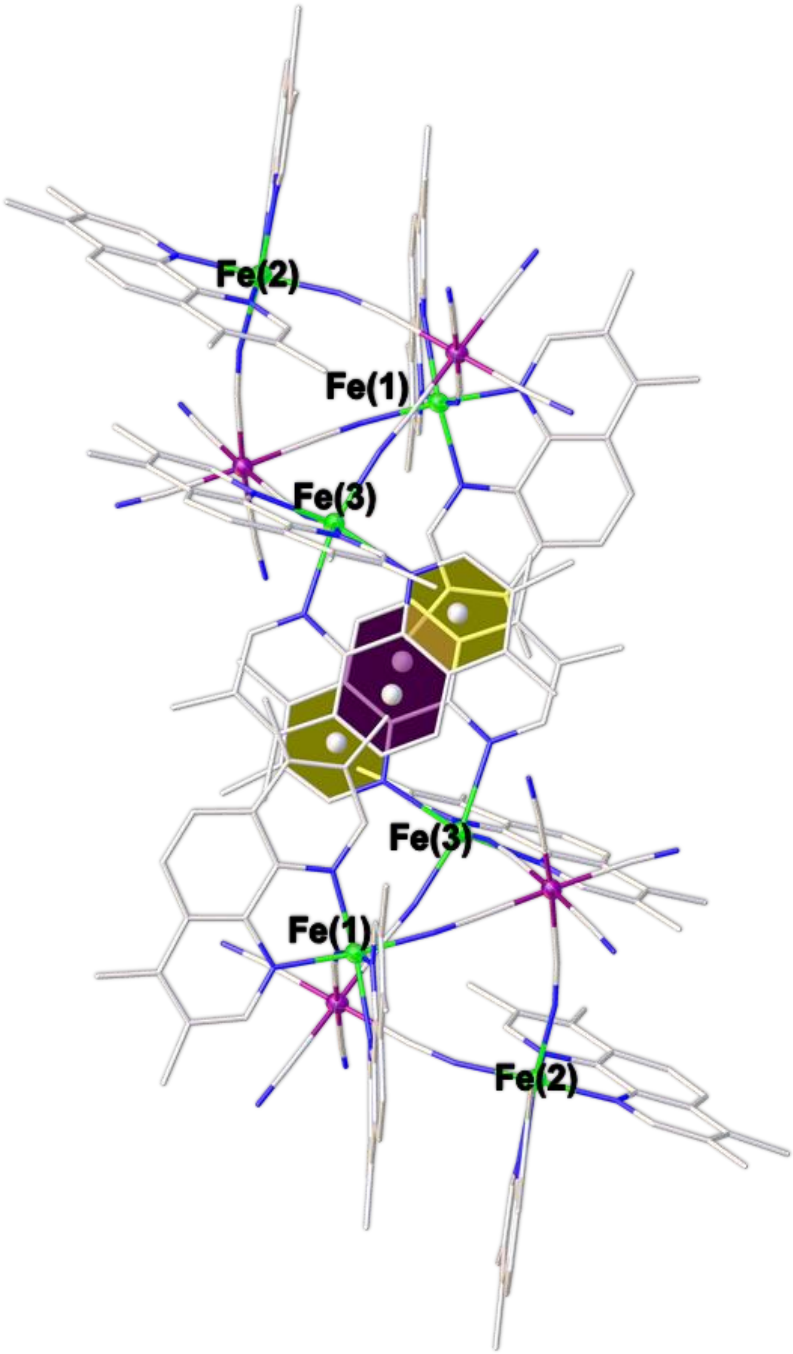

Figure 4-2. View of the Fe_3Ru_2 TBPs stacking in a dimeric unit due to the intermolecular π-π stacking interactions between neighboring TBP molecules. The purple and yellow planes highlight the rings within the tmphen ligands that have the intermolecular interactions. Color code: Fe is green, Ru is violet, C is gray and N is blue. Hydrogen and solvent have been omitted for clarity.

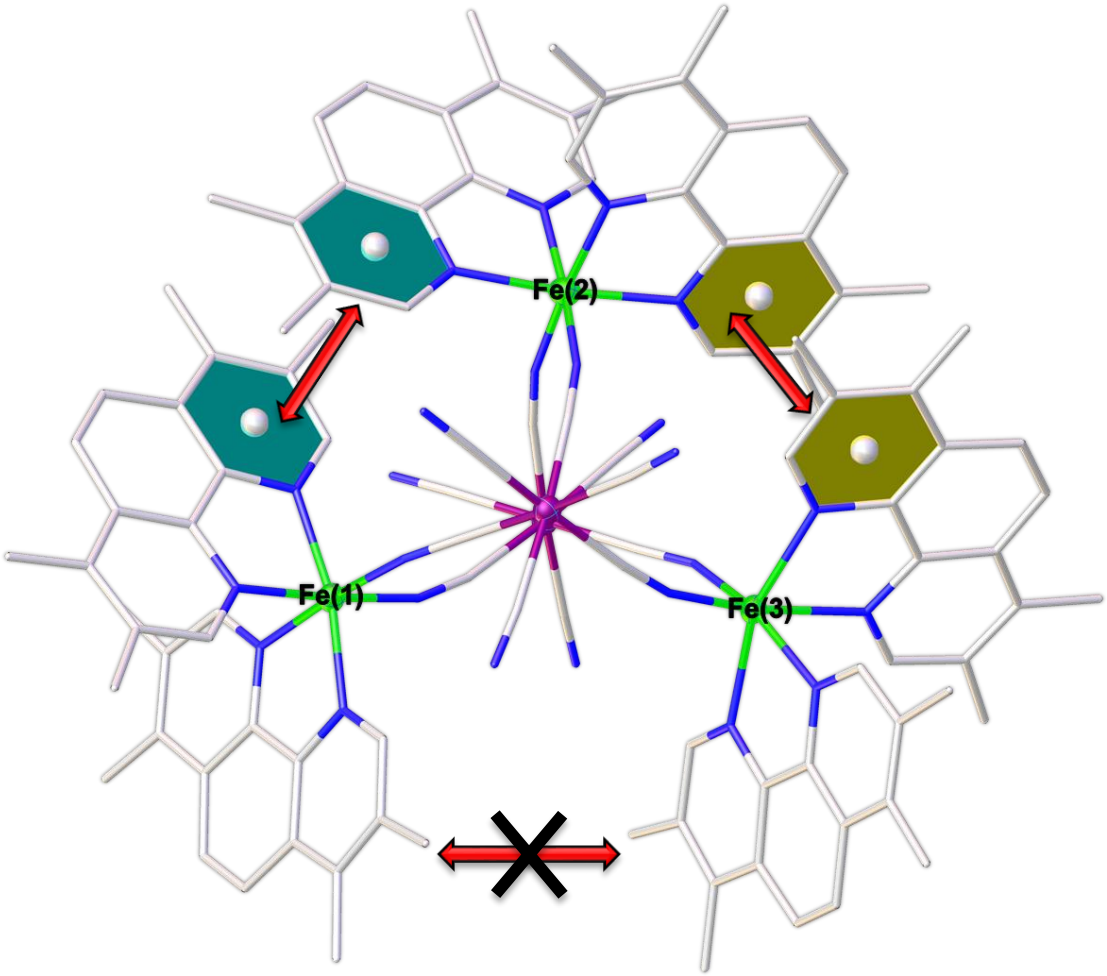

Figure 4-3. View of the Fe_3Ru_2 TBP looking down the apical hexacyanoruthenate centers. The turquoise and yellow planes coupled with the red arrows highlight the rings within the tmphen ligands that have intramolecular π-π stacking interactions within the TBP. Color code: Fe is green, Ru is violet, C is gray and N is blue. Hydrogen and solvent have been omitted for clarity.

0.1440 Å for the Fe(1)–Fe(3), Fe(1)–Fe(2) and Fe(2)–Fe(3) distances, respectively. Structures of the 3 hour and filtered samples were not obtained.

Fe_3Ru_2 Solvated (7a)

Structural data at 150 K, 100 K, 50 K, 20 K, 200 K and then 250 K were obtained (in that order of temperature) on the same crystal. Unfortunately, during the data collection at 300 K, the crystallinity of the crystal deteriorated and diffraction data could no longer be obtained. This is most likely due to the rapid desolvation that can occur in these TBP molecules at room temperature.[145] Table 4-3 gives relevant structural data and refinement parameters for the solvated Fe_3Ru_2 TBPs. At the temperatures in which data was obtained, the space group remains unchanged. As the temperature increases from 20 K to 250 K, however, the cell edges and the unit cell volume increase as well. This is not uncommon for spin-transition complexes and is well documented in the literature.[82,222,223] This effect is easily explained by the increase in the Fe-N bond distances as temperature increases. This lengthening is propagated throughout the crystal lattice causing the overall expansion of the unit cell parameters.[65,82] The disordered solvent was refined at 20 K but could not be modeled at higher temperatures. The PLATON SQUEEZE[190] procedure, as contained in the PLATON[224] software package, was used to remove residual electron density due to disordered solvent from the remaining structures and the built-in solver add-in contained within Microsoft Excel was used to model the interstitial MeCN and

water molecules based upon electron density found within the voids. Table 4-4 gives the results from the SQUEEZE analysis. An interesting trend is the increase of 2.5 % in the amount of void space as the temperature is increased from 20 K to 250 K, a possible effect from the natural expansion of the unit cell with the increase in temperature coupled with the iron centers undergoing a spin-transition. Parameters in Table 4-3 are for the structures where SQUEEZE was employed. Full refinement of the disordered solvent for 7a at 20 K resulted in 3.2 MeCN molecules and 9.8 water molecules per TBP. Upon solving for the residual electron density given from the SQUEEZE analysis at all temperatures, it was determined that the TBP has an average of approximately three MeCN and thirteen water molecules per formula unit (7a·3MeCN·13H_2O). The results from the SQUEEZE analysis are fairly close to the results from structure refinement for MeCN but estimates a larger amount of water in the crystal. As neither of these methods will give perfect values, the similarity of their values is acceptable and considered to be in good accord with each other. Although these samples were prepared in a strictly anaerobic manner, the short period of time the crystals were exposed to air in order to mount the crystal onto a MiTeGen loop before being put into a He cold stream at 150 K, is sufficient for the TBP to absorb several water molecules. In contrast to the TGA data obtained for 7a which suggests more molecules of MeCN should be present, it would seem that interstitial MeCN molecules were rapidly exchanged for water molecules upon exposure to air. At 250 K, SQUEEZE analysis suggests that one of the MeCN molecules has been

Table 4-3. Crystal structure data and refinement parameters for the solvated Fe_3Ru_2 TBP at multiple temperatures.

Fe_3Ru_2 Solvated	**20 K**	**50 K**	**100 K**	**150 K**	**200 K**	**250 K**
Space Group	*P*2$_1$/*c*	*P*2$_1$/*c*	*P*2$_1$/*c*	*P*2$_1$/*c*	*P*2$_1$/*c*	*P*2$_1$/*c*
a/ Å	19.0959(6)	19.1001(8)	19.1318(16)	19.1600(15)	19.2675(6)	19.3787(6)
b/ Å	24.9486(7)	25.0143(10)	25.075(2)	25.1157(19)	25.0897(7)	25.1159(7)
c/ Å	24.3846(7)	24.4167(10)	24.471(2)	24.5366(19)	24.5796(7)	24.6325(7)
β/ °	98.471(2)	98.400(2)	98.309(4)	98.257(4)	98.480(2)	98.726(2)
Volume/ Å^3	11490.5(6)	11540.6(8)	11616.0(16)	11685.0(16)	11752.3(6)	11850.2(6)
[a]Interstitial Solvent	3 MeCN 13 H_2O	3 MeCN 13 H_2O	3 MeCN 13 H_2O	3 MeCN 13 H_2O	3 MeCN 13 H_2O	2 MeCN 13 H_2O
μ/ mm^{-1}	0.735	0.732	0.727	0.723	0.719	0.713
Crystal Size/ mm^3	0.047 × 0.047 x 0.3102 ; reddish-purple prism					
2Θ Range for Data Collection/ °	4.09 to 47.976	4.258 to 54.236	4.248 to 47.844	4.242 to 53.554	4.238 to 40.81	4.228 to 40.476
Integration Resolution/ Å	0.95	0.84	0.96	0.85	1.11	1.11
Independent Reflections	13821 R_{int} = 0.1247 R_{sigma} = 0.0670	19658 R_{int} = 0.1736 R_{sigma} = 0.0951	13875 R_{int} = 0.1568 R_{sigma} = 0.0810	19248 R_{int} = 0.1004 R_{sigma} = 0.0600	8906 R_{int} = 0.1153 R_{sigma} = 0.0507	8822 R_{int} = 0.1028 R_{sigma} = 0.0475
Data/Restraints/ Parameters	13821/585/1414	19658/120/1258	13875/0/1256	19248/0/1258	8906/1377/1258	8822/1377/1258
[b]GooF on F^2	1.014	1.031	1.033	1.042	1.014	1.015
[c,d]Final R Indexes [I>=2σ (I)]	R_1 = 0.0482 wR_2 = 0.1169	R_1 = 0.0668 wR_2 = 0.1618	R_1 = 0.0593 wR_2 = 0.1517	R_1 = 0.0570 wR_2 = 0.1401	R_1 = 0.0379 wR_2 = 0.0952	R_1 = 0.0383 wR_2 = 0.0951
[c,d]Final R Indexes [all data]	R_1 = 0.0721 wR_2 = 0.1310	R_1 = 0.1130 wR_2 = 0.1869	R_1 = 0.0878 wR_2 = 0.1682	R_1 = 0.0828 wR_2 = 0.1613	R_1 = 0.0554 wR_2 = 0.1031	R_1 = 0.0548 wR_2 = 0.1047
Largest Diff. Peak/Hole/ e Å^{-3}	1.06 / -0.74	1.87 / -0.92	1.19/-0.69	1.56 / -1.05	1.07 / -0.33	1.37 / -0.28

Radiation = synchrotron (λ = 0.7749), α = γ = 90°, Z = 4, [a]*Calculated from SQUEEZE data.* [b]GooF: Goodness-of-fit = $\{\sum[w(F_o^2 - F_c^2)^2]/(n-p)\}^{1/2}$, where *n* is the number of reflections and *p* is the total number of parameters refined. [c]$R = \sum ||F_o| - |F_c|| / \sum |F_o|$. [d]$wR = \{\sum[w(F_o^2 - F_c^2)^2] / \sum w(F_o^2)^2]\}^{1/2}$.

Table 4-4. Void space and residual electron density for the solvated Fe_3Ru_2 TBPs (7a), as calculated from SQUEEZE analysis. Interstitial solvent was calculated using the electron density and the solver add-in in Excel 2013**.**

Fe_3Ru_2 Solvated	Void Space (Å)	Number of Electrons	% Void Space	H_2O/TBP	MeCN/TBP
20 K	2889.1	755.0	25.1	13.0	2.7
50 K	3020.3	840.0	26.2	13.4	3.4
100 K	3094.0	830.0	26.6	13.5	3.3
150 K	3135.5	783.0	26.8	13.3	2.9
200 K	3194.9	753.0	27.2	13.2	2.5
250 K	3268.3	731.0	27.6	13.2	2.3
Average	**3100.4**	**782.0**	**26.6**	**13.3**	**2.8**

lost, leaving two MeCN and thirteen water molecules in the interstitial sites ($7a{\cdot}2MeCN{\cdot}13H_2O$).

The metal–ligand (M–L) bond lengths are listed in Table 4-5. The average Fe–N distances in LS and HS FeN_6 complexes are 1.92 – 2.00 Å and 2.16 – 2.21 Å, respectively.[82] The structure at 20 K has eight Fe(1)–N bond distances given instead of the usual six due to disorder in one of the tmphen ligands. Throughout the temperature range (20 – 250 K) the average Fe(1)–N bond distance remains relatively unchanged around 2.07 – 2.08 Å. This is a typical Fe–N bond distance for an iron center in the middle of a SCO. The average Fe(2)–N bond length slowly increases from 1.9616(48) Å at 20K to 2.0317(59) Å at 150 K. Although the lengthening of this bond is not a Δ = 0.2 Å, it still suggests that a spin transition, either a SCO or CTIST, is possible at this iron center and is likely to occur at higher temperatures. As with the average Fe(1)–N bond distances, the average

Fe(3)–N bond distances remain relatively unchanged from 20 K to 250 K (2.08 Å to 2.11 Å). Again, these bond lengths are typical for an iron center in an intermediate spin-transition. It is interesting to note that the Fe–N bond lengths that come from the bridging cyanide (the first two Fe–N bond lengths given at each temperature) are consistently shorter (~0.2 Å) than the Fe–N distances that come from the tmphen ligands. This is most likely due to the rigid bonding motif imposed upon the iron center from the bridging cyanide coupled with the fact that the cyanide is electron-dense and allows for strong σ bonding with the metal centers.[221,225] The Ru–C bond length are given but do not give any insight into the oxidation state of the ruthenium centers. They are both very similar and remain relatively unchanged with temperature changes. As expected, the Ru–C bond lengths from the bridging cyanide (the first three bond lengths for Ru–C given at each temperature) are constantly shorter than the Ru–C bond lengths from the terminal cyanide.

The structure of 7a with the disordered water and MeCN molecules modeled at 20 K is shown in Figure 4-4. In order for the structure to converge, the hydrogen atoms were removed from the water molecules. At 20 K, the Fe(1) center has a tmphen ligand that is disordered over two positions. This is an indication that the Fe center is undergoing a spin-transition in this temperature. At all of the other temperatures, this disordered tmphen ligand was modeled in one place but the thermal ellipsoids are slightly oblong. When the average Fe(1)–N bond lengths are considered throughout the temperatures, it becomes more

Table 4-5. Metal–Ligand (M–L) bond lengths (in Å) for the solvated Fe_3Ru_2 TBP (7a).

Temperature	Fe(1)–N	Fe(2)–N	Fe(3)–N	Ru(1)–C	Ru(2)–C
20 K	1.965(05)	1.929(5)	1.938(5)	1.979(6)	1.970(7)
	1.936(05)	1.926(5)	1.971(6)	2.038(7)	2.019(6)
	2.105(05)	1.987(4)	2.124(4)	1.964(7)	1.989(7)
	2.140(04)	1.964(5)	2.182(5)	2.069(8)	2.040(7)
	2.163(65)	1.985(5)	2.172(5)	2.069(7)	2.059(8)
	2.132(41)	1.980(5)	2.146(5)	2.060(7)	2.041(8)
	1.959(38)				
	2.196(19)				
Avg M–L	***2.066(16)***	***1.962(5)***	***2.089(5)***	***2.030(7)***	***2.020(7)***
50 K	1.978(5)	1.934(5)	1.950(6)	2.000(6)	1.962(6)
	1.949(6)	1.926(5)	1.968(6)	2.043(7)	2.042(6)
	2.111(5)	1.987(5)	2.116(5)	1.957(6)	1.992(7)
	2.143(5)	1.970(5)	2.185(5)	2.070(7)	2.051(7)
	2.147(5)	1.975(5)	2.163(5)	2.077(6)	2.063(8)
	2.108(5)	1.982(5)	2.157(5)	2.058(7)	2.038(9)
Avg M–L	***2.073(52)***	***1.963(5)***	***2.090(5)***	***2.034(6)***	***2.025(7)***
100 K	1.966(6)	1.930(6)	1.955(6)	1.985(7)	1.973(8)
	1.942(6)	1.926(6)	1.974(7)	2.038(8)	2.026(7)
	2.107(6)	1.989(6)	2.125(5)	1.967(8)	1.979(8)
	2.148(6)	1.972(6)	2.194(5)	2.049(8)	2.047(8)
	2.158(5)	1.986(6)	2.170(6)	2.069(8)	2.049(9)
	2.112(6)	1.986(5)	2.154(5)	2.048(8)	2.045(9)
Avg M–L	***2.072(6)***	***1.965(6)***	***2.095(6)***	***2.026(8)***	***2.020(8)***
150 K	1.973(4)	1.939(4)	1.949(4)	1.994(5)	1.958(5)
	1.949(5)	1.931(4)	1.974(5)	2.050(5)	2.042(5)
	2.128(4)	1.988(4)	2.135(4)	1.956(5)	1.997(6)
	2.154(4)	1.969 (4)	2.193(4)	2.057(6)	2.049(6)
	2.161(4)	1.990(4)	2.176(4)	2.071(6)	2.061(7)
	2.119(4)	1.986(4)	2.164(4)	2.055(6)	2.049(7)
Avg M–L	***2.081(4)***	***1.967(4)***	***2.098(4)***	***2.030(5)***	***2.026(6)***
200 K	1.975(6)	1.937(6)	1.958(6)	1.992(7)	1.957(7)
	1.949(6)	1.946(6)	1.978(6)	2.030(7)	2.032(7)
	2.117(5)	2.009(5)	2.115(5)	1.956(8)	1.986(7)
	2.137(5)	1.997(6)	2.198(5)	2.054(8)	2.047(8)
	2.160(5)	2.009(5)	2.177(5)	2.063(8)	2.048(8)
	2.108(5)	2.012(5)	2.150(5)	2.050(8)	2.030(9)
Avg M–L	***2.074(5)***	***1.985(6)***	***2.096(5)***	***2.024(8)***	***2.017(8)***
250 K	1.982(6)	1.957(6)	1.977(6)	1.987(7)	1.958(7)
	1.944(6)	1.966(6)	2.011(6)	2.012(8)	2.011(7)
	2.127(5)	2.061(6)	2.139(5)	1.960(8)	1.986(7)
	2.150(5)	2.064(6)	2.197(5)	2.056(8)	2.053(8)
	2.165(5)	2.078(6)	2.183(6)	2.061(8)	2.047(9)
	2.112(5)	2.065 (5)	2.153(5)	2.051(8)	2.043(9)
Avg M–L	***2.080(5)***	***2.032(6)***	***2.110(6)***	***2.021(8)***	***2.016(8)***

apparent as to why the tmphen ligand is disordered. As discussed earlier, this Fe center is undergoing a very gradual spin-transition as temperature changes, leading to the thermal movement of the tmphen ligand throughout the lattice. The pink circles in Figure 4-4 highlight the disordered tmphen ligand as well as the disordered MeCN molecules. The solvent molecules in this figure were arbitrarily moved to a symmetrically equivalent position in order to obtain a clear view of the disordered tmphen ligand. The packing diagram in Figure 4-5 gives a simple view of how the solvent packs between the dimeric units of the TBP. Each dimeric unit is colored differently (green, yellow and cyan) in order to show the packing arrangement of the units in the lattice. It can be seen that the water and MeCN molecules fill the voids between the dimeric units and has very little interaction with the Fe(3) centers, as those are involved in the π-π stacking between neighboring TBPs. The solvent mostly resides around the Fe(1), Fe(2) and ruthenium centers as the water appears to hydrogen bond to the terminal cyanide ligands. This creates what is most likely a hydrogen bonding network between the dimeric units in the TBP. This structure, however, is not an accurate representation of what the TBP made in a strictly anaerobic environment should be though. It is reasonable that the MeCN molecules that were most likely exchanged for water upon exposure to air, still reside in these cavities that exist between the dimers. The main difference is their inability to hydrogen bond to the terminal cyanide ligands on the ruthenium centers.

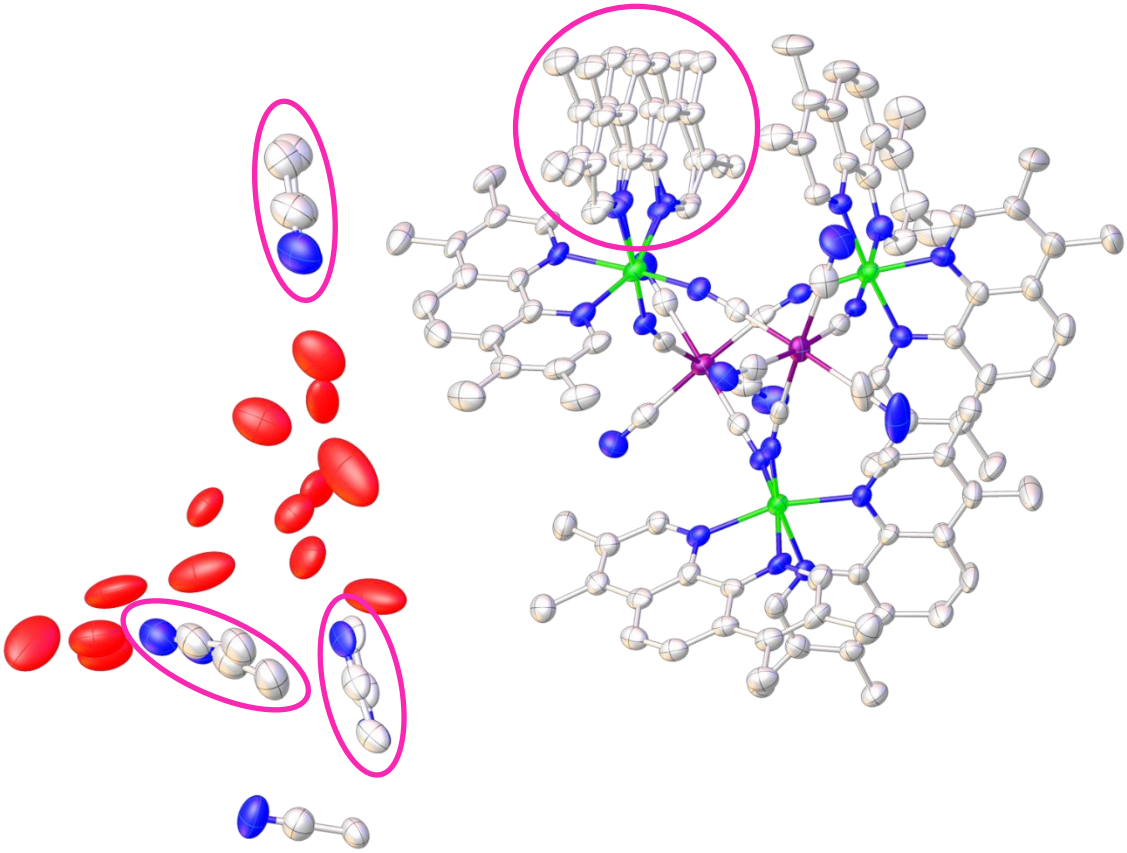

Figure 4-4. Asymmetric unit of the solvated Fe_3Ru_2 TBP (7a) at 20 K. Pink circles highlight the disordered tmphen and MeCN molecules within the crystal. Color code: Fe is green, Ru is violet, C is gray, N is blue and O is red. Oxygen atoms were refined without hydrogen in order to obtain convergence of the structure. Hydrogen from all other atoms have been omitted for the sake of clarity.

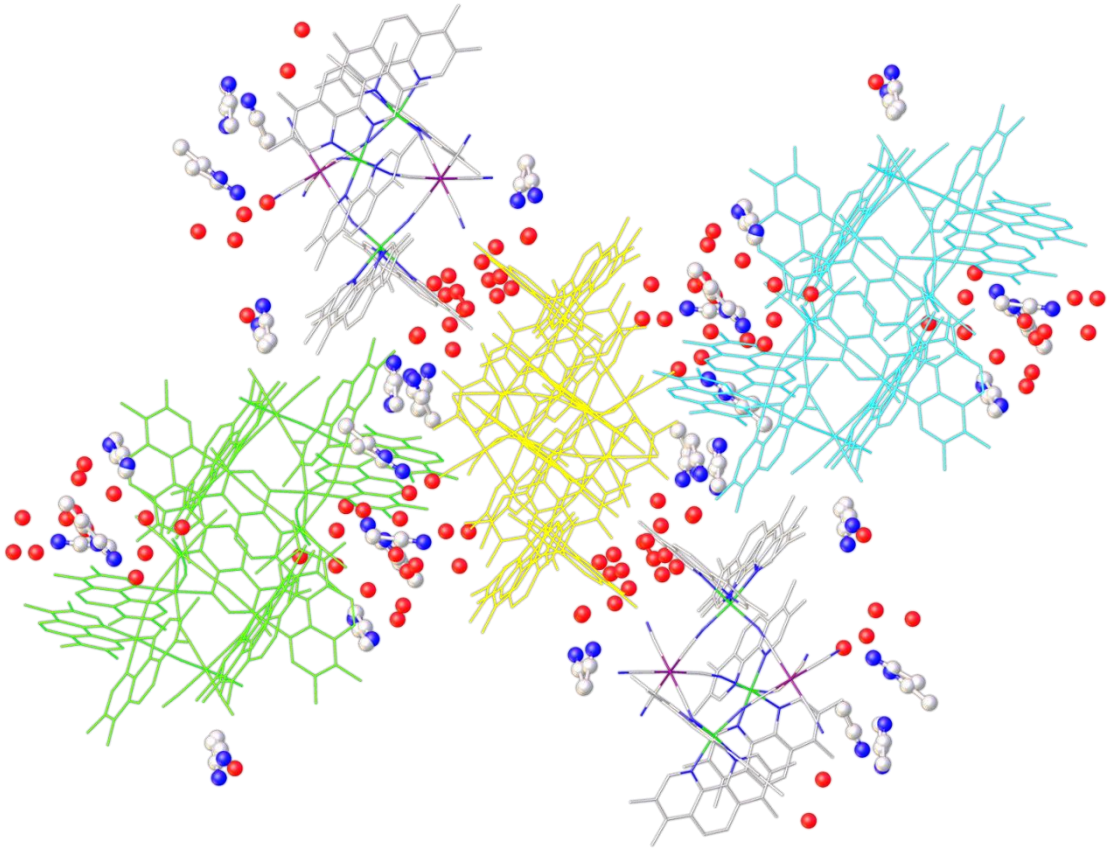

Figure 4-5. Simple packing diagram of the solvated Fe_3Ru_2 TBP (7a). Dimeric units of the TBPs are colored using the same color (three dimeric units shown – green, yellow and cyan). Two individual TBP molecules shown using the following color scheme: Fe is green, Ru is violet, C is gray, N is blue and O is red. Oxygen atoms were refined without hydrogen in order to obtain convergence of the structure. Hydrogen from all other atoms have been omitted for the sake of clarity.

Analysis of the π-π stacking interactions gives three relevant structural parameters: centroid-centroid distances, shift distances between the centroids and angles between the planes involved (given in Table 4-6). As stated earlier, the parameters Olex2 uses to detect intermolecular interactions is a centroid-centroid distance and shift distance less than 4 and 3 Å, respectively. A 4 Å distance for the centroid-centroid distance is considered to be slightly long for π-π stacking interactions, as discussed by Janiak.[201] Strong π-π interactions are considered to be at a distance ~3.3 Å with weaker interactions ~3.6 – 3.8 Å. The distance of 3.8 Å is generally considered the maximum distance for which π-π interactions are acknowledged, which is in accordance with the sum of Van der Waals radii's (with 1.77 Å the proposed radii for C).[202] From the analysis, no clear temperature dependence for the three parameters is observed but the centroid-centroid distance does vary slightly. The inter-pp interaction is the strongest π-π interaction with the shortest distance (average 3.529 Å). The other three interactions, with values slightly longer than 3.8 Å, can be considered weak π-π interactions. From the shift distances observed, all inter- and intramolecular interactions are slipped instead of face-to-face, which is common for ligands with N donor atoms.[201] The inter-pp interaction (the strongest) is also the one with the smaller lateral displacement between the pyridine rings. Below 250 K, there is not a large variation in shift distances with temperature but at 250 K the inter-pp interaction exhibits an increase (~0.15 Å) in the shift distance while the inter-py shift distance decreases slightly (~0.13 Å). This suggests a lateral displacement

of the tmphen ligands involved in the intermolecular π-π stacking interactions at elevated temperatures and could be a consequence of several factors, the main one most likely being the thermal expansion of the bonds. The angles between the planes formed by the rings in the tmphen ligands are smaller than 7º in all cases, an indication that the interacting tmphen ligands are close to being parallel to one another which allows for stronger interactions between them. In the inter-pp interaction, the angle is 0º due to these planes being related by inversion. Interestingly, only for the intra-tt interaction (intramolecular interaction between Fe(1) and Fe(2) centers) is a clear temperature dependence observed for the angle between the planes. As temperature increases from 20 K to 250 K, the angle increases 4.74º, a large change compared to the 0.471° maximum variation within the other interactions. It possible that the increased bending of these planes away from 0° as temperature increases is related with the fact that the average Fe(2)–N bond distances also increase due to a spin-transition. However, the largest differences in the angle between the planes is between 20 and 50 K while the largest change in the average Fe(2)–N bond lengths are above 200 K, so no direct relationship can be inferred.

Table 4-6. Geometric parameters (centroid-centroid distance, shift distance and angle) for the inter- and intramolecular π-π stacking interactions in the solvated Fe_3Ru_2 TBPs (7a). The average values (avg) and the differences between the minimum and maximum values (Δ) have been included. *Indicates symmetry equivalent metal center.

Interaction-Plane Fe Centers Involved	Temperature	Centroid-Centroid Distance (Å)	Shift Distance (Å)	Angle (º)
inter-pp Fe(3)–Fe(3)*	20 K	3.505	0.632	0
	50 K	3.503	0.613	0
	100 K	3.516	0.639	0
	150 K	3.531	0.650	0
	200 K	3.545	0.773	0
	250 K	3.573	0.923	0
	Avg	**3.529**	**0.705**	**0**
	Δ	*0.068*	*0.291*	*0*
inter-py Fe(3)–Fe(3)*	20 K	3.851	1.782	1.218
	50 K	3.864	1.801	1.067
	100 K	3.867	1.775	0.781
	150 K	3.867	1.761	1.088
	200 K	3.813	1.649	0.878
	250 K	3.749	1.512	0.849
	Avg	**3.835**	**1.713**	**0.980**
	Δ	*0.118*	*0.289*	*0.437*
intra-tt Fe(1)–Fe(2)	20 K	3.891	1.273	1.997
	50 K	3.818	1.238	4.639
	100 K	3.821	1.241	4.659
	150 K	3.835	1.234	5.035
	200 K	3.870	1.249	5.476
	250 K	3.909	1.259	6.737
	Avg	**3.857**	**1.249**	**4.757**
	Δ	*0.091*	*0.030*	*4.740*
intra-yy Fe(2)–Fe(3)	20 K	3.836	1.426	6.860
	50 K	3.840	1.411	6.832
	100 K	3.841	1.435	6.526
	150 K	3.841	1.420	6.389
	200 K	3.852	1.406	6.512
	250 K	3.855	1.365	6.808
	Avg	**3.844**	**1.410**	**6.654**
	Δ	*0.019*	*0.070*	*0.471*

Fe_3Ru_2 24 Hours (7d)

Table 4-7 contains the usual structural parameters and Table 4-8 contains the results from the SQUEEZE analysis. According to the SQUEEZE analysis, the evacuated sample has a slightly higher percentage of void space in comparison to the solvated sample at 150 K and also contains more interstitial solvent. Complete structure refinement of the crystal resulted in a near identical number of water molecules per TBP (23.4) as calculated from SQUEEZE (23.7). Parameters in Table 4-7 are from the refinement using SQUEEZE. This is mainly for consistency between the solvated and humid samples discussed here. The data for the evacuated sample are not ideal (as indicated by the usual refinement parameters such as R_1, wR_2, R_{int} and a low resolution cut-off of 1.03 Å) but it is actually impressive that the crystal did not disintegrate entirely which is attributed to the fact that the packing of the molecules allows for large void spaces for solvent loss and absorption in a manner similar to MOFs.

Table 4-7. Crystal structure data and refinement parameters for the Fe_3Ru_2 TBP evacuated for 24 hours.

Fe_3Ru_2 24 Hour	**150 K**
Space Group	$P2_1/c$
a/ Å	19.6693(13)
b/ Å	24.8293(16)
c/ Å	24.4678(16)
β/ °	98.644(4)
Volume/ Å^3	11813.7(13)
[a]Interstitial Solvent	24 H_2O
μ/ mm^{-1}	0.715
Crystal Size/ mm^3	0.094 × 0.094 x 0.254 reddish-purple prism
2Θ Range for Data Collection/ °	4.02 to 44.048
Integration Resolution/ Å	1.03
Independent Reflections	11142 R_{int} = 0.1452 R_{sigma} = 0.0697
Data/Restraints/ Parameters	11142/702/1256
[b]GooF on F^2	1.052
[c,d]Final R Indexes [I>=2σ (I)]	R_1 = 0.0949 wR_2 = 0.2168
[c,d]Final R Indexes [all data]	R_1 = 0.1739 wR_2 = 0.2866
Largest Diff. Peak/Hole/ e Å^{-3}	1.28 / -0.49

Radiation = synchrotron (λ = 0.7749), α = γ = 90°, Z = 4, [a]*Calculated from SQUEEZE data.* [b]GooF: Goodness-of-fit = $\{\sum[w(F_o^2 - F_c^2)^2]/(n-p)\}^{1/2}$, where n is the number of reflections and p is the total number of parameters refined. [c]$R = \sum ||F_o| - |F_c|| / \sum |F_o|$. [d]$wR = \{\sum[w(F_o^2 - F_c^2)^2]/\sum w(F_o^2)^2]\}^{1/2}$.

Table 4-8. Void space and residual electron density for the Fe_3Ru_2 TBPs exposed to vacuum for 24 hours (7d), as calculated from SQUEEZE analysis. Interstitial solvent was calculated using the electron density.

Fe_3Ru_2 24 Hours	**Void Space (Å)**	**Number of Electrons**	**% Void Space**	**H_2O/TBP**
150 K	3218	949.0	27.4	23.7

Table 4-9. M–L bond lengths (in Å) for the Fe_3Ru_2 TBP under vacuum for 24 hours (7d).

Temperature	Fe(1)–N	Fe(2)–N	Fe(3)–N	Ru(1)–C	Ru(2)–C
150 K	1.956(19)	1.918(21)	1.930(17)	1.973(27)	1.975(26)
	1.903(18)	1.950(17)	1.971(17)	2.001(26)	1.934(21)
	2.000(16)	2.005(15)	2.070(15)	1.987(24)	1.958(23)
	2.013(15)	1.970(18)	2.190(14)	2.042(26)	2.021(24)
	2.023(13)	1.979(17)	2.161(15)	2.095(23)	1.957(25)
	2.039(12)	2.021(16)	2.124(13)	2.003(25)	1.969(26)
Avg M–L	***1.989(16)***	***1.9738(17)***	***2.074(15)***	***2.017(25)***	***1.969(24)***

The M–L bond lengths listed in Table 4-9 differ from those in the solvated structure collected at 150 K. In contrast to two iron centers with average Fe–N bond lengths indicative of the iron center existing in an intermediate spin-transition state, the evacuated structure clearly indicates that the Fe(1) and Fe(2) centers are in a LS state with average Fe–N bond length of ~1.99 Å and ~1.97 Å, respectively. The average Fe(3)–N bond length is ~2.07 Å which suggests the Fe center is in between the LS and HS states. The average Ru(2)–C distance (~1.97 Å) is relatively shorter than the Ru(1)–C bond length and is also shorter than those found in the solvated sample (~2.02 Å). This might suggest a difference in oxidation states between the two ruthenium centers but with such large standard deviations on the bond distances in this structure, it would be unwise to commit to that theory based solely off of X-ray data. The π-π stacking parameters obtained are given in Table 4-10. In this structure, the centroid-centroid distances are shorter in both intermolecular interactions (still the inter-pp interaction being the strongest) compared to the solvated sample. The solvated

structures exhibit inter-py interactions considerably longer than in the 24 hour sample (3.867 Å vs 3.654 Å) while the intra-tt centroid-centroid distance in the 24 hour sample elongates (3.930 Å vs 3.835 Å). There is also a larger shift and angle associated with the intra-tt interaction in the 24 hour sample while the π-π stacking parameters for the intra-yy interaction are smaller when compared to the solvated structures. These intramolecular interactions indicate that a contraction between the Fe(2) and Fe(3) centers and an expansion between the Fe(1) and Fe(2) centers is occurring in the 24 hour sample.

Table 4-10. Geometric parameters (centroid-centroid distances, shift distances and angles) for the inter- and intramolecular π-π stacking interactions in the 24 hour evacuated Fe_3Ru_2 TBPs at 150 K. *Indicates symmetry equivalent metal center.

Interaction-Plane Fe Centers Involved	**Centroid-Centroid Distance (Å)**	**Shift Distance (Å)**	**Angle (º)**
inter-pp Fe(3)–Fe(3)*	3.546	1.049	0
inter-py Fe(3)–Fe(3)*	3.654	1.374	0.871
intra-tt Fe(1)–Fe(2)	3.930	1.496	7.327
intra-yy Fe(2)–Fe(3)	3.804	1.283	4.542

It must be stated that although a structure of the evacuated TBP was obtained, the data must be taken lightly as it shows more water content than the humid sample does. Obviously, the rapid absorption of water molecules no longer give a true representation of what the evacuated sample is truly like, structurally.

As expected, the packing diagram with the modeled water (Figure 4-6) show that even though the solvent had been removed from the TBP, it quickly re-absorbed water. The arrangement of the absorbed water fills the cavities that lie between the dimers, just as it did in the solvated sample.

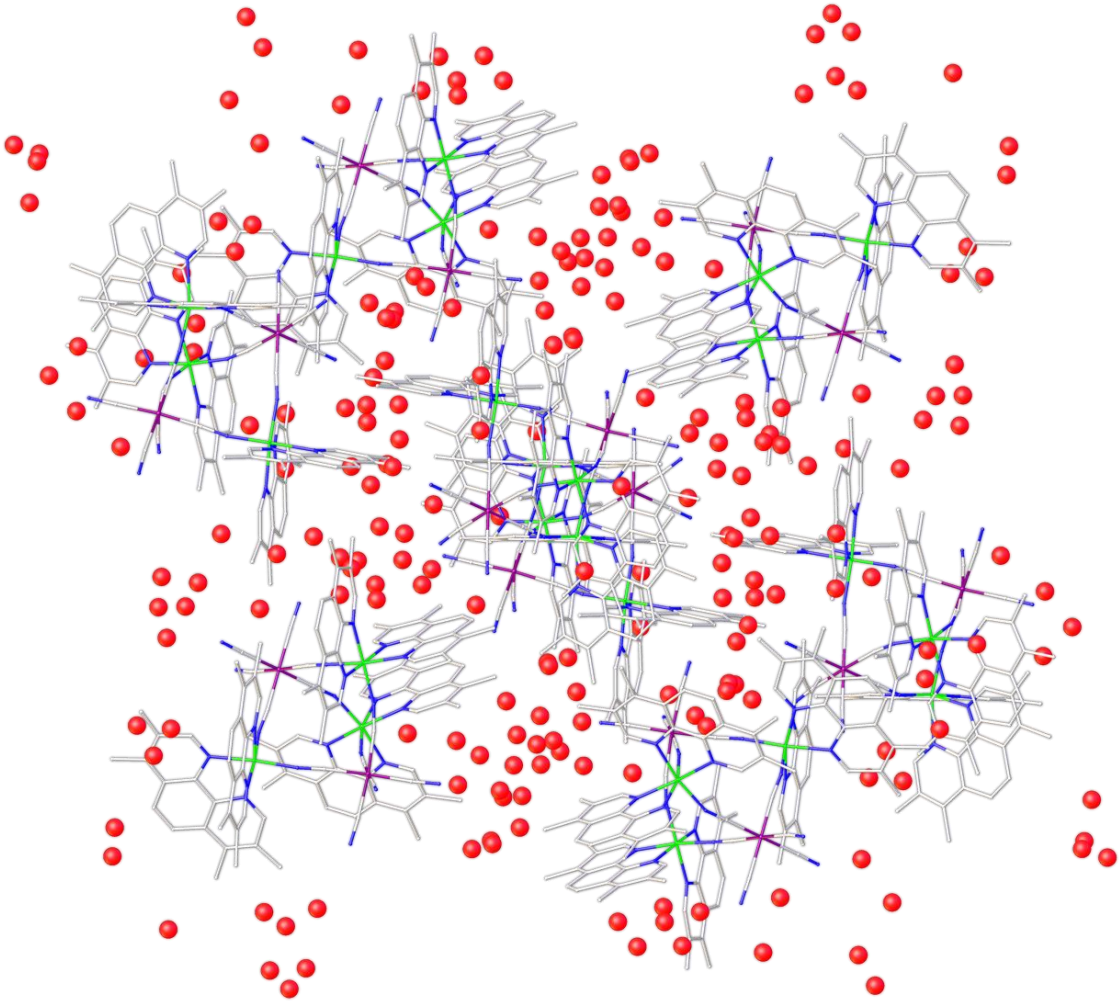

Figure 4-6. Packing diagram of the 24 hour evacuated Fe_3Ru_2 TBP. Color code: Fe is green, Ru is violet, C is gray, N is blue and O is red. Oxygen atoms were refined without hydrogen in order to obtain convergence of the structure. Hydrogen from all other atoms have been omitted for the sake of clarity.

Fe_3Ru_2 Humid (7e)

The usual structure and refinement parameters can be found in Table 4-11 and the SQUEEZE analysis in Table 4-12. The humid samples were fully refined for solvent content for all temperatures. SQUEEZE was still employed as a comparison of experimental and calculated solvent content and for consistency between samples. The differences in structural data found between the modeled and SQUEEZED data sets were negligible in all aspects except solvent content. As can be seen by the refinement parameters and the resolution cut-off, this crystal diffracted better than the solvated and the evacuated crystals which led to better structure refinement. Much like the solvated structure, the volume of the unit cell increases with increasing temperature. In contrast to the solvated sample however, all cell edge lengths did not continually increase throughout the temperature regime. From 20 – 200 K the cell edges expanded as expected but at 250 K, there was a contraction of both the a and c axes. This trend is in accord with the percent of void space in the lattice at these temperatures. This could possibly indicate a difference in the spin-transitions occurring around 250 K between the solvated and humid Fe_3Ru_2 TBPs. The analysis of the SQUEEZED solvent is less than consistent. The amount of water fluctuates a great deal between lower temperatures, which is unlikely to occur naturally. However, during data collection in a He cold stream at the ALS, ice tends to accumulate on the loops and crystals below 150 K, which can lead to extra diffraction spots on the frames and incorrect spot intensities. This could be a reason for the inconsistent

Table 4-11. Crystal structure data and refinement parameters for the humid Fe_3Ru_2 TBP at multiple temperatures.

Fe_3Ru_2 Humid	**20 K**	**50 K**	**100 K**	**150 K**	**200 K**	**250 K**
Space Group	*P*2$_1$/*c*	*P*2$_1$/*c*	*P*2$_1$/*c*	*P*2$_1$/*c*	*P*2$_1$/*c*	*P*2$_1$/*c*
a/ Å	19.5291(8)	19.5287(5)	19.5496(8)	19.5885(12)	19.6694(7)	19.6400(5)
b/ Å	24.7058(10)	24.7166(6)	24.7642(11)	24.8103(15)	24.8678(9)	24.9411(7)
c/ Å	24.1203(9)	24.1330(6)	24.1847(10)	24.2531(14)	24.3597(9)	24.3104(6)
β/ °	98.314(2)	98.2950(10)	98.252(3)	98.272(4)	98.534(2)	98.709(2)
Volume/ Å^3	11515.3(8)	11526.7(5)	11587.3(9)	11664.3(12)	11783.2(7)	11771.0(5)
[a]Interstitial Solvent	21 H_2O	20 H_2O	23 H_2O	20 H_2O	20 H_2O	20 H_2O
μ/ mm^{-1}	0.758	0.757	0.754	0.749	0.741	0.741
Crystal Size/ mm^3	0.0376 × 0.0376 x 0.1692 ; reddish-purple prism					
2Θ Range for Data Collection/ °	2.298 to 63.346	4.13 to 60.604	2.58 to 59.81	4.11 to 55.654	4.096 to 53.152	4.102 to 44.156
Integration Resolution/ Å	0.74	0.77	0.78	0.82	0.87	1.03
Independent Reflections	29942 R_{int} = 0.0675 R_{sigma} = 0.0496	26610 R_{int} = 0.0684 R_{sigma} = 0.0466	25751 R_{int} = 0.1029 R_{sigma} = 0.0712	21345 R_{int} = 0.1084 R_{sigma} = 0.0680	18879 R_{int} = 0.0632 R_{sigma} = 0.0385	11170 R_{int} = 0.0723 R_{sigma} = 0.0364
Data/Restraints/ Parameters	29942 /29/1533	26610/23/1533	25751/24/1533	21345/28/1533	18879/19/1475	11170/19/1475
[b]GooF on F^2	1.043	1.039	1.041	1.041	1.073	1.089
[c,d]Final R Indexes [I>=2σ (I)]	R_1 = 0.0587 wR_2 = 0.1465	R_1 = 0.0562 wR_2 = 0.1387	R_1 = 0.0649 wR_2 = 0.1690	R_1 = 0.0623 wR_2 = 0.1617	R_1 = 0.0649 wR_2 = 0.1656	R_1 = 0.0741 wR_2 = 0.1813
[c,d]Final R Indexes [all data]	R_1 = 0.0932 wR_2 = 0.1754	R_1 = 0.0844 wR_2 = 0.1634	R_1 = 0.0972 wR_2 = 0.2046	R_1 = 0.0896 wR_2 = 0.1903	R_1 = 0.1011 wR_2 = 0.2020	R_1 = 0.1105 wR_2 = 0.2257
Largest Diff. Peak/Hole/ e Å^{-3}	1.89 / -0.89	1.57 / -0.73	2.06 / -1.08	1.40 / -0.82	1.40 / -0.66	1.20 / -0.54

Radiation = synchrotron (λ = 0.7749), α = γ = 90°, Z = 4, [a]*Calculated from SQUEEZE data.* [b]GooF: Goodness-of-fit = $\{\sum[w(F_o^2 - F_c^2)^2]/(n-p)\}^{1/2}$, where *n* is the number of reflections and *p* is the total number of parameters refined. [c]R = $\sum||F_o|-|F_c||/\sum|F_o|$. [d]*w*R = $\{\sum[w(F_o^2 - F_c^2)^2]/\sum w(F_o^2)^2]\}^{1/2}$.

Table 4-12. Void space and residual electron density for the humid Fe_3Ru_2 TBPs (7e), as calculated from SQUEEZE analysis. Interstitial solvent was calculated using the solver add-in in Excel 2013 by considering both the electron density and void space. Water was treated as occupying 40 Å.

Fe_3Ru_2 Humid	Void Space (Å)	Number of Electrons	% Void Space	H_2O/TBP SQUEEZE	H_2O/TBP Modeled
20 K	3019	1218	26.2	21.2	21.2
50 K	3029	922	26.3	19.8	21.3
100 K	3064	1463	26.4	22.6	21.4
150 K	3105	918	26.6	20.1	21.4
200 K	3158	870	26.8	20.1	22.0
250 K	3121	793	26.5	19.6	22.0
Average	**3083**	**1031**	**26.5**	**20.6**	**21.6**

electron densities in the void spaces. Below 150 K, finding the number of water molecules in the crystal using SQUEEZE data was more accurate when both the electron density and void space was taken into account. Above 150 K though, using just the residual electron density gave values closer to those obtained from modeling the disordered water in the structures (values are in Table 4-12). For the sake of consistency, both the electron density and void space were used for all temperatures and are reported here.

The M–L bond lengths for the humid crystal are in Table 4-13. The average Fe(1)–N and Fe(2)–N bond lengths from 20 K to 150 K steadily increase, indicating a gradual spin-transition is occurring at both the Fe(1) and Fe(2) centers. At 20 K, the Fe(3) center has an average Fe–N bond length indicative of an iron center between the LS and HS states. As the temperature increases to 250 K, the average Fe(3)–N bond length stays relatively stagnant with only a

minute lengthening in the distance. This suggests that the Fe(3) center is not undergoing a LS↔HS transition below 250 K. As with the other structures, the Ru–C bond distances are not distinct enough to interpret oxidation states of the ruthenium centers. When the TBP contains water in the interstitial sites though, a network of hydrogen bonding water molecules appear to occur between the terminal cyanide ligands on the ruthenium centers and neighboring TBP molecules. The asymmetric unit in Figure 4-7 shows the water molecules forming a hydrogen bonding network beginning at one of the terminal cyanide molecules (circled in pink). This network is formed on both sides of the dimeric unit (Figure 4-8). The extensive network of hydrogen bonding can clearly be seen in the packing diagram (Figure 4-9) when looking down the b-axis. Channels of solvent form around the dimeric unit in such a way that the intermolecular interaction between TBP molecules can easily be seen due to the absence of solvent near this site.

Table 4-13. M–L bond distances (in Å) for the humid Fe_3Ru_2 TBP (7e).

Temperature	Fe(1)–N	Fe(2)–N	Fe(3)–N	Ru(1)–C	Ru(2)–C
20 K	1.956(3)	1.894(3)	1.954(3)	2.053(4)	2.027(4)
	1.940(3)	1.895(3)	1.984(3)	2.002(4)	1.998(4)
	1.976(3)	1.978(3)	2.124(3)	1.967(4)	1.987(4)
	1.971(3)	1.967(3)	2.181(3)	2.058(4)	2.066(4)
	1.981(3)	1.972(3)	2.180(3)	2.068(4)	2.048(4)
	1.992(3)	1.978(3)	2.138(3)	2.039(4)	2.044(4)
Avg M–L	***1.969(3)***	***1.947(3)***	***2.094(3)***	***2.031(4)***	***2.028(4)***
50 K	1.958(3)	1.896(3)	1.956(3)	2.055(4)	2.025(3)
	1.936(3)	1.898(3)	1.983(3)	2.004(4)	1.999(4)
	1.979(3)	1.980(3)	2.122(3)	1.966(3)	1.988(4)
	1.972(3)	1.968(3)	2.185(3)	2.056(4)	2.068(4)
	1.981(3)	1.973(3)	2.179(3)	2.064(4)	2.043(4)
	1.992(3)	1.981(3)	2.143(3)	2.037(4)	2.039(4)
Avg M–L	***1.970(3)***	***1.949(3)***	***2.095(3)***	***2.030(4)***	***2.027(4)***
100 K	1.954(4)	1.892(4)	1.949(4)	2.056(5)	2.032(4)
	1.944(4)	1.895(4)	1.985(4)	2.003(5)	1.999(5)
	1.980(4)	1.985(4)	2.129(4)	1.960(4)	1.984(4)
	1.977(4)	1.967(4)	2.189(4)	2.056(5)	2.065(5)
	1.986(4)	1.976(4)	2.180(4)	2.061(5)	2.049(5)
	1.999(4)	1.982(4)	2.144(4)	2.038(5)	2.045(5)
Avg M–L	***1.973(4)***	***1.950(4)***	***2.096(4)***	***2.029(5)***	***2.029(5)***
150 K	1.954(3)	1.903(4)	1.957(4)	2.049(5)	2.025(4)
	1.942(4)	1.901(4)	1.990(4)	2.004(5)	2.000(5)
	1.994(4)	1.989(4)	2.130(4)	1.970(5)	1.994(5)
	1.990(4)	1.977(4)	2.189(4)	2.058(5)	2.071(5)
	2.001(3)	1.994(4)	2.181(4)	2.058(5)	2.045(5)
	2.006(4)	1.998(4)	2.152(4)	2.042(5)	2.040(5)
Avg M–L	***1.981(4)***	***1.960(4)***	***2.100(4)***	***2.030(5)***	***2.029(5)***
200 K	1.966(4)	1.947(5)	1.978(4)	2.012(5)	1.992(5)
	1.941(5)	1.938(5)	2.020(5)	1.997(6)	1.993(6)
	2.057(4)	2.044(5)	2.134(4)	1.992(5)	2.006(6)
	2.072(4)	2.032(6)	2.196(4)	2.059(7)	2.069(6)
	2.084(4)	2.050(5)	2.188(4)	2.056(6)	2.046(6)
	2.060(4)	2.053(5)	2.153(4)	2.048(6)	2.033(6)
Avg M–L	***2.030(4)***	***2.011(5)***	***2.112(4)***	***2.027(6)***	***2.023(6)***
250 K	1.972(8)	1.972(10)	1.991(8)	1.989(11)	1.947(11)
	1.922(9)	1.952(09)	2.043(9)	1.972(12)	1.987(11)
	2.117(7)	2.087(09)	2.123(8)	2.004(11)	2.009(11)
	2.132(7)	2.088(10)	2.215(7)	2.033(13)	2.071(12)
	2.145(6)	2.081(10)	2.187(8)	2.066(11)	2.066(13)
	2.110(7)	2.098(08)	2.156(7)	2.048(12)	2.014(14)
Avg M–L	***2.066(7)***	***2.046(09)***	***2.119(8)***	***2.019(11)***	***2.016(12)***

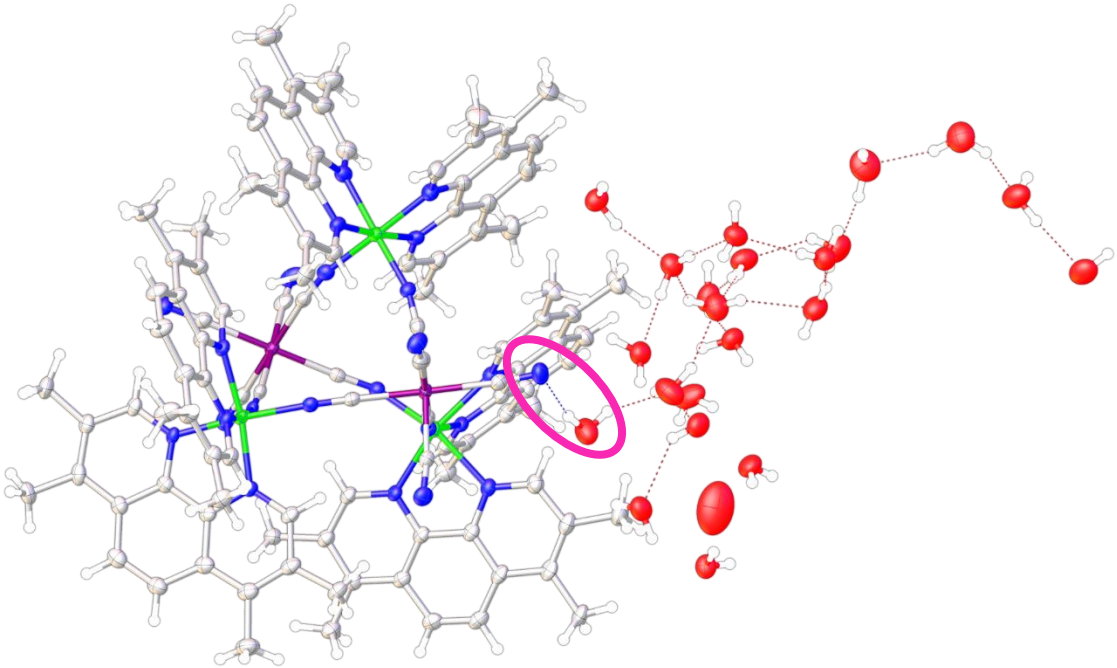

Figure 4-7. The asymmetric unit of the Fe_3Ru_2 TBP left in a humid environment for a day. The pink circle highlights the hydrogen bond to a terminal cyanide ligand. Color code: Fe is green, Ru is violet, C is gray, N is blue and O is red. The dashed lines represent hydrogen bonds.

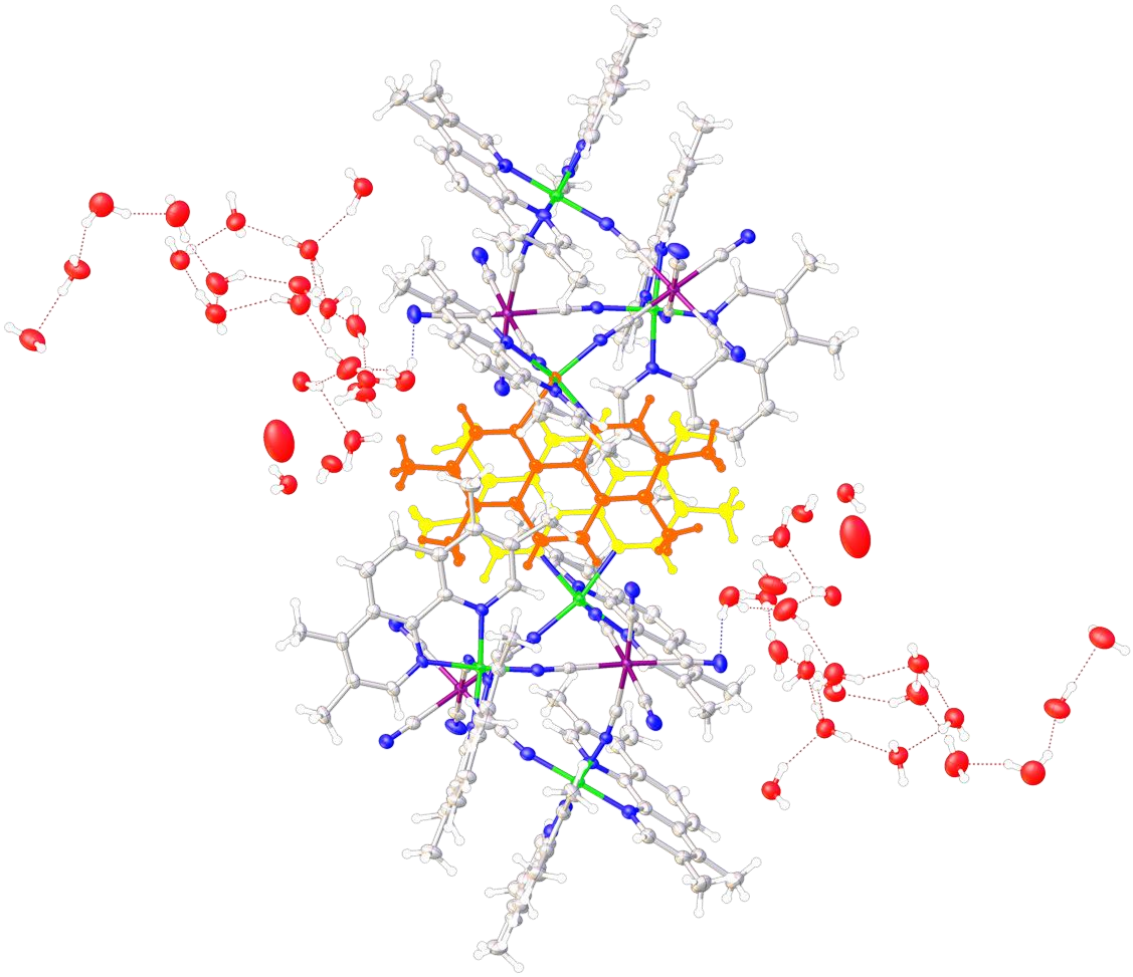

Figure 4-8. Dimeric unit of 7e at 50 K. The orange and yellow tmphen ligands are on opposite Fe(3) centers involved in π-π stacking. Water forms a hydrogen bonding network with a cyanide ligand on the Ru(2) center. Color code: Fe is green, Ru is violet, C is gray, N is blue and O is red. The orange and yellow tmphen ligands are the ones involved in the intermolecular interactions in the dimeric unit. The dashed lines represent the hydrogen bonds.

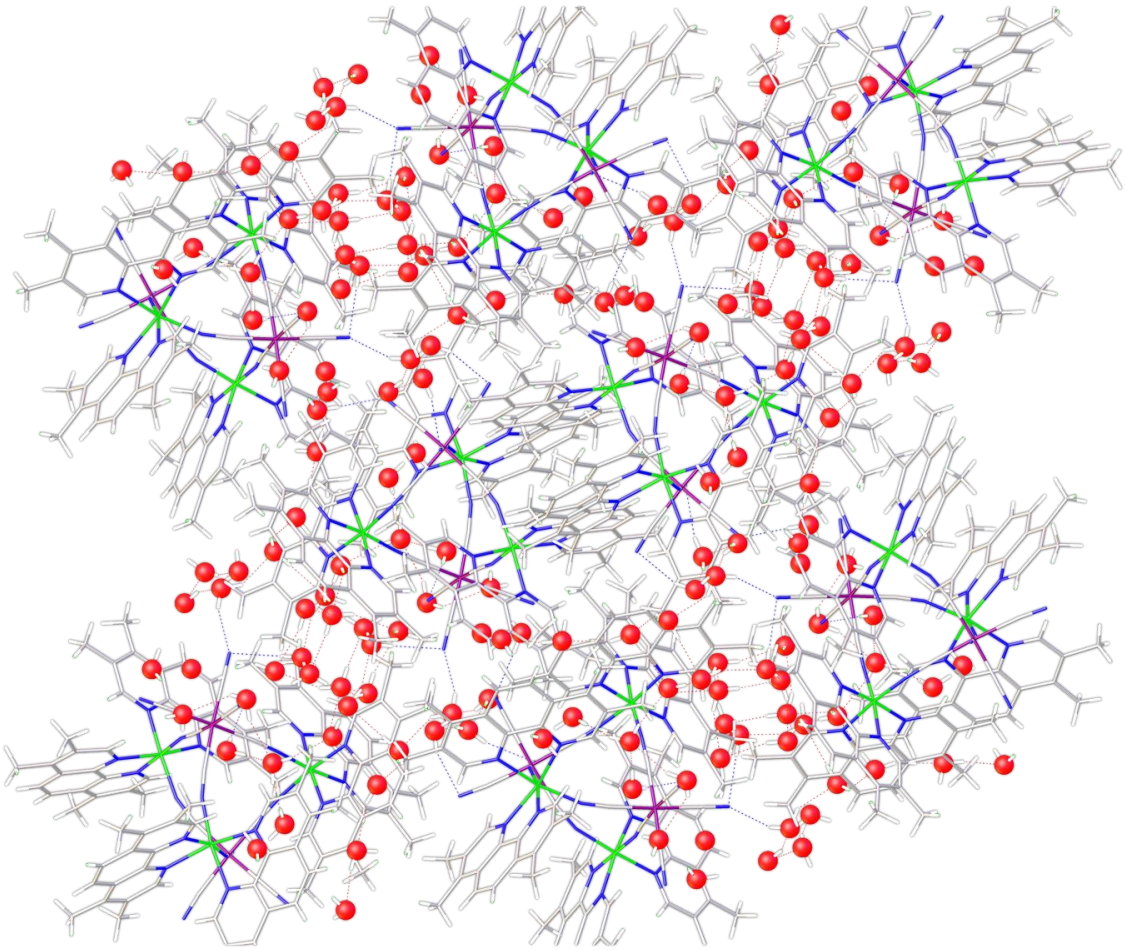

Figure 4-9. Packing diagram of 7e looking down the b-axis. Color code: Fe is green, Ru is violet, C is gray, N is blue and O is red. The dashed lines represent the hydrogen bonds.

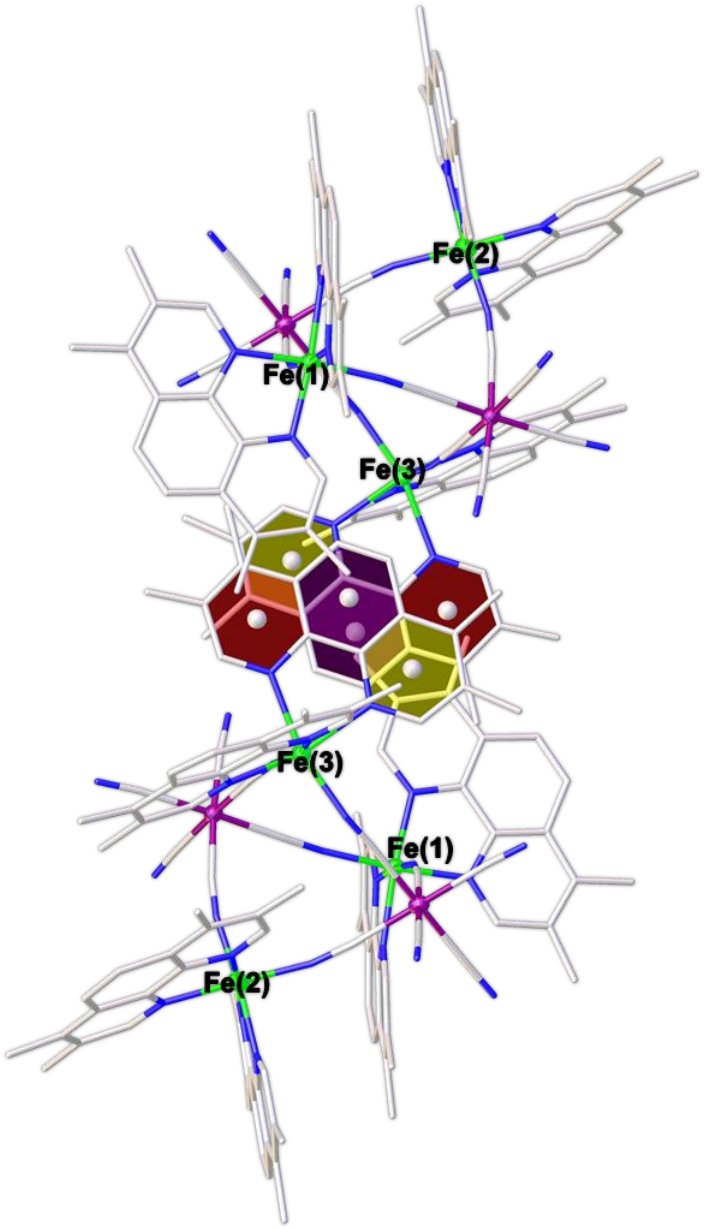

Figure 4-10. View of the humid Fe_3Ru_2 TBP (7e) at 20 K stacking in a dimeric unit due to the intermolecular π-π stacking interactions between neighboring TBP molecules. The purple and yellow planes highlight the rings within the tmphen ligands that are common between all of the structures discussed. The maroon plane highlights the additional interaction found only in this solvation state at this temperature. Color code: Fe is green, Ru is violet, C is gray and N is blue. Hydrogen and solvent have been omitted for the sake of clarity.

An interesting difference between the humid structure at 20 K and all other structures analyzed, are the intermolecular π-π stacking interactions. The 20 K structure has the same intra- and intermolecular interactions as the other samples with the exception that the Olex2 software detects an additional intermolecular interaction with the third ring in the tmphen ligands on the Fe(3) centers already involved in the inter-pp and inter-py interactions. Figure 4-10 shows the overlap between the two symmetrically related tmphen ligands at 20 K. The additional intermolecular interaction between the third ring in the tmphen ligands (maroon-colored planes in Figure 4-10) and the yellow-colored planes on the inversely symmetrical tmphen ligands will be referred to as inter-my. The π-π stacking parameters obtained for the different temperatures of the humid Fe_3Ru_2 TBP are given in Table 4-14. The additional intermolecular interaction at 20 K (inter-my) has a centroid-centroid distances of 3.992 Å. This value is practically at the limit of what Olex2 defines as a π-π interaction and is longer than the usually accepted distance of 3.8 Å, so a slight displacement of the tmphen ligand would make this interaction undetectable by the employed analysis methodology. As with the other structures analyzed, the strongest interaction is inter-pp. The inter-py interaction is slightly stronger than in the humid structures than in the other samples while the intra-tt interaction is slightly weaker. No correlation of temperature dependence with the centroid-centroid distances can be made as there is no clear variation in the values. In contrast to the solvated structures, the humid structures seem to mirror the expansion and increased twisting between the planes of the

Table 4-14. Geometric parameters (centroid-centroid distance, shift distance and angle) for the inter- and intramolecular π-π stacking interactions in the humid Fe_3Ru_2 TBPs (7e). The average values (avg) and the differences between the minimum and maximum values (Δ) have been included. *Indicates symmetry equivalent metal center.

Interaction-Plane Fe Centers Involved	Temperature	Centroid-Centroid Distance (Å)	Shift Distance (Å)	Angle (º)
inter-pp Fe(3)–Fe(3)*	20 K	3.519	0.847	0
	50 K	3.521	0.85	0
	100 K	3.521	0.85	0
	150 K	3.527	0.869	0
	200 K	3.542	0.932	0
	250 K	3.544	0.922	0
	Avg	**3.529**	**0.878**	**0**
	Δ	*0.025*	*0.085*	*0*
inter-py Fe(3)–Fe(3)*	20 K	3.738	1.598	1.09
	50 K	3.74	1.59	0.829
	100 K	3.74	1.59	0.829
	150 K	3.733	1.559	0.682
	200 K	3.694	1.478	1.169
	250 K	3.711	1.484	0.888
	Avg	**3.726**	**1.550**	**0.914**
	Δ	*0.046*	*0.120*	*0.487*
inter-my Fe(3)–Fe(3)*	20 K	**3.992**	**2.198**	**4.124**
intra-tt Fe(1)–Fe(2)	20 K	3.931	1.614	7.09
	50 K	3.942	1.598	6.764
	100 K	3.942	1.598	6.764
	150 K	3.946	1.578	7.191
	200 K	3.94	1.508	7.264
	250 K	3.963	1.434	6.192
	Avg	**3.944**	**1.555**	**6.877**
	Δ	*0.032*	*0.180*	*1.072*
intra-yy Fe(2)–Fe(3)	20 K	3.788	1.335	3.596
	50 K	3.795	1.347	3.831
	100 K	3.795	1.347	3.831
	150 K	3.795	1.113	3.91
	200 K	3.806	1.335	4.279
	250 K	3.832	1.299	4.236
	Avg	**3.802**	**1.296**	**3.947**
	Δ	*0.044*	*0.234*	*0.683*

intra-tt interaction as well as the contraction and decreased twisting between the planes in the intra-yy interactions as exhibited in the 24 hour structure.

Upon comparing the average Fe–N bond lengths for all of the compounds discussed in this section, it becomes evident that the Fe(2) centers in the humid and solvated compounds have similar average Fe–N bond lengths to each other between 20 – 250- K. The Fe(3) centers also have similar bond lengths throughout that temperature range when comparing the solvated and humid samples to each other. A graph of the average Fe–N bond distances for all temperatures of the solvated, 24 hour and humid compounds (Figure 4-11) illustrates this similarity in the Fe centers between samples. This suggests that they behave similarly as far as the spin-transition is concerned. The Fe(2) centers (circles in Figure 4-11) in both compounds are clearly undergoing a gradual spin transition with thermal perturbation, as indicated by the increase in the bond lengths. The Fe(3) centers (squares in Figure 4-11) in these compounds stay relatively unchanged at a bond distance typical for an iron center between a LS and HS state. The difference between the solvated and the humid TBPs, as far as the bond lengths are concerned, comes from the Fe(1) centers (triangles in Figure 4-11). In the compound containing MeCN, the Fe(1) center behaves similarly to the Fe(3) and the bond length remains relatively stable up to 250 K. For the humid sample however, the Fe(1) center behaves more like the Fe(2) center and shows a lengthening in the bond distances above 100 K. At low temperatures, the humid sample contains two Fe centers in a LS state that are undergoing a gradual spin-

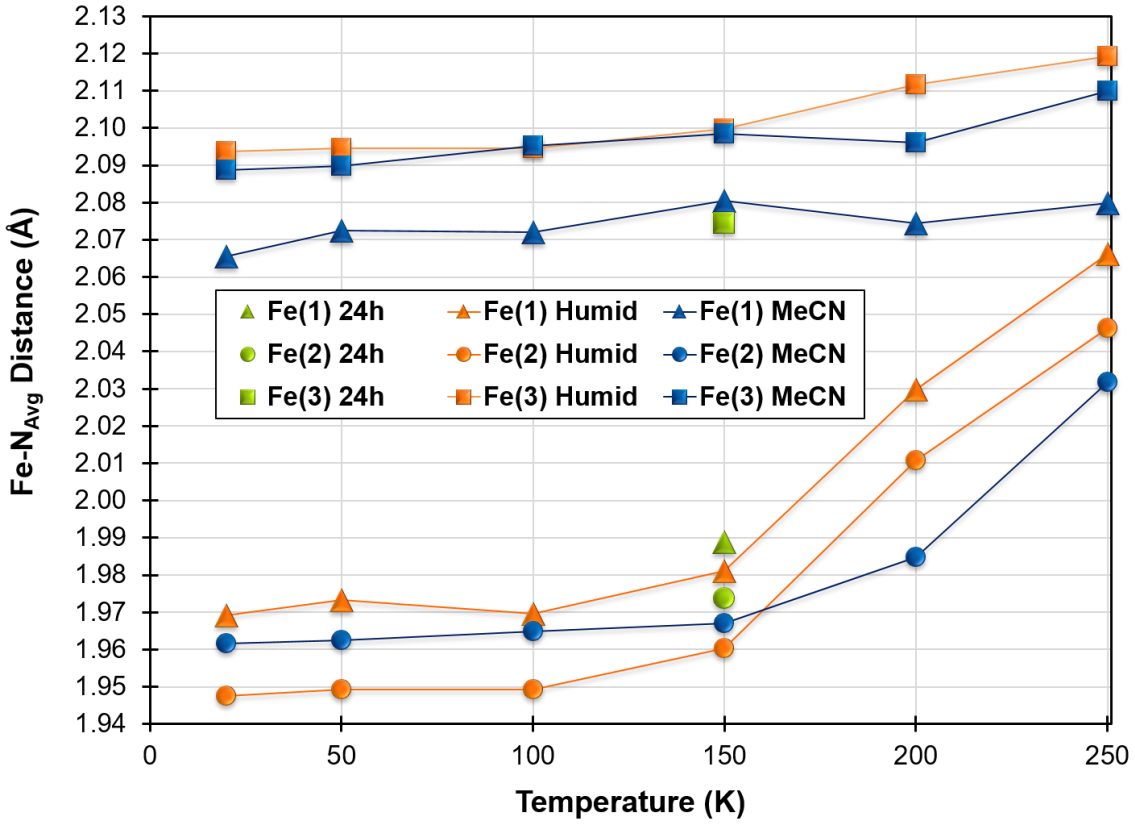

Figure 4-11. Graph of average Fe–N bond lengths for all temperatures of 7a (blue markers and lines), 7d (green markers) and 7e (orange markers and lines). The triangles represent the Fe(1) centers, the circles represent the Fe(2) centers and the squares represent the Fe(3) centers for each compound.

transition above 100 K while the MeCN sample only has one Fe center exhibiting this behavior. This comparison suggests that these two TBPs exhibit different types of spin-transition behaviors. With only obtaining data at one temperature with the evacuated sample, nothing can be determined from structural data as to whether a change in temperature has an effect on the Fe–N bond lengths. It can be said, however, that at 150 K the Fe centers in the evacuated sample that

contains more water than the humid sample have bond lengths for each Fe center that correspond well with those found in the humid sample.

Overall, the Fe_3Ru_2 TBP has similar structural data to the isostructural Fe_3Fe_2 and Fe_3Os_2 congeners reported previously.[116,145] The Fe_3Fe_2 crystal data at 110 K have average Fe-N bond lengths consistent with three LS Fe centers, which is in agreement with the magnetic data showing concurrent SCO events that start above 110 K. For the Fe_3Os_2 TBP it was found that the Fe(1) and Fe(3) centers undergo a $\Delta d_{(Fe\text{-}N)} \approx 0.2$ Å, consistent with a LS ↔ HS transition of some type. It was determined through ^{57}Fe Mössbauer and magnetic data that this was due to CTIST events. The Fe(2) center remained relatively unchanged between 110 and 300 K.

Magnetic Properties

These compounds are made with trivalent ruthenium and divalent iron metals at room temperature. If these oxidation states are unchanged when the TBP forms, an $Fe^{II}_3Ru^{III}_2$ electronic configuration is expected. Temperature dependent DC susceptibility (χT) values expected for HS Fe^{II} (d^6) in an octahedral coordination environment can vary from a spin-only value of 3.0 emu·K/mol (less likely) to ~3.8 emu·K/mol for compounds with larger Landé g-factors due to the additional angular momentum contribution stemming from the S = 2 electronic configuration.[65] No contribution to χT is expected for LS Fe^{II} (d^6) in an octahedral coordination environment as it is diamagnetic due to its t_{2g}^6 electronic

configuration. This means that for an Fe^{II} center to undergo a LS ↔ HS SCO event, a Δ ~3.0 – 3.8 emu·K/mol is expected. For octahedral Ru^{III} ions, a spin-only χT value of 0.375 emu·K/mol is expected, but can decrease to ~0.27 emu·K/mol as the g-factor decreases, as it commonly does for these S = ½ ions.[168-170,187] Ruthenium surrounded by a strong-field ligand such as cyanide will not undergo SCO. However, as it was shown in Chapter 3, $[Ru^{III}(CN)_6]^{3-}$ can be reduced to $[Ru^{II}(CN)_6]^{4-}$ in TBP compounds, just as it was in the Co_3Ru_2 TBP. This will result in a diamagnetic t_{2g}^6 electronic configuration of the Ru^{II} center and consequently, no contribution to χT. If a charge transfer does occur between an Fe^{II} and Ru^{III} center, several configurations are possible due to the SCO capability of iron in an all nitrogen, octahedral coordination environment. Charge-wise, an Fe^{III}–Ru^{II} pair will result. Owing to the nature of $Fe–N_6$ to undergo SCO, the resulting pair could be LS Fe^{III}–Ru^{II} or HS Fe^{III}–Ru^{II}. Generally, if a SCO is possible and a charge transfer event occurs between two bridging metal centers, the two events occur concomitantly with each other and is termed a charge-transfer-induced spin transition (CTIST). The outcome of this being that the only electronic configurations possible are LS Fe^{II}–Ru^{III} ↔ HS Fe^{III}–Ru^{II}, as was seen in the Fe_3Os_2 congener,[116] or HS Fe^{II}–Ru^{III} ↔ LS Fe^{III}–Ru^{II}, the latter being very unlikely in this case (vide infra). The CTIST phenomena is still relatively understudied as it has only occurred in a limited number of compounds.[215] If the SCO doesn't occur at all, then the other possible transitions allowed due to charge-transfer are LS Fe^{II}–Ru^{III} ↔ LS Fe^{III}–Ru^{II} or HS Fe^{II}–Ru^{III} ↔ HS Fe^{III}–Ru^{II}. To the best of my

knowledge, an instance where the charge-transfer and SCO were not concomitant events in the overall spin-transition of a compound has not been reported. This being said, a LS Fe^{III} center (t_{2g}^5 electronic configuration) will be spin one-half (S = ½) with a χT value around 0.375 emu·K/mol and a HS Fe^{III} center ($t_{2g}^3e_g^2$) will have a χT value around 4.375 emu·K/mol. These spin-only values can fluctuate slightly when orbital angular momentum is taken into account. Table 4-15 represents the typical values of χT expected for the possible electronic configurations of the Fe and Ru centers discussed above and Table 4-16 is the change in the spin-only values of χT based upon the type of transition possible in this molecule. If the change in configuration is due to a charge transfer, the χT values associated with the change in the ruthenium center must also be accounted for. The first column is the ΔχT expected if just the iron center is considered. The second column is the overall change in χT when the ruthenium is taken into account.

Table 4-15. Typical and spin-only χT values and electronic configurations of Fe and Ru.

Metal Center Configuration	Electronic O_h Configuration	Total Spin	Range of Typical χT Values (emu·K/mol)	Spin-Only χT Values (emu·K/mol)
LS Fe^{II} (d^6)	t_{2g}^6	S = 0	0	0.000
HS Fe^{II} (d^6)	$t_{2g}^4e_g^2$	S = 2	3.0 – 4.3	3.000
LS Fe^{III} (d^5)	t_{2g}^5	S = ½	0.36 – 0.41	0.375
HS Fe^{III} (d^5)	$t_{2g}^3e_g^2$	S = ⅝	4.36 – 5.29	4.375
LS Ru^{II} (d^6)	t_{2g}^6	S = 0	0	0.000
LS Ru^{III} (d^5)	t_{2g}^5	S = ½	0.29 – 0.38	0.375

Table 4-16. Types of spin-transitions possible in the Fe_3Ru_2 TBP. The spin-only values of χT are used for the Δ values. If a charge transfer (CT) is involved, then the ΔχT associated with the Ru is included in the last column.

Possible Electronic Transitions	Type of Transition	ΔχT (Fe Only) (emu·K/mol)	Total ΔχT (Ru Included) (emu·K/mol)
LS Fe^{II} ↔ HS Fe^{II}	SCO	3.0	3.0
LS Fe^{II} ↔ LS Fe^{III}	CT	0.375	0.0
LS Fe^{II} ↔ HS Fe^{III}	CTIST	4.375	4.0
HS Fe^{II} ↔ HS Fe^{III}	CT	1.375	1.0
LS Fe^{III} ↔ HS Fe^{III}	SCO	4.0	4.0

Fe_3Ru_2 Solvated (7a)

When the Fe_3Ru_2 TBP is measured under MeCN, the temperature-dependent susceptibility data (Figure 4-12) indicate that a spin-transition occurs in the molecule. At room temperature, when taking a g-factor of 2.1 for Fe^{II} and 1.9 for Ru^{III} into account, the χT value of 10.6 emu·K/mol is consistent with a SCO event occurring in all three Fe^{II} centers. This results in a TBP configuration of three HS Fe^{II} centers and two LS Ru^{III} centers, $[(HS\text{-}Fe^{II})_3Ru^{III}_2]$. Unfortunately, this value is also consistent with other electronic configurations when other g-factors are taken into account. EPR was collected on these molecules but the data for these complex molecules were inconclusive and will not be discussed. It is also possible that the TBP exhibits a $[(HS\text{-}Fe^{II})_2(HS\text{-}Fe^{III})Ru^{II}Ru^{III}]$ electronic configuration, owing to an electron charge-transfer between an Fe^{II} and Ru^{III} center. This configuration would be similar to the Fe_3Os_2 congener at room temperature with the exception that one of the Fe^{II} sites is HS instead of LS. This

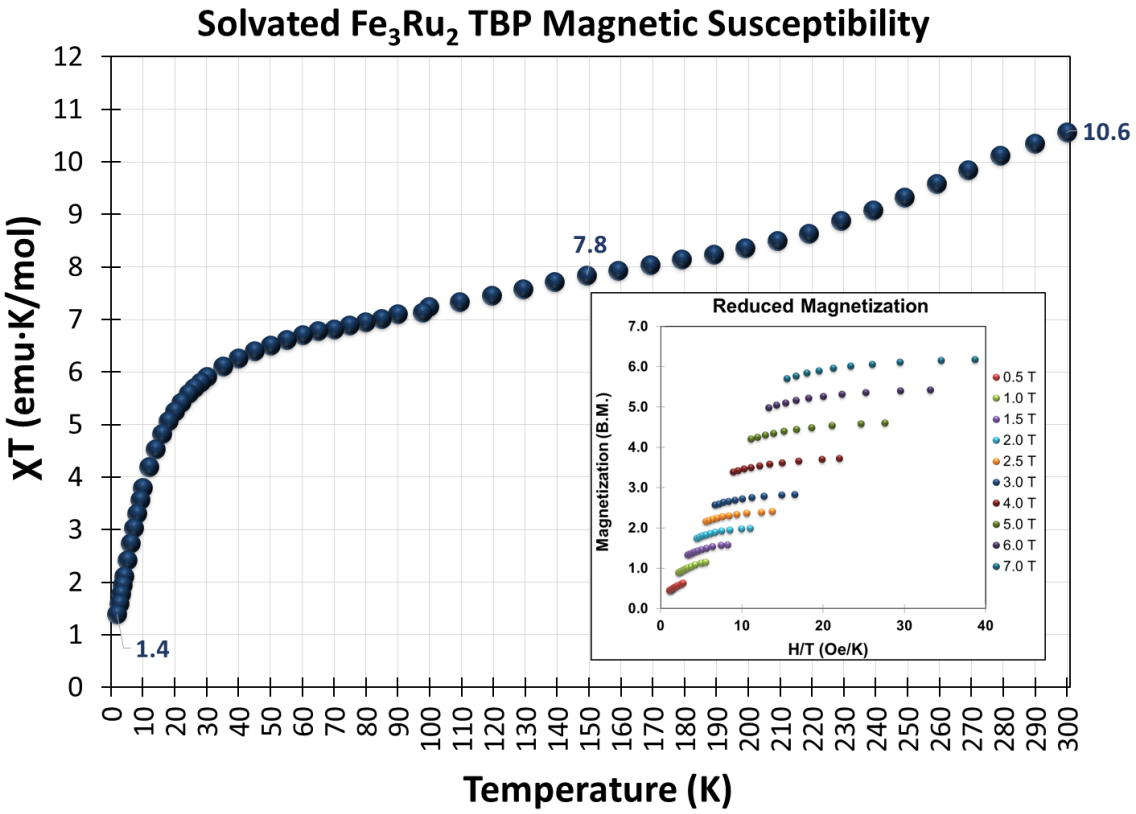

Figure 4-12. Temperature-dependent susceptibility data for the Fe_3Ru_2 TBP measured under MeCN (**7a**). The inset is the reduced magnetization data.

however, is a reasonable configuration in comparison to the Fe_3Os_2 congener considering there is about a 3 emu·K/mol difference in χT between the two analogs at room temperature, with the Fe_3Ru_2 TBP having the larger χT value. Another reasonable assumption is that both Ru centers were reduced upon formation of the TBP, like in the Co_3Ru_2 analog. This results in a configuration somewhere between $[(LS\text{-}Fe^{II})(HS\text{-}Fe^{III})_2Ru^{II}_2]$ exhibited by the Fe_3Os_2 analog at 350 K and $[(HS\text{-}Fe^{II})(HS\text{-}Fe^{III})_2Ru^{II}_2]$. These four scenarios are the most probable, as the other M_3Ru_2 TBPs and M_3Os_2 congeners studied suggest. These four

configurations allow for a χT value between ~8.5 – 12 emu·K/mol when moderate Landé g-factors are used. As temperature is decreased, the χT curve decreases ~4 emu·K/mol very gradually until about 50 K where χT is 6.5 emu·K/mol. Below 50 K, the decrease is much more rapid and changes by 5.1 emu·K/mol as 2 K is reached (1.4 emu·K/mol). From 300 K to 150 K, the gradual decrease in susceptibility of 3 emu·K/mol indicates that a HS ↔ LS transition at an Fe^{II} center is occurring within this molecule. At 2 K, with such a small paramagnetic signal (1.4 emu·K/mol), the more reasonable spin and oxidation states are for a $[(LS\text{-}Fe^{II})_3Ru^{III}_2]$ configuration (0.75 emu·K/mol) with a small percentage of remnant HS Fe^{II}. Reduced magnetization data (inset of Figure 4-12) is of little help in determining the ground state of the TBP as it lacks any form of saturation and is a straight line nearing 6 B.M., indicating the presence of low lying excited states. For a $[(LS\text{-}Fe^{II})_3Ru^{III}_2]$ configuration, one would expect magnetization data to saturate near 2 B.M. The splitting of the iso-field lines do indicate an appreciable amount of anisotropy present in the TBP though. The lack of saturation is generally due to low lying excited states. If the $[(LS\text{-}Fe^{II})_3Ru^{III}_2]$ ground state configuration is considered along with the possible room temperature configurations discussed earlier, it can be said that overall, the molecule is either undergoing three Fe SCO events, one CTIST and two SCO events or one SCO and two CTIST events. Without ^{57}Fe Mössbauer data, assignment of the TBP electronic configuration and the phenomena occurring is just speculation. Mössbauer data will be discussed in the next section.

Fe_3Ru_2 Filtered (7b)

Ultimately, the point of preparing and measuring the filtered sample was to see if a simple lab technique of separating the product from the mother liquor could alter the magnetic behavior of it. Filtering is a common technique and is rarely given a second thought when it comes to collecting the product. Figure 4-13 shows the difference in χT between a sample measured under MeCN and a sample that had been filtered, briefly. Both the χT curvature and values along with the reduced magnetization data are fairly consistent with the sample measured under solvent. This suggests that filtering the sample in a way that doesn't pull off interstitial solvent will result in the same spin transition behavior as a sample measured under solvent. The data also suggests that measuring the sample under the mother liquor does not impose a chemical pressure on the sample, which usually leads to an altering of the spin transition behavior in these samples. The filtered sample was measured to 350 K and the data shows the very gradual spin transition continues, with no sign of a plateau.

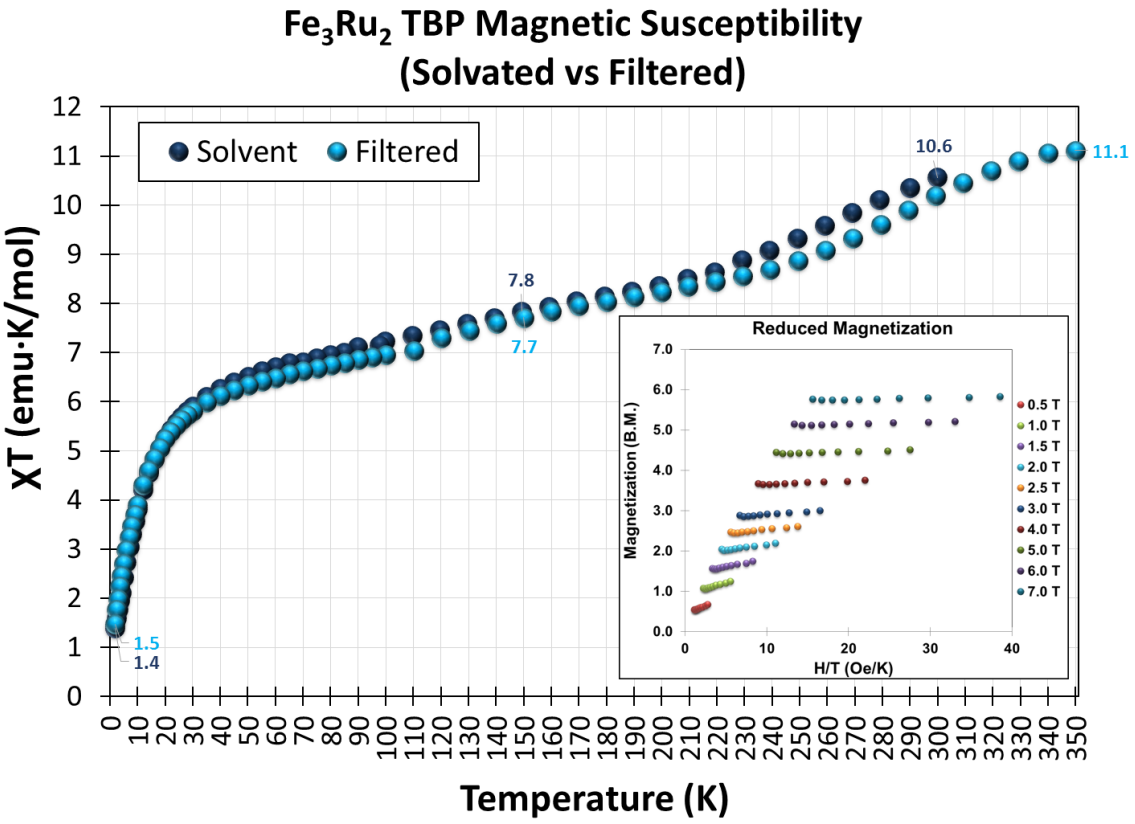

Figure 4-13. Temperature dependence of χT for the solvated (7a – dark blue circles) and filtered (7b – light blue circles) Fe_3Ru_2 TBPs. This filtered sample is easily recognized as it is measured up to 350 K. The inset is the reduced magnetization for the filtered sample.

Fe_3Ru_2 3 Hours (7c)

The susceptibility data at 300 and 350 K (Figure 4-14) is about 3 emu·K/mol higher than the solvent/filtered samples (13.3 and 13.6 emu·K/mol, respectively) The only electronic configuration that would result in such a large value of χT is $[(HS\text{-}Fe^{II})(HS\text{-}Fe^{III})_2Ru^{II}_2]$. As stated earlier, the expected spin-only value for this state is 11.75 emu·K/mol with a total of fourteen unpaired electrons. The susceptibility data suggests that larger g values are at play here. The decrease in χT with decreasing temperature is slightly more cooperative than in the solvated and filtered samples. By the time 150 K is reached, the χT decreases 4 emu·K/mol, suggesting that either a SCO at the Fe^{II} or one of the Fe^{III} centers has occurred or that a CTIST has taken place. As temperature is continually decreased, another spin transition is evident by the rapid decrease in χT between 50 and 2 K, with a $\Delta \cong 6$ emu·K/mol. As with the solvated and filtered samples, the χT data at 2 K suggests that the TBP is leading to ground state configuration of $[(LS\text{-}Fe^{II})_3Ru^{III}_2]$. Reduced magnetization data for the 3 hour sample is nearly identical to the filtered and solvated samples in that it lacks any suggestion of saturation and is a straight line up to ~6 B.M. The anisotropic splitting of the iso-field lines are similar to the previous samples as well. Again, without Mössbauer data, assignment of the TBP configuration between 2 K and 350 K is speculative and a non-trivial task.

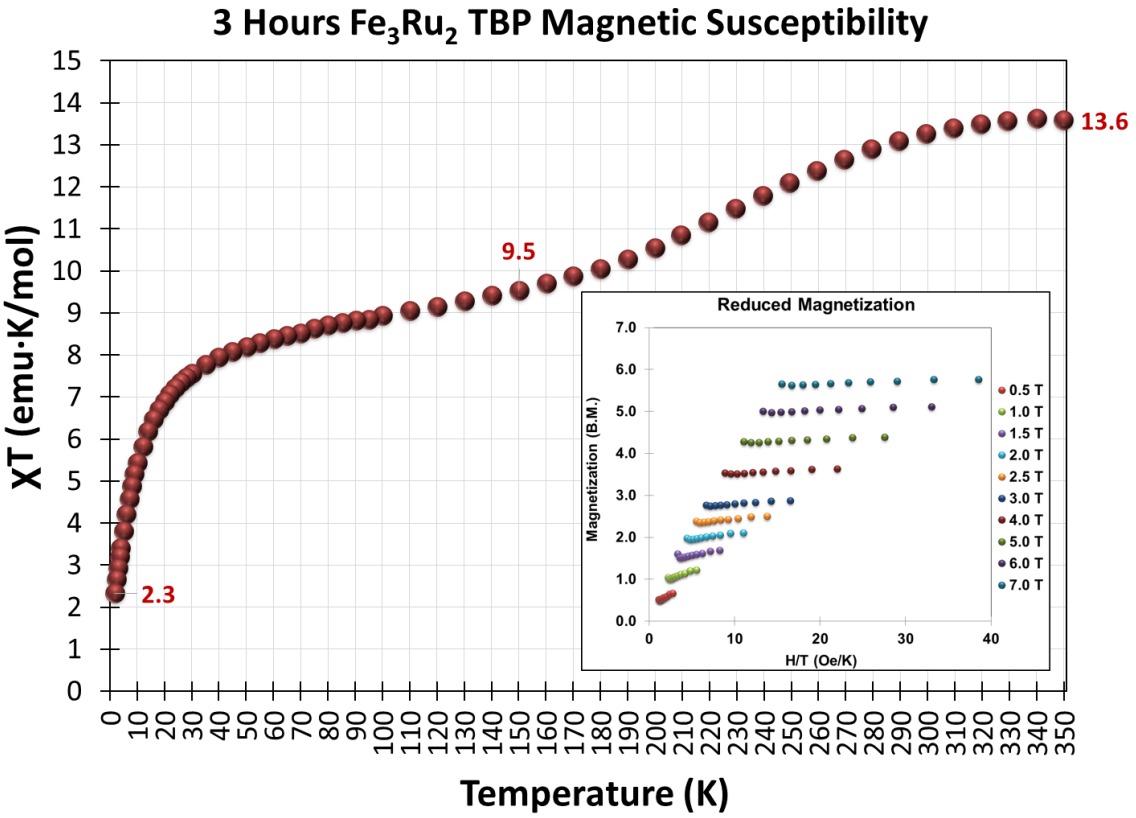

Figure 4-14. Temperature dependent susceptibility of the Fe_3Ru_2 TBP put under vacuum for three hours. Inset: reduced magnetization data for the sample.

Fe_3Ru_2 24 Hours (7d)

Similarly to the sample put under vacuum for three hours, the sample put under vacuum for twenty-four hours has a very telling TBP configuration at 350 K due to its large χT value in Figure 4-15. Between 300 and 350 K the curve of the spin transition appears to plateau at 14.5 emu·K/mol, an even higher value than in the 3 hour sample. Just like in the previous samples, the most reasonable state of the TBP at 350 K is $[(HS\text{-}Fe^{II})(HS\text{-}Fe^{III})_2Ru^{II}_2]$ and at 2 K is $[(LS\text{-}Fe^{II})_3Ru^{III}_2]$ from the value of χT at these two temperatures. As temperature is decreased from

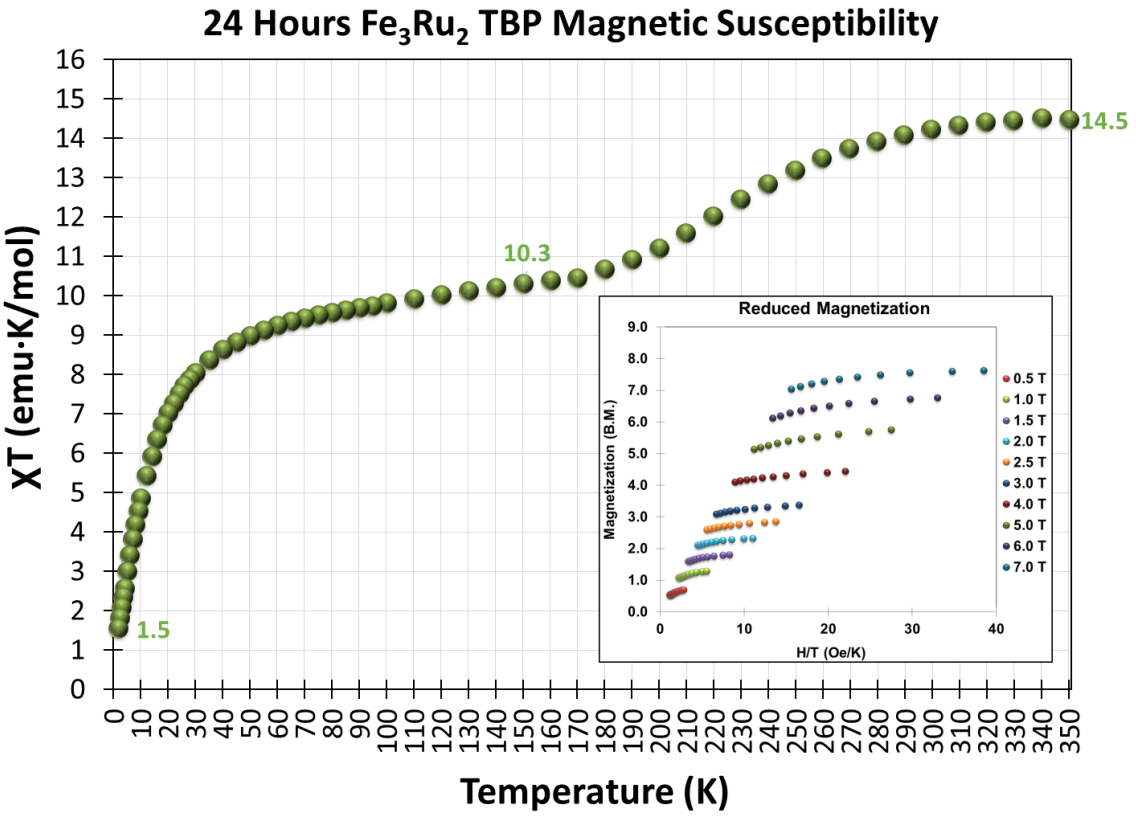

Figure 4-15. Temperature dependent χT curve for the Fe_3Ru_2 TBP (7d) exposed to vacuum for 24 hours prior to measurement. Inset: reduced magnetization data for the compound.

350 – 150 K, a spin transition is evident with a gradual decrease in χT from 14.5 to 10.3 emu·K/mol, a similar value to the solvated and filtered samples at 300 K. This change of ~4 emu·K/mol in χT could be due to either SCO or CTIST but is most likely the result of a HS → LS SCO on the Fe^{II} center owing to the fact that the second transition step in the χT curve (between 150 – 2 K) is much larger than in previous samples and accounts for two transitions. From 150 K to 2 K, the second transition step occurs with a change of nearly 9 emu·K/mol, which is

consistent for two CTIST events from HS Fe^{III} → LS Fe^{II}. Considering the high-temperature configuration of $[(HS\text{-}Fe^{II})(HS\text{-}Fe^{III})_2Ru^{II}_2]$ and the ground state for the TBP most likely being $[(LS\text{-}Fe^{II})_3Ru^{III}_2]$ (as the small value of χT suggests) there are two CTISTs and one SCO event that must take place as temperature is decreased from 350 to 2 K. It makes more chemical sense if the transitions that occur simultaneously are of the same type. Reduced magnetization data in the inset of Figure 4-15 is very similar to the previous samples except that it is a straight line nearing 8 B.M. instead of 6 B.M.

Fe_3Ru_2 Humid (7e)

Out of the five different solvation states studied for this compound, the humid sample has a more distinct susceptibility curve from 2 – 350 K (Figure 4-16). Whereas the samples under vacuum have a transition step on either side of ~120 K, the humid sample has the transition steps on either side of ~70 K. resulting in the higher temperature transition in the humid sample to begin at a lower temperature than the similar transitions in the other samples. At 350 K, 7e has a similar χT value to the filtered sample, and most likely has a very similar electronic configuration tending to $[(HS\text{-}Fe^{II})(HS\text{-}Fe^{III})_2Ru^{II}_2]$. The most noticeable difference between the previous four samples and this one, other than the lower transition temperature and the change in cooperativity of the transitions, is the ground state. At 2 K the χT value is 3.5 emu·K/mol instead of 1.5 emu·K/mol Reduced magnetization for the humid sample is also notably different in that the

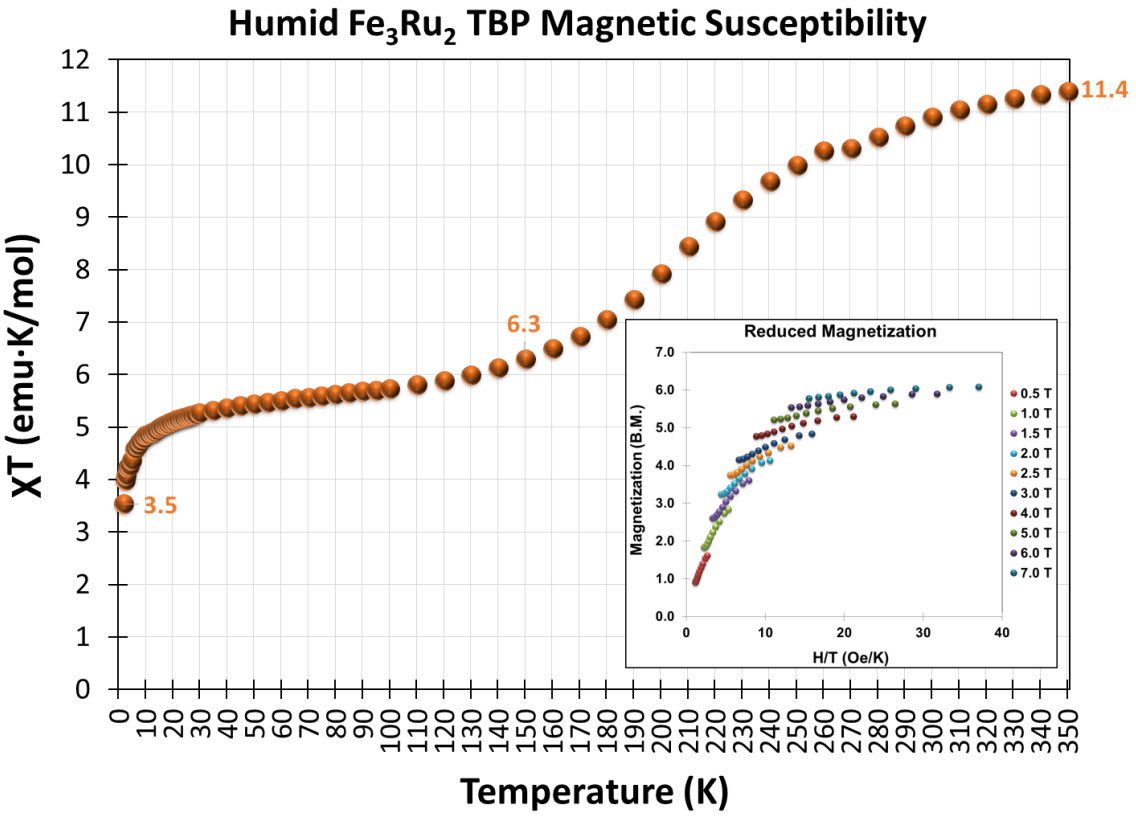

Figure 4-16. Temperature dependent susceptibility of the water-containing Fe_3Ru_2 TBP (7e). The reduced magnetization for this humid sample can be found in the inset.

splitting of the iso-field lines is much smaller, indicating a decrease in the anisotropy of the compound. If the ground states in the previous samples have been assigned correctly and the TBP is mostly in the $[(LS\text{-}Fe^{II})_3Ru^{III}_2]$ state, then the inherent anisotropy found in these complexes are most likely coming from the Ru^{III} centers due to LS Fe^{II} being diamagnetic. The decrease in anisotropy in the humid sample suggests a decrease in the amount of Ru^{III} present in the ground state. Taking the decrease in anisotropy into account, as well as the higher value

of χT, it can be argued that the water has caused a change in the ground state of the TBP to $[(LS\text{-}Fe^{II})_2(LS\text{-}Fe^{III})Ru^{II}Ru^{III}]$. With this configuration at low temperatures and $[(HS\text{-}Fe^{II})(HS\text{-}Fe^{III})_2Ru^{II}{}_2]$ at higher temperatures, it can be said that this TBP exhibits one reversible CTIST event and one SCO event on an Fe^{III} center that is a result of an irreversible charge-transfer between Fe^{II} and Ru^{III} during formation of the TBP. It is well known that Fe^{II} salts will often oxidize to Fe^{III} in air with time and rapidly oxidize to Fe^{III} in the presence of moisture. The fact that these crystals seem to contain only water in the interstitial sites now, could be a factor as to why only one CTIST occurs as temperature is decreased. Although it seems that hexacyanoruthenate seems to prefer a trivalent oxidation state at low temperatures in the Fe_3Ru_2 TBPs, when water is in the interstitial sites one of the Ru centers remain in a divalent oxidation state which could be due to the hydrogen bonding of the water molecules to the terminal cyanide ligands of the Ru center ultimately changing the redox properties of the ruthenium. Figure 4-17 is a comparison of the temperature dependent susceptibility data for all five solvation states studied and demonstrates that changes in the lattice due to solvent can cause non trivial changes in the spin-transition of the Fe_3Ru_2 TBP.

Upon comparing the magnetic data with the Fe_3Fe_2 and Fe_3Os_2 congeners, clear differences and similarities are noticed. Below 100 K, the susceptibility data for the Fe_3Fe_2 TBP containing water as the interstitial solvent (analogous to the humid Fe_3Ru_2 sample) is consistent with an electronic configuration of $[(LS\text{-}Fe^{II})_3(LS\text{-}Fe^{III})_2]$. As temperature is increased to 375 K, the χT value

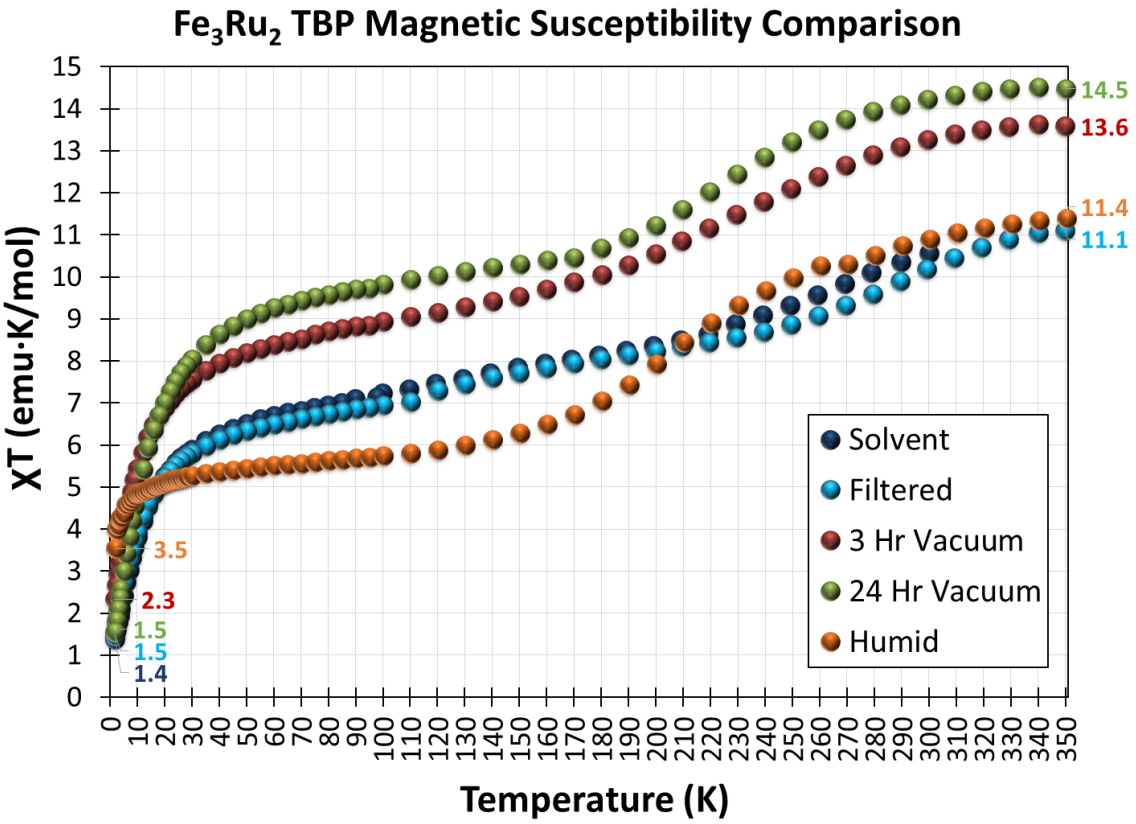

Figure 4-17. A comparison of spin-transition curves exhibited in the temperature dependent χT data of Fe_3Ru_2 TBPs with different levels of solvation.

increases ~9 emu·K/mol due to three gradual SCO events occurring on the three Fe^{II} centers simultaneously. When the Fe_3Fe_2 TBP was measured under MeCN (analogous to the solvated Fe_3Ru_2 TBP), the SCO events begin to occur just below 100 K and are slightly more gradual in nature than in the water-containing sample. The fact that the SCO events do not occur below 100 K in the analogous Fe_3Fe_2 TBPs supports the theory that the major spin-transitions occurring in the Fe_3Ru_2 TBPs below 100 K is due to CTIST events. The Fe_3Os_2 TBP exists as

[(LS-Fe^{II})$_3$$Os^{III}_2$] at low temperatures and undergoes two concurrent CTIST events above 220 K. The Fe_3Ru_2 susceptibility data exhibit two clear steps from 2 K to 350 K, indicative of at least two spin-transitions occurring separately throughout the temperature range. One of these steps occur below 220 K in all of the Fe_3Ru_2 sample measured. By exchanging Ru for Os, the spin transitions that are occurring have clearly been shifted to lower temperatures and seem to have increased in number as well.

^{57}Fe Mössbauer Properties

In order to try to deconvolute the complex spin-transitions that occur as the level of solvation changes in these TBPs, ^{57}Fe Mössbauer data was collected and simulated by Dr. Catalina Achim and her graduate student Heather Stout at Carnegie Melon University. Data was collected at zero field on crystals that came from the same batch of samples used for magnetic measurements. Without having simulated Mössbauer data under an applied field, the distinction between LS Fe^{II} and HS Fe^{III} cannot be ascertained with any percent of certainty, but with the combination of magnetic and crystallography data, reasonable assumptions about the overall type of spin-transitions occurring can be made. Details on the instrument and methods used to collect the data can be found in Appendix A. The percent of iron given are for the total iron in the molecule. Considering there are three iron centers in these molecules and a total percentage is not particularly helpful when considering what each iron center is doing, there are two easy ways

to relate the total percent of iron given to the actual iron centers. One iron center is considered to be approximately 33.$\overline{3}$% of the total iron, or the total iron percentage can be multiplied by 3 to obtain the percentage of one iron center. For consistency, the latter method will be used to discuss what is most likely occurring at each iron center, with the inclusion of the magnetic and crystallography data for support.

Fe_3Ru_2 Solvated (7a)

Spectra for this sample were collected at 150 K and 4.2 K without an applied field. Relevant parameters and data can be found in Table 4-17. These parameters are simulated with an orange line in Figure 4-18. At 150 K (Figure 4-18a), the main feature of the spectra is a doublet just to the right of 0 mm/s with a quadrupole splitting (ΔE_Q) of 0.485 mm/s and a chemical shift (δ) of 0.417 mm/s and accounts for 80% of the iron in the sample. These parameters are typical for either LS Fe^{II} or HS Fe^{III}. The minor feature with a peak just above a velocity of 2 mm/s signifies the presence of HS Fe^{II} and accounts for 7% of the total iron (or 21% of one iron center, possibly) in the sample. As temperature is decreased to 4.2 K (Figure 4-18b), the main doublet remains unchanged and still accounts for 80% of the total iron in the sample measured under MeCN. The peak above 2 mm/s that corresponds to HS Fe^{II} is visibly smaller and now and only account for 5% of the total iron (or 15% of one iron center). What is more notable is the emergence of a new doublet with one peak at a lower velocity of the main doublet

and the other peak appearing as a shoulder at a higher velocity of the main doublet. This doublet is attributed to LS Fe^{III} and accounts for 12% of the total iron (or 36% of one iron center) in the sample. With the LS Fe^{II} and HS Fe^{III} doublet remaining unchanged and the amount of HS Fe^{II} remaining relatively unchanged between 150 K and 4.2 K, this suggests that the emergence of LS Fe^{III} is coming from either LS Fe^{II} or HS Fe^{III}. This means that two spin-transitions are possible – a LS Fe^{II} → LS Fe^{III} charge transfer as temperature is decreased, or a HS Fe^{III} → LS Fe^{III} SCO.

Table 4-17. ^{57}Fe Mössbauer data collected with no applied field for 7a.

Sample Conditions	T(K)	δ (mm/s)	ΔE_Q (mm/s)	%	Fe Type
Crystals Under Acetonitrile (7a)	**4.2**	0.180	2.085	12	LS Fe^{III}
		0.450	0.520	80	LS Fe^{II} or HS Fe^{III}
		1.100	3.050	5	HS Fe^{II}
	150				Broad
		0.417	0.485	80	LS Fe^{II} or HS Fe^{III}
		1.050	3.000	7	HS Fe^{II}

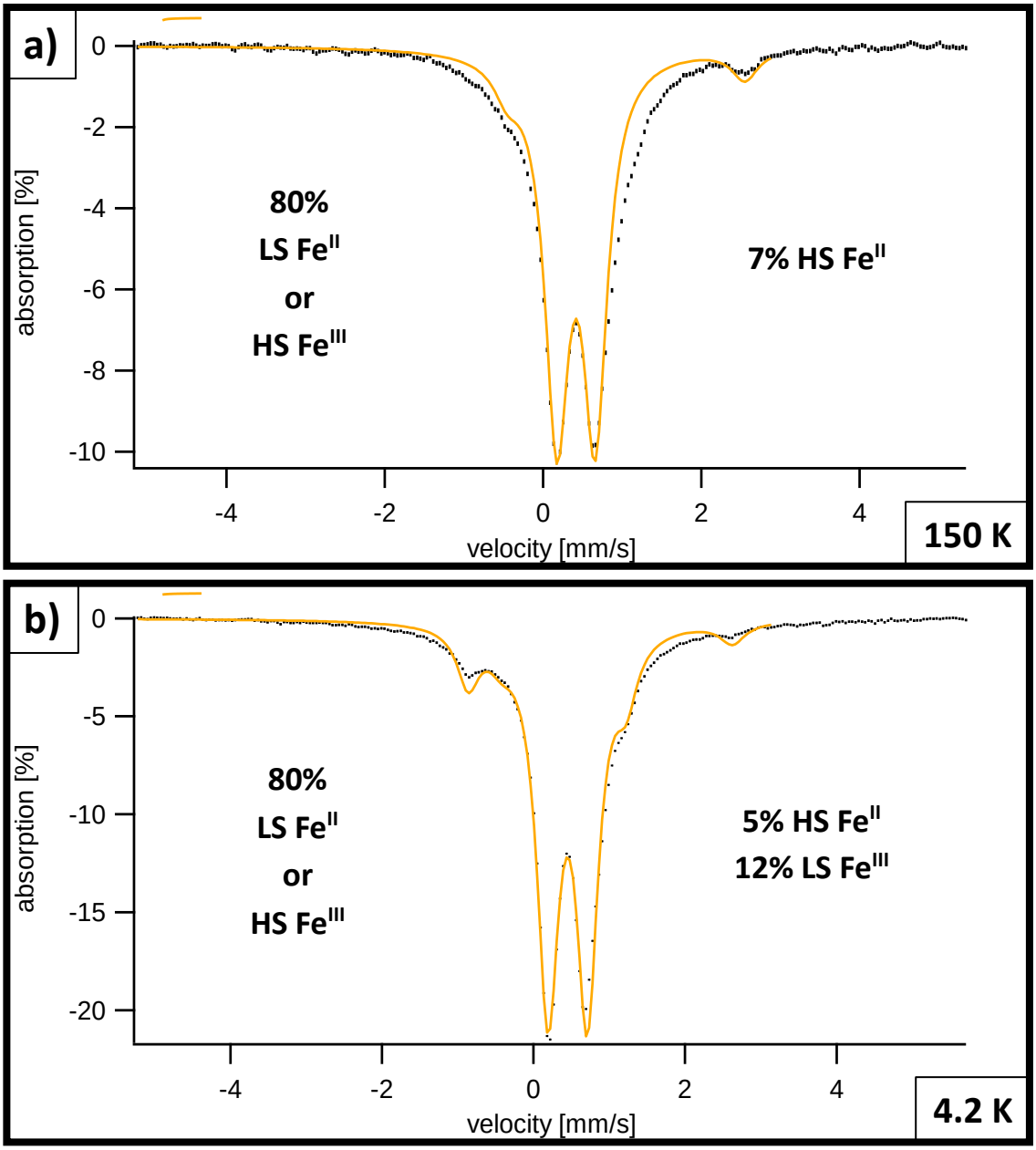

Figure 4-18. ^{57}Fe Mössbauer data for the solvated crystals of Fe_3Ru_2 (7a) at 150 K (a) and 4.2 K (b). Spectra were obtained without an applied field. Orange line is the simulation using the parameters in Table 4-17. Percentages of iron used in simulation are displayed on each figure for convenience.

The continual decrease in the magnetic susceptibility data as temperature decreases is not consistent with an increase in unpaired electrons however, ruling out the former possibility. With the percentage of this doublet remaining unchanged at 80% at both temperatures and the continual decrease in susceptibility, the amounts of HS Fe^{III} and LS Fe^{II} must change in ratio between themselves. In other words, HS Fe^{III} is likely undergoing a CTIST to LS Fe^{II} as temperature decreases. At 2 K, the susceptibility of the molecule is 1.4 emu·K/mol and at 4 K, it is 2.1 emu·K/mol. These values, in conjunction with Mössbauer data, are consistent for a TBP with a configuration headed towards $[(LS\text{-}Fe^{II})_3Ru^{III}{}_2]$ with one Fe center that did not complete a charge-transfer from LS Fe^{III} to LS Fe^{II}. The unlikelihood of LS Fe^{II} becoming LS Fe^{III} as temperature decreases requires the presence of Fe^{III} at higher temperatures. Susceptibility data at room temperature offered four possibilities for the state of the TBP, three of which demanded the presence of HS Fe^{III} and none that suggested the presence of LS Fe^{III}. With this knowledge, and the presence of 12% LS Fe^{III} (or 36% of one iron center) detected at 4.2 K, it becomes clear that there is some HS Fe^{III} undergoing a SCO to LS Fe^{III} as temperature is decreased. The amount of HS Fe^{II} present in the Mössbauer spectra at 150 K coupled with the relatively small change in χT, from 300 K to 150 K, preclude the configuration of $[(HS\text{-}Fe^{II})_2(HS\text{-}Fe^{III})Ru^{II}Ru^{III}]$ at room temperature. This leaves the TBP in a $[(HS/LS\text{-}Fe^{II})(HS\text{-}Fe^{III})_2Ru^{II}{}_2]$ configuration, where the SCO in the Fe^{II} center is in an intermediate state. From the combination of magnetic, Mössbauer and crystallography data it is likely that the Fe(2) center

in the TBP is undergoing a continuous HS → LS Fe^{II} SCO with the majority of the remaining SCO occurring between 300 K and 150 K. This accounts for the sharp decrease in the average Fe(2)–N bond length between these temperatures and also the ~Δ = 3 emu·K/mol in the χT data. The other bond lengths stay relatively unchanged through these temperatures, as discussed earlier. If there was an abrupt CT, CTIST or SCO through these temperatures, it could be seen in the χT data as well as the Fe–N bond lengths. This does not preclude the possibility of a gradual spin-transition at the other two remaining Fe centers from occurring though. Between 150 K and 2 K, there is a ~Δ = 6 emu·K/mol in the χT data and the emergence of LS Fe^{III} at low temperatures, according to Mössbauer data. It is clear from the magnetic data that no, or very little HS Fe^{III} is present in the sample at 2 K, meaning that one of the HS Fe^{III} centers at elevated temperatures undergoes a CTIST to become LS Fe^{II} as temperature is decreased. The other center appears to be undergoing a HS Fe^{III} → LS Fe^{III} SCO first, followed by a charge-transfer to LS Fe^{II}. This is the first time that I am aware of, where a SCO and charge-transfer event occur on the same metal at different times. In the literature, these two events have been observed as concomitant phenomena known as CTIST. Mössbauer in an applied field and at room temperature is needed to confirm these theories, obviously.

Fe_3Ru_2 Filtered (7b)

The filtered sample has similar magnetic and ^{57}Fe Mössbauer data (Table 4-18 and Figure 4-19) and should behave in the same manner as explained above. It can be seen from the Mössbauer data at 4.2 K (Figure 4-19b), that the spin-transitions occurring, go more toward completion than the sample measured under MeCN. The red line in the figure corresponds to the simulation of the data using the parameters in Table 4-18.

Table 4-18. ^{57}Fe Mössbauer data for 7b at 4.2 K and 150 K.

Sample Conditions	T(K)	δ (mm/s)	ΔE_Q (mm/s)	%	Fe Type
Filtered Crystals (7b)	**4.2**	0.190	2.000	3	LS Fe^{III}
		0.480	0.550	93	LS Fe^{II} or HS Fe^{III}
		1.100	3.100	2	HS Fe^{II}
	150				Broad
		0.425	0.510	79	LS Fe^{II} or HS Fe^{III}
		1.050	2.900	8	HS Fe^{II}

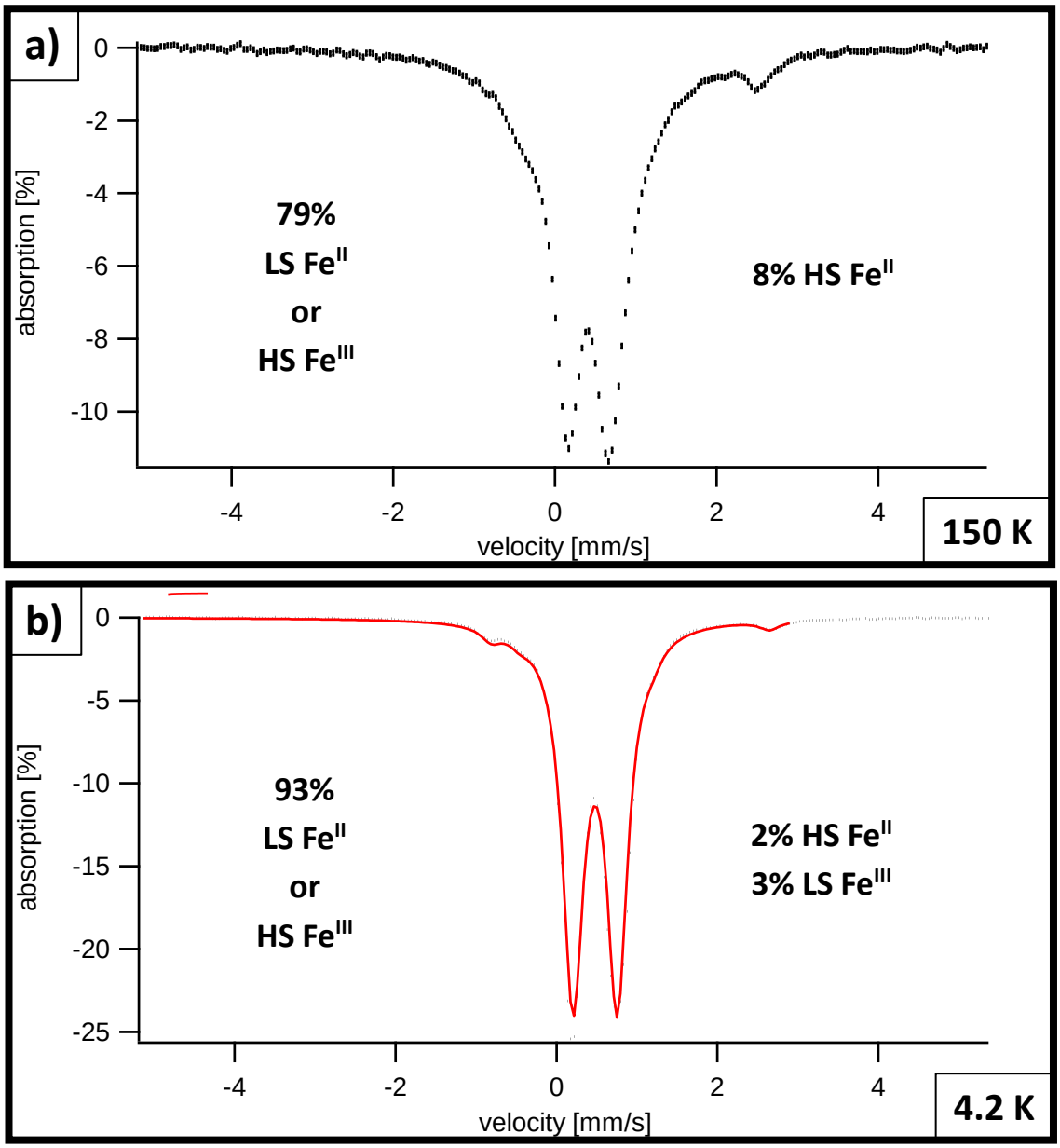

Figure 4-19. ^{57}Fe Mössbauer spectra for the filtered sample (7b) at 150 K (a) and 4.2 K (b). Measurements done in zero field. The red line represents the simulation of the data with the parameters in Table 4-18. Total iron percentages are displayed on the spectra for convenience.

Fe_3Ru_2 3 Hours (7c)

^{57}Fe Mössbauer data were collected at 250 K and 150 K for this sample. The relevant parameters are in Table 4-19 and the spectra are in Figure 4-20. According to magnetic susceptibility data discussed previously, the only plausible configuration of the TBP above room temperature was that of $[(HS\text{-}Fe^{II})(HS\text{-}Fe^{III})_2Ru^{II}_2]$. This configuration holds true down to about 250 K as the decrease in χT is only 1.5 emu·K/mol resulting in a total χT value of 12.1 emu·K/mol. This is consistent with a gradual SCO from HS to LS on the Fe^{II} center. The Mössbauer spectrum at 250 K (Figure 4-20a) exhibits two sets of doublets. The main quadrupole doublet centered just above 0 mm/s has parameters typical for LS Fe^{II} or HS Fe^{III} and accounts for 63% of the total iron in the sample (100% of one iron center and ~90% of another iron center, possibly). The less intense doublet that exists as a shoulder on the left side of the main doublet and a peak above a velocity of 2 mm/s is typical for HS Fe^{II} and represents

Table 4-19. ^{57}Fe Mössbauer parameters for 7c at 150 K and 250 K in zero field.

Sample Conditions	T(K)	δ (mm/s)	ΔE_Q (mm/s)	%	Fe Type
Crystals Under Vacuum for 3 Hours (7c)	**150**				Broad
		0.425	0.555	82	LS Fe^{II} or HS Fe^{III}
		1.090	2.850	9	HS Fe^{II}
	250				Broad
		0.410	0.550	63	LS Fe^{II} or HS Fe^{III}
		1.020	2.450	30	HS Fe^{II}

30% of the total iron in the sample, or 90% of one entire iron center, possibly. In conjunction with magnetic data, this could be looked at as one Fe center exists as ~90% HS Fe^{II} and ~10% LS Fe^{II}, exhibiting SCO behavior between 350 K and 250 K. The other iron centers remain as mostly HS Fe^{III} as mandated by the susceptibility value of 12.1 emu·K/mol. As temperature is decreased to 150 K, the main doublet grows in intensity at a nearly equivalent magnitude at which the doublet for HS Fe^{II} decreases. That is, there is a decrease of 21% in the amount of HS Fe^{II} and an increase of 19% in the amount of LS Fe^{II}/HS Fe^{III} in the sample. As stated earlier, it is unlikely that HS Fe^{III} will emerge as temperature is decreased, and especially not from HS Fe^{II}. That leaves the reasonable assumption that the increase in the main doublet is due to a HS to LS SCO event of Fe^{II}. As of now, all that can be said for this sample, is that from 350 K to 150 K, there is an Fe^{II} center undergoing a HS to LS SCO with the decrease in temperature and that the other iron contribution comes from mostly HS Fe^{III}. As with the previous samples, magnetic data suggests that the sample is ultimately transitioning, incompletely, to a [(LS-Fe^{II})$_3$$Ru^{III}$$_2$] configuration. The mechanism in which this occurs is unknown without conclusive Mössbauer data but it is clear that this sample undergoes at least one Fe^{II} SCO and most likely, two CTIST events. Whether this sample mirrors the solvent and filtered sample by separating the charge-transfer and SCO event on one of the iron sites remains unknown for now.

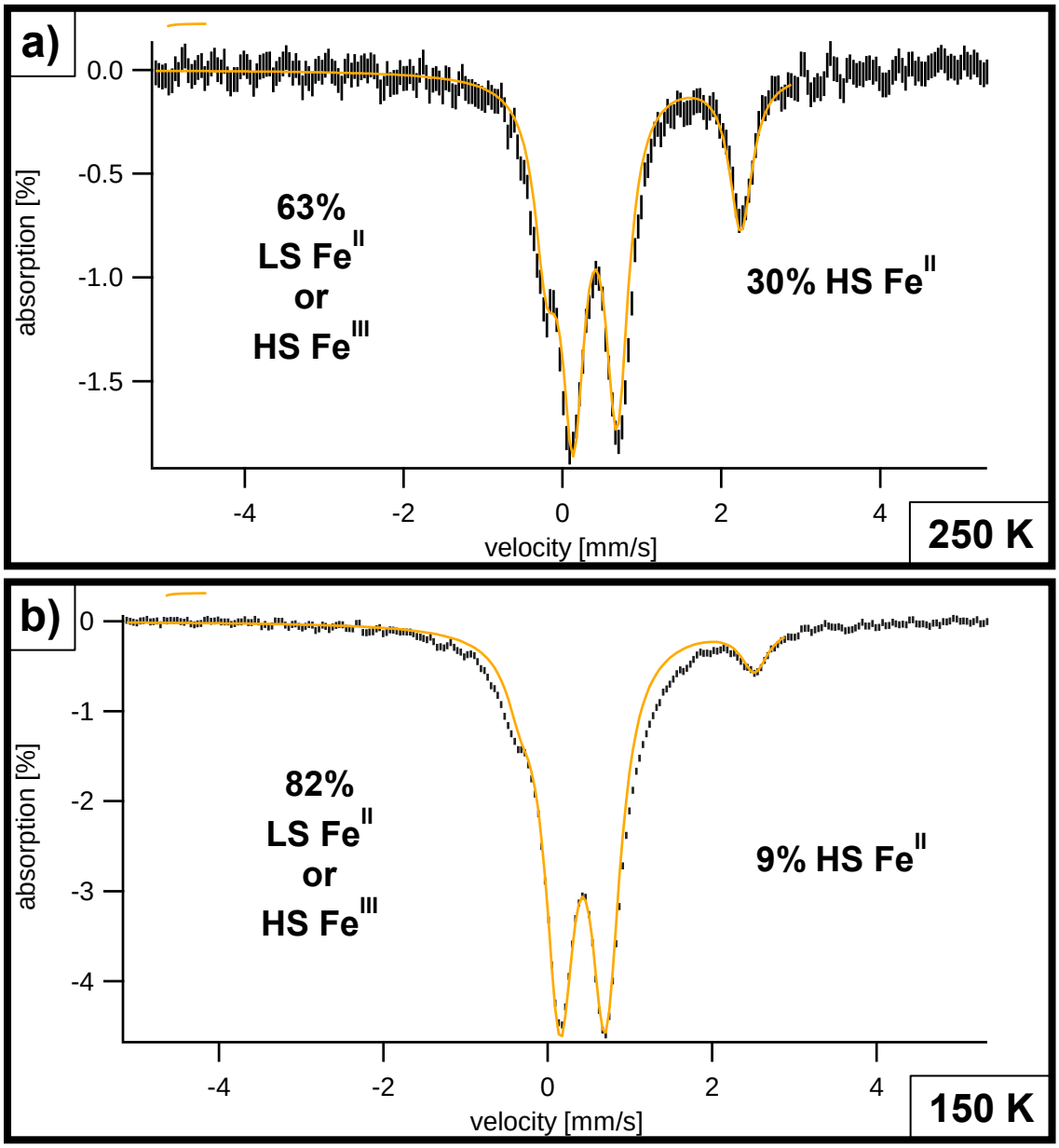

Figure 4-20. ^{57}Fe Mössbauer spectra for 7c collected at 250 K (a) and 150 K (b) in zero field. The orange line is the simulation of the data with the parameters in **Table 4-19**. The iron percentage and type is displayed on the figure for convenience.

Fe_3Ru_2 24 Hours (7d)

The crystals exposed to vacuum for 24 hours were measured using ^{57}Fe Mössbauer spectroscopy in zero field at room temperature, 150 K and 4.2 K. The relevant data can be found in Table 4-20 and the spectra in Figure 4-21. The Mössbauer and magnetic data for this sample is much more conclusive and provides a good idea of the spin-transitions occurring when solvent is removed from the sample. The spectrum at room temperature (Figure 4-21a) features the usual main doublet indicative of LS Fe^{II} or HS Fe^{III} and represents 67% of all iron present in the sample (or two complete iron centers, in other words). The doublet that corresponds to HS Fe^{II} is also present and is simulated to account for 31% of all iron in the sample, or ~93% of one iron center. In combination with the magnetic data that has a spin-transition curve which is nearly plateaued at 300 K at

Table 4-20. ^{57}Fe Mössbauer data for 7d at 4.2 K, 250 K and room temperature.

Sample Conditions	T(K)	δ (mm/s)	ΔE_Q (mm/s)	%	Fe Type
Crystals Under Vacuum for 24 Hours (7d)	4.2				Broad
		0.460	0.540	90	LS Fe^{II} or HS Fe^{III}
		1.140	2.950	7	HS Fe^{II}
	150				Broad
		0.415	0.525	77	LS Fe^{II} or HS Fe^{III}
		1.100	2.900	10	HS Fe^{II}
	RT				Broad
		0.380	0.525	67	LS Fe^{II} or HS Fe^{III}
		0.980	2.300	31	HS Fe^{II}

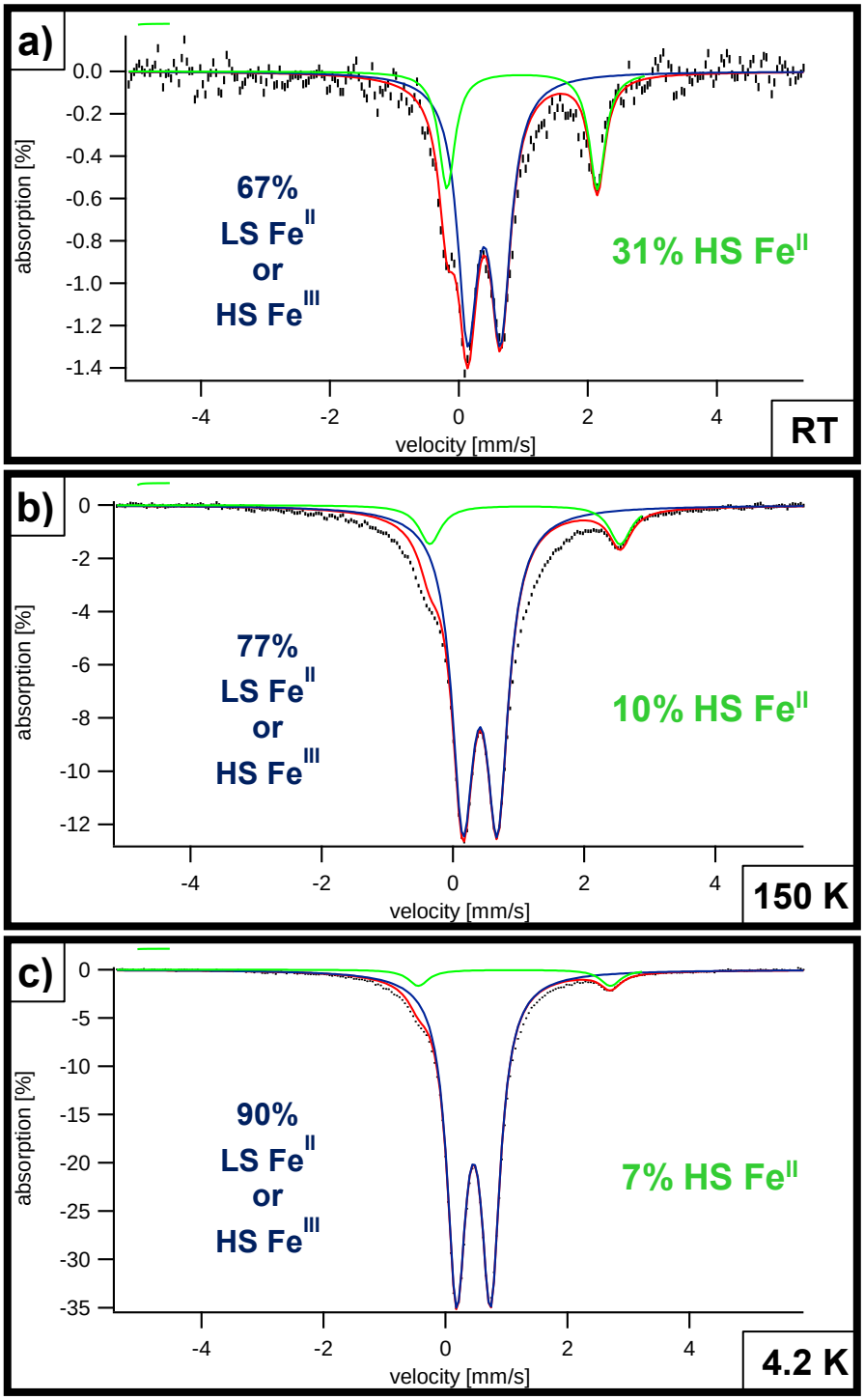

Figure 4-21. ^{57}Fe Mössbauer spectra for **7d** at room temperature (a), 150 K (b) and 4.2 K (c) in zero field. The green lines are the simulation of the HS Fe^{II} doublets, the blue lines are the simulations for the LS Fe^{II}/HS Fe^{III} doublets and the red lines are the overall simulations with all parameters in Table 4-20 for each temperature.

14.2 emu·K/mol, there is only one possible configuration for the TBP at this temperature and that is [(HS-Fe^{II})(HS-Fe^{III})$_2$$Ru^{II}_2$]. The small percentage of iron that is not HS at room temperature, according to Mössbauer data, is most likely all HS at 350 K as suggested by the increase of χT to 14.5 emu·K/mol. As temperature decreases to 150 K, The doublet for HS Fe^{II} decreases but still accounts for 10% of the Fe in the compound (or 30% of one center). This decrease inevitably causes an increase in the main doublet characteristic of LS Fe^{II} or HS Fe^{III}. Unfortunately, only 87% of the iron in the sample at this temperature could be accounted for, partly due to the broadening of the main doublet. Magnetic data indicates that the majority of the sample still contains HS Fe^{III}. At this point, it would appear that the main phenomena that occurs between 150 K and 350 K is still the Fe^{II} SCO and is most likely occurring on the Fe(2) center as suggested by crystallography data. As 4.2 K is reached however, Mössbauer data can account for 98% of all iron in the sample again and shows that only a small amount (3%) of the Fe^{II} center continued the SCO event. The main doublet represents 90% of the iron in the compound and with the help of susceptibility data (1.5 emu·K/mol), it can be considered to be caused by the presence of LS Fe^{II}. This indicates a ground state configuration of [(LS-Fe^{II})$_3$$Ru^{III}_2$] with some remnant HS Fe^{II}. Without the emergence of LS Fe^{III}, it would appear that when solvent is removed from the compound and temperature is decreased, an Fe^{II} HS→LS SCO event will occur along with two CTIST events from HS Fe^{III} → LS Fe^{II}.

Fe_3Ru_2 Humid (7e)

Just as the magnetic data for this compound was the most distinct of all the samples, so is the Mössbauer data (Table 4-21 and Figure 4-22). Spectra were obtained at 150 K and 4.2 K in zero field. Just like all of the other samples, the main doublet characteristic of either LS Fe^{II} or HS Fe^{III} is present but unlike any of the other spectra obtained, there is an emergence of a significant signal that corresponds to LS Fe^{III} at 150 K (Figure 4-22a). This doublet only grows in intensity at 4.2 K (Figure 4-22b), resulting in an increase in the amount of LS Fe^{III} present from 20 to 25%, or 60 to 75% of one iron center. Again, as temperature decreases it is very unlikely that LS Fe^{III} will be formed from HS Fe^{II} and even less likely from LS Fe^{II}. The Mössbauer spectra show that the LS Fe^{II}/HS Fe^{III} doublet decreases in intensity as temperature decreases from 150 K to 4.2 K, unlike all of the other samples that showed an increase in this feature (except for the solvent sample which remained unchanged in magnitude). This suggests that some of the

Table 4-21. ^{57}Fe Mössbauer data for **7e** at 4.2 and 150 K collected with zero field.

Sample Conditions	T(K)	δ (mm/s)	ΔE_Q (mm/s)	%	Fe Type
Humid Crystals (7e)	**4.2**	0.180	2.085	25	LS Fe^{III}
		0.445	0.480	57	LS Fe^{II} or HS Fe^{III}
		1.120	2.950	7	HS Fe^{II}
	150	0.150	2.070	20	LS Fe^{III}
		0.425	0.475	65	LS Fe^{II} or HS Fe^{III}
		1.100	2.900	9	HS Fe^{II}

HS Fe^{III} present at higher temperatures is not undergoing a CTIST to LS Fe^{II}, but is becoming LS Fe^{III} due to SCO. The amount of HS Fe^{II} at both temperatures remain relatively similar which supports the conclusion that the change in susceptibility ($\Delta \cong 2.0$ emu·K/mol) and Mössbauer data between 150 and 4.2 K is mostly due to an incomplete SCO of an Fe^{III} center. The larger decrease in magnetic susceptibility data comes from the 350 K → 150 K transition. At 150 K, the spin-transition/s are still not complete as the curve does not “plateau” until around 70 K, resulting in a change of ~ 6 emu·K/mol. This is consistent with a portion of an Fe^{II} center undergoing a HS → LS SCO, a portion of a HS Fe^{III} transitioning to a LS Fe^{II} center through CTIST and another Fe^{III} center that is gradually undergoing a SCO from HS Fe^{III} → LS Fe^{III} as temperature is decreased. The crystallography data supports the conclusion that all three iron centers undergo a different type of spin-transition. The Fe(1) center has Fe–N bond lengths that rapidly decrease from 250 K to 150 K with respect to the other Fe center distances. The Fe(2) center also shows this same trend but has smaller bond lengths throughout the temperature regime. The Fe–N bond lengths for the Fe(3) center however, remain very similar to one another throughout the temperature range with distances characteristic of an Fe center in the middle of a SCO. With this information, it is reasonable to suggest: i) the Fe(2) center is the Fe^{II} center undergoing a gradual SCO between 350 and 2 K, ii) the Fe(3) center is the Fe^{III} center undergoing the gradual CTIST and iii) the Fe(1) center is the Fe^{III} center that is now undergoing a gradual SCO instead of a CTIST like in the

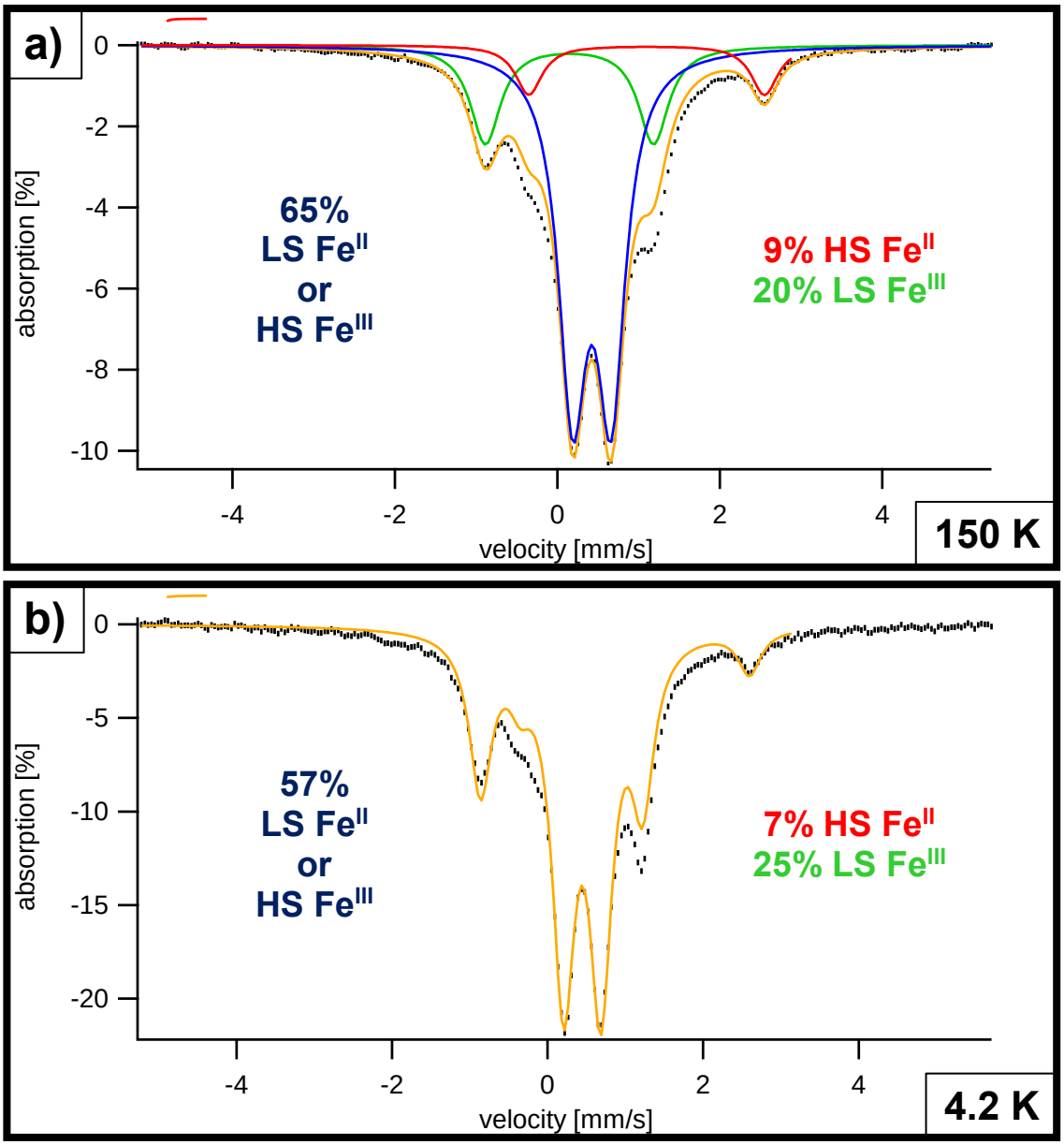

Figure 4-22. ^{57}Fe Mössbauer spectra for 7e at 150 K (a) and 4.2 K (b). The lines simulate the parameters in Table 4-21. The red lines are for HS Fe^{II}, the green lines simulate LS Fe^{III}, the blue lines simulate the LS Fe^{II}/HS Fe^{III} doublet and the orange line represents the overall simulation with the indicated parameters. The percentages attributed to each type of iron is displayed on the spectra for convenience.

solvated and evacuated samples. So it seems that when the TBP contains water, the electronic configuration above room temperature tends toward the usual [(HS-Fe^{II})(HS-Fe^{III})$_2$$Ru^{II}_2$] and as temperature is decreased the TBP transitions toward a ground state of [(LS-Fe^{II})$_2$(LS-Fe^{III})$Ru^{II}Ru^{III}$].

Again, without more conclusive Mössbauer data, these assignments are educated conjectures as to the most reasonable spin-transitions occurring in these compounds containing different levels of solvation. By comparing the data for all of the samples at 150 K (Figure 4-23), one trend can be concluded. And that is, when solvent is removed from the compound, the amount of HS Fe^{II} present in the sample increases, as indicated by the increase in the characteristic HS Fe^{II} doublet circled in red in Figure 4-23. This is a reasonable occurrence because removing solvent from the lattice affects the TBPs in at least two ways – more void space is available which allows expansion of the TBP from the increase in Fe–N bond lengths as a consequence of SCO and it also imparts less of a chemical pressure on the TBP itself. As stated in the main introduction, pressure often causes a compound to become LS at elevated temperatures where it would normally be HS without the applied pressure. The solvent in the lattice can act as an applied pressure and is often referred to as a chemical pressure. This chemical pressure can stabilize the LS state. When removed, the HS state is preferred, as is exhibited by this study.

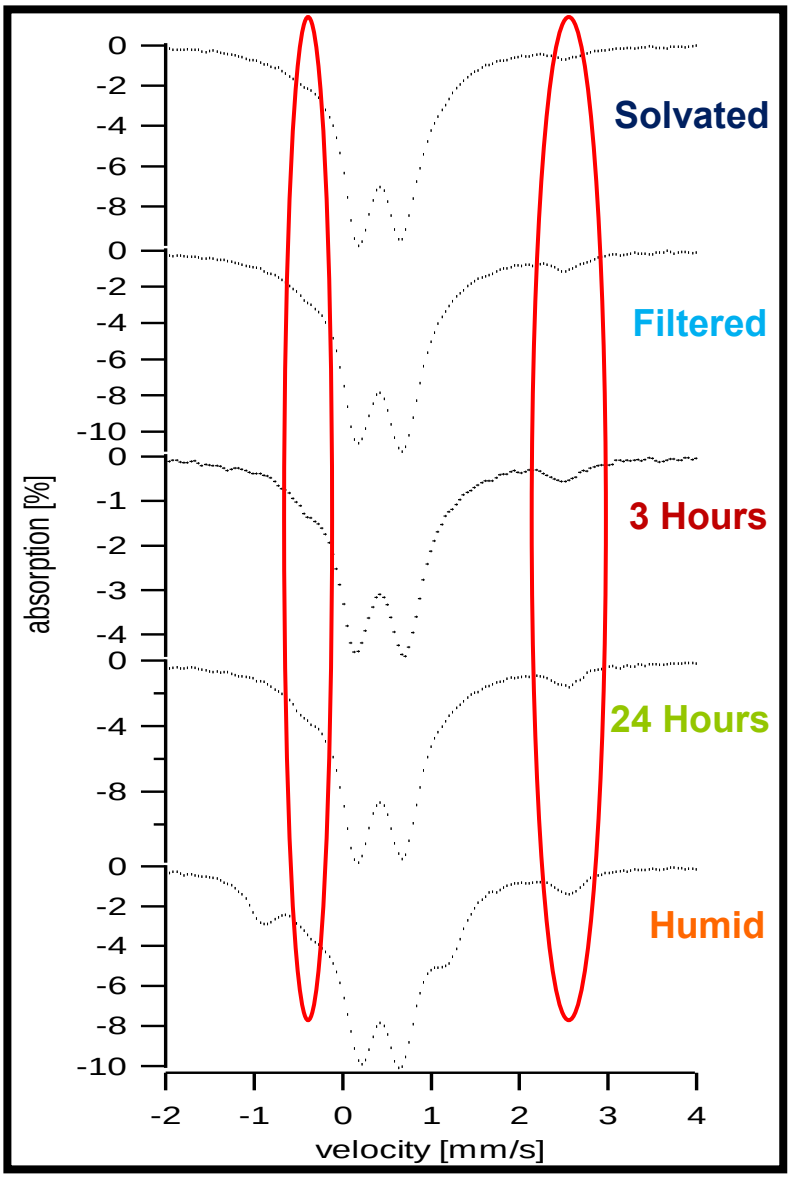

Figure 4-23. Comparison of the ^{57}Fe Mössbauer data at 150 K for all solvation states (7a-7e). The HS Fe^{II} doublets are circled in red.

Concluding Remarks

From the magnetic, Mössbauer and variable temperature X-ray crystallography data obtained for the Fe_3Ru_2 TBPs with different interstitial solvent, it can be said that as temperature decreases from 350 K to 2 K:

i) The 3 and 24 hour samples undergo a SCO event (HS Fe^{II} → LS Fe^{II}) at the Fe(2) center, followed by two CTIST events (HS Fe^{III} → LS Fe^{II}) at the Fe(1) and Fe(3) centers.

ii) The solvated and filtered samples undergo a gradual SCO event (HS Fe^{II} → LS Fe^{II}) at the Fe(2) center, one CTIST (HS Fe^{III} → LS Fe^{II}) and one SCO (HS Fe^{III} → LS Fe^{III}) followed by a charge-transfer to LS Fe^{II} as indicated by the small amount of LS-Fe^{III} detected by Mössbauer.

iii) The humid sample undergoes a gradual SCO event (HS Fe^{II} → LS Fe^{II}) at the Fe(2) center, one CTIST event (HS Fe^{III} → LS Fe^{II}) at the Fe(3) center and one SCO event (HS Fe^{III} → LS Fe^{III}) at the Fe(1) center.

iv) The Fe(2) center is always involved in a gradual SCO event (HS Fe^{II} → LS Fe^{II}), is the center furthest from the other TBP in the dimeric unit and participates in two very weak intramolecular interactions.

v) The SCO event occurring at the Fe(2) center is more prominent at higher temperatures, as indicated by the increase in the average Fe-N distances above 150 K for both the humid and solvent samples and is also suggested by the small percentage of HS-Fe^{II} detected by Mossbauer below 150 K. Also,

the lack of a plateau at 350 K in the susceptibility data in the solvated and humid samples indicate that this SCO event is not complete.

vi) The Fe(3) center always exhibits CTIST (HS Fe^{III} → LS Fe^{II}) and is the center involved in the intermolecular π-π interactions, which are the stronger π-π stacking interactions exhibited in these molecules.

vii) The Fe(1) center displays different behavior amongst the samples – exhibiting CTIST (HS Fe^{III} → LS Fe^{II}) in the 24 hour sample, SCO (HS Fe^{III} → LS Fe^{III}) in the humid sample and SCO (HS Fe^{III} → LS Fe^{III}) followed by an incomplete charge-transfer event (LS Fe^{III} → LS Fe^{II}) in the solvent sample, which is a phenomenon not yet seen in literature to the best of my knowledge.

viii) This TBP is the first example of a pentanuclear TBP molecule containing LS Fe^{III} in an equatorial position, demonstrating that CTIST is not always a concomitant process (as in the solvated and filtered samples).

ix) The absence of solvent stabilizes the HS states at lower temperatures due to the absence of chemical pressure. When comparing water and MeCN as interstitial solvent in these TBPs, the water stabilizes LS states.

The data presented here shows that not only does the identity of solvent but also the amount of solvent can impose non-trivial changes to both SCO and CTIST behavior in the Fe_3Ru_2 TBPs. This idea is not new in the world of SCO compounds but is still under investigation as it still cannot be predicted, nor generalized as to how solvent will affect the spin-transitions in molecules, for the most part. Most SCO compounds studied in literature are mononuclear salts with

few examples of dinuclear compounds, in comparison, and even fewer multinuclear compounds being reported. This study not only shows the occurrence of SCO and CTIST in a pentanuclear compound, but it does it in one that is neutral and can lose or exchange interstitial solvent without causing significant structural changes/rearrangement to the TBP by doing so. This is novel in the fact that it is a neutral, pentanuclear compound and that it is does not need to be crystalized using different solvents in order to study the effect solvent has on the spin-transitions of the molecule. It was also shown that this TBP exhibits more intricate spin-transition behavior than both of the Fe_3Fe_2 and Fe_3Os_2 analogs – a consequence related to the exchange of Fe/Os for Ru. With thermal perturbation, the Fe_3Fe_2 congener (solvated and humid samples) only exhibits reversible Fe^{II} SCO behavior while the Fe_3Os_2 analog (with interstitial MeCN molecules) exhibits two, reversible, concurrent CTIST events at the Fe(1) and Fe(3) centers.

Mössbauer data was not as conclusive as it was anticipated to be, but more measurements under an applied field may help confirm the spin-transition assignments made for these samples. Despite that, it can be said that this TBP is the first one to have equatorial iron centers in the LS Fe^{III} electronic configuration. This occurred in not one, but three of the Fe_3Ru_2 compounds studied here and appears to be a result of two different phenomena occurring. This demonstrates that the CTIST is not always a concomitant process (as in the solvated and filtered samples). This study also adds more polynuclear SCO complexes to the relatively

small collection of data in the literature and to the fewer studies reported on polynuclear Fe^{III} SCO compounds. This study has proven to be a non-trivial task of adhering to good, consistent, lab practices and intricate data analysis but has also rewarded us with a complex compound capable of exhibiting up to three different, reversible spin-transitions within one molecule, an unprecedented behavior in the field of spin-transition.

CHAPTER V

INVESTIGATION OF π-π STACKING INTERACTIONS IN SPIN CROSSOVER Fe_3Co_2 TRIGONAL BIPYRAMIDAL COMPLEXES

Background

Spin-crossover behavior is a well-documented phenomenon whose cooperativity and transition temperature is affected by many factors. The types of perturbations that cause changes to SCO behavior are either chemical or physical in nature.[85] Typical chemical influences that are often investigated are ligand substitution and solvate effects while the more common physical influences are the use of light and pressure. These parameters allow chemists to modify the SCO behavior of compounds with the ultimate goal being to achieve materials that exhibit an abrupt, wide hysteretic transition that spans room temperature. Researchers in this field are striving to predict how these different chemical and physical perturbations will affect SCO but it is not often that generalizations can be made. This is, in part, due to multiple, subtle influences that all effect SCO and are inherent in most studies. Some researchers have discredited the ability to "fine-tune" the SCO behavior due to these multiple influences that are difficult to control synthetically.[88] Despite this situation, a considerable body of research has led to three synthetic strategies to impart and strengthen cooperativity in SCO molecules: (a) incorporation of a network capable of hydrogen bonding (*e.g.*, through the use of solvent such as water or through ligands), (b) incorporation of

moieties capable of π-π stacking interactions and (c) coordination of ligands capable of bridging.[83] Most research in the field of SCO pertains to mononuclear, soluble salts of Fe^{II} and as such, there is little known about how the results of these studies translate to polynuclear molecules.

The research discussed herein is aimed at studying the effect of π-π stacking interactions in TBP molecules that are insoluble, neutral, pentanuclear compounds that typically exhibit a gradual spin-crossover. The complexity of the TBPs discussed in this dissertation thus far (due to the facile redox properties of $[Ru^{III}(CN)_6]^{3-}$ and $[Os^{III}(CN)_6]^{3-}$ precursors) make deconvoluting the spin and oxidation states of the metal centers a non-trivial task. For this reason, the Fe_3Co_2 TBP presents itself as an ideal scaffold among the possible TBPs that undergo a spin-transition due to the stability of the oxidation states of the Co^{III} and Fe^{II} centers. Cobalt(III) in a cyanide environment is LS and remains diamagnetic in these molecules. The Fe^{II} centers are diamagnetic in the LS state and any magnetic signal observed is a direct result of the amount of HS Fe^{II} present in the sample. Therefore, the assignment of the electronic states of the metal centers in these systems allow for the effect of π-π stacking interactions on the Fe^{II} SCO in these TBPs to be evaluated. The ligands that have been investigated are illustrated in Figure 5-1. The 3,4,7,8-tetramethyl-1,10-phenanthroline (tmphen) and 4,4',5,5'-tetramethyl-2,2'-bipyridine (tmbpy) ligands offer a direct comparison between the effects of π-π stacking on the SCO behavior. The 4,4'-dimethyl-2,2'-bipyridine (4dmbpy) and 5,5'-dimethyl-2,2'-bipyridine (5dmbpy) ligands also offer

this comparison but have additional steric differences than the tmphen and tmbpy ligands.

tmphen (8)

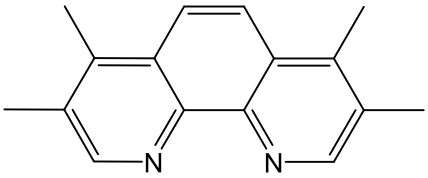

3,4,7,8-tetramethyl-1,10-phenanthroline
Chemical Formula: $C_{16}H_{16}N_2$

4dmbpy (9)

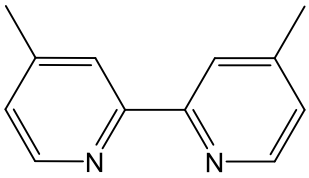

4,4'-dimethyl-2,2'-bipyridine
Chemical Formula: $C_{12}H_{12}N_2$

tmbpy (11)

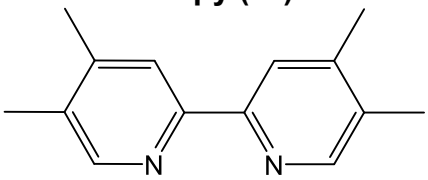

4,4',5,5'-tetramethyl-2,2'-bipyridine
Chemical Formula: $C_{14}H_{16}N_2$

5dmbpy (10)

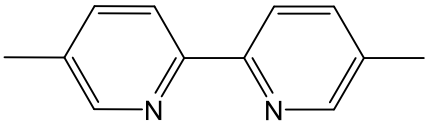

5,5'-dimethyl-2,2'-bipyridine
Chemical Formula: $C_{12}H_{12}N_2$

Figure 5-1. ChemDraw structures of the bidentate ligands used to make the Fe_3Co_2 TBPs. The number in parenthesis following the abbreviation of the name in bold-type font corresponds to the number of the compound in which the ligand is used.

Experimental Details

Materials

All chemicals and solvents were of ACS reagent grade or higher and used as received unless stated otherwise. ***Reagents for the synthesis of 4,4',5,5'-tetramethyl-2,2'-bipyridine (tmbpy or Me_4Bpy), ($C_{14}H_{16}N_2$):*** 3,4-lutidine (C_7H_9N, hygroscopic liquid, 98%, Alfa Aesar), palladium over carbon (Pd/C, dry support, powder, 10% by weight, Sigma Aldrich) and activated charcoal (untreated powder, 100-400 mesh, Sigma Aldrich). ***Reagents for the synthesis of $(PPN)_3[Co^{III}(CN)_6]$:*** potassium hexacyanocobaltate(III) ($K_3[Co^{III}(CN)_6]$, powder, 97+%, Pfaltz and Bauer). ***Reagents for the synthesis of $\{[Fe^{II}(tmphen)_2]_3[Co^{III}(CN)_6]_2\}\cdot nSolv$:*** iron(II) tetrafluoroborate hexahydrate ($Fe^{II}(BF_4)_2\cdot 6H_2O$, hygroscopic crystalline solid, 97%, Sigma Aldrich) and 3,4,7,8-tetramethyl-1,10-phenanthroline (**tmphen**) ($C_{16}H_{16}N_2$, crystalline powder that varies in color from pinkish to off-white, 98+%, Alfa Aesar). ***Reagents for the synthesis of $\{[Fe^{II}(4dmbpy)_2]_3[Co^{III}(CN)_6]_2\}\cdot nSolv$:*** iron(II) tetrafluoroborate hexahydrate ($Fe^{II}(BF_4)_2\cdot 6H_2O$, hygroscopic crystalline solid, 97%, Sigma Aldrich) and 4,4'-dimethyl-2,2'-bipyridine (**4dmbpy**) ($C_{12}H_{12}N_2$, crystalline solid, 99%, Sigma Aldrich). ***Reagents for the synthesis of $\{[Fe^{II}(5dmbpy)_2]_3[Co^{III}(CN)_6]_2\}\cdot nSolv$:*** iron(II) tetrafluoroborate hexahydrate ($Fe^{II}(BF_4)_2\cdot 6H_2O$, hygroscopic crystalline solid, 97%, Sigma Aldrich) and 5,5'-dimethyl-2,2'-bipyridine (**5dmbpy**) ($C_{12}H_{12}N_2$, crystalline solid, 98%, Sigma Aldrich). ***Reagents for the synthesis of $\{[Fe^{II}(tmbpy)_2]_3[Co^{III}(CN)_6]_2\}\cdot nSolv$:***

iron(II) tetrafluoroborate hexahydrate ($Fe^{II}(BF_4)_2 \cdot 6H_2O$, hygroscopic crystalline solid, 97%, Sigma Aldrich). ***Solvents used:*** dichloromethane (DCM) (Fisher Scientific), toluene (Fisher Scientific), diethyl ether (EMD Millipore), acetonitrile (MeCN) (Fisher Scientific), and tetrahydrofuran (THF) (EMD Millipore) were purchased from the Texas A&M University chemistry stockroom and used as received. All water used was distilled by Texas A&M University. All reactions were performed in a fume hood in an aerobic manner, unless stated otherwise.

Syntheses

4,4',5,5'-tetramethyl-2,2'-bipyridine (tmbpy or Me_4Bpy)

CAUTION: 3,4-lutidine is a very hazardous material that can cause several immediate and serious toxic effects, including death. The MSDS states that it is fatal if it comes into contact with skin (the dermal LD_{50} on rabbits is 134 mg/kg).[226] *The chemical is toxic if inhaled, harmful if swallowed, causes skin and serious eye irritation and may cause respiratory irritation. It is prudent that proper safety attire (protective gloves and clothing) be worn when handling this chemical!*

This organic compound was prepared in a fume hood using aerobic methods in a similar manner to previously reported literature methods.[227-229] To a 100 mL Schlenk flask outfitted with a large egg-shaped stir bar was added 10% Pd/C (2.45 g, 0.023 mmol) and 3,4-lutidine (21 mL, 0.187 mmol, ρ = 0.955 g/mL). The reaction was refluxed for fifteen days, resulting in long, white needles of the product. DCM (~80 mL) was added to the flask and the solution was gently heated

and filtered while still warm. Once the light brown solution cooled, it was stirred over activated charcoal for a few hours. The solution was filtered and reduced to dryness. The product was recrystallized from hot toluene to give white crystals/powder upon cooling. The product obtained (3.6 g) was collected by filtration and rinsed with diethyl ether (18% yield). ^{1}H NMR (500 MHz, $CDCl_3$): δ 2.29 (s, 3H), 2.34 (s, 3H), 8.12 (s, 1H), 8.36 (s, 1H); Literature values: 2.28 (s), 2.33 (s), 8.11 (s), 8.36 (s).[227] *Refer to page sixty-four in notebook six for a detailed description of the procedure and observations for the synthesis of 4,4',5,5'-tetramethyl-2,2'-bipyridine.*

$(PPN)_3[Co^{III}(CN)_6]$

This compound was prepared similarly to previously reported methods[180] by performing an aqueous metathesis of K^+ for PPN^+ and then recrystallizing the material from MeCN, THF and diethyl ether. An Erlenmeyer flask containing H_2O (~350 mL) was treated with PPNCl (11.21 g, 19.53 mmol). The solution was stirred and warned to dissolve the PPNCl (~50 °C). Yellow crystals of $K_3[Co^{III}(CN)_6]$ (1.99 g, 6.0 mmol) were dissolved in warm distilled water (150 mL). The cobalt solution was slowly poured into the PPNCl solution as it was heating. The white powder was filtered while the solution was warm and rinsed with warm water (60 mL x 3) to remove excess PPNCl. Diethyl ether (30 mL x 3) was used to help dry the wet product before being recrystallized in the same manner as the $(PPN)_3[Ru^{III}(CN)_6]$ and $(PPN)_3[Os^{III}(CN)_6]$ salts from chapter 2 by dissolving the

product in a minimal volume of MeCN to obtain a clear, colorless solution. Subsequently, a larger volume of THF was added to the solution before small aliquots of diethyl ether were added, over time, to precipitate white crystals from the solution. The crystals were collected by filtration and rinsed with diethyl ether (30 mL x 3). After the recrystallization step/s, 7.86 g of white crystals were recovered for a yield of 88%. IR, v(C≡N): 2113 (m, sp, sh) and 2105 (m, sp) cm^{-1} where m = medium, sp = sharp and sh = shoulder. TGA generally exhibits a 2-3% mass loss over a 50 °C temperature range centered around 60 °C, which is equivalent to ~2-3 water molecules per formula unit. *Refer to page four in notebook five for a detailed description of the procedure and observations for the preparation of* $(PPN)_3[Co^{III}(CN)_6]$*.*

$\{[Fe^{II}(tmphen)_2]_3[Co^{III}(CN)_6]_2\}\cdot$nSolv ($Fe_3Co_2$) (8)

With the exception of the Fe^{II} starting material used and the fact that the chemistry was performed in air instead of in a N_2 atmosphere glove box, this compound was prepared in a similar fashion to previously reported methods.[116,145] In air, $Fe^{II}(BF_4)_2\cdot 6H_2O$ (0.0452 g, 0.133 mmol) and tmphen (0.0726 g, 0.31 mmol) were dissolved in acetonitrile (21 mL). The dark red solution was stirred for twenty minutes before being poured slowly into a 40 mL vial containing a 20 mL MeCN solution of $(PPN)_3[Co^{III}(CN)_6]$ (0.1483 g, 0.081 mmol). Red powder precipitated from the red solution immediately. Within one day, the powder had redissolved and dark, red crystals had appeared. To purify the sample, the mother liquor was

decanted and replaced with MeCN until the solvent remained clear and colorless for several hours. Typical yields are 30-40%. IR, ν(C≡N): 2155 (m, sp) and 2129 cm^{-1} (s, sp) where m = medium, s = strong and sp = sharp. TGA was performed on the sample immediately after SQUID measurements were performed on it and revealed a continuous mass loss of 10.4% between room temperature and ~120 °C with the majority of the mass loss occurring below ~67 °C. The compound is thermally stable up to ~260 °C. *Refer to page ninety-two in notebook six for an in-depth description of the procedure and detailed observations for the synthesis of {[Fe(tmphen)$_2$]$_3$[Co(CN)$_6$]$_2$}·nSolv (8).*

{[Fe^{II}(4dmbpy)$_2$]$_3$[Co^{III}(CN)$_6$]$_2$}·nSolv (Fe_3Co_2 4dmbpy) (9)

This reaction is performed in an analogous manner to the Fe_3Co_2 reaction with tmphen described above (**8**). Acetonitrile (~20 mL) was used to dissolve both $Fe^{II}(BF_4)_2·6H_2O$ (0.0419 g, 0.124 mmol) and 4dmbpy (0.0510 g, 0.277 mmol) to give a dark, red solution. The solution was stirred for 25 minutes before being poured slowly into a 40 mL vial containing a 20 mL MeCN solution of $(PPN)_3[Co^{III}(CN)_6]$ (0.1486 g, 0.081 mmol). The mixture turned a dark, red-purple color and, after a few minutes, powder had settled to the bottom of the vial. Within one day, the powder had redissolved and dark crystals had taken its place. As more crystals formed over the next few days, the color of the solution became less intense and the color became more red than purple. The crystals were purified in the usual manner through decantation and soaking in fresh MeCN. Yield is

typically ~35%. IR, v(C≡N): 2164 (vw) and 2130 cm^{-1} (m, sp) where vw = very weak, m = medium and sp = sharp. TGA performed on the sample immediately after SQUID measurements show an immediate mass loss of 6.6% between room temperature and 60 °C where the temperature was held for 1 hour. After resuming heating to 150°C, a gradual mass lass of 1.5% occurred. The compound begins to decompose at ~160 °C. *Refer to page eighty-three in notebook six for a detailed description of the procedure and observations for the synthesis of* $\{[Fe(4dmbpy)_2]_3[Co(CN)_6]_2\}\cdot nSolv$ *(9).*

$\{[Fe^{II}(5dmbpy)_2]_3[Co^{III}(CN)_6]_2\}\cdot nSolv$ (Fe_3Co_2 5dmbpy) (10)

This reaction is carried out in an analogous manner as the Fe_3Co_2 reactions (**8-9**). MeCN (~40 mL) was used to dissolve both $Fe^{II}(BF_4)_2\cdot 6H_2O$ (0.024 g, 0.072 mmol) and 5dmbpy (0.021 g, 0.11 mmol) to give a dark, red solution. The solution was stirred for five minutes after which time half of the solution was added dropwise to 20 mL of the MeCN solution of $(PPN)_3[Co^{III}(CN)_6]$ (0.102 g, 0.056 mmol) in a 20 mL vial. This procedure was performed twice. The solution turned red with no powder formation being observed. Dark red, block-shaped crystals formed after several days. The crystals were treated in the usual manner through decantation and soaking in fresh MeCN. Yield is ~20%. IR, v(C≡N): 2177 (vw, sp), 2151 (w, sp) and 2123 cm^{-1} (m, sp) where vw = very weak, w = weak, m = medium and sp = sharp. TGA analysis of the sample after being measured in the SQUID magnetometer exhibits a gradual loss of mass between room

temperature and ~60 °C which accounts for 4.8% of the sample. This mass loss is attributed to ~4.8 water molecules. The TBP is thermally stable until ~180 °C. *Refer to page eighty-three in notebook six for a detailed description of the procedure and observations for the synthesis of {[Fe(5dmbpy)$_2$]$_3$[Co(CN)$_6$]$_2$}·nSolv (10).*

{[Fe^{II}(tmbpy)$_2$]$_3$[Co^{III}(CN)$_6$]$_2$}·nSolv (Fe_3Co_2 tmbpy) (11)

This reaction is carried out in a similar manner as all of the Fe_3Co_2 reactions discussed above (8-10). MeCN (~20 mL) was used to dissolve both $Fe^{II}(BF_4)_2 \cdot 6H_2O$ (0.0439 g, 0.130 mmol) and tmbpy (0.0528 g, 0.249 mmol) to give a dark, red solution. The solution was stirred for ten minutes. One-half of the solution was quickly pipetted into a 20 mL vial containing half of a 20 mL MeCN solution of $(PPN)_3[Co^{III}(CN)_6]$ (0.1486 g, 0.081 mmol). This was performed twice. The mixtures turned a dark, red-purple color and, within a few days, dark crystals had formed. The crystals were purified in the usual manner through decantation and soaking in fresh MeCN. Typical yields are 30-40%. IR, v(C≡N): 2175 (vw, sp), 2166 (vw, sp) and 2126 cm^{-1} (m, sp) where vw = very weak, m = medium and sp = sharp. TGA performed on a portion of the sample being measured in the SQUID shows an immediate mass loss of 12.6% between room temperature and ~150 °C with the majority of the mass occurring before 55 °C. TGA performed on the sample after being measured in the SQUID exhibits mass loss over the same temperature range as before the SQUID analysis but the sample only loses ~5.2%

of its mass before decomposing before 200 °C. *Refer to page sixty-seven in notebook six for a detailed description of the procedure and observations for the synthesis of {[Fe(tmbpy)$_2$]$_3$[Co(CN)$_6$]$_2$}·nSolv (11).*

Results and Discussion

Synthesis and Characterization

Fe$_3$Co$_2$ tmphen (8)

The synthesis of this molecule is straightforward. Out of all of the ligands that were used, TBPs with tmphen are the most readily isolated. Generally, it is not crucial whether the precursor solutions for this reaction are layered or mixed quickly, as the product forms with little to no contamination when performed on a small scale as reported here. The crystals that form are a very characteristic dark red color and needle shaped. The reaction can easily be scaled up to make these crystals in bulk but more powder will precipitate initially upon mixing of the solutions.

IR spectra show $\nu_{C\equiv N}$ peaks at 2155 cm^{-1} and 2129 cm^{-1} which are attributed to the bridging and terminal cyanide ligands, respectively. The $\nu_{C\equiv N}$ modes for (PPN)$_3$[Co^{III}(CN)$_6$] are 2139, 2127, 2114 and 2106 cm^{-1} and correspond well to the peak at 2129 cm^{-1} assigned to the terminal cyanide ligands. The spectra indicate the presence of interstitial water with a strong, broad peak around 3406 cm^{-1} (typical for symmetric and antisymmetric stretching of the OH in H_2O) and the HOH bending mode at 1622 cm^{-1}.

TGA was performed on the sample after being measured in the SQUID magnetometer where it was warmed to 390 K twice with the intention of removing solvent. The thermogram shows an immediate mass loss between room temperature and ~67 °C. The mass loss continues at a more gradual rate until about 140 °C and has a total mass loss of 10.4% which is attributed to ~12.9 H_2O molecules per TBP. The compound begins to decompose just after ~260 °C.

Fe_3Co_2 4dmbpy (9)

This reaction is similar to the tmphen containing congener but is not as reliable. This reaction can co-crystallize with $[Fe^{II}(4dmbpy)_3]_2[Co^{II}(CN)_6]$ (determined by X-ray crystallography) as a by-product, fortunately, is soluble in copious amounts of MeCN. The scaling up of this reaction (to prepare in a bulk manner analogous to the Fe_3Ru_2 TBPs) was not attempted.

IR spectra for this TBP exhibit very similar $\nu_{C\equiv N}$ as those for the Fe_3Co_2 TBP with tmphen (8), which is to be expected as the M–C≡N–M' core remains unchanged between the two TBPs. The $\nu_{C\equiv N}$ at 2164 cm^{-1} is assigned to the bridging cyanide and the mode at 2130 cm^{-1} is assigned to the terminal cyanide ligands. Again, the spectra indicate the presence of water with peaks at 3352 and 1617 cm^{-1}.

TGA was performed on the sample immediately upon removing it from the SQUID after measuring the magnetic properties up to 390 K twice. The thermogram shows that the TBP loses the majority of the interstitial solvent

between room temperature and 55 °C but continues to lose mass until ~150 °C. The molecule is thermally stable up to ~160 °C before it decomposes, which is 100 °C lower than the tmphen congener. The total mass loss of 8.1% is attributed to ~8.4 H_2O molecules per TBP.

Fe_3Co_2 5dmbpy (10)

This synthesis is the most difficult to control of all of the ones discussed here. The formation of crystals appears to be most dependent upon the rate of addition of the Fe containing solution to the Co containing solution. It also seems that the concentration of the solutions plays a partial role in product formation as well. In order for the product to form, the Fe containing solution must be added dropwise to the vial containing the Co solution. Rapid mixing of the solutions results in the immediate precipitation of a reddish-orange microcrystalline solid as does layering of the two solutions. It was found that a concentration of ~1.3 mM for the two solutions works best as it results in the least amount of powder formation. As the solutions become more concentrated, the amount of solid that precipitates increases. The co-crystallization of $[Fe^{II}(5dmbpy)_3]_2[Co^{II}(CN)_6]$ is also a possibility for this reaction but this can be removed with MeCN rinses. The scaling up of this reaction (to prepare in a bulk manner analogous to the Fe_3Ru_2 TBPs) was not attempted.

IR spectra for this TBP exhibit very similar $\nu_{C\equiv N}$ stretches to those of the Fe_3Co_2 TBPs with tmphen (8) and 4dmbpy (9). The $\nu_{C\equiv N}$ absorptions at 2177 and

2151 cm^{-1} are assigned to the bridging cyanide and the mode at 2123 cm^{-1} is assigned to the terminal cyanide ligands. The presence of water is evident from the features at 3351, 1623 and 1605 cm^{-1}.

TGA was performed on the sample immediately upon removing it from the SQUID after two cycles of warming to 390 K. The thermogram shows that the TBP loses the majority of the interstitial solvent between room temperature and 60 °C but continues to lose mass until ~100 °C. The TBP is thermally stable up to ~180 C before a very slight loss in mass begins which leads to rapid decomposition at ~270 °C. The total mass loss of 4.8% is attributed to ~4.8 H_2O molecules per TBP.

Fe_3Co_2 tmbpy (11)

This synthesis is more subtle than the synthesis of the TBP with tmphen but is not as challenging as the TBP with the 5dmbpy or 4dmbpy ligands. Controlling the concentration of the solutions in a similar fashion to that of the 5dmbpy congener results in a higher yield of crystal formation and less powder precipitation upon mixing the solutions. When the solutions are mixed, the color of the solution is markedly different from all of the other syntheses as it turns a dark purple color instead of a dark red. The $[Fe^{II}(tmbpy)_3]_2[Co^{II}(CN)_6]$ by-products that co-crystallize with the product can be removed with copious amounts of MeCN. The scaling up of this reaction (to prepare in a bulk manner analogous to the Fe_3Ru_2 TBPs) was not tried.

IR spectra for this TBP correspond well with the previous Fe_3Co_2 TBPs with $\nu_{C\equiv N}$ at 2175, 2166 and 2126 cm^{-1} and stretching/bending bands for interstitial water at 3399, 1641 and 1613 cm^{-1}. Table 5-1 lists the $\nu_{C\equiv N}$ and stretching/bending modes for compounds 8-11 as well as the $\nu_{C\equiv N}$ stretches for $(PPN)_3[Co^{III}(CN)_6]$ for comparison sake.

Table 5-1. The $\nu_{C\equiv N}$ and H_2O stretching/bending modes for compounds **8-11** and $(PPN)_3[Co^{III}(CN)_6]$ for comparison.

Fe_3Co_2 TBPs	**Bridging CN (cm^{-1})**	**Terminal CN (cm^{-1})**	**H_2O Stretching (cm^{-1})**	**H_2O Bending (cm^{-1})**
tmphen (8)	2155	2129	3406	1622
4dmbpy (9)	2164	2130	3352	1617
5dmbpy (10)	2177, 2151	2123	3351	1623, 1605
tmbpy (11)	2175, 2166	2126	3399	1641, 1613
$(PPN)_3[Co^{III}(CN)_6]$	—	2139, 2127 2114, 2106	—	—
Typical Range for Lattice H_2O[122]	—	—	3550–3200	1630–1600

TGA was performed on two samples: a portion of a sample prepared for magnetic measurements and on the sample measured in the SQUID immediately after being removed from the instrument. This procedure was done to compare the amount of solvent in the sample before and after being measured in the SQUID. The sample was warmed to 390 K twice within the SQUID with the

expectation of solvent loss within the instrument. The thermogram of the sample before being measured in the SQUID showed an immediate mass loss between room temperature and 54 °C. The mass loss continues at a more gradual rate after 54 °C until ~150 °C for a total loss of 12.6% of its original mass (~14.9 H_2O molecules per TBP). The TBP is thermally stable until ~190 °C, which is nearly 70 °C lower than the TBP with tmphen as the capping ligand. The thermogram of the sample measure in the SQUID portrays the same attributes as the previous one but has a total mass loss of only 5.2% (~5.7 H_2O molecules per TBP).

Single Crystal X-ray Diffraction

By looking at the disordered electron density in the void spaces, it was determined that both water and MeCN molecules are present in all of the crystal structures. Due to the disorder, the electron density in the voids were SQUEEZED. The amount of solvent was determined by minimizing the differences between the calculated electron density and void space. To do this, 54 Å/MeCN and 40 Å/H_2O molecules were used to determine the volume of space each solvent molecule is estimated to require. A solution using the built-in Excel Solver add-in was obtained so that the calculated number of MeCN molecules per TBP resembled what was estimated from looking at the disordered electron density for each structure. Table 5-2 summarizes the results from the SQUEEZE analysis and calculated solvent content for compounds 8-11.

As the differences in the π-π stacking interactions are at the heart of this study, the focus of the discussion is on these interactions. The interactions will be referred to by intermolecular (inter) or intramolecular (intra) interactions with the color of the planes involved (p is purple, y is yellow, t is teal, r is red and g is green). The structures with the colored planes are provided for each TBP with a different ligand. The teal planes are on ligands coordinated to the Fe(1) and Fe(2) centers, the red planes are on ligands coordinated to the Fe(2) and Fe(3) centers and the green planes are on ligands coordinated to the Fe(1) and Fe(3) centers. The purple and yellow planes are on the same ligand as each other and are coordinated to the Fe(3) center of the two TBPs related by an inversion center.

Table 5-2. SQUEEZE analysis and calculated interstitial solvent for compounds **8-11**.

Fe_3Co_2 TBP (Ligand)	Temp (K)	Void Space (Å)	Number of Electrons	% Void Space	H_2O	MeCN
tmphen (8)	15	2949	698	26.1	8.9	6.2
	50	2954	698	26.2	9.3	5.9
	100	2982	692	26.3	8.6	6.4
	150	3064	655	26.7	8.3	6.8
	200	3164	648	27.3	9.6	6.2
	220	3225	650	27.7	9.7	6.4
	Average	**2620**	**674**	**26.7**	**9.1**	**6.3**
4dmbpy (9)	20	2558	679	26.6	12.4	2.5
	100	2593	684	26.9	12.6	2.5
	200	2732	692	27.9	13.0	2.7
	250	2863	647	28.7	14.2	2.2
	Average	**2687**	**676**	**27.5**	**13.0**	**2.5**
5dmbpy (10)	110	**2841**	**856**	**28.5**	**10.4**	**5.3**
tmbpy (11)	20	2697	725	26.2	10.0	5.4
	50	2899	756	26.0	9.2	5.9
	100	2878	763	28.5	11.1	5.5
	150	3190	715	28.8	11.2	5.7
	200	3307	705	29.1	11.2	5.8
	250	3356	686	29.1	11.3	5.9
	Average	**2697**	**725**	**28.0**	**10.7**	**5.7**

Fe_3Co_2 tmphen (8)

This TBP crystallizes in the usual *$P2_1/c$* space group in which most other TBPs with tmphen crystallize. The asymmetric unit of 8 can be seen in Figure 5-2, the structural data and cell parameters are in Table 5-3 and Table 5-4 lists the

M–L bond lengths at various temperatures. All of these details are consistent with the reported structure.[145] As this TBP has been studied thoroughly by previous group members, it is known that there is no CTIST behavior expected. The TBP consists of 2 LS Co^{III} centers and 3 Fe^{II} centers that undergo a LS ↔ HS transition as temperature is changed. As stated before, the average Fe–N_6 bond lengths are very telling as to the spin state of the Fe^{II} center as they change ~0.2 Å from the LS to HS state. At 20 K, all 3 Fe^{II} centers have an average Fe–N bond length of ~1.97 Å but as temperature increases, it becomes clear that the Fe(3) center is undergoing a gradual SCO. At 220 K, the Fe(1) and Fe(2) centers still have average Fe–N bond lengths ~1.98 Å but the Fe(3) center has an average Fe–N bond length of 2.14 Å. When the π-π stacking interactions are taken into account, it becomes evident that the Fe(3) center is being stabilized by the intermolecular interaction within the dimeric unit and is the first center to undergo SCO with a change in temperature as a result.

Table 5-3. Crystal structure data and refinement parameters for the Fe_3Co_2 TBP with tmphen (8).

Fe_3Co_2 tmphen (8)	**15 K**	**50 K**	**100 K**	**150 K**	**200 K**	**220 K**
Space Group	*P*2$_1$/*c*	*P*2$_1$/*c*	*P*2$_1$/*c*	*P*2$_1$/*c*	*P*2$_1$/*c*	*P*2$_1$/*c*
a/ Å	18.8722(6)	18.8686(5)	18.8945(5)	18.9446(9)	19.0530(5)	19.0810(5)
b/ Å	24.7681(8)	24.7635(7)	24.8106(7)	24.8932(12)	24.9734(7)	25.0057(7)
c/ Å	24.3977(8)	24.3901(7)	24.4446(7)	24.5078(12)	24.6142(7)	24.6491(7)
β/ °	97.5740(10)	97.5990(10)	97.5810(10)	97.559(3)	97.6090(10)	97.6410(10)
Volume/ Å^3	11304.7(6)	11296.2(5)	11359.1(5)	11457.2(10)	11608.8(6)	11850.2(6)
[a]Interstitial Solvent	6 MeCN 9 H_2O	6 MeCN 9 H_2O	6 MeCN 9 H_2O	7 MeCN 8 H_2O	6 MeCN 10 H_2O	6 MeCN 10 H_2O
μ/ mm^{-1}	0.861	0.860	0.857	0.850	0.839	0.835
Crystal Size/ mm^3 Habitat	0.564 × 0.244 x 0.094 Dark, red needle					
2Θ Range for Data Collection/ °	4.3 to 56.698	4.302 to 57.456	4.08 to 58.26	4.068 to 52.63	4.264 to 56.394	4.258 to 57.408
Independent Reflections	21737 R_{int} = 0.0679 R_{sigma} = 0.0433	22403 R_{int} = 0.0640 R_{sigma} = 0.0417	23407 R_{int} = 0.0650 R_{sigma} = 0.0415	17758 R_{int} = 0.0678 R_{sigma} = 0.0385	22036 R_{int} = 0.0606 R_{sigma} = 0.0366	23155 R_{int} = 0.0540 R_{sigma} = 0.0344
Data/Restraints/ Parameters	21737/54/1257	22403/51/1257	23407/51/1257	17758/60/1255	22036/0/1257	23155/0/1256
[b]GooF on F^2	1.077	1.082	1.089	1.072	1.050	1.049
[c,d]Final R Indexes [I>=2σ (I)]	R_1 = 0.1108 wR_2 = 0.2506	R_1 = 0.1130 wR_2 = 0.2520	R_1 = 0.1105 wR_2 = 0.2488	R_1 = 0.0922 wR_2 = 0.2305	R_1 = 0.0599 wR_2 = 0.1610	R_1 = 0.0561 wR_2 = 0.1501
[c,d]Final R Indexes [all data]	R_1 = 0.1339 wR_2 = 0.2650	R_1 = 0.1355 wR_2 = 0.2657	R_1 = 0.1347 wR_2 = 0.2646	R_1 = 0.1140 wR_2 = 0.2478	R_1 = 0.0860 wR_2 = 0.1820	R_1 = 0.0830 wR_2 = 0.1710
Largest Diff. Peak / Hole/ e Å^{-3}	2.12 / -0.84	2.19 / -0.93	2.19 / -0.90	2.40 / -0.76	1.64 / -0.68	1.36 / -0.59

Radiation = synchrotron (λ = 0.7749), α = γ = 90°, Z = 4, [a]*Calculated from SQUEEZE data.* [b]GooF: Goodness-of-fit = $\{\sum[w(F_o^2 - F_c^2)^2]/(n-p)\}^{1/2}$, where *n* is the number of reflections and *p* is the total number of parameters refined. [c]$R = \sum||F_o|-|F_c||/\sum|F_o|$. [d]$wR = \{\sum[w(F_o^2 - F_c^2)^2]/\sum w(F_o^2)^2]\}^{1/2}$.

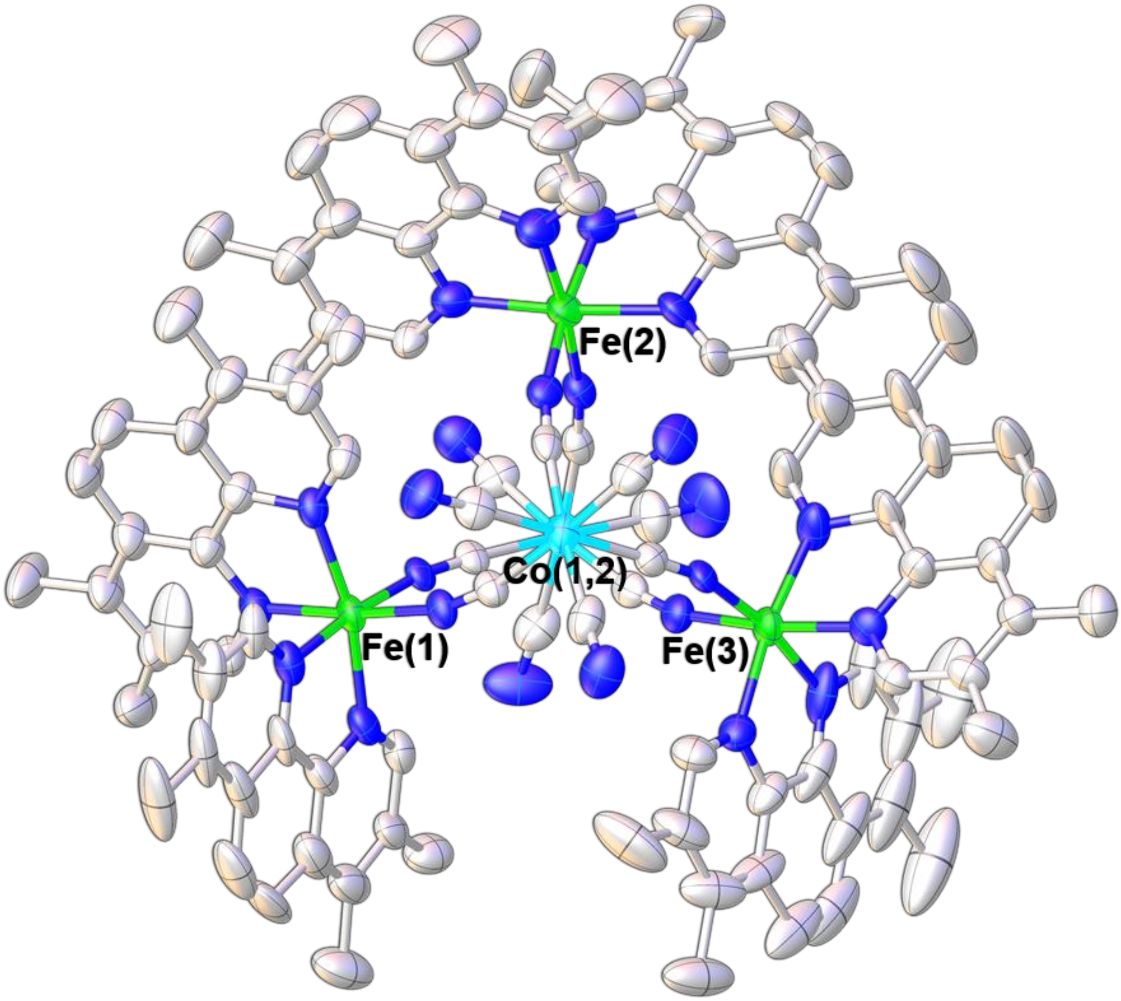

Figure 5-2. Asymmetric unit of the Fe_3Co_2 TBP looking down the axial metal centers. Color scheme: Co is cyan, Fe is green, N is blue and C is grey. Hydrogen atoms have been omitted for the sake of clarity.

Table 5-4. The M–L bond distances (in Å) for the Fe_3Co_2 TBP with tmphen (8).

Temperature	Fe(1)–N	Fe(2)–N	Fe(3)–N	Co(1)–C	Co(2)–C
15 K	1.936 (6)	1.924 (7)	1.946 (6)	1.883 (8)	1.878 (1)
	1.945 (6)	1.937 (6)	1.962 (7)	1.887 (8)	1.878 (8)
	1.975 (6)	1.956 (7)	1.990 (1)	1.891 (10)	1.895 (7)
	1.986 (1)	1.965 (8)	1.991 (8)	1.896 (1)	1.913 (9)
	1.987 (7)	1.975 (7)	1.992 (7)	1.911 (8)	1.917 (8)
	1.995 (6)	1.979 (7)	2.014 (6)	1.911 (8)	1.928 (7)
Avg M–L	**1.971 (5)**	**1.956 (7)**	**1.983 (6)**	**1.897 (7)**	**1.902 (7)**
50 K	1.938 (6)	1.928 (7)	1.947 (6)	1.886 (8)	1.880 (8)
	1.951 (6)	1.938 (6)	1.964 (7)	1.888 (8)	1.880 (10)
	1.979 (6)	1.953 (7)	1.995 (7)	1.889 (10)	1.892 (7)
	1.986 (6)	1.966 (7)	1.996 (8)	1.898 (7)	1.903 (9)
	1.987 (7)	1.976 (7)	1.998 (7)	1.908 (8)	1.916 (8)
	1.998 (6)	1.981 (7)	2.019 (6)	1.917 (8)	1.921 (7)
Avg M–L	**1.973 (6)**	**1.957 (7)**	**1.987 (7)**	**1.898 (8)**	**1.899 (8)**
100 K	1.932 (5)	1.931 (7)	1.943 (6)	1.887 (7)	1.878 (8)
	1.952 (6)	1.938 (6)	1.965 (7)	1.889 (9)	1.888 (9)
	1.981 (6)	1.962 (7)	1.990 (7)	1.890 (8)	1.894 (6)
	1.983 (6)	1.967 (7)	1.990 (6)	1.905 (7)	1.900 (9)
	1.984 (6)	1.978 (6)	1.996 (7)	1.906 (8)	1.911 (8)
	1.997 (6)	1.981 (6)	2.022 (6)	1.917 (8)	1.925 (7)
Avg M–L	**1.972 (6)**	**1.960 (7)**	**1.984 (7)**	**1.899 (8)**	**1.899 (8)**
150 K	1.929 (6)	1.941 (6)	1.976 (6)	1.890 (8)	1.879 (7)
	1.954 (6)	1.942 (6)	2.001 (7)	1.891 (9)	1.882 (9)
	1.976 (6)	1.960 (7)	2.014 (7)	1.896 (8)	1.892 (7)
	1.980 (6)	1.970 (6)	2.035 (7)	1.898 (9)	1.896 (8)
	1.994 (6)	1.973 (6)	2.047 (9)	1.898 (8)	1.902 (8)
	2.007 (6)	1.989 (6)	2.077 (6)	1.903 (7)	1.935 (7)
Avg M–L	**1.973 (6)**	**1.963 (6)**	**2.025 (7)**	**1.896 (8)**	**1.898 (8)**
200 K	1.949 (4)	1.941 (3)	2.046 (4)	1.895 (5)	1.883 (4)
	1.975 (3)	1.943 (4)	2.077 (4)	1.898 (5)	1.889 (4)
	1.978 (4)	1.968 (4)	2.135 (4)	1.900 (4)	1.893 (5)
	1.985 (4)	1.973 (3)	2.173 (4)	1.901 (5)	1.902 (4)
	1.993 (3)	1.976 (4)	2.175 (4)	1.902 (4)	1.907 (5)
	2.002 (3)	1.982 (3)	2.194 (4)	1.906 (5)	1.927 (4)
Avg M–L	**1.980 (4)**	**1.964 (4)**	**2.133 (4)**	**1.900 (5)**	**1.900 (4)**
220 K	1.953 (3)	1.945 (3)	2.057 (3)	1.894 (4)	1.883 (4)
	1.981 (3)	1.946 (3)	2.090 (4)	1.894 (5)	1.890 (4)
	1.987 (3)	1.969 (3)	2.148 (3)	1.896 (4)	1.894 (4)
	1.993 (3)	1.975 (3)	2.184 (4)	1.902 (4)	1.906 (4)
	2.005 (3)	1.976 (3)	2.187 (3)	1.902 (4)	1.907 (4)
	2.010 (3)	1.981 (3)	2.194 (4)	1.906 (5)	1.925 (4)
Avg M–L	**1.988 (3)**	**1.965 (3)**	**2.143 (4)**	**1.899 (4)**	**1.901 (4)**

The π-π stacking interactions present in the Fe_3Co_2 TBP containing tmphen ligands are very similar to those present in the Zn_3Os_2 and Fe_3Ru_2 TBPs discussed already. There are two intermolecular interactions involving the Fe(3) centers in two TBPs and two intramolecular interactions involving the Fe(1) with the Fe(2) center and the Fe(2) with the Fe(3) center. Figure 5-3 portrays the intermolecular interactions that occur between the two TBPs that stack in a dimeric unit. For compound 8, as with the other TBPs, the intermolecular interactions are the strongest of the π-π stacking interactions with the inter-pp being stronger than the inter-py interaction owing to the shortest centroid-centroid and shift distances. The geometric parameters (Table 5-5) remain relatively constant as temperature changes except for the shift distance between the centroids in the inter-pp interactions. As compared to the lower temperature structures, the 200 and 220 K structures show a significant decrease in the shift distance between centroids. These temperatures coincide with the Fe(3) center involved in this intermolecular interaction becoming HS, according to the average Fe–N bond length. The intramolecular interactions are weak and as temperature increases above 200 K, the shift distances and angles between the planes increase. Figure 5-4 portrays the intramolecular interactions and Figure 5-5 shows how the compound packs down the *a*-axis with the planes intact to offer perspective.

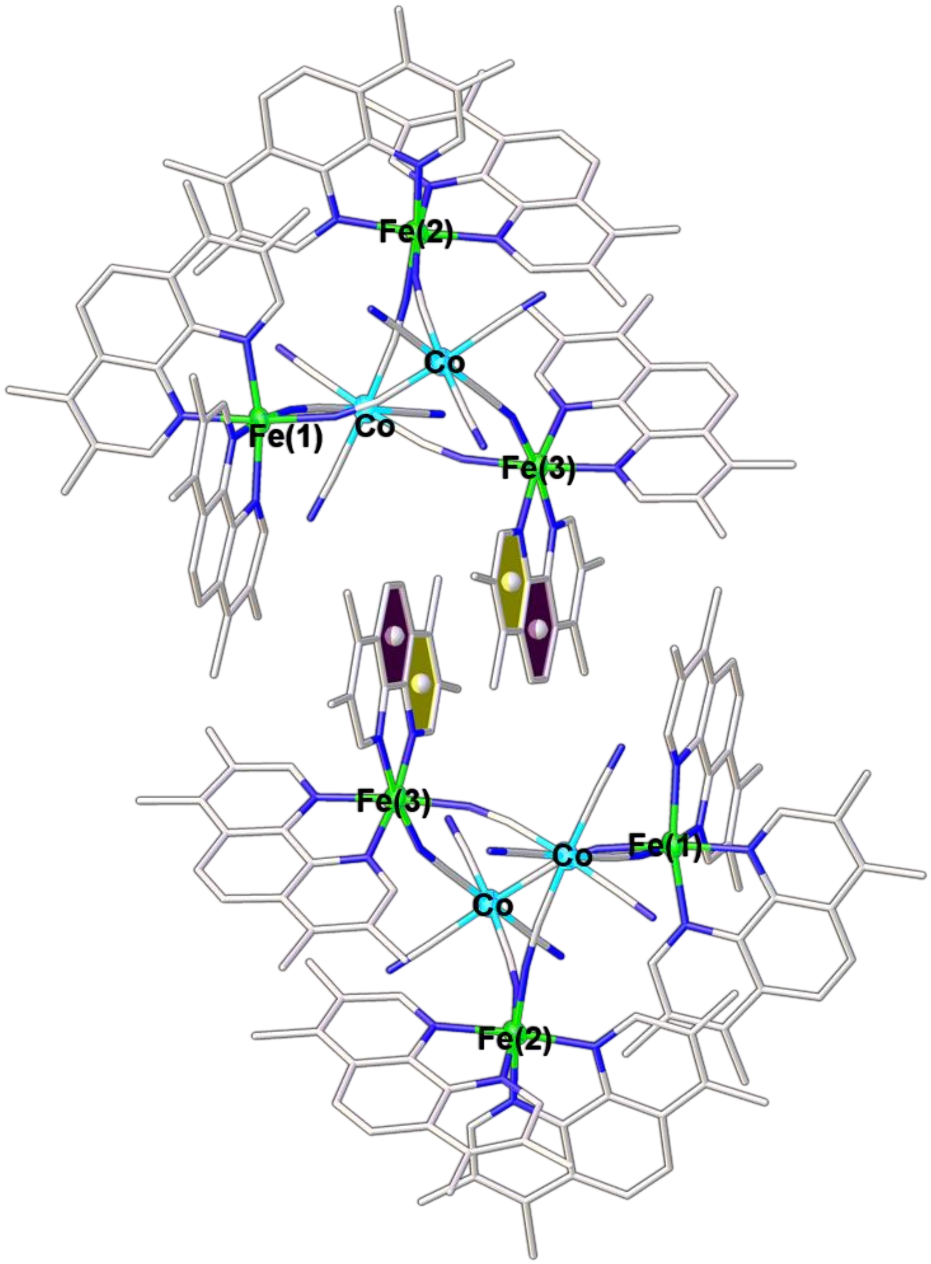

Figure 5-3. View of the dimeric unit of the Fe_3Co_2 TBP with tmphen ligands (8). The purple and yellow colored planes are the rings within the tmphen ligands that are involved in the intermolecular interactions.

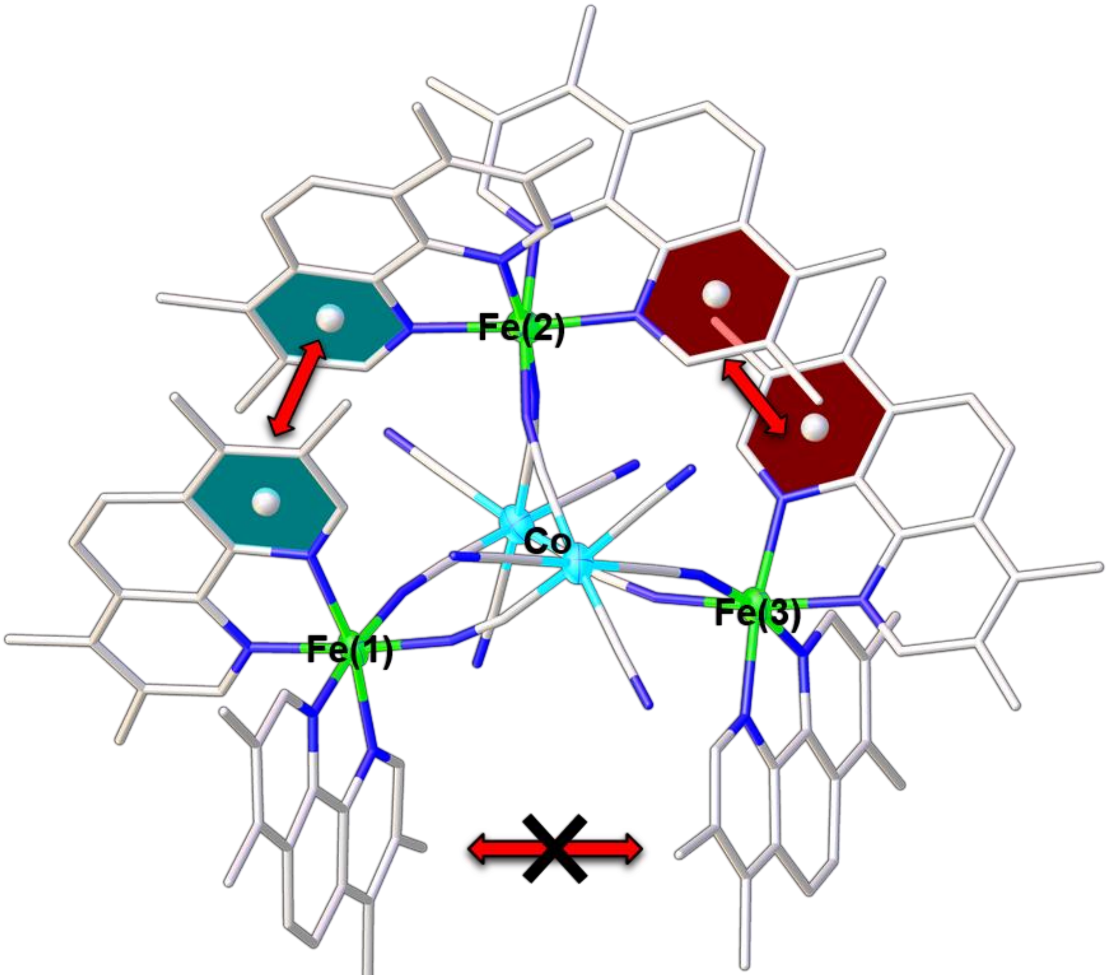

Figure 5-4. Depiction of the intramolecular interactions in the Fe_3Co_2 TBP with tmphen (8). Arrows indicate the interaction between the planes.

Table 5-5. Geometric parameters (centroid-centroid distance, shift distance and angle) for the inter- and intramolecular π-π stacking interactions in the Fe_3Co_2 TBP with tmphen (8). The average values (avg) and the differences between the minimum and maximum values (Δ) have been included. *Indicates symmetry equivalent metal center.

Interaction-Plane Fe Centers Involved	Temperature	Centroid-Centroid Distance (Å)	Shift Distance (Å)	Angle (º)
inter-pp Fe(3) – Fe(3)*	15 K	3.495	1.187	0
	50 K	3.492	1.170	0
	100 K	3.506	1.216	0
	150 K	3.461	1.031	0
	200 K	3.459	0.732	0
	220 K	3.473	0.746	0
	Avg	**3.481**	**1.014**	**0**
	Δ	0.047	0.484	0
inter-py Fe(3) – Fe(3)*	15 K	3.634	1.613	1.778
	50 K	3.638	1.619	1.773
	100 K	3.633	1.596	1.449
	150 K	3.638	1.579	1.785
	200 K	3.748	1.666	1.096
	220 K	3.756	1.660	1.034
	Avg	**3.675**	**1.622**	**1.486**
	Δ	0.123	0.087	0.751
intra-tt Fe(1) – Fe(2)	15 K	3.761	1.288	4.201
	50 K	3.762	1.286	4.048
	100 K	3.767	1.288	4.050
	150 K	3.780	1.318	4.259
	200 K	3.799	1.352	4.767
	220 K	3.809	1.363	4.907
	Avg	**3.780**	**1.316**	**4.372**
	Δ	0.048	0.077	0.859
intra-rr Fe(2) – Fe(3)	15 K	3.769	1.390	5.154
	50 K	3.763	1.388	5.455
	100 K	3.764	1.385	5.294
	150 K	3.797	1.399	5.551
	200 K	3.883	1.505	6.943
	220 K	3.890	1.516	6.948
	Avg	**3.811**	**1.431**	**5.891**
	Δ	0.127	0.131	1.794

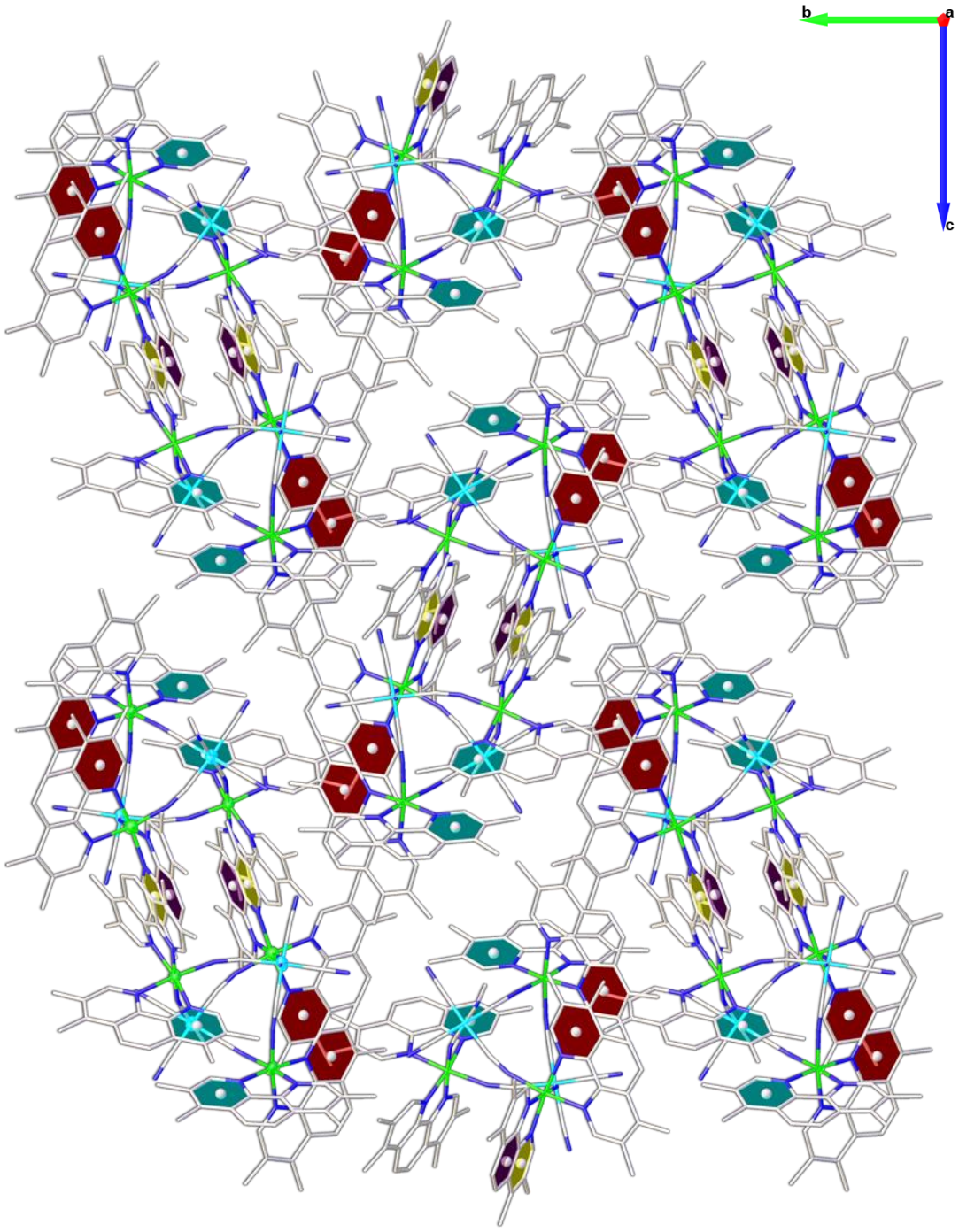

Figure 5-5. Packing diagram looking down the *a*-axis for compound 8. The colored planes offer perspective and help distinguish the packing of the dimeric unit. Color scheme: Co is cyan, Fe is green, N is blue and C is grey. Hydrogen atoms have been omitted for the sake of clarity.

Fe_3Co_2 4dmbpy (9)

The Fe_3Co_2 TBP with 4dmbpy ligands coordinated to the equatorial Fe^{II} centers crystallizes in the $P2_1/n$ space group which is equivalent to $P2_1/c$ through the transformation matrix (0 0 -1 0 1 0 1 0 -1). The unit cells are slightly different than the tmphen cousins as they have three distinct cell edge lengths instead of two as in the case of the tmphen containing TBPs. The structural parameters for several temperatures are in Table 5-6, the relevant M–L bond lengths are in Table 5-7 and the asymmetric unit can be seen in Figure 5-6. The structure obtained at 20 K was taken on a different crystal than the structures obtained at 100, 200 and 250 K which were all collected on the same crystal. Throughout the 20 – 250 K range, all of the Fe^{II}–N bond lengths are shorter than 2.0 Å suggesting that all of the Fe centers remain LS below 250 K. The Fe(2) center shows a slight lengthening in the average Fe–N bond length at 250 K compared to the other Fe centers suggesting that this center is the first to undergo a SCO event from LS → HS as temperature is increased above 250 K.

Table 5-6. Structural data and cell refinement parameters for compound 9 at variable temperatures. Structural data at 20 K is for a different crystal than the data at 100, 200 and 250 K which were obtained on the same crystal.

Fe_3Co_2 4dmbpy (9)	**20 K**	**100 K**	**200 K**	**250 K**
Space Group	*P*2$_1$/*n*	*P*2$_1$/*n*	*P*2$_1$/*n*	*P*2$_1$/*n*
a/ Å	20.6763(7)	20.6052(9)	20.6988(9)	21.1144(5)
b/ Å	18.4954(6)	18.5218(9)	18.6027(8)	17.8678(4)
c/ Å	25.2796(8)	25.4483(12)	25.6542(12)	26.8639(6)
β/ °	96.657(2)	97.228(3)	97.378(3)	100.6440(10)
Volume/ Å^3	9602.2(5)	9635.0(8)	9796.5(8)	9960.5(4)
[a]Interstitial Solvent	2 MeCN 12 H_2O	3 MeCN 13 H_2O	3 MeCN 13 H_2O	2 MeCN 14 H_2O
μ/ mm^{-1}	1.005	1.001	0.985	0.969
Crystal Size/ mm^3 Habitat	0.113 x 0.094 x 0.047 Dark, Red Needle		0.075 x 0.047 x 0.028 Dark, Red Needle	
2Θ Range for Data Collection/ °	4.276 to 59.808	4.258 to 49.542	4.23 to 45.882	4.182 to 57.316
Independent Reflections	21294 R_{int} = 0.0872 R_{sigma} = 0.0696	12642 R_{int} = 0.1064 R_{sigma} = 0.0.630	10364 R_{int} = 0.0971 R_{sigma} = 0.0531	19703 R_{int} = 0.0708 R_{sigma} = 0.0464
Data/Restraints/ Parameters	21294/0/1030	12642/0/1030	10364/0/1030	19703/0/1030
[b]GooF on F^2	1.049	1.072	1.049	1.035
[c,d]Final R Indexes [I>=2σ (I)]	R_1 = 0.0517 wR_2 = 0.1187	R_1 = 0.0932 wR_2 = 0.2763	R_1 = 0.0951 wR_2 = 0.2849	R_1 = 0.0434 wR_2 = 0.1151
[c,d]Final R Indexes [all data]	R_1 = 0.0764 wR_2 = 0.1284	R_1 = 0.1231 wR_2 = 0.3027	R_1 = 0.1210 wR_2 = 0.3107	R_1 = 0.0696 wR_2 = 0.1279
Largest Diff. Peak / Hole/ e Å^{-3}	0.69 / -0.59	1.52 / -0.64	1.06 / -0.59	0.50 / -0.31

Radiation = synchrotron (λ = 0.7749), α = γ = 90°, Z = 4, [a]*Calculated from SQUEEZE data.* [b]GooF: Goodness-of-fit = $\{\sum[w(F_o^2 - F_c^2)^2]/(n-p)\}^{1/2}$, where *n* is the number of reflections and *p* is the total number of parameters refined. [c]$R = \sum ||F_o| - |F_c|| / \sum |F_o|$. [d]$wR = \{\sum[w(F_o^2 - F_c^2)^2] / \sum w(F_o^2)^2]\}^{1/2}$..

Table 5-7. The M–L bond distances (in Å) for the Fe_3Co_2 TBP with 4dmbpy (9).

Temperature	Fe(1)–N	Fe(2)–N	Fe(3)–N	Co(1)–C	Co(2)–C
20 K	1.943 (3)	1.934 (3)	1.937 (3)	1.887 (4)	1.892 (3)
	1.964 (3)	1.937 (3)	1.963 (3)	1.888 (4)	1.897 (4)
	1.965 (3)	1.947 (3)	1.965 (3)	1.897 (3)	1.898 (4)
	1.967 (3)	1.962 (3)	1.967 (3)	1.897 (3)	1.901 (4)
	1.983 (3)	1.970 (3)	1.985 (3)	1.898 (4)	1.902 (3)
	1.985 (3)	1.976 (3)	1.986 (3)	1.921 (3)	1.916 (3)
Avg M–L	**1.968 (3)**	**1.954 (3)**	**1.967 (3)**	**1.898 (4)**	**1.901 (4)**
100 K	1.944 (10)	1.916 (10)	1.932 (10)	1.900 (12)	1.885 (12)
	1.959 (9)	1.935 (10)	1.966 (9)	1.904 (13)	1.898 (13)
	1.965 (8)	1.949 (10)	1.970 (8)	1.906 (11)	1.900 (11)
	1.969 (8)	1.959 (8)	1.979 (8)	1.917 (11)	1.902 (12)
	1.979 (8)	1.966 (9)	1.981 (9)	1.926 (13)	1.906 (12)
	1.994 (8)	1.980 (9)	1.986 (8)	1.948 (13)	1.918 (13)
Avg M–L	**1.968 (9)**	**1.951 (9)**	**1.969 (9)**	**1.917 (12)**	**1.902 (12)**
200 K	1.947 (13)	1.921 (13)	1.927 (11)	1.886 (17)	1.864 (15)
	1.958 (11)	1.932 (12)	1.972 (10)	1.887 (16)	1.883 (14)
	1.977 (10)	1.937 (11)	1.974 (9)	1.892 (17)	1.883 (17)
	1.978 (10)	1.944 (10)	1.981 (9)	1.905 (14)	1.886 (15)
	1.980 (10)	1.970 (10)	1.985 (9)	1.924 (15)	1.917 (14)
	2.002 (9)	1.979 (10)	1.986 (11)	1.941 (16)	1.925 (16)
Avg M–L	**1.974 (11)**	**1.947 (11)**	**1.971 (10)**	**1.906 (16)**	**1.893 (15)**
250 K	1.944 (2)	1.963 (3)	1.926 (3)	1.898 (4)	1.887 (3)
	1.963 (2)	1.974 (3)	1.967 (3)	1.900 (3)	1.896 (3)
	1.968 (2)	1.994 (3)	1.967 (3)	1.902 (3)	1.900 (3)
	1.970 (3)	2.002 (3)	1.971 (3)	1.902 (3)	1.901 (3)
	1.973 (2)	2.005 (3)	1.972 (3)	1.903 (3)	1.903 (4)
	1.990 (2)	2.012 (3)	1.980 (3)	1.909 (3)	1.912 (3)
Avg M–L	**1.968 (2)**	**1.992 (3)**	**1.964 (3)**	**1.902 (3)**	**1.900 (3)**

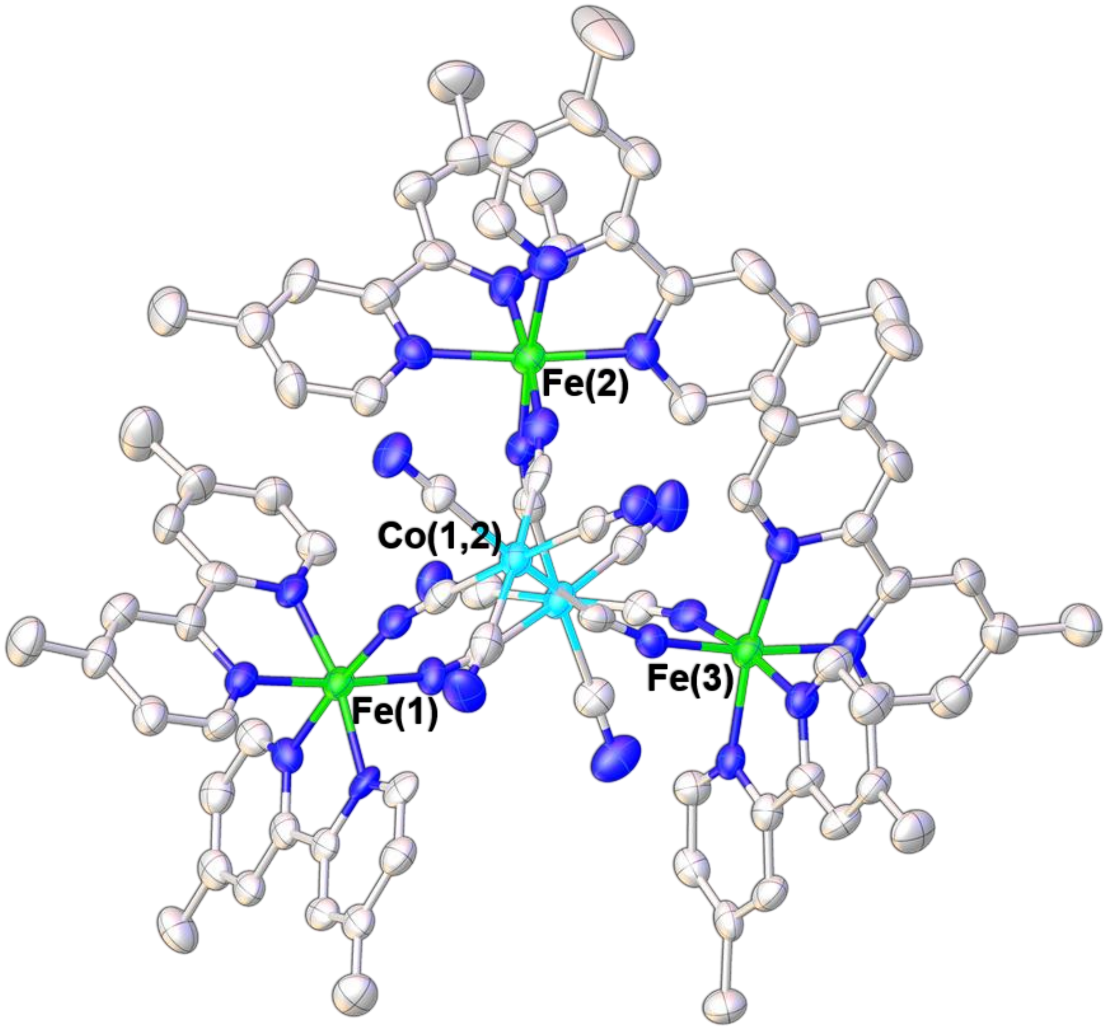

Figure 5-6. Asymmetric unit of the Fe_3Co_2 TBP at 100 K with 4dmbpy coordinated to the equatorial Fe centers. Color scheme: Co is cyan, Fe is green, N is blue and C is grey. Hydrogen atoms have been omitted for the sake of clarity.

Analysis of the π-π stacking interactions with Olex2 reveals a decrease in the number of intermolecular interactions from two in the TBP with tmphen, to one in this TBP. Figure 5-7 depicts the intermolecular interaction that involves the Fe(3) centers in the dimeric unit and Figure 5-8 portrays the intramolecular interactions that occur between the 4dmbpy ligands in an analogous fashion to those between tmphen ligands. The inter-py is the strongest interaction of the three total π-π interactions as the inter-pp is no longer an interaction in this molecule. The centroid-centroid distance decreases slightly from 20 K to 250 K and the shift distance between centroids decreases significantly from 1.69 Å at 20 K to 1.02 Å at 250 K. The intra-rr interaction is very weak at 20 K with a centroid-centroid distance of 3.98 Å and becomes undetectable by Olex2 at 100 and 200 K with centroid-centroid distances greater than 4 Å. At 250 K this interaction is strengthened as the centroid-centroid distance becomes 3.78 Å. Table 5-8 lists the relevant geometric parameters and Figure 5-9 shows how the compound packs down the *a*-axis with the planes intact to offer perspective.

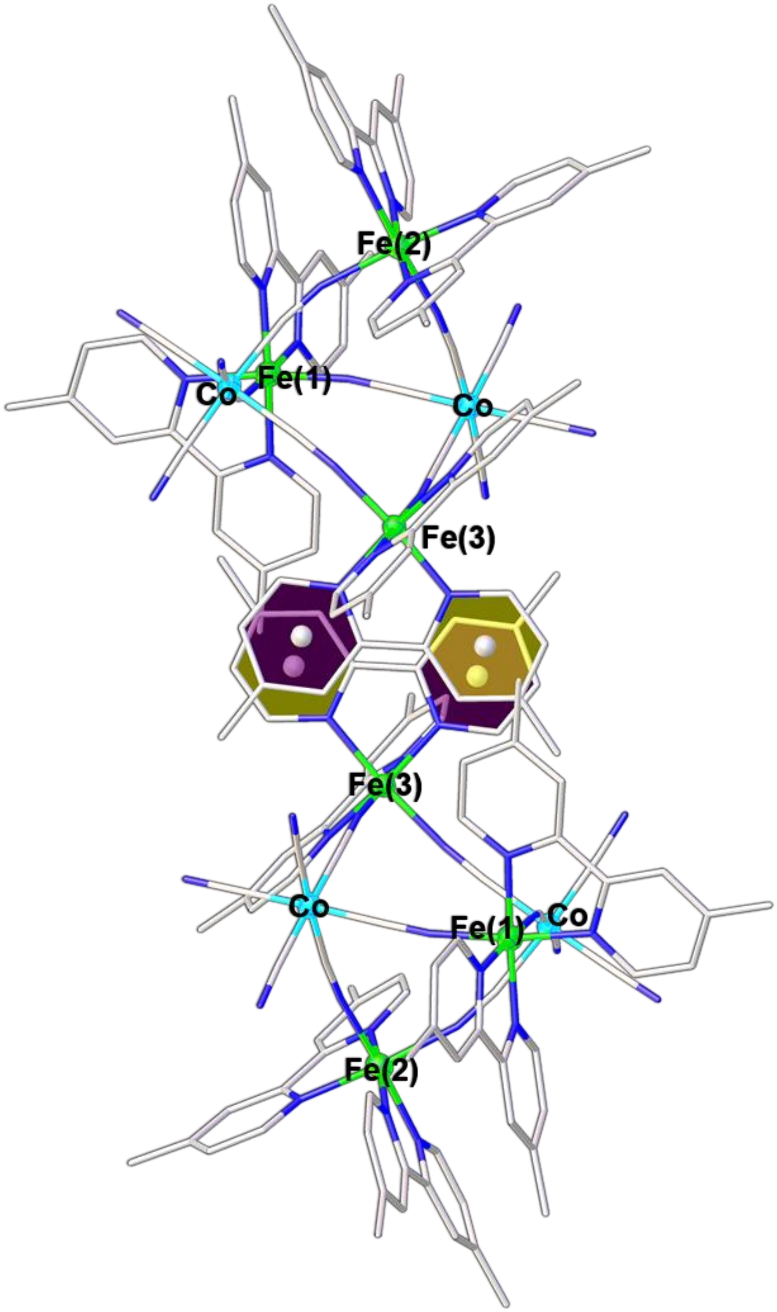

Figure 5-7. View of intermolecular π-π stacking interactions in the Fe_3Co_2 TBP with 4dmbpy (9). The purple and yellow planes portray the inter-py interaction.

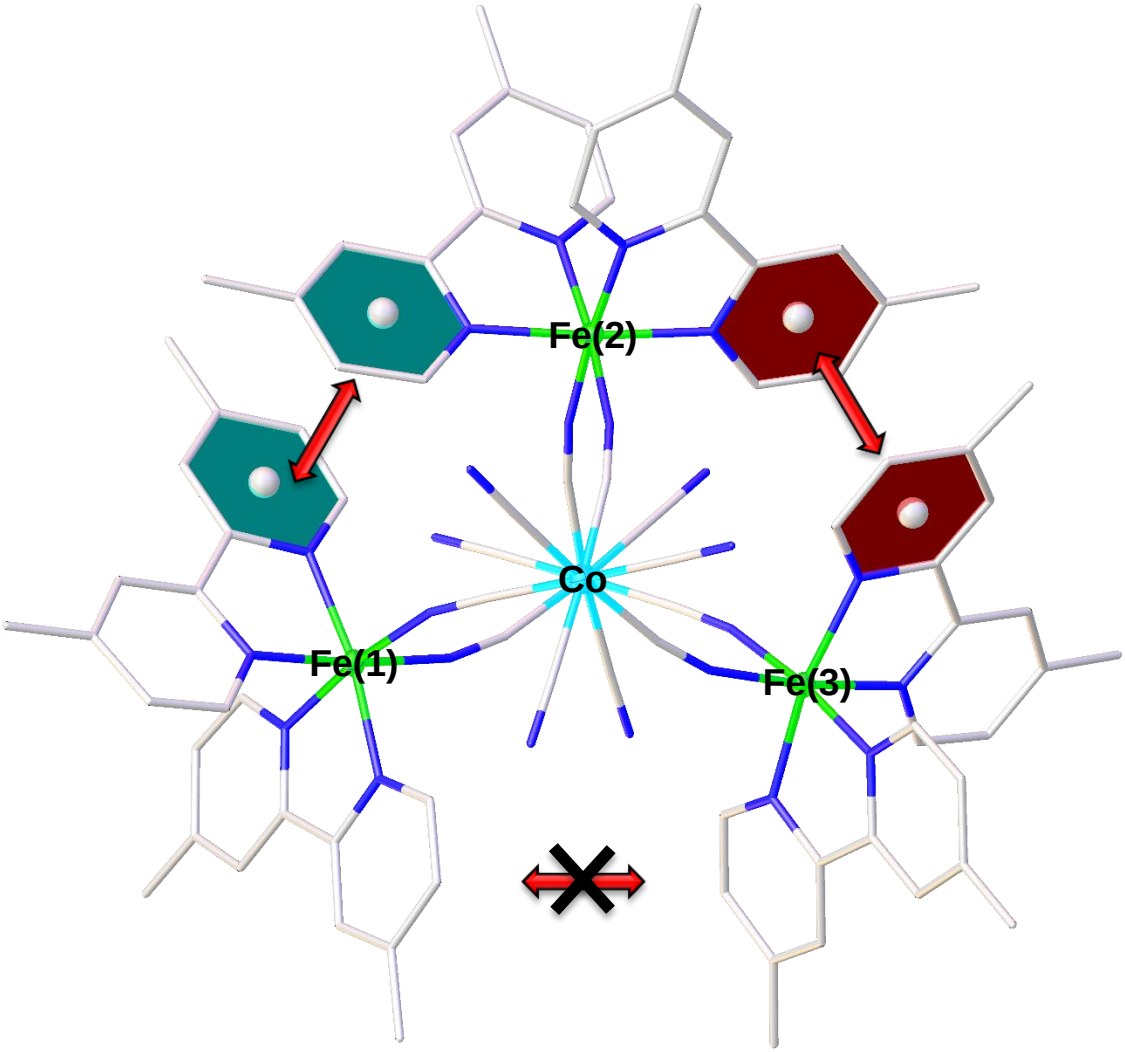

Figure 5-8. View of the intramolecular interactions in the Fe_3Co_2 TBP with the 4dmbpy ligands. The teal colored planes denote the intra-tt interaction and the red colored planes portray the intra-rr interaction.

Table 5-8. Geometric parameters (centroid-centroid distance, shift distance and angle) for the inter- and intramolecular π-π stacking interactions in the Fe_3Co_2 TBP with 4dmbpy (9). The average values (avg) and the differences between the minimum and maximum values (Δ) have been included. *Indicates symmetry equivalent metal center.

Interaction-Plane Fe Centers Involved	Temperature	Centroid-Centroid Distance (Å)	Shift Distance (Å)	Angle (º)
inter-py **Fe(3) – Fe(3)***	20 K	3.557	1.691	8.939
	100 K	3.543	1.675	8.938
	200 K	3.579	1.710	8.906
	250 K	3.513	1.015	9.157
	Avg	**3.548**	**1.523**	**8.985**
	Δ	0.066	0.695	0.251
intra-tt **Fe(1) – Fe(2)**	20 K	3.743	1.106	6.798
	100 K	3.759	1.049	8.873
	200 K	3.778	1.015	9.407
	250 K	3.779	1.106	7.593
	Avg	**3.765**	**1.069**	**8.168**
	Δ	0.036	0.091	2.609
intra-rr **Fe(2) – Fe(3)**	20 K	3.983	1.749	12.621
	100 K	—	—	—
	200 K	—	—	—
	250 K	3.779	1.022	9.377
	Avg	**3.881**	**1.386**	**10.999**
	Δ	0.204	0.727	3.244

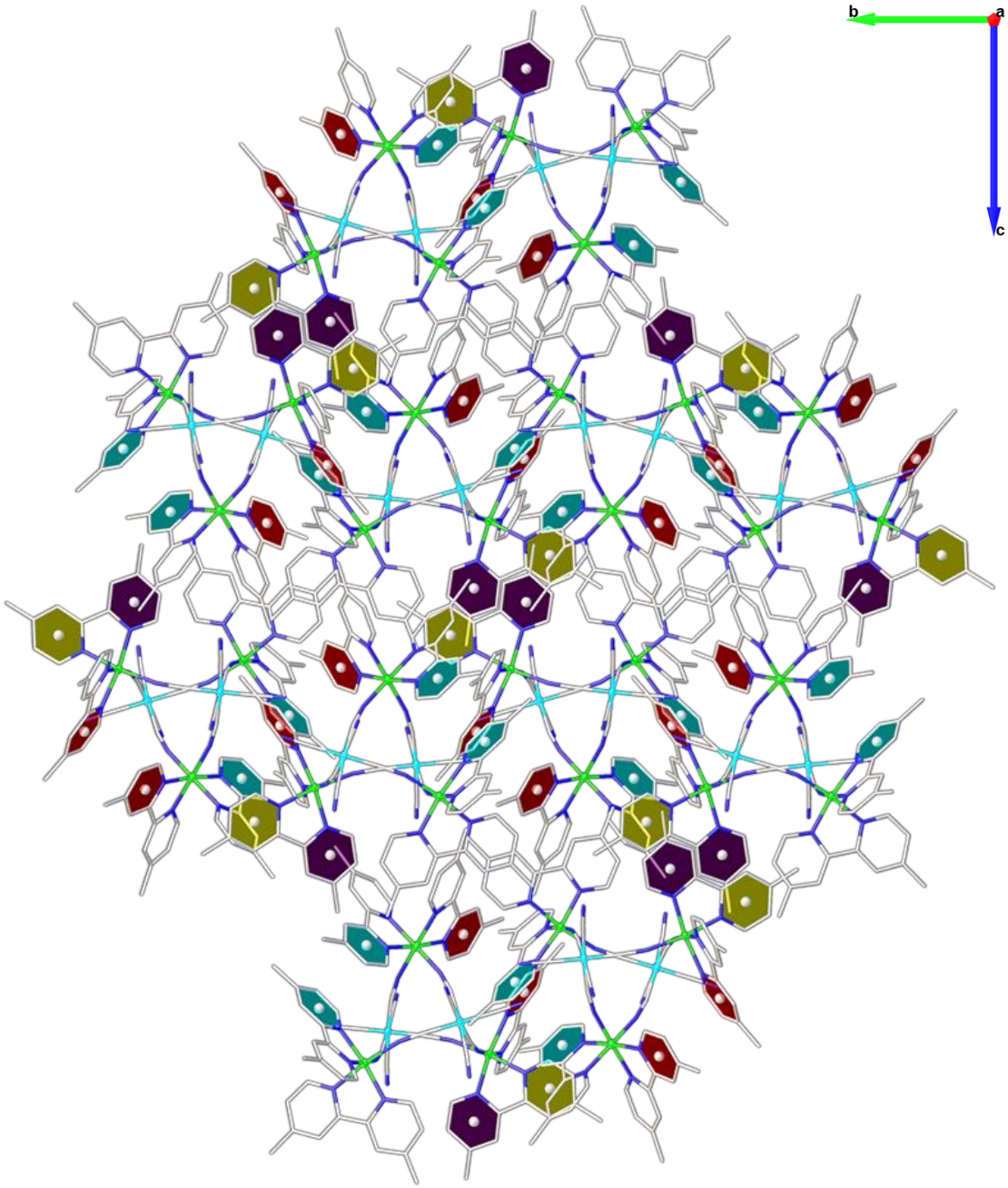

Figure 5-9. Packing diagram looking down the *a*-axis for compound 9. The colored planes offer perspective and help distinguish the packing of the dimeric unit. Color scheme: Co is cyan, Fe is green, N is blue and C is grey. Hydrogen atoms have been omitted for the sake of clarity.

Fe_3Co_2 5dmbpy (10)

Unlike any other TBP studied by the Dunbar group, the Fe_3Co_2 TBP with 5dmbpy ligands coordinated to the equatorial Fe centers crystallizes in the orthorhombic space group of *Pca*2_1. Refer to Table 5-9 for the unit cell and structural data. The structure was collected at 110 K (Figure 5-10) and has average Co^{III}–C bond lengths consistent with those found in the Fe_3Co_2 tmphen and 4dmbpy structures. The average Fe^{II}–N bond lengths for all 3 Fe centers are ~1.96 Å (Table 5-10) which is typical for LS Fe^{II} ions surrounded by nitrogen atoms in an octahedral environment. As no variable temperature data were obtained, the specific Fe center that undergoes SCO cannot be discerned.

Table 5-9. Crystal structure data and refinement parameters for the Fe_3Co_2 TBP with 5dmbpy (10).

Fe_3Co_2 5dmbpy (10)			
Crystal System	Orthorhombic	**Space Group**	*Pca*2_1
Temperature	110 K	**Formula**	$C_{84}N_{24}H_{72}Fe_3Co_2$
a/ Å	25.109(6)	**b/ Å**	15.821(4)
c/ Å	25.060(6)	**α = β = γ/ °**	90
Volume/ Å^3	9955(4)	**Z**	4
[a]Interstitial Solvent	5 MeCN 10 H_2O	**Radiation**	MoK$_\alpha$ (λ = 0.71073)
μ/ mm^{-1}	0.802	**Crystal Habitat**	Dark Red Block
2Θ Range for Data Collection/ °	2.574 to 54.37	**Independent Reflections**	21996 R_{int} = 0.0575 R_{sigma} = 0.0514
Data/Restraints/ Parameters	21996/1/1026	**[b]GooF on F^2**	1.034
[c,d]Final R Indexes [I>=2σ (I)]	R_1 = 0.0390 wR_2 = 0.0834	**[c,d]Final R Indexes [all data]**	R_1 = 0.0502 wR_2 = 0.0884
Largest Diff. Peak / Hole/ e Å^{-3}	0.46 / -0.36	**Flack Parameter**	0.017(4)

[a]*Calculated from SQUEEZE data.* [b]GooF: Goodness-of-fit = $\{\sum[w(F_o^2 - F_c^2)^2]/(n-p)\}^{1/2}$, where n is the number of reflections and p is the total number of parameters refined. [c]$R = \sum||F_o| - |F_c||/\sum|F_o|$. [d]$wR = \{\sum[w(F_o^2 - F_c^2)^2]/\sum w(F_o^2)^2]\}^{1/2}$

Table 5-10. The M–L bond distances (in Å) for the Fe_3Co_2 TBP with 5dmbpy (10).

Temperature	Fe(1)–N	Fe(2)–N	Fe(3)–N	Co(1)–C	Co(2)–C
110 K	1.936 (4)	1.932 (4)	1.937 (4)	1.893 (5)	1.886 (4)
	1.943 (4)	1.953 (4)	1.948 (3)	1.897 (4)	1.888 (5)
	1.951 (3)	1.961 (3)	1.960 (4)	1.900 (4)	1.895 (5)
	1.963 (4)	1.963 (3)	1.965 (4)	1.905 (5)	1.897 (4)
	1.966 (3)	1.966 (4)	1.977 (4)	1.907 (4)	1.901 (4)
	1.971 (4)	1.979 (4)	1.986 (4)	1.917 (5)	1.910 (5)
Avg M–L	**1.955 (4)**	**1.959 (4)**	**1.962 (4)**	**1.903 (5)**	**1.896 (5)**

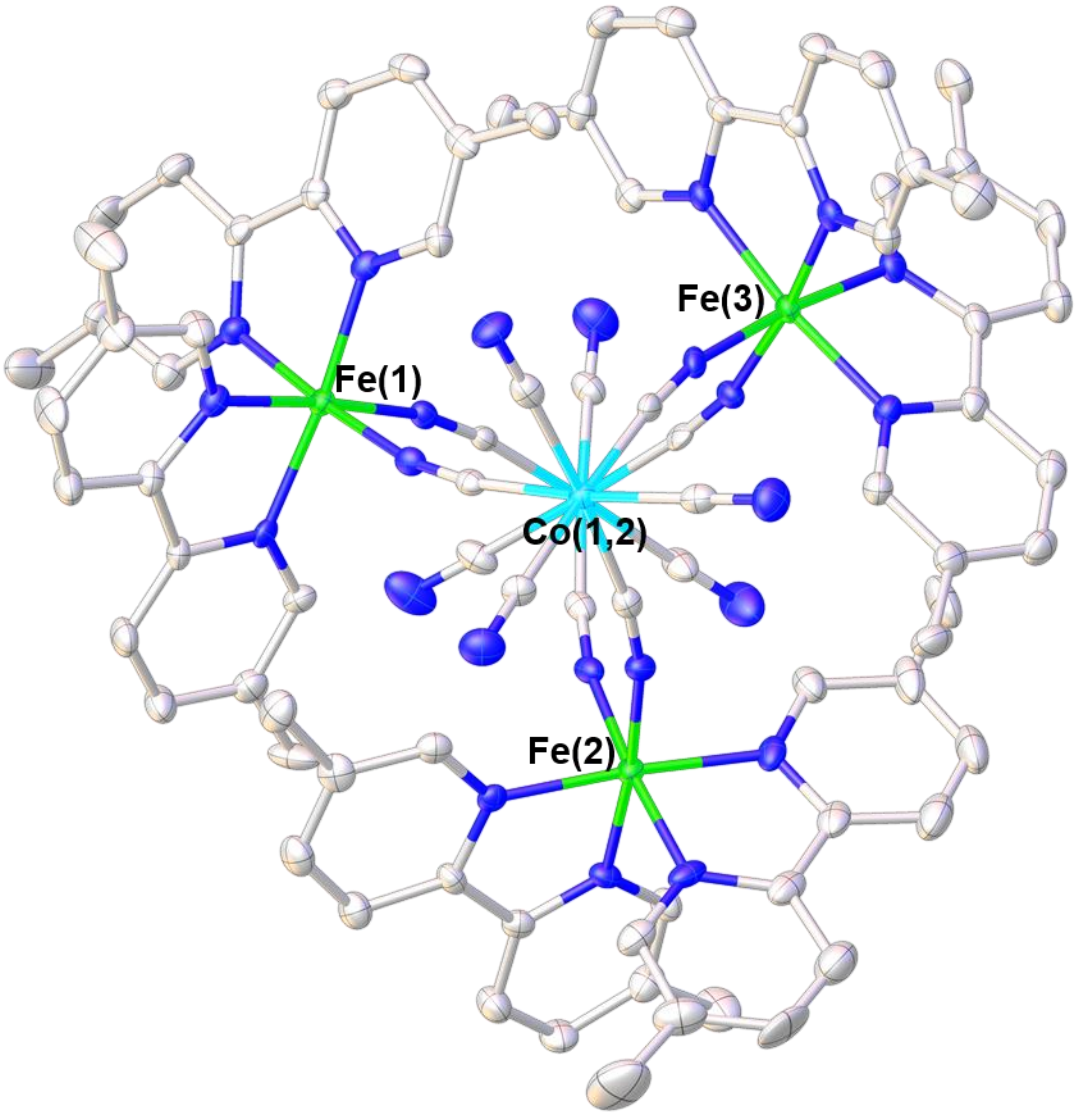

Figure 5-10. Axial view of the asymmetric unit of the Fe_3Co_2 TBP with 5dmbpy ligands coordinated to the equatorial Fe centers. Color scheme: Co is cyan, Fe is green, N is blue and C is grey. Hydrogen atoms have been omitted for the sake of clarity.

Analysis of the π-π stacking interactions with Olex2 reveals that this TBP has even fewer interactions than the two previous Fe_3Co_2 TBPs discussed herein. The intermolecular interaction of this TBP is no longer present as this TBP does not stack in a dimeric fashion analogous to the TBP with tmphen or 4dmbpy. Despite the appearance of near trigonal symmetry when looking down the axial metal positions, the TBP only has 2 intramolecular interactions (Table 5-11). The intra-tt and intra-gg interactions (Figure 5-11) involve the Fe(1)–Fe(2) and Fe(1)–Fe(3) centers, respectively but the intra-rr is no longer considered an interaction in this TBP due to a centroid-centroid distance greater than 4 Å. With tmphen and 4dmbpy, the Fe(1)–Fe(3) interaction (intra-gg) was not seen due to the much larger distance between the Fe(1) and Fe(3) metal centers than in the TBP with 5dmbpy. It should be noted that these two interactions are very weak with centroid-centroid distances of ~3.98 and 3.95 Å and could be considered as non-interactions by literature standards. Figure 5-12 portrays how the molecule packs looking down the *a*-axis.

Table 5-11. Geometric parameters (centroid-centroid distance, shift distance and angle) for the intramolecular π-π stacking interactions in the Fe_3Co_2 TBP with 5dmbpy (10).

Interaction-Plane Fe Centers Involved	Temperature	Centroid-Centroid Distance (Å)	Shift Distance (Å)	Angle (º)
intra-tt Fe(1) – Fe(2)	110 K	3.984	1.756	10.978
intra-gg Fe(1) – Fe(3)	110 K	3.953	1.841	11.941

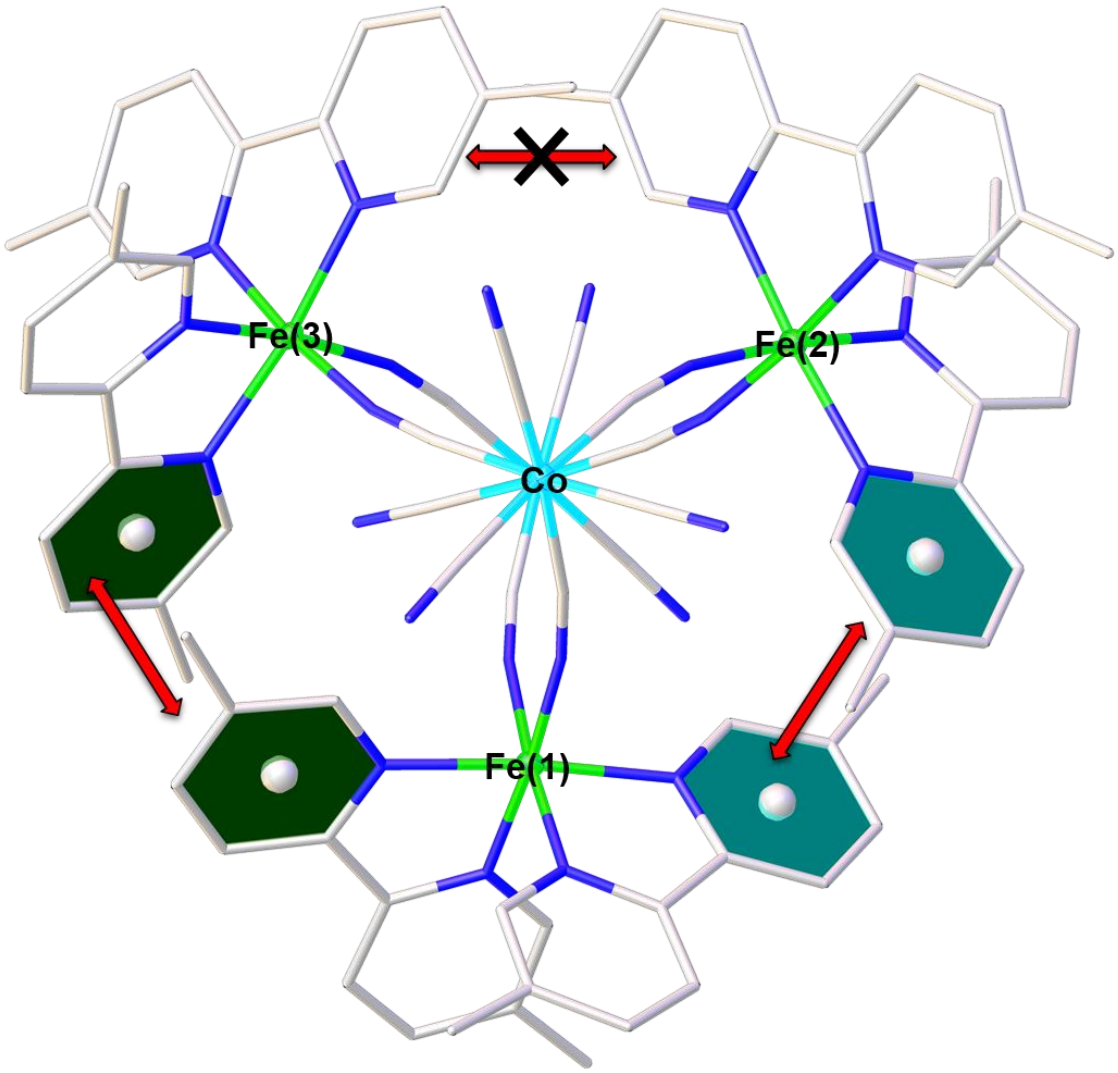

Figure 5-11. View looking down the axial metal positions of the intramolecular interactions occurring in the Fe_3Co_2 5dmbpy TBP (10). The intra-gg interaction is indicated by the green planes and the intra-tt interaction is shown with the teal planes. This TBP does not exhibit the intra-rr interaction between the Fe(2) and Fe(3) centers. Color scheme: Co is cyan, Fe is green, N is blue and C is grey. Hydrogen atoms have been omitted for clarity.

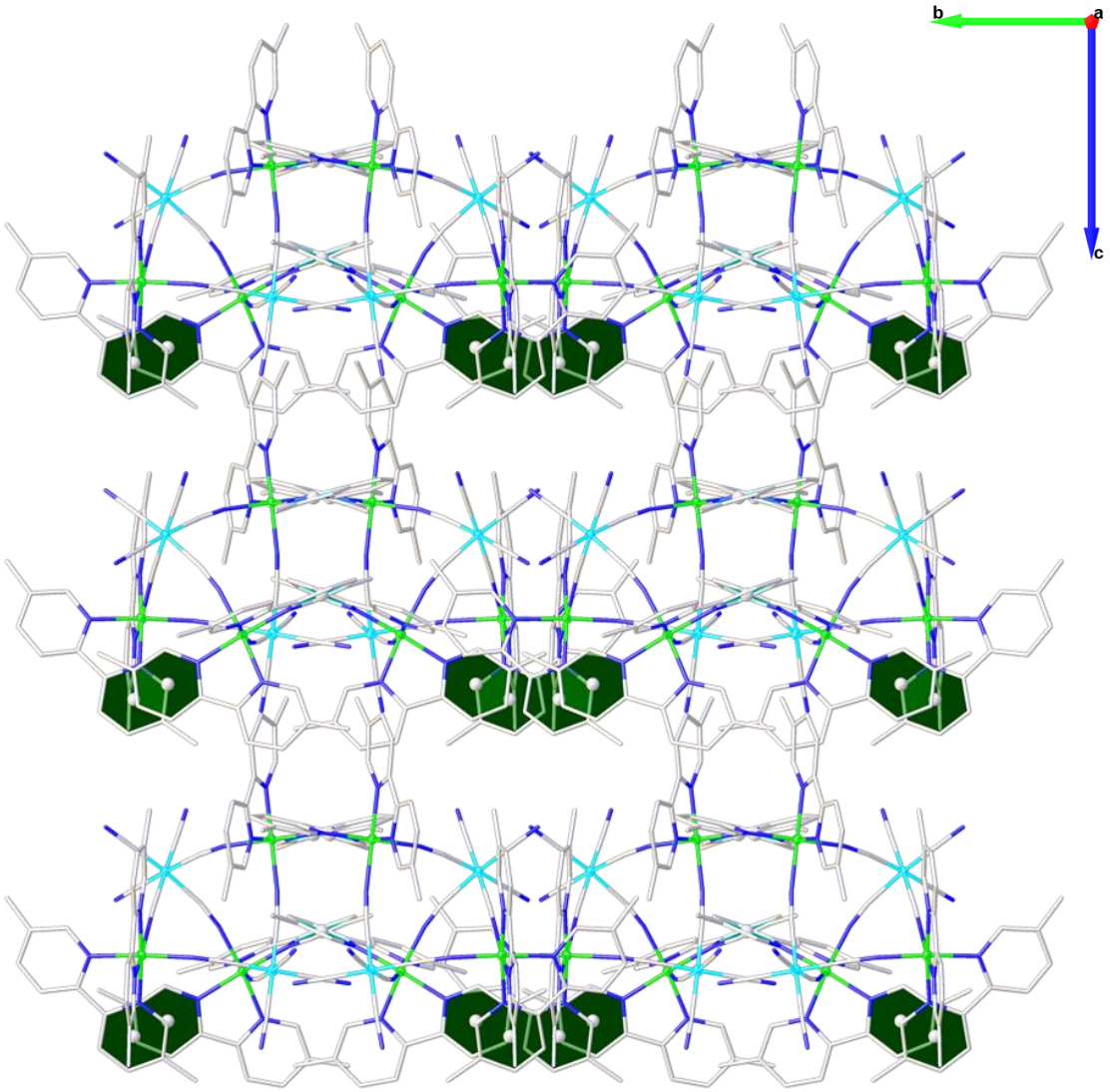

Figure 5-12. Packing diagram of Fe_3Co_2 5dmbpy (10) looking down the *a*-axis. The planes indicating the intra-gg interaction offer perspective on the packing of the molecules. Color scheme: Co is cyan, Fe is green, N is blue and C is grey. Hydrogen atoms have been omitted for clarity

Fe_3Co_2 tmbpy (11)

Variable temperature data was collected on two different crystals for this TBP. The data obtained at 20 and 50 K from one of the crystals could not be refined anisotropically in its entirety. The metal centers were the only atoms refined anisotropically for these two structures. The space group obtained for the crystal for these two temperatures was $P2_1/c$ while the crystal used for data collection at 100, 150, 200 and 250 K was $P2_1/n$, like the Fe_3Co_2 4dmbpy TBP. As stated earlier, these two space groups are related by the transformation matrix 0 0 -1 0 1 0 1 0 -1. The unit cell data and refinement parameters for all of the structures at the various temperatures (Table 5-12) are very close to one another regardless of the change in the unique axis between the two crystals. Unlike the TBPs with tmphen and 4dmbpy, when looking down the axial metal positions, the asymmetric unit (Figure 5-13) has nearly 3-fold symmetry owing to Fe–Fe distances of ~6.5 Å for both Fe(1)–Fe(2) and Fe(2)–Fe(3) centers and ~6.3 Å for the Fe(1)–Fe(3) centers. As expected, the average Co^{III}–C bond distances stay relatively constant (~1.9 Å) at all temperatures (Table 5-13). Similarly to the Fe_3Co_2 TBP with 4dmby, the structures collected at all of the temperatures up to 250 K indicate that all 3 Fe^{II} centers remain in the LS state as the average Fe–N bond lengths of ~1.96–1.97Å remain unchanged throughout the temperature range.

Table 5-12. Crystal structure data and refinement parameters for the Fe_3Co_2 TBP with tmbpy (11).

Fe_3Co_2 tmbpy (11)	**20 K**	**50 K**	**100 K**	**150 K**	**200 K**	**250 K**
Space Group	*P*2$_1$/c	*P*2$_1$/*c*	*P*2$_1$/*n*	*P*2$_1$/*n*	*P*2$_1$/*n*	*P*2$_1$/*n*
a/ Å	16.4982(15)	16.497(2)	16.5343(6)	16.5840(6)	16.6104(4)	16.6594(4)
b/ Å	24.144(2)	24.137(3)	24.2217(8)	24.2647(8)	24.3336(6)	24.4056(6)
c/ Å	28.969(3)	28.949(3)	29.1116(9)	29.1574(10)	29.2480(7)	29.3250(7)
β/ °	106.159(7)	106.191(9)	106.072(2)	105.895(2)	105.7620(10)	105.6330(10)
Volume/ Å^3	11083.7(18)	11070(2)	11203.2(7)	11284.5(7)	11377.3(5)	11482.0(5)
[a]Interstitial Solvent	5 MeCN 10 H_2O	6 MeCN 9 H_2O	6 MeCN 11 H_2O	6 MeCN 11 H_2O	6 MeCN 11 H_2O	6 MeCN 11 H_2O
μ/ mm^{-1}	0.873	0.876	0.866	0.859	0.852	0.844
Crystal Size/ mm^3 Habitat	0.075 × 0.047 x 0.019 Dark, red needle		0.132 × 0.094 x 0.047 Dark, red needle			
2Θ Range for Data Collection/ °	4.056 to 36.72	4.012 to 35.718	4.61 to 57.934	4.6 to 56.392	4.588 to 55.654	4.572 to 55.134
Independent Reflections	6231 R_{int} = 0.1639 R_{sigma} = 0.0815	5642 R_{int} = 0.1854 R_{sigma} = 0.0993	22917 R_{int} = 0.0758 R_{sigma} = 0.0485	21430 R_{int} = 0.0745 R_{sigma} = 0.0444	20815 R_{int} = 0.0700 R_{sigma} = 0.0447	20387 R_{int} = 0.0697 R_{sigma} = 0.0435
Data/Restraints/ Parameters	6231/0/550	5642/0/550	22917/0/1172	21430/0/1149	20815/0/1129	20387/0/1132
[b]GooF on F^2	1.049	1.021	1.109	1.120	1.085	1.055
[c,d]Final R Indexes [I>=2σ (I)]	R_1 = 0.0827 wR_2 = 0.1966	R_1 = 0.0869 wR_2 = 0.2072	R_1 = 0.0821 wR_2 = 0.1790	R_1 = 0.0826 wR_2 = 0.1960	R_1 = 0.0719 wR_2 = 0.1743	R_1 = 0.0587 wR_2 = 0.1435
[c,d]Final R Indexes [all data]	R_1 = 0.1160 wR_2 = 0.2182	R_1 = 0.1261 wR_2 = 0.2321	R_1 = 0.1070 wR_2 = 0.1904	R_1 = 0.1050 wR_2 = 0.2074	R_1 = 0.0948 wR_2 = 0.1862	R_1 = 0.0837 wR_2 = 0.1570
Largest Diff. Peak / Hole/ e Å^{-3}	0.51 / -0.48	0.49 / -0.51	0.94 / -1.17	0.98 / -1.12	1.51 / -1.15	1.45 / -1.00

Radiation = synchrotron (λ = 0.7749), α = γ = 90°, Z = 4, [a]*Calculated from SQUEEZE data.* [b]GooF: Goodness-of-fit = $\{\sum[w(F_o^2 - F_c^2)^2]/(n-p)\}^{1/2}$, where *n* is the number of reflections and *p* is the total number of parameters refined. [c]$R = \sum||F_o|-|F_c||/\sum|F_o|$. [d]$wR = \{\sum[w(F_o^2 - F_c^2)^2]/\sum w(F_o^2)^2]\}^{1/2}$.

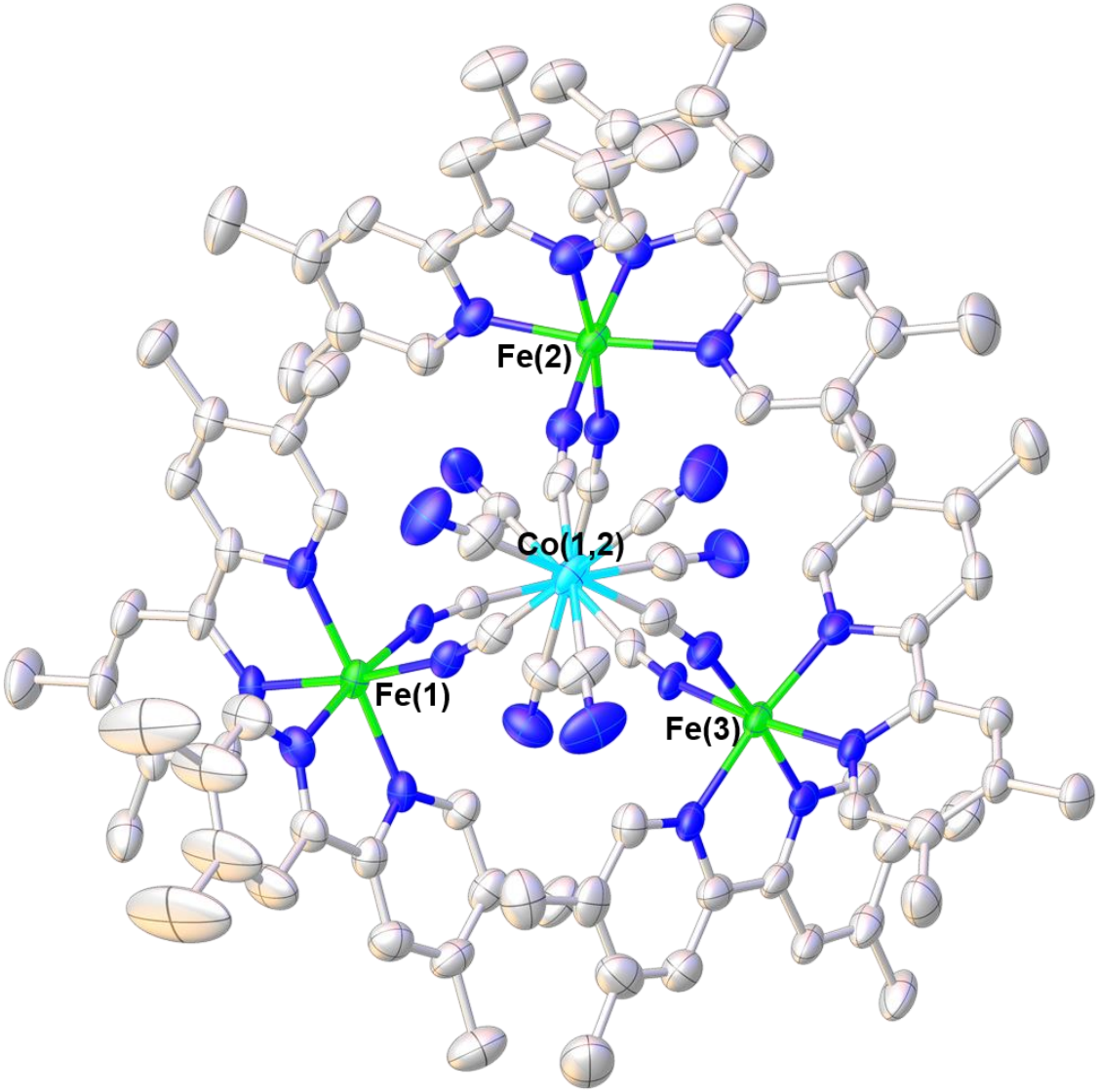

Figure 5-13. View of the asymmetric unit of Fe_3Co_2 tmbpy (11) looking down the axial Co metal centers. Color scheme: Co is cyan, Fe is green, N is blue and C is grey. Hydrogen atoms have been omitted for the sake of clarity.

Table 5-13. The M–L bond distances (in Å) for the Fe_3Co_2 TBP with tmbpy (11).

Temperature	Fe(1)–N	Fe(2)–N	Fe(3)–N	Co(1)–C	Co(2)–C
20 K	1.940 (15)	1.928 (14)	1.936 (13)	1.862 (20)	1.870 (19)
	1.956 (13)	1.950 (13)	1.948 (13)	1.871 (19)	1.875 (18)
	1.956 (13)	1.956 (14)	1.948 (13)	1.873 (19)	1.877 (19)
	1.958 (12)	1.963 (13)	1.970 (12)	1.892 (18)	1.879 (18)
	1.972 (12)	1.967 (13)	1.976 (12)	1.897 (17)	1.913 (18)
	1.988 (12)	1.971 (12)	1.977 (13)	1.904 (19)	1.916 (17)
Avg M–L	**1.962 (13)**	**1.956 (13)**	**1.959 (13)**	**1.883 (19)**	**1.888 (18)**
50 K	1.935 (15)	1.940 (16)	1.931 (14)	1.873 (22)	1.873 (22)
	1.940 (17)	1.944 (14)	1.940 (15)	1.889 (22)	1.879 (20)
	1.960 (15)	1.958 (15)	1.950 (16)	1.891 (20)	1.891 (21)
	1.965 (14)	1.960 (16)	1.974 (14)	1.895 (20)	1.921 (22)
	1.967 (14)	1.960 (15)	1.979 (15)	1.912 (22)	1.926 (22)
	1.970 (14)	1.987 (14)	1.987 (15)	1.933 (24)	1.926 (21)
Avg M–L	**1.956 (15)**	**1.958 (15)**	**1.960 (15)**	**1.899 (22)**	**1.903 (21)**
100 K	1.949 (4)	1.936 (5)	1.925 (5)	1.866 (6)	1.884 (6)
	1.952 (5)	1.944 (5)	1.942 (4)	1.884 (5)	1.899 (6)
	1.954 (4)	1.954 (5)	1.952 (4)	1.896 (6)	1.899 (7)
	1.973 (4)	1.959 (5)	1.953 (5)	1.899 (5)	1.900 (7)
	1.979 (5)	1.959 (5)	1.958 (5)	1.900 (6)	1.903 (6)
	1.989 (4)	1.967 (5)	1.976 (5)	1.911 (5)	1.904 (6)
Avg M–L	**1.966 (4)**	**1.953 (5)**	**1.951 (5)**	**1.893 (6)**	**1.898 (6)**
150 K	1.947 (5)	1.939 (5)	1.923 (5)	1.862 (6)	1.881 (7)
	1.953 (5)	1.944 (5)	1.940 (5)	1.891 (6)	1.891 (7)
	1.956 (5)	1.956 (5)	1.952 (5)	1.897 (6)	1.899 (7)
	1.974 (4)	1.958 (5)	1.957 (5)	1.898 (6)	1.900 (7)
	1.979 (5)	1.962 (5)	1.961 (5)	1.900 (6)	1.904 (6)
	1.991 (5)	1.965 (5)	1.988 (5)	1.913 (6)	1.907 (7)
Avg M–L	**1.967 (5)**	**1.954 (5)**	**1.954 (5)**	**1.894 (6)**	**1.897 (7)**
200 K	1.951 (4)	1.933 (5)	1.926 (5)	1.867 (5)	1.884 (6)
	1.956 (4)	1.945 (4)	1.942 (4)	1.896 (6)	1.888 (6)
	1.959 (4)	1.959 (4)	1.950 (4)	1.898 (5)	1.898 (7)
	1.973 (4)	1.960 (5)	1.962 (4)	1.900 (5)	1.900 (6)
	1.979 (4)	1.963 (4)	1.964 (4)	1.904 (6)	1.900 (6)
	1.993 (4)	1.966 (5)	1.974 (5)	1.906 (6)	1.903 (6)
Avg M–L	**1.969 (4)**	**1.954 (5)**	**1.953 (4)**	**1.895 (6)**	**1.896 (6)**
250 K	1.960 (4)	1.932 (4)	1.935 (4)	1.882 (4)	1.882 (5)
	1.961 (3)	1.944 (4)	1.946 (3)	1.896 (5)	1.894 (5)
	1.962 (4)	1.963 (4)	1.950 (3)	1.897 (4)	1.894 (5)
	1.981 (4)	1.964 (4)	1.963 (3)	1.898 (5)	1.901 (5)
	1.988 (3)	1.967 (4)	1.970 (3)	1.901 (4)	1.903 (5)
	2.003 (3)	1.970 (4)	1.973 (4)	1.905 (5)	1.907 (5)
Avg M–L	**1.976 (4)**	**1.957 (4)**	**1.956 (3)**	**1.897 (5)**	**1.897 (5)**

Analysis of the π-π stacking interactions of this TBP with Olex2 revealed that this ligand is involved in even fewer interactions than the three previous ligands discussed. The only π-π stacking interaction recognized is an intramolecular interaction involving the Fe(1) and Fe(3) center which has the shorter distance of ~6.3 Å between the two centers. Figure 5-14 is a depiction of the intra-gg interaction that occurs in this molecule. Although this interaction is recognized by Olex2, it is a very weak interaction with a centroid-centroid distance ~3.93 Å at all temperatures. There is no real change in centroid-centroid or shift distances as temperature increases but there is an obvious decrease in the angle between the planes involved in this interaction that occurs as temperature is increased (Δ = 2.9 °). The geometric parameters for the intramolecular interaction in this TBP are listed in Table 5-14. Figure 5-15 is a packing diagram of the TBP looking down the *a*-axis. The green planes indicating the intramolecular interaction cannot be easily seen as they were in the packing diagrams for the other TBPs.

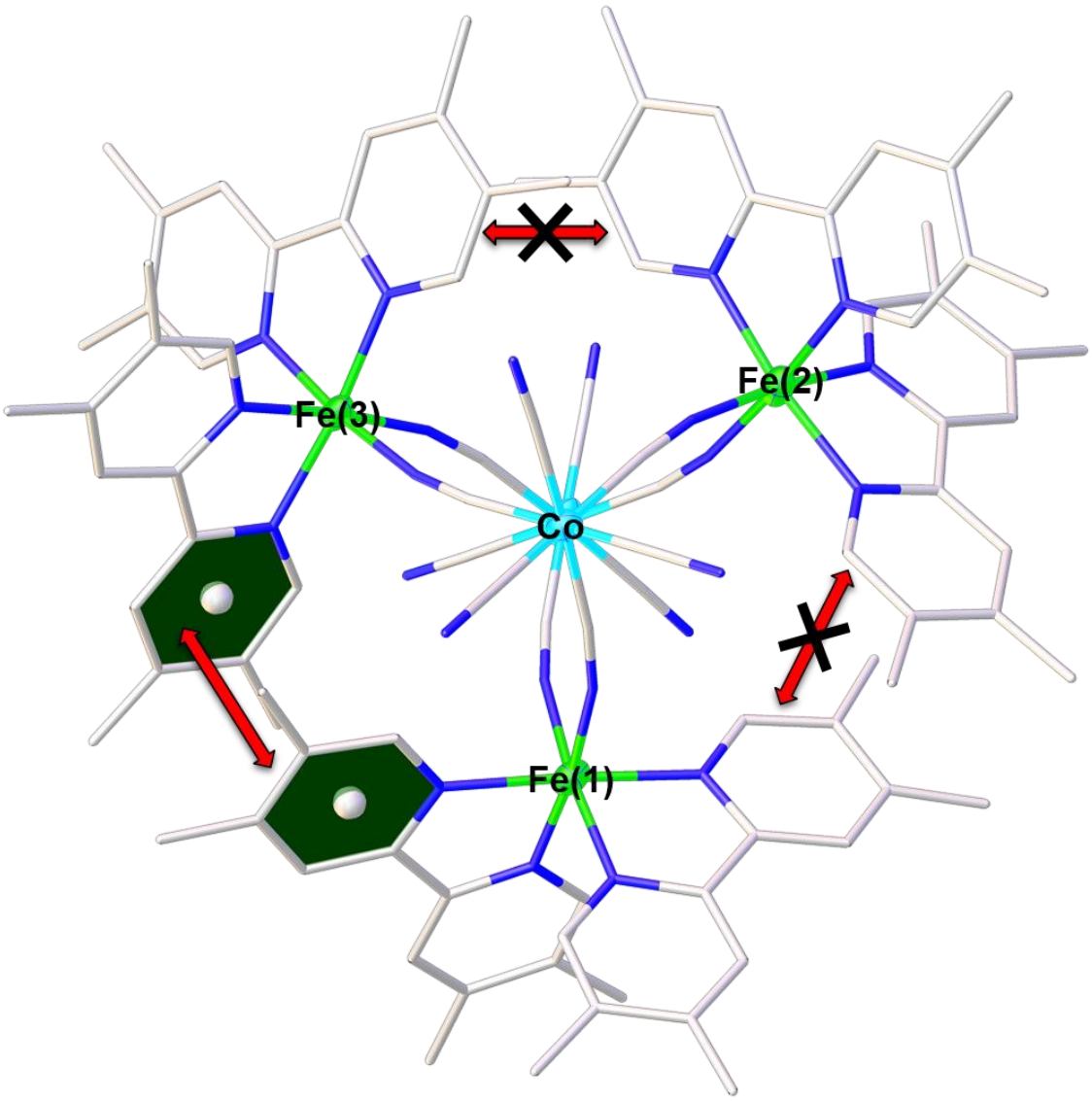

Figure 5-14. Depiction of the intramolecular π-π stacking interaction in the Fe_3Co_2 tmbpy TBP (11). The green planes indicate the rings involved in the intramolecular interation. Color scheme: Co is cyan, Fe is green, N is blue and C is grey. Hydrogen atoms have been omitted for the sake of clarity.

Table 5-14. Geometric parameters (centroid-centroid distance, shift distance and angle) for the intramolecular π-π stacking interactions in the Fe_3Co_2 TBP with tmbpy (11). The average values (avg) and the differences between the minimum and maximum values (Δ) have been included.

Interaction-Plane Fe Centers Involved	Temperature	Centroid-Centroid Distance (Å)	Shift Distance (Å)	Angle (º)
intra-gg Fe(1) – Fe(3)	20 K	3.933	1.350	11.557
	50 K	3.938	1.353	11.750
	100 K	3.928	1.452	10.440
	150 K	3.927	1.462	10.023
	200 K	3.932	1.455	9.563
	250 K	3.941	1.443	8.824
	Avg	**3.933**	**1.419**	**10.360**
	Δ	0.014	0.112	2.926

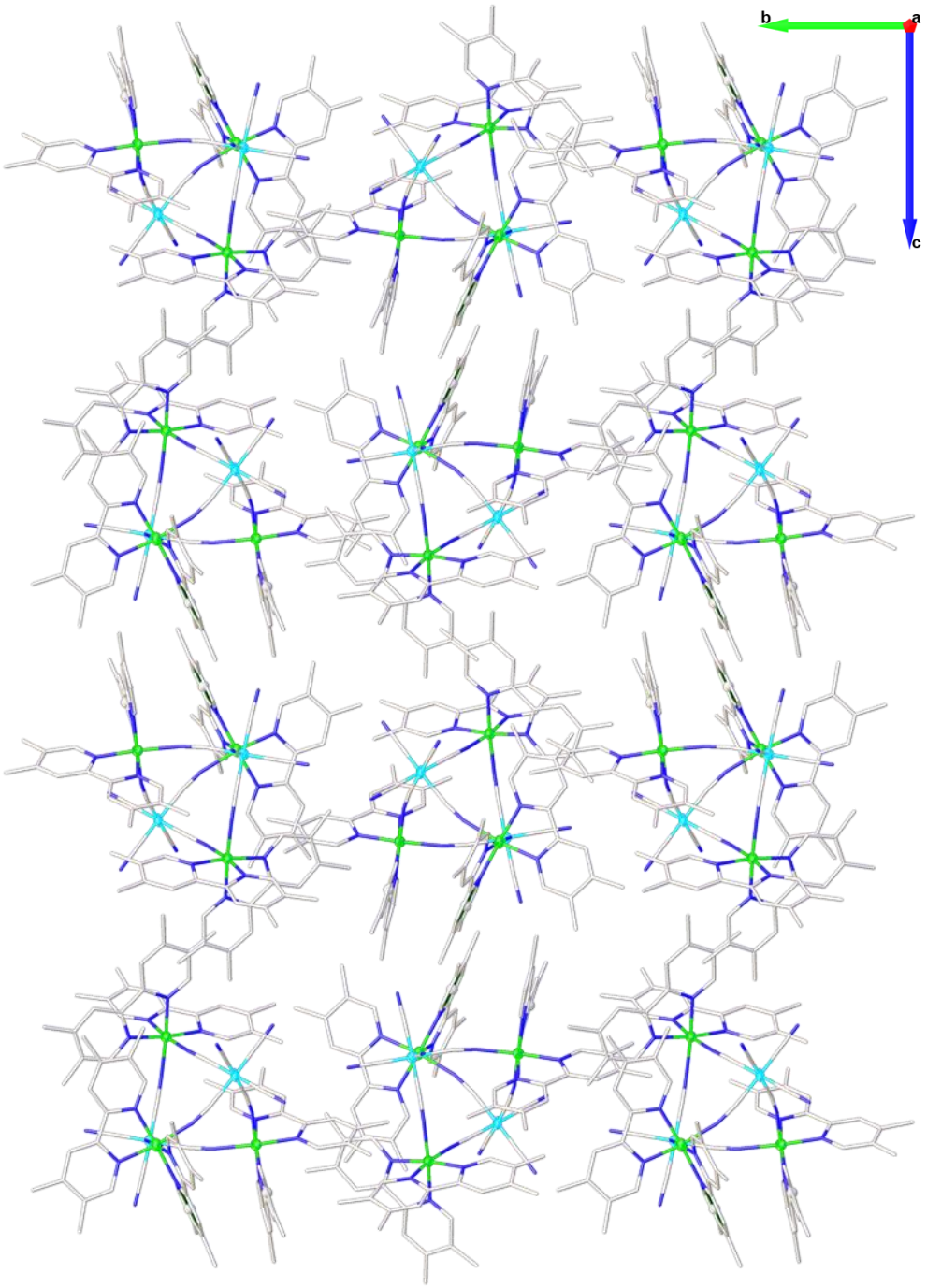

Figure 5-15. Packing diagram of Fe_3Co_2 tmbpy (11) looking down the *a*-axis. Color scheme: Co is cyan, Fe is green, N is blue and C is grey. Hydrogen atoms have been omitted for the sake of clarity.

Upon comparing the crystal structures and the π-π stacking interactions, it becomes clear that the TBP with tmphen has the most interactions. Table 5-15 contains a list of the type and number of π-π stacking interactions for each of the ligands in the Fe_3Co_2 TBPs. It is clear that the number of interactions are changed by exchanging tmphen for similar ligands that are expected to be less capable of engaging in π-π stacking interactions. The ligands also seem to dictate the packing arrangement of these molecules in the crystal as the molecules exhibit vastly different packing arrangements even though three of the four TBPs crystallize in the same space group (Figure 5-16). According to the crystallography, the TBP that participated in the most π-π stacking interactions is also the TBP that has one Fe center undergoing a SCO event before 250 K. This observation indicates that the number of interactions play a role in stabilizing SCO in that the LS → HS transition occurs at lower temperatures than molecules with less interactions. The Fe center that was found to undergo the SCO before 250 K is the center involved in the only intermolecular interaction within the TBP, indicating that the type of interaction also plays a role in the SCO phenomena.

Table 5-15. Number of π-π stacking interactions found by Olex2 in the Fe_3Co_2 TBPs with different capping ligands (8-11). *Indicates very weak interactions that could be considered irrelevant by literature standards.

Number of π-π Stacking Interactions	tmphen (8)	4dmbpy (9)	5dmbpy (10)	tmbpy (11)
Inter-	2	1	0	0
Intra-	2	2	2*	1*
Total Number of Interactions	**4**	**3**	**2***	**1***

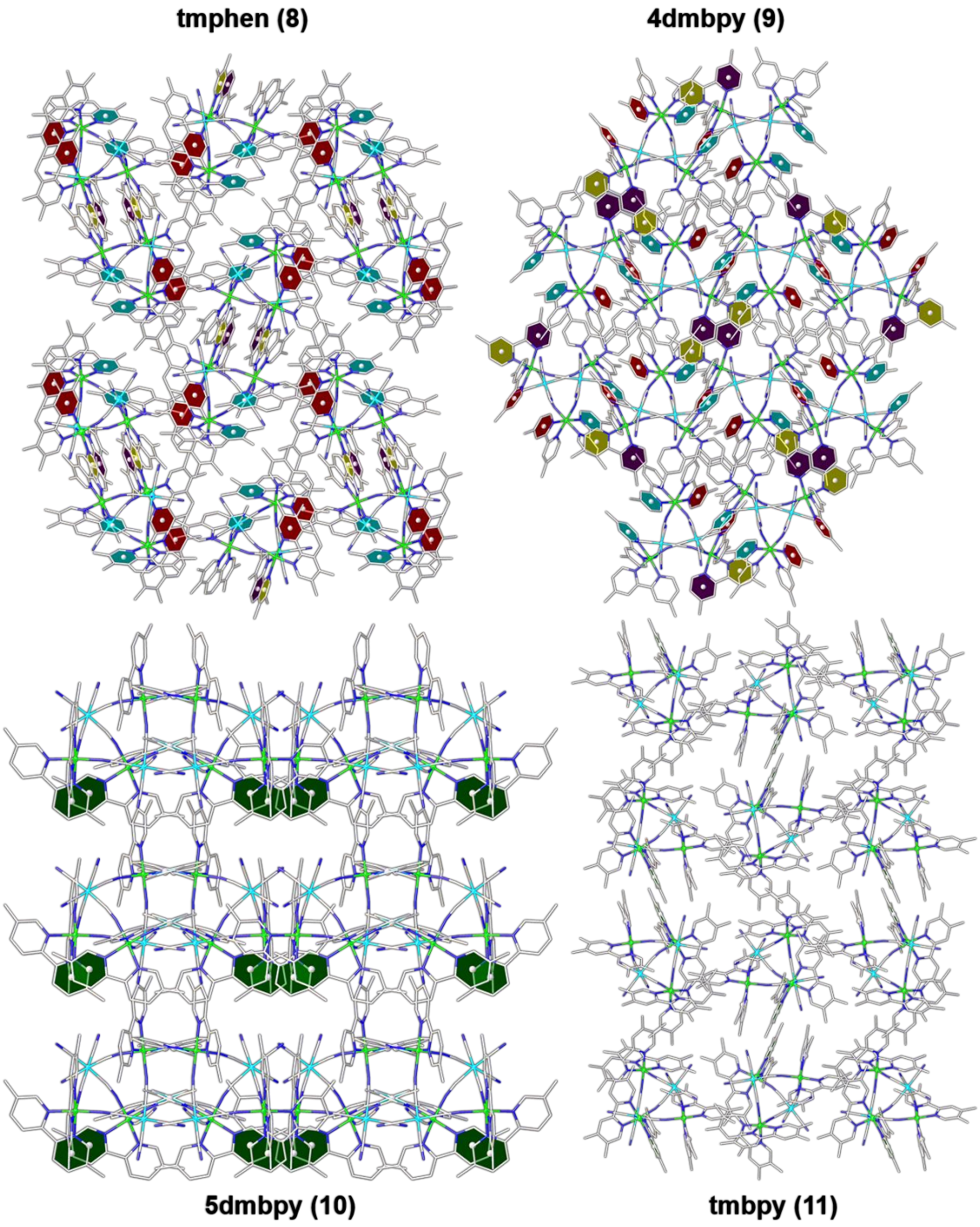

Figure 5-16. Comparison of how compounds 8-11 pack looking down the *a*-axis. The colored planes indicating the π-π stacking interactions for each TBP offer perspective on the orientation of the molecules.

Magnetic Properties

The transition event in the Fe_3Co_2 TBP with tmphen as a capping ligand has been thoroughly studied by previous members in our group.[111,145,146,230] The TBP was found to undergo SCO at the Fe^{II} centers as a result of temperature changes and white light irradiation at 5 K. The fact that this TBP exhibits straightforward SCO and does not undergo CTIST behavior is the driving force behind studying the effect of ligand exchange on this TBP. Exchanging the tmphen for very similar ligands that are less capable of π-π stacking is not expected to change the inherent redox properties of the Fe_3Co_2 core so any changes in χT in these molecules are expected to be due to SCO at the Fe^{II} centers. The $[(LS\text{-}Fe^{II})_3Co^{III}_2]$ configuration is completely diamagnetic and will not contribute to any magnetic signal observed so any magnetic moment observed is due to the presence of HS Fe^{II}. The value of χT for one HS Fe^{II} center typically ranges from the spin-only value of 3 emu·K/mol to ~4.3 emu·K/mol if orbital contributions are included. Considering all of this, analyzing the magnetic data is more clear-cut than in previous cases presented in this dissertation. In order to limit the differences in magnetic behavior due to extrinsic factors, all of the TBPs discussed herein were measured using the same capsule, brass rod and sequence. The details of the measurement and sample preparation can be found in Appendix A.

Fe_3Co_2 tmphen (8)

Thorough studies on this TBP have shown that the transition temperature and, more so, the cooperativity of the SCO events that occur in this TBP change depending on solvent content and preparation technique. For this reason, this TBP was prepared and measured again but in the same manner as the TBPs containing 4dmbpy, 5dmbpy and tmbpy. This procedure allows for more accurate comparisons and conclusions about the effect that π-π stacking has on the SCO behavior in the Fe_3Co_2 TBPs and, by extension, how it could affect congeners containing different metal combinations.

At 2 K, the TBP with tmphen has almost entirely LS Fe^{II} centers as indicated by the χT value of 0.3 emu·K/mol (orange circles in Figure 5-17) and the parameters obtained from crystallography. Although the χT value changes to ~12 emu·K/mol as the temperature is increased to 390 K, the susceptibility data only display one transition step in the curve indicating that either the Fe centers are transitioning simultaneously or that one center begins to undergo SCO as the previous center nears completion of the SCO. The crystallographic data discussed earlier suggests that the ladder is the most likely event as there is an obvious lengthening of the Fe(3)–N bond distances from 15 K to 220 K but not in the Fe(1)–N and Fe(2)–N bond lengths. At 220 K, the χT value is 4.5 emu·K/mol which is slightly higher than the typical range of 3 – 4.3 emu·K/mol for one HS Fe^{II} ion. As the temperature is raised to 390 K, the χT value is 12.2 emu·K/mol and the curve appears to reach a plateau indicating the completion of the SCO events

for all three Fe^{II} centers. As it is known that solvent content can play a pivotal role in the SCO behavior of these TBPs, the sample was measured while being cooled from 390 K to 2 K to probe if the SCO events would change with the loss of solvent that was expected to occur by warming the sample to 390 K. The yellow circles in Figure 5-17 represent the χT data as the sample is cooled to 2 K and the dark green circles represent the χT data as the sample is warmed from 2 K to 390 K a second time. These two transition curves are nearly identical to each other indicating that this TBP does not exhibit hysteresis upon the loss of solvent but the data are quite different from the original data collected from 2 to 390 K, *i.e.*, before solvent was lost. As solvent is removed with heat inside the magnetometer, the SCO events become less cooperative and the HS state of the Fe^{II} center is more favored. The decrease in χT becomes very gradual around 100 K where the value of χT is ~4.1 emu·K/mol which is typical for approximately one HS Fe^{II} center. Below 20 K, χT decreases quickly to 0.1 emu·K/mol. Before the loss of solvent, the temperature required to obtain a χT value within the range typical of one HS Fe^{II} center (~3 – 4.3 emu·K/mol) is ~190–220 K. After some solvent is removed, the temperature required to obtain the same range in values is ~14–110 K. Although the range in temperature required for the value of χT to increase from 3 to 4.3 emu·K/mol increased from 30 to 96 K due to the loss of solvent, the χT values were obtained much earlier in the warming process (110 K after solvent loss vs 220 K before solvent loss). This indicates that the first LS → HS transition occurs much more rapidly and is initially more cooperative

once the solvent is removed. However, the second and third SCO events that occur when there is less solvent in the interstices are much more gradual as they occur over a 280 K range instead of a 170 K range. The HS state of the Fe^{II} center is clearly favored in this TBP when solvent is removed which could be due to a reduction in mechanical pressure exerted on the molecules.

The magnetic behavior of the TBP was also measured as the sample was cooled from 390 K for the second time (light green circles in Figure 5-17); the data reveal that more solvent is lost resulting in further stabilization of the HS state as indicated by the higher χT values than in the previous measurements. Interestingly, however, at 390 K the magnitude of χT (12.2 emu·K/mol) remains constant although more of the sample remains in a HS state upon cooling the sample for the last time, as compared to the previous time. As observed for several TBPs (including the Fe_3Ru_2 discussed earlier), the removal of solvent results in more of the sample remaining in the HS state at the same temperatures as compared to the solvated sample. The increase in the χT values below 390 K indicates that more solvent is lost from the sample after being warmed to 390 K for the second time but it is noted that the absolute magnitude of χT at 390 K remains constant. This is unexpected behavior given the solvent loss and suggests that the LS → HS transition for all three Fe^{II} centers is complete at 390 K in this sample. If this is the case, the χT value for one HS Fe^{II} center in this TBP is ~4.06 emu·K/mol and will be used, as such, for comparisons between the samples throughout this discussion.

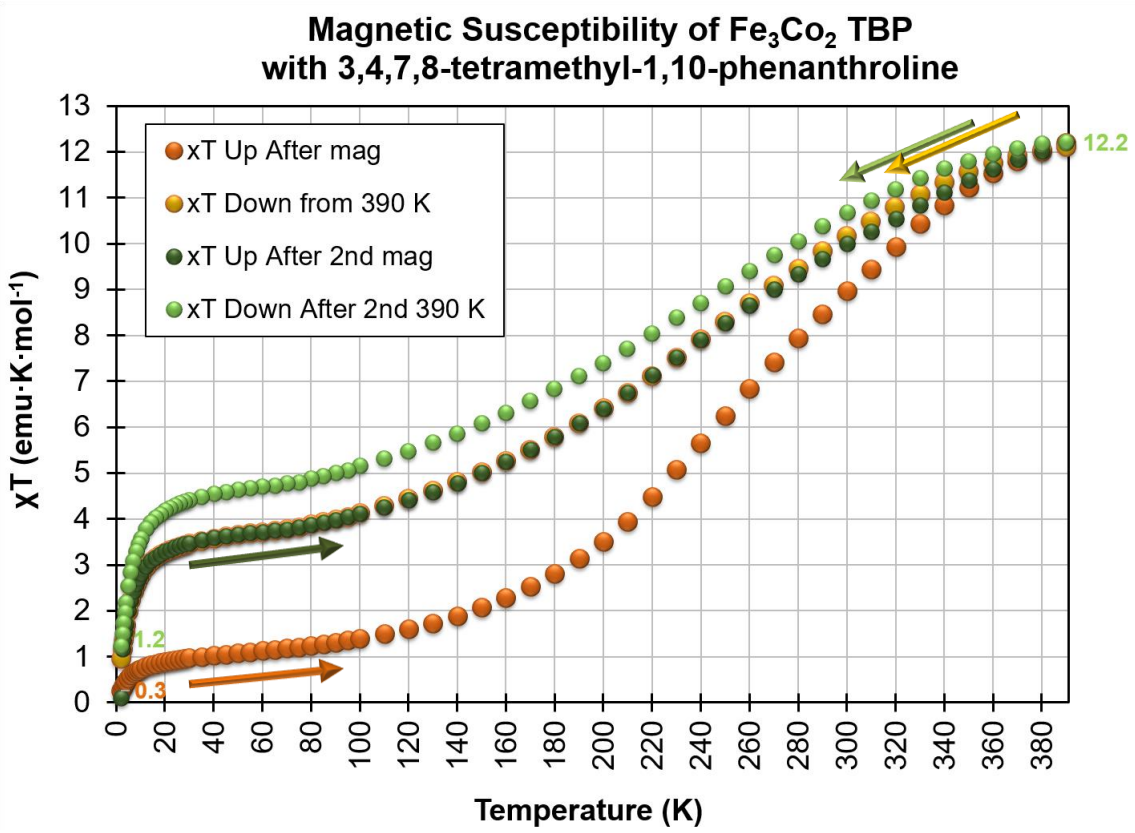

Figure 5-17. Temperature dependent susceptibility data for Fe_3Co_2 with tmphen (8). The order of measurement follows the order of the legend where the orange circles were 1st, the yellow circles 2nd, the dark green circles 3rd and the light green circles are the 4th measurement.

Fe_3Co_2 4dmbpy (9)

The SCO events in compound 9 are similar to those discussed above for compound 8 but the transitions occur at higher temperatures and are more abrupt in comparison. For the Fe_3Co_2 molecule with the 4dmbpy ligands coordinated to the equatorial Fe^{II} centers, the maximum χT value at 390 K for all measured states of the sample is ~11.5 emu·K/mol, which is slightly lower than the 12.2 emu·K/mol obtained for the TBP containing tmphen. The curves do not reach a plateau

indicating that the SCO event is incomplete or that the orbital contribution of the Fe^{II} centers is slightly different when 4dmbpy is coordinated to the Fe^{II} metal. As there is no further solvent loss between cycles and no increase in the magnitude of the susceptibility it is not possible to conclude if the SCO events are complete. Higher temperatures and/or Mössbauer data would be useful in this regard but it is likely that the SCO is incomplete. When warming the sample from 2 K to 390 K for the first time (orange circles in Figure 5-18), the χT value of 4 emu·K/mol is not obtained until ~290 K whereas for the tmphen analog, that value was obtained at ~210 K. When the sample is cooled back down from 390 K for the first time after losing solvent (dark green circles in Figure 5-18), the decrease in χT becomes much more gradual and the HS state is retained longer. In fact, the value of χT is still 1.9 emu·K/mol at 2 K as there is a significant amount of remnant HS Fe^{II} in the TBP. The χT value of 4.0 emu·K/mol occurs at ~10 K once solvent is removed instead of at 290 K. This is a huge shift in temperature resulting from loss of solvent. As the sample is warmed back up to 390 K (dark green circles in Figure 5-18), the SCO behavior remains identical as for the previous cooling cycle from 390 K except for the data between ~260 and 360 K where the transition shows hysteresis. The possibility of this difference originating from the sample shifting during the measurement was ruled out because as the sample is cooled back down (light green circles in Figure 5-18) the hysteresis is still present (the 2^{nd} cooling curve tracks the 1^{st} cooling curve). This is the first case in which a TBP molecule exhibits hysteresis in the SCO behavior. The occurrence of this

hysteresis could be a result of a crystallographic or phase transition not exhibited by the other TBPs. Without higher temperature X-ray data this hypothesis cannot be confirmed.

Overall, by exchanging the tmphen ligand for 4dmbpy, which is less capable of engaging in π-π stacking interactions, the majority of the SCO events shift to elevated temperatures and the LS state is favored. As with the TBP containing tmphen, as solvent is removed the transitions become more gradual and the HS state is favored. Removal of solvent also results in a new high temperature hysteretic behavior in the SCO when 4dmbpy is used as the capping ligands.

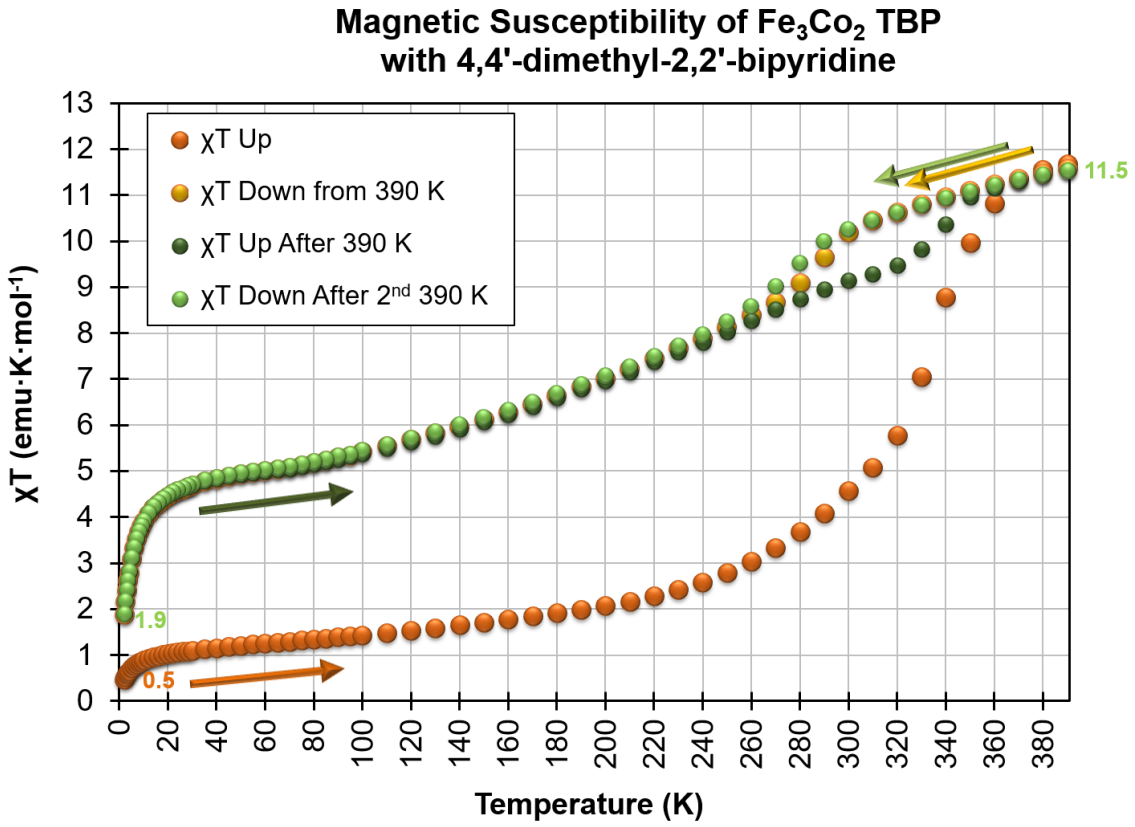

Figure 5-18. Temperature dependent susceptibility data for Fe_3Co_2 with 4dmbpy (9). The order of measurement follows the order of the legend where the orange circles were 1st, the yellow circles 2nd, the dark green circles 3rd and the light green circles are the 4th measurement.

Fe_3Co_2 5dmbpy (10)

The SCO behavior for the Fe_3Co_2 TBP when 5dmbpy is used as a capping ligand instead of 4dmpby or tmphen is quite different at high temperatures. The cooperativity in the LS → HS transition as the sample is warmed from 2 K to 390 K (orange circles in Figure 5-19) is relatively similar to the 4dmbpy analog. At 2 K, the TBP is nearly diamagnetic (χT = 0.4 emu·K/mol) with only a small amount of HS Fe^{II} being present. There is a gradual increase in χT at higher temperatures,

and the value of 4.0 emu·K/mol is reached at 300 K as compared to 290 K in the 4dmbpy analog. Once this value is reached at 300 K, the transition becomes more abrupt until ~350 K where a plateau is reached with a maximum χT of 9.5 emu·K/mol at 390 K. If the same contribution of ~4 emu·K/mol for the χT value for one HS Fe^{II} center is used, it can be concluded that two Fe centers undergo a complete SCO event whereas the transition in the third center is incomplete. The sample was measured in the same manner with the same cycles as compounds 8 and 9. The first cooling measurement from 390 K and the 2^{nd} warming measurement to 390 K are identical to the final cooling cycle (light green circles in Figure 5-19) and are not shown in the figure. Upon losing solvent, the transition from HS → LS becomes more gradual as observed previously with the HS state being favored. The χT value of 4.0 emu·K/mol is obtained at ~26 K once solvent has been removed and more HS Fe^{II} is retained at 2 K (χT = 1.4 emu·K/mol).

Overall, this TBP packs with fewer π-π stacking interactions which are two very weak intramolecular interactions according to crystallographic data. Before solvent loss, the LS state is favored more as compared to the 4dmbpy and tmphen containing analogs. Two Fe^{II} centers undergo a complete SCO between 2 and 390 K in this TBP while the SCO event for the third Fe^{II} center is incomplete, in contrast to the other two analogs where the SCO is nearly complete for all three Fe^{II} centers.

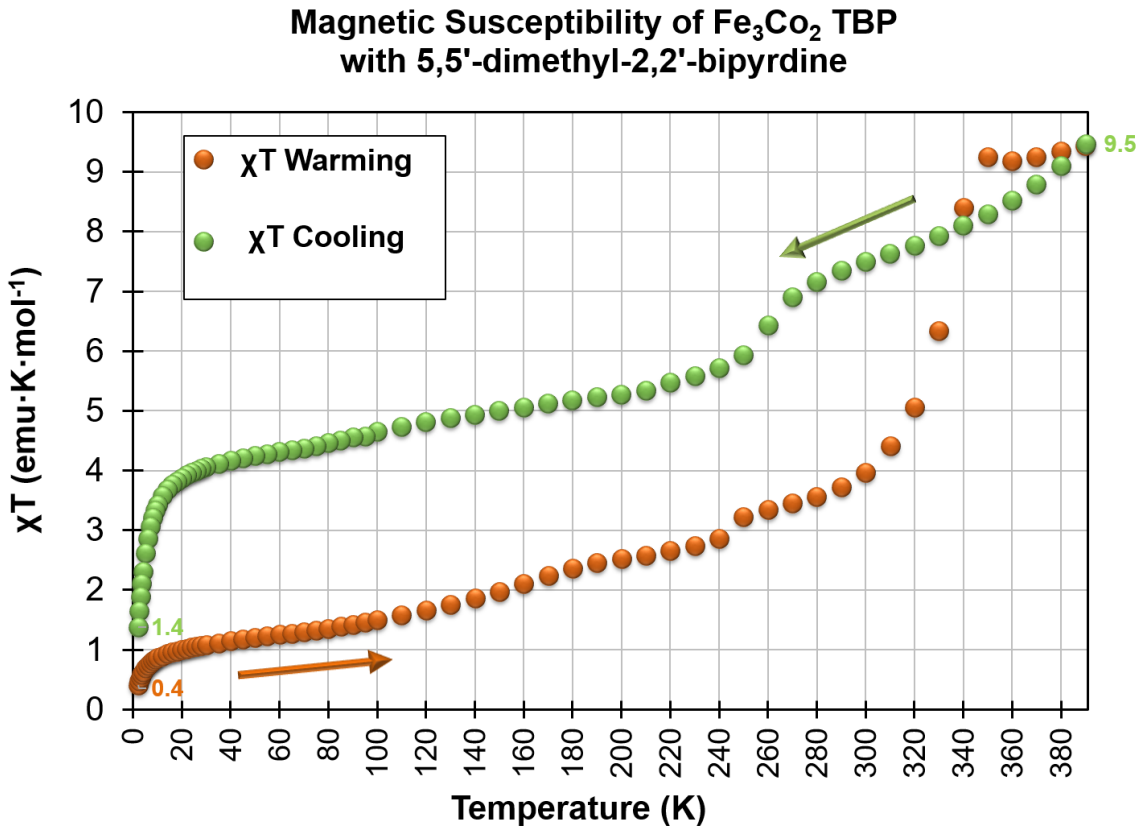

Figure 5-19. Temperature dependent susceptibility data for Fe_3Co_2 with 5dmbpy (10). The orange circles are the data for the sample as it was warmed from 2 K to 390 K for the 1st time and the light green circles are the data as the sample was cooled from 390 K to 2 K for the 2nd time.

Fe_3Co_2 tmbpy (11)

As is the case with the other ligands, the SCO events in this TBP occur as one step instead of a multi-step transition. At 2 K the χT value is nearly diamagnetic (0.2 emu·K/mol) as expected for the electronic configuration of $[(LS\text{-}Fe^{II})_3Co^{III}_2]$ but a small amount of HS Fe^{II} is present. As the temperature is increased to 390 K for the first time (orange circles in Figure 5-20), the SCO is very gradual and χT does not reach a value of 4.0 emu·K/mol for one HS Fe^{II} until

~337 K. At 390 K, all four curves remain at a χT value between 8.3 and 8.7 emu·K/mol. This value is too low for 3 Fe^{II} centers to be completely HS and is more likely due to two HS Fe^{II} centers. Once the sample is warmed to 390 K and loses solvent, the HS → LS transition is very gradual as the temperature is decreased (yellow circles in Figure 5-20) and the χT value of 4.0 emu·K/mol for one HS Fe^{II} center is obtained when the temperature reaches 160 K. At 2 K, more HS Fe^{II} is present in the sample than before solvent had been removed. No hysteresis is observed in the SCO behavior upon warming the sample to 390 K for the second time (dark green circles in Figure 5-20) as the warming and cooling curves are nearly identical. It is evident that more solvent was removed from the sample (resulting in more HS Fe^{II}) upon warming to 390 K a second time as the magnitude of χT at 390 K is slightly higher and the overall χT values are higher as the sample is cooled back down to 2 K (light green circles in Figure 5-20).

Overall, this TBP has the least number of π-π stacking interactions and also has the least amount of HS Fe^{II} present in the sample at 390 K. Like the other TBPs, when solvent is removed, the Fe^{II} centers adopt a HS state.

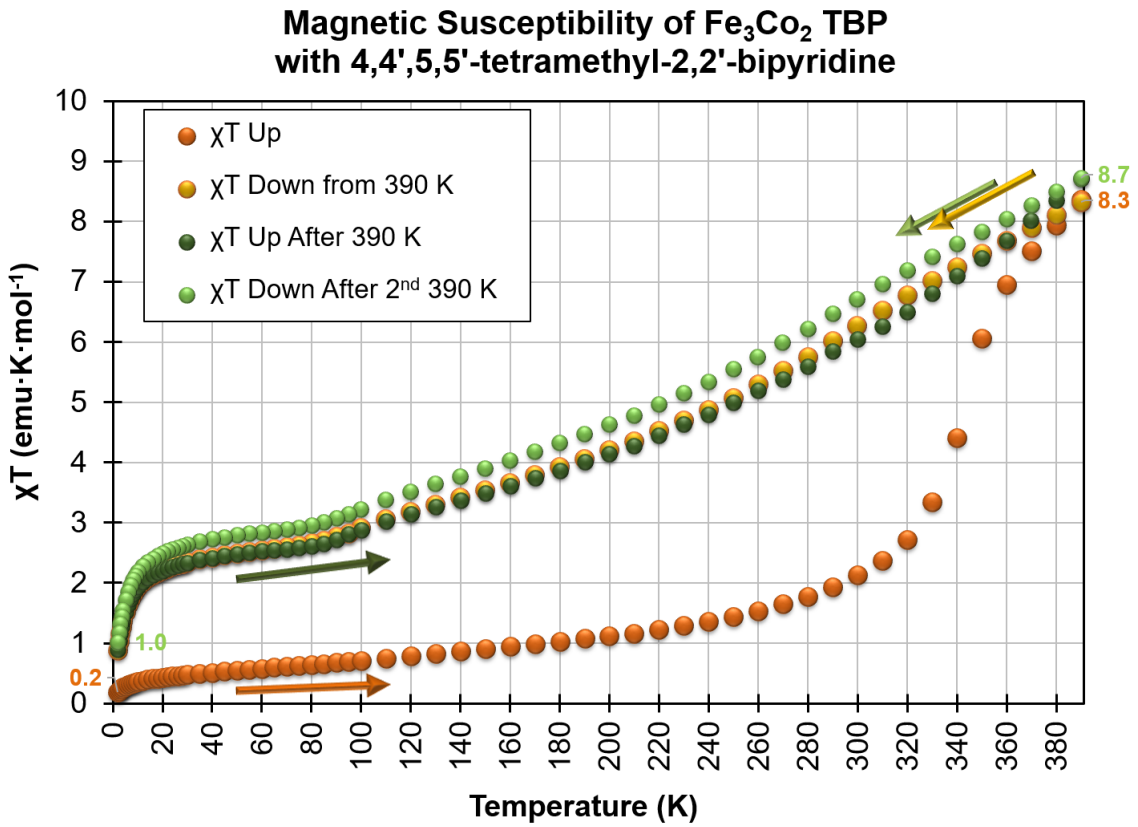

Figure 5-20. Temperature dependent susceptibility data for Fe_3Co_2 with tmbpy (11). The order of measurement follows the order of the legend where the orange circles are 1st, the yellow circles 2nd, the dark green circles 3rd and the light green circles are the 4th measurement.

The plot at the top of Figure 5-21 depicts the χT curves for all four TBPs with the different ligands as the samples are warmed to 390 K for the first time (before solvent was removed) and the bottom of Figure 5-21 compares the χT curves for the TBPs upon cooling for the last time (after solvent was removed). A trend can clearly be seen as the compounds are warmed to 390 K. As the number of π-π stacking interactions in the TBPs decrease (tmphen > 4dmbpy > 5dmbpy > tmbpy) the LS → HS transitions on the Fe^{II} centers are shifted to higher

temperatures and the transitions are no longer complete for all three Fe centers. Once the solvent is removed, the trend exhibited by these TBPs is that the HS state is favored as the number of π-π stacking interactions decreases. Table 5-16 lists the temperatures at which the χT value of 4.0 emu·K/mol (assumed contribution to the χT value for 1 HS Fe^{II} center in these TBPs) is observed before and after solvent was removed from the crystals. A trend can clearly be seen before solvent is removed, namely, that as the number of π-π stacking interactions decreases, the LS → HS transition for the first HS Fe^{II} center is shifted to higher temperatures. The LS state is preferred for the Fe centers when there are fewer π-π stacking interactions. Once solvent has been removed, a similar trend that the LS state is favored as the number of π-π stacking interactions are decreased is observed in most of the transition temperatures (Table 5-16). Below 240 K, however, there is more HS Fe^{II} present in compound 9 (4dmbpy) than in 8 (tmphen). Also, below 140 K there is more HS Fe^{II} in compound 10 (5dmbpy) than in compound 8 as well. This does not follow the trend expected for the number of π-π stacking interactions and suggests that there is another factor governing the SCO behavior in these TBPs once solvent has been removed. As the trend does not exactly follow the previous one noted for the Fe_3Ru_2 TBP in where an inverse relationship exists between the amount of HS Fe^{II} and the amount of solvent, it is difficult to say which factor is the driving force behind the change in SCO behavior in these TBPs once solvent is removed. Another perspective of this trend is given in Table 5-17 where the magnitude of χT before the sample loses solvent is given

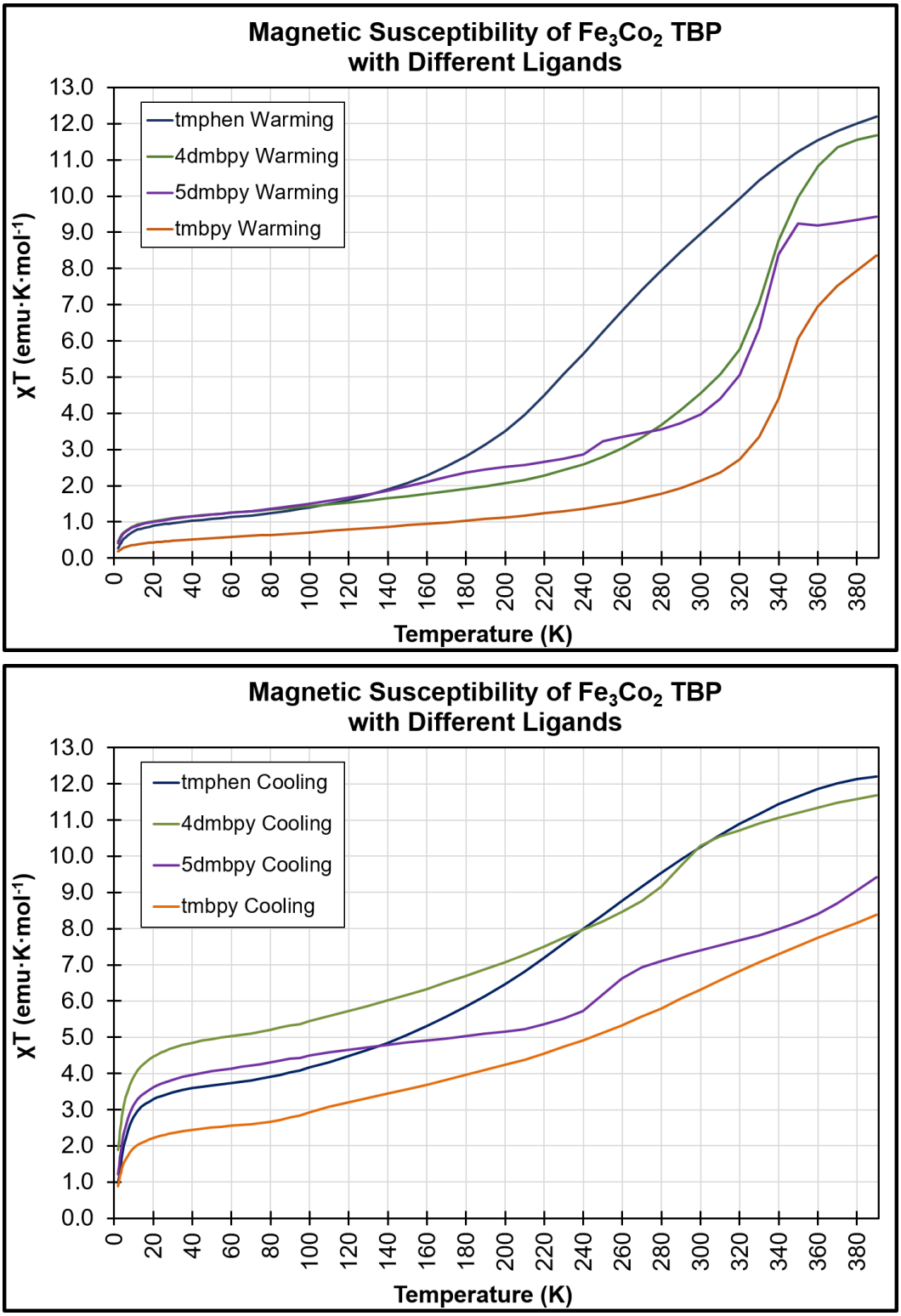

Figure 5-21. Comparison of the temperature dependent susceptibilities for compounds 8-11 before (top) and after (bottom) solvent is removed.

for all compounds at 2 K, 300 K and 390 K. It is clearly seen by these values that there is less HS Fe^{II} present at these temperatures as the π-π interactions in the TBP are decreased.

Table 5-16. Temperatures where the χT = 4.0 emu·K/mol is observed for the samples before and after losing solvent. This χT value was chosen as a representative value for 1 HS Fe^{II} center based upon the maximum χT value reached for compound **8** at 390 K.

Fe_3Co_2 TBP with Ligand	Before Solvent Loss	After Solvent Loss	Number of π-π Stacking Interactions
tmphen (8)	210 K	16 K	4
4dmbpy (9)	290 K	10 K	3
5dmbpy (10)	300 K	26 K	2
tmbpy (11)	337 K	160 K	1

Table 5-17. Comparison of χT values (before solvent loss) for molecules 8-11 at 2 K, 300 K and 390 K.

Fe_3Co_2 TBP with Ligand	χT Value at 2 K (emu·K/mol)	χT Value at 300 K (emu·K/mol)	χT Value at 390 K (emu·K/mol)	Number of π-π Stacking Interactions
tmphen (8)	0.3	9.0	12.2	4
4dmbpy (9)	0.5	4.6	11.5	3
5dmbpy (10)	0.4	4.0	9.5	2
tmbpy (11)	0.2	2.1	8.7	1

Table 5-18. Comparison of χT values for compounds 8-11 at 2 K and 300 K before losing solvent (initially) and after losing solvent (after warming). Solvent content was determined through a combination of the difference in mass of the sample before and after measurement in the SQUID and analysis of the sample with TGA after being measured in the SQUID.

Fe_3Co_2 TBP with Ligand		Water Content Per TBP	χT Value at 2 K (emu·K/mol)	χT Value at 300 K (emu·K/mol)
tmphen (8)	Initially	33.0	0.3	9.0
	After Warming	12.9	1.2	10.7
4dmbpy (9)	Initially	30.2	0.5	4.6
	After Warming	8.4	1.9	10.3
5dmbpy (10)	Initially	19.9	0.4	4.0
	After Warming	4.8	1.4	7.5
tmbpy (11)	Initially	16.6	0.2	2.1
	After Warming	5.7	1.0	6.7

Table 5-18 lists the number of solvent molecules as determined by the combination of TGA measurements and the mass difference in the sample before and after SQUID measurements. All solvent was assumed to be H_2O molecules. It can be seen that the samples did, in fact, lose solvent content in the SQUID and that all compounds retain some H_2O molecules despite being heated to 390 K (117 °C) twice. The magnitude of χT at 2 K and 300 K (Table 5-18) for the compounds before and after solvent loss clearly illustrates the fact that the HS state of Fe^{II} in each sample is favored, regardless of π-π stacking interactions, once solvent has been removed.

Concluding Remarks

SCO is a highly complex phenomenon that is affected by chemical and physical changes in the environment of the metal center. These perturbations, even if seemingly minor, can have non-trivial effects on the transition which makes elucidating or predicting the behavior difficult. Without careful systematic studies, it is often unclear which factor is the main driving force behind the change in transition behavior. This study illustrates that SCO behavior in Fe_3Co_2 TBPs can be changed effectively by two different methods. The SCO behavior in these molecules can be altered by the structural influence of π-π stacking interactions and the solvent content. It was shown that a decrease in π-π stacking interactions results in the LS state being favored over the HS state, as evidenced by the shift in transition temperatures and the decrease in the amount of HS Fe^{II} present in each sample as measured by SQUID magnetometry. By exchanging the tmphen ligand for 4dmbpy, hysteresis in the SCO behavior has been exhibited for the first time in a TBP molecule. This study also lends further evidence to the conclusion obtained for the Fe_3Ru_2 TBPs that the HS state of Fe^{II} is preferred as solvent is removed from the interstices of the crystal. This study also suggests that once solvent is removed from the molecules, the π-π stacking interactions still play a pivotal role in determining the spin state of the molecules. These influences have been shown to be major factors in determining the spin state of Fe^{II} and lend insight into how to modify these Fe-containing TBPs (and possibly other metal combinations) in order to tune the SCO behavior exhibited by these TBPs.

CHAPTER VI

SUMMARY AND FUTURE OUTLOOK

The work presented in this dissertation has resulted in the addition of new molecules to the largest homologous family of cyanide compounds in the whole of the literature. The research encompasses structural and magnetic studies of new and previously known trigonal bipyramidal molecules from the Dunbar laboratories, the results of which lend insight into how SCO and CTIST behavior can be modified with chemical influences such as solvation and π-π stacking interactions.

In Chapter II, a fast and reliable method for the preparation of the anisotropic $[Ru^{III}(CN)_6]^{3-}$ and $[Os^{III}(CN)_6]^{3-}$ cyanometallate anions as organic soluble salts is presented. The $(PPN)^+$ salts of these anions were structurally and electrochemically characterized for the first time. The facile reduction of these trivalent 4d and 5d Group VIII hexacyanometallates to their divalent analogs was confirmed by electrochemistry which corroborates the synthetic difficulties faced in avoiding decomposition by-products during the oxidation of the divalent species. EPR and magnetic studies support the conclusion that Os has more intrinsic anisotropy as compared to its 4d and 3d counterparts which could potentially lead to enhanced magnetic exchange and interesting magnetic behavior when incorporated into compounds.

Chapter III revealed the successful incorporation of $[Ru^{III}(CN)_6]^{3-}$ and

$[Os^{III}(CN)_6]^{3-}$ into the Co_3M_2 TBP motif which had evaded previous group members. The Co_3Ru_2 and Co_3Os_2 TBPs further exemplify the facile redox properties of the $[Ru^{III}(CN)_6]^{3-}$ and $[Os^{III}(CN)_6]^{3-}$ precursors and constitute interesting additions to the large homologous family of TBPs studied by our group. Both the Co_3Ru_2 and Co_3Os_2 TBPs undergo two metal-to-metal charge transfers between the axial Ru/Os and the equatorial Co^{II} centers. The Co_3Ru_2 TBP does this irreversibly and adopts a configuration of $[(HS\text{-}Co^{II})(LS\text{-}Co^{III})_2Ru^{II}_2]$ that behaves magnetically as an isolated HS Co^{II} ion at all temperatures since it is the only non-diamagnetic metal center in the molecule. Splitting of the iso-field lines in the reduced magnetization data was not observed. In contrast, the $[(HS\text{-}Co^{II})_3Os^{III}_2]$ TBP at room temperature undergoes two reversible CTIST events as the temperature is decreased resulting in a low temperature configuration of $[(HS\text{-}Co^{II})(LS\text{-}Co^{III})_2Os^{II}_2]$. This TBP is an interesting addition to the small number of compounds that exhibit CTIST as it is only the second Co/Os metal combination to show this behavior (the first being the Co_3Os_2 PB analog) and complements the findings observed for the Co_3Fe_2 TBP which exhibits one CTIST event. A slight splitting of the iso-field lines was observed in the reduced magnetization suggesting the presence of anisotropy. The model Zn_3Os_2 compound was also added to the family of TBPs studied and was fit to Curie-Weiss behavior with a Weiss constant (θ) of 0.05 indicating very weak ferromagnetic coupling between the axial Os^{III} centers through the long, diamagnetic $–C{\equiv}N–Zn^{II}–N{\equiv}C–$ linkage. This suggests that Os has stronger

exchange through the diamagnetic bridge than Fe since the Zn_3Fe_2 TBP did not exhibit this coupling behavior. Although the Mn_3Ru_2 TBP could not be crystallized, a $Mn^{II}_2Ru^{II}_2$ square-like compound was obtained, the formation of which involves the reduction and labilization of two CN^- ligands from each $[Ru^{III}(CN)_6]^{3-}$ moiety. This result underscores the facile redox properties of $[Ru(CN)_6]^{3/4-}$ and the synthetic challenges faced in preparing the $[Ru^{III}(CN)_6]^{3-}$ starting material.

In Chapter IV interesting solvent-dependent redox behavior for the Fe_3Ru_2 TBP was reported. The TBP was studied under MeCN solvent, after being freshly filtered, after exposed to vacuum for both 3 and 24 hours and with interstitial water molecules from being exposed to a humid atmosphere. Through the use of X-ray crystallography, ^{57}Fe Mössbauer and SQUID magnetometry, the most likely electronic configurations for the spin centers in each solvation environment was determined between the temperature range of 2 – 350 K. Above room temperature, the TBPs were all determined to contain $[(LS/HS\text{-}Fe^{II})(HS\text{-}Fe^{III})_2Ru^{II}_2]$ where the SCO event that occurs on the Fe^{II} center ranges from complete for the TBP exposed to vacuum for 24 hours to incomplete for the remaining solvation states studied. As the temperature is lowered, the first event to occur for all five TBPs is the HS → LS SCO on the Fe(2) center that remains divalent throughout all temperatures. Afterward, a combination of two events occur as temperature is decreased to 2 K at the Fe(1) and Fe(3) centers for all solvation states studied. One of them is a CTIST that occurs at the Fe(3) center that is engaged in intermolecular π-π stacking. The phenomena that occur

at the Fe(1) center were found to differ depending on the solvation environments however. The TBPs exposed to vacuum undergo another CTIST at the Fe(1) center while the TBPs studied under MeCN and after immediate filtration appear to undergo a SCO first which is then followed by a MMCT. The lack of concomitant MMCT and SCO events at the same metal center is a phenomenon that has not been reported in the literature to the best of our knowledge. With the exchange of interstitial MeCN for water, the trivalent Fe(1) center appears to undergo a HS → LS SCO event only, ultimately changing the redox properties observed in the other solvation states of the Fe_3Ru_2 TBP. Table 6-1 shows a summary of the Fe centers and the transition events that occur based upon the solvation. The clear trend observed from this study is that the percent of HS Fe^{II} that occurs increases as solvent is removed and that solvent can change the redox properties of these TBPs. The Fe_3Ru_2 TBP can exhibit a variety of spin transition behaviors which complement the Fe_3Fe_2 TBP that only undergoes SCO of all three equatorial Fe^{II} centers and the Fe_3Os_2 TBP that mirrors the evacuated Fe_3Ru_2 analogs and exhibits two reversible CTIST events but no SCO on the remaining Fe^{II} center.

Table 6-1. Summary of the transition events on the Fe centers in the Fe_3Ru_2 TBPs (7a-e).

Fe_3Ru_2 TBP	Fe(1)	Fe(2)	Fe(3)	Total Events	Type
Solvated (7a)	SCO LS Fe^{III} ↔ HS Fe^{III} CT LS Fe^{II} ↔ LS Fe^{III}	SCO LS Fe^{II} ↔ HS Fe^{II}	CTIST LS Fe^{II} ↔ HS Fe^{III}	SCO CTIST SCO CT	Fe^{II} Fe^{III} Fe^{III} ↔ Fe^{II}
Filtered (7b)	SCO LS Fe^{III} ↔ HS Fe^{III} CT LS Fe^{II} ↔ LS Fe^{III}	SCO LS Fe^{II} ↔ HS Fe^{II}	CTIST LS Fe^{II} ↔ HS Fe^{III}	SCO CTIST SCO CT	Fe^{II} Fe^{III} Fe^{III} ↔ Fe^{II}
3 hours (7c)	CTIST LS Fe^{II} ↔ HS Fe^{III}	SCO LS Fe^{II} ↔ HS Fe^{II}	CTIST LS Fe^{II} ↔ HS Fe^{III}	SCO 2 CTIST	Fe^{II}
24 hours (7d)	CTIST LS Fe^{II} ↔ HS Fe^{III}	SCO LS Fe^{II} ↔ HS Fe^{II}	CTIST LS Fe^{II} ↔ HS Fe^{III}	SCO 2 CTIST	Fe^{II}
Humid (7e)	SCO LS Fe^{III} ↔ HS Fe^{III}	SCO LS Fe^{II} ↔ HS Fe^{II}	CTIST LS Fe^{II} ↔ HS Fe^{III}	SCO CTIST SCO	Fe^{II} Fe^{III}

Chapter V is devoted to a study of the effects of π-π stacking on the SCO events at the equatorial Fe^{II} centers in the Fe_3Co_2 TBP. It was found that there is a correlation between intermolecular interactions and the stabilization of spin states. As the number of π-π stacking interactions are fewer in number, the percent of HS Fe^{II} present between 2 K and 390 K decreases. This trend indicates that suppressing the π-π stacking interactions in these polynuclear SCO compounds stabilizes the LS state of Fe^{II} and leads to a more cooperative SCO

at elevated temperatures. This study also revealed that losing interstitial water affects the SCO behavior in a similar manner to the Fe_3Ru_2 TBPs in that the HS state of the Fe^{II} centers are stabilized in the absence of solvent.

A summary of the low and high temperature electronic configurations of the TBPs studied in this dissertation and their previously reported congeners is contained in Table 6-2. Note that the configurations given are for complete transition events which is not always the case. The Zn_3Os_2 TBP is not included, as the electronic configuration does not change with temperature. For the family of Co_3M_2 TBPs (M = Fe, Ru or Os) a very different behavior is observed when descending the Group VIII elements. For the Fe congener there is a reversible CTIST event involving one of the axial Fe and equatorial Co centers as well as a SCO event in one of the Co^{II} centers. In the case of the Ru analog two MMCT events occur during synthesis and are irreversible. However, for the Os cousin there are two thermally reversible CTIST events that occur. When comparing the three analogs at high temperatures the Os and Fe centers remain in the trivalent state (no spontaneous MMCT occurs during the synthesis) which is in contrast to the Ru analog where the MMCT occurs during synthesis and is irreversible. Upon decreasing the temperature, both Os centers participate in CTIST events while the Fe analog has only one of the Fe centers participating in a CTIST which indicates a more facile reduction of the $[Os^{III}(CN)_6]^{3-}$ moiety in comparison to the Fe analog. In the case of the Fe_3M_2 TBP analogs (M = Fe, Ru or Os), the Fe_3Fe_2 TBP shows only one SCO event at the three equatorial Fe^{II} centers.

Table 6-2. A summary of the electronic configurations that are observed for the TBPs discussed. * Indicates when the transition is not complete. The state that is given with the * is the majority of the spin state present. # Indicates an incomplete charge transfer process where the majority of the observed configuration is given. Note that there is no change in electronic configuration of the Co_3Ru_2 TBP.

M_3M_2 TBP	Low Temperature	High Temperature
Co_3M_2		
Co_3Fe_2	$(HS\text{-}Co^{II})(LS\text{-}Co^{II})(LS\text{-}Co^{III})Fe^{II}Fe^{III}$	$(HS\text{-}Co^{II})_3Fe^{III}_2$
Co_3Ru_2 (3)	$(HS\text{-}Co^{II})(LS\text{-}Co^{III})_2Ru^{II}_2$	$(HS\text{-}Co^{II})(LS\text{-}Co^{III})_2Ru^{II}_2$
Co_3Os_2 (4)	$(HS\text{-}Co^{II})(LS\text{-}Co^{III})_2Os^{II}_2$	$(HS\text{-}Co^{II})_3Os^{III}_2$
Fe_3M_2		
Fe_3Fe_2	$(LS\text{-}Fe^{II})_3Fe^{III}_2$	$(HS\text{-}Fe^{II})_3Fe^{III}_2$
Fe_3Ru_2 Solvated (7a)	$(LS\text{-}^{\#}Fe^{II})(*LS\text{-}Fe^{II})_2Ru^{III}_2$	$(*HS\text{-}Fe^{II})(HS\text{-}Fe^{III})_2Ru^{II}_2$
Fe_3Ru_2 Filtered (7b)	$(LS\text{-}^{\#}Fe^{II})(*LS\text{-}Fe^{II})_2Ru^{III}_2$	$(*HS\text{-}Fe^{II})(HS\text{-}Fe^{III})_2Ru^{II}_2$
Fe_3Ru_2 3 Hours (7c)	$(LS\text{-}Fe^{II})_3Ru^{III}_2$	$(*HS\text{-}Fe^{II})(HS\text{-}Fe^{III})_2Ru^{II}_2$
Fe_3Ru_2 24 Hours (7d)	$(LS\text{-}Fe^{II})_3Ru^{III}_2$	$(HS\text{-}Fe^{II})(HS\text{-}Fe^{III})_2Ru^{II}_2$
Fe_3Ru_2 Humid (7e)	$(LS\text{-}Fe^{II})_2(^{\#}LS\text{-}Fe^{III})Ru^{II}Ru^{III}$	$(*HS\text{-}Fe^{II})(HS\text{-}Fe^{III})_2Ru^{II}_2$
Fe_3Os_2	$(LS\text{-}Fe^{II})_3Os^{III}_2$	$(LS\text{-}Fe^{II})(HS\text{-}Fe^{III})_2Os^{II}_2$
Fe_3Co_2		
Fe_3Co_2 tmphen (8)	$(LS\text{-}Fe^{II})_3Co^{III}_2$	$(HS\text{-}Fe^{II})_3Co^{III}_2$
Fe_3Co_2 4dmbpy (9)	$(LS\text{-}Fe^{II})_3Co^{III}_2$	$(*HS\text{-}Fe^{II})_3Co^{III}_2$
Fe_3Co_2 5dmbpy (10)	$(LS\text{-}Fe^{II})_3Co^{III}_2$	$(*LS\text{-}Fe^{II})(HS\text{-}Fe^{II})_2Co^{III}_2$
Fe_3Co_2 tmbpy (11)	$(LS\text{-}Fe^{II})_3Co^{III}_2$	$(*LS\text{-}Fe^{II})(HS\text{-}Fe^{II})_2Co^{III}_2$

Depending on the solvent content, the Ru congener exhibits different, complex behaviors from one SCO and two CTIST events to one CTIST along with two incomplete SCO and one incomplete CT events, as explained earlier. The Os analog undergoes two CTIST events while the remaining equatorial Fe^{II} center stays LS at all temperatures. When comparing the group (Fe, Ru and Os), at high temperatures, only the axial Fe centers (Fe_3Fe_2 TBP) remain in their trivalent state which is in contrast to both the Ru and Os analogs that undergo spontaneous MMCT during synthesis. At low temperatures however, Ru and Os are re-oxidized (returning to their trivalent state), consequently reducing two of the equatorial Fe centers to their divalent state. This underscores the rich redox properties of Group VIII elements.

SCO is a complex phenomenon that is affected by many different, and often, subtle perturbations. Further studies are required to ascertain whether generalizations about these perturbations and their corresponding effects on the spin-transition behavior of TBPs can be made. Ideally, an investigation of these fundamental aspects is better when all variables except one that contribute to changes in SCO or CTIST are held constant. Considering the non-trivial changes that can occur due to subtle differences, this is a very challenging task in the study of SCO compounds.

For these TBPs, replacing tmphen for other ligands capable of different degrees of π-π stacking is a rewarding endeavor, especially as they are incorporated into TBPs that have rich redox properties like the Fe_3Ru_2, Fe_3Os_2,

Co_3Ru_2 and Co_3Os_2 analogs. In order to best correlate the changes in ligand to changes in spin-transition behavior, it would be ideal to conduct these studies with TBPs that contain only water in the interstitial molecules and to limit the amount of solvent loss during sample preparation and measurement.

The effect of interstitial solvent is an interesting study in these TBPs and although difficult, it should be conducted on the analogs that have rich redox behavior like the Fe_3Ru_2, Fe_3Os_2, Co_3Ru_2 Co_3Os_2 and Co_3Fe_2 TBPs with the Fe_3Fe_2 and Fe_3Co_2 analogs as models. An extensive solvent exchange study for the Fe_3Co_2 TBP is still underway and confirms that the type of solvent within the interstitial lattice plays a vital role in the cooperativity and spin states of SCO.

These TBPs should be studied for photomagnetic behavior since the Fe_3Co_2 and Co_3Fe_2 TBPs both display this phenomenon. It would be interesting to see how the photomagnetic behavior changes upon solvent and ligand exchange.

Future work will include the preparation of new metal combinations of these TBPs. The Mn_3Ru_2 TBP is still of very high priority as the Mn_3Os_2 TBP exhibits SMM behavior similar to the Mn_3Mn_2 TBP compound. The Cr_3Os_2 TBP is of interest as well since the Cr_3Fe_2 TBP undergoes cyanide linkage isomerism and the Cr_3Ru_2 analog undergoes two irreversible MMCT events during synthesis but still displays very weak ferromagnetic coupling between the Cr metal centers despite the fact that the Ru^{II} centers are diamagnetic. Obtaining the Zn_3Ru_2 model compound will be useful for probing if there are any long range exchange

interactions between the Ru^{III} centers as was found for the Zn_3Os_2 analog. Attempts to prepare the Zn_3Ru_2 TBP led to formation of tiny yellow crystal rods that will need to be measured at the ALS synchrotron source. It appears that these crystals may be very sensitive to solvent loss because filtering the crystals for magnetic measurements eventually led to an olive green material after several minutes. Magnetic measurements were obtained but did not correlate well to what was expected for the Zn_3Ru_2 TBP, most likely due to decomposition of the solid upon solvent loss. This TBP should be prepared again and measured under solvent. The synthesis of this compound is intricate as it is not the same as the Zn_3Os_2 TBP. Prussian Blue analogs containing vanadium have been theorized to behave as high temperature magnets so the incorporation of V^{II} into the M_3Ru_2 and M_3Os_2 should be carried out as well.

REFERENCES

1. Wiltschko, R.; Stapput, K.; Thalau, P.; Wiltschko, W. *Journal of The Royal Society Interface* **2010**, *7*, S163.

2. Walker, M. M.; Diebel, C. E.; Haugh, C. V.; Pankhurst, P. M.; Montgomery, J. C.; Green, C. R. *Nature* **1997**, *390*, 371.

3. Landler, L.; Gollmann, G. *Frontiers in Zoology* **2011**, *8*, 6.

4. Mora, C. V.; Bingman, V. P. *PLoS One* **2013**, *8*, e72869.

5. Liang, C.-H.; Chuang, C.-L.; Jiang, J.-A.; Yang, E.-C. *Scientific Reports* **2016**, *6*, 23657.

6. Belova, N. A.; Acosta-Avalos, D. *Journal of Biophysics* **2015**, *2015*, 423838.

7. Foley, L. E.; Gegear, R. J.; Reppert, S. M. *Nat Commun* **2011**, *2*, 356.

8. Coey, J. M. D. *Magnetism and Magnetic Materials*; Cambridge University Press, 2009.

9. Global Magnet Market Report 2015 - Industry Trends, Magnet Types, Major Markets Manafacturing and Applications http://www.prnewswire.com/news-releases/global-magnet-market-report-2015---industrytrends-magnet-types-major-markets-manufacturing-and-applications-300189817.html (accessed May 23, 2016).

10. Markets And Markets http://www.marketsandmarkets.com/PressReleases/magnetic-materials.asp (accessed May 23 2016).

11. Bain, G. A.; Berry, J. F. *J. Chem. Educ.* **2008**, *85*, 532.

12. Carlin, R. L. *Magnetochemistry*; Springer-Verlag: West Berlin, Heidelberg: New York, Tokyo, 1986.

13. Spaldin, N. A. *Magnetic materials : fundamentals and applications*; Cambridge University Press: Cambridge; New York, 2011.

14. Orchard, A. F. *Magnetochemistry*; Oxford University Press: Oxford, New York, 2003.

15. Kahn, O. *Molecular Magnetism*; VCH: New York, 1993.

16. Gatteschi, D.; Sessoli, R.; Villain, J. *Molecular nanomagnets*; Oxford University Press: Oxford ;, 2006.

17. Magnet Manufacturing Process http://www.arnoldmagnetics.com/en-us/Technical-Library/Magnet-Manufacturing-Process (accessed May 23, 2016).

18. Pei, Y.; Verdaguer, M.; Kahn, O.; Sletten, J.; Renard, J. P. *Inorg. Chem.* **1987**, *26*, 138.

19. Manriquez, J. M.; Yee, G. T.; Mclean, R. S.; Epstein, A. J.; Miller, J. S. *Science* **1991**, *252*, 1415.

20. Moore, G. E. *IEEE Solid-State Circuits Newsletter* **2006**, *20*, 33.

21. The Story of Intel 4004 http://www.intel.com/content/www/us/en/history/museum-story-of-intel-4004.html (accessed May 27, 2016).

22. Peercy, P. S. *Nature* **2000**, *406*, 1023.

23. Rohrer, H. *Japanese Journal of Applied Physics* **1993**, *32*, 1335.

24. Keyes, R. W. *Proceedings of the IEEE* **2001**, *89*, 227.

25. Gadet, V.; Mallah, T.; Castro, I.; Verdaguer, M.; Veillet, P. *J. Am. Chem. Soc.* **1992**, *114*, 9213.

26. Mallah, T.; Thiebaut, S.; Verdaguer, M.; Veillet, P. *Science* **1993**, *262*, 1554.

27. Ferlay, S.; Mallah, T.; Ouahes, R.; Veillet, P.; Verdaguer, M. *Nature* **1995**, *378*, 701.

28. Verdaguer, M.; Bleuzen, A.; Train, C.; Garde, R.; Biani, F. F. d.; Desplanches, C. *Philosophical Transactions: Mathematical, Physical and Engineering Sciences* **1999**, *357*, 2959.

29. Sense Jan van der, M.; Peter, L. *J. Phys.: Condens. Matter* **2010**, *22*, 133001.

30. Tsutsui, M.; Taniguchi, M. *Sensors* **2012**, *12*, 7259.

31. Raymo, F. M.; Giordani, S. *Proceedings of the National Academy of Sciences* **2002**, *99*, 4941.

32. Sanvito, S. *Chem. Soc. Rev.* **2011**, *40*, 3336.

33. Bogani, L.; Wernsdorfer, W. *Nat. Mater.* **2008**, *7*, 179.

34. Pedersen, K. S.; Bendix, J.; Clerac, R. *Chem. Commun. (Cambridge, U. K.)* **2014**, *50*, 4396.

35. de Silva, P. A.; Gunaratne, N. H. Q.; McCoy, C. P. *Nature* **1993**, *364*, 42.

36. Collier, C. P.; Wong, E. W.; Belohradský, M.; Raymo, F. M.; Stoddart, J. F.; Kuekes, P. J.; Williams, R. S.; Heath, J. R. *Science* **1999**, *285*, 391.

37. Palii, A.; Tsukerblat, B.; Klokishner, S.; Dunbar, K. R.; Clemente-Juan, J. M.; Coronado, E. *Chem. Soc. Rev.* **2011**, *40*, 3130.

38. Caneschi, A.; Gatteschi, D.; Sessoli, R.; Barra, A. L.; Brunel, L. C.; Guillot, M. *J. Am. Chem. Soc.* **1991**, *113*, 5873.

39. Sessoli, R.; Tsai, H. L.; Schake, A. R.; Wang, S.; Vincent, J. B.; Folting, K.; Gatteschi, D.; Christou, G.; Hendrickson, D. N. *J. Am. Chem. Soc.* **1993**, *115*, 1804.

40. Sessoli, R.; Gatteschi, D.; Caneschi, A.; Novak, M. A. *Nature* **1993**, *365*, 141.

41. Christou, G.; Gatteschi, D.; Hendrickson, D. N.; Sessoli, R. *MRS Bulletin* **2000**, *25*, 66.

42. Chen, Y.-C.; Liu, J.-L.; Ungur, L.; Liu, J.; Li, Q.-W.; Wang, L.-F.; Ni, Z.-P.; Chibotaru, L. F.; Chen, X.-M.; Tong, M.-L. *J. Am. Chem. Soc.* **2016**, *138*, 2829.

43. Rinehart, J. D.; Fang, M.; Evans, W. J.; Long, J. R. *J. Am. Chem. Soc.* **2011**, *133*, 14236.

44. Ruiz, E. *Phys. Chem. Chem. Phys.* **2014**, *16*, 14.

45. In *Spin-Crossover Materials*; John Wiley & Sons Ltd: 2013, p i.

46. Lefter, C.; Tan, R.; Tricard, S.; Dugay, J.; Molnár, G.; Salmon, L.; Carrey, J.; Rotaru, A.; Bousseksou, A. *Polyhedron* **2015**, *102*, 434.

47. Létard, J.-F.; Guionneau, P.; Goux-Capes, L. In *Spin Crossover in Transition Metal Compounds III*; Springer Berlin Heidelberg: Berlin, Heidelberg, 2004, p 221.

48. Muller, R. N.; Vander Elst, L.; Laurent, S. *J. Am. Chem. Soc.* **2003**, *125*, 8405.

49. Nakano, K.; Suemura, N.; Yoneda, K.; Kawata, S.; Kaizaki, S. *Dalton Trans.* **2005**, 740.

50. Feltham, H. L. C.; Johnson, C.; Elliott, A. B. S.; Gordon, K. C.; Albrecht, M.; Brooker, S. *Inorg. Chem.* **2015**, *54*, 2902.

51. Halder, G. J.; Kepert, C. J.; Moubaraki, B.; Murray, K. S.; Cashion, J. D. *Science* **2002**, *298*, 1762.

52. Jordi, C. *Rev. Inorg. Chem.* **2014**, *0*.

53. Bao, X.; Shepherd, H. J.; Salmon, L.; Molnár, G.; Tong, M.-L.; Bousseksou, A. *Angew. Chem.* **2013**, *125*, 1236.

54. Bilbeisi, R. A.; Zarra, S.; Feltham, H. L. C.; Jameson, G. N. L.; Clegg, J. K.; Brooker, S.; Nitschke, J. R. *Chemistry – A European Journal* **2013**, *19*, 8058.

55. Ksenofontov, V.; Gaspar, A. B.; Gütlich, P. In *Spin Crossover in Transition Metal Compounds III*; Springer Berlin Heidelberg: Berlin, Heidelberg, 2004, p 23.

56. Cowan, M. G.; Olguín, J.; Narayanaswamy, S.; Tallon, J. L.; Brooker, S. *J. Am. Chem. Soc.* **2012**, *134*, 2892.

57. Linares, J.; Codjovi, E.; Garcia, Y. *Sensors* **2012**, *12*, 4479.

58. Garcia, Y.; Robert, F.; Naik, A. D.; Zhou, G.; Tinant, B.; Robeyns, K.; Michotte, S.; Piraux, L. *J. Am. Chem. Soc.* **2011**, *133*, 15850.

59. Grondin, P.; Roubeau, O.; Castro, M.; Saadaoui, H.; Colin, A.; Clérac, R. *Langmuir* **2010**, *26*, 5184.

60. Zhao-Yang Li, O. S.; Yao, Z.-S.; Kang, S.; Kanegawa, S. In *Spin-Crossover Materials*; John Wiley & Sons Ltd: 2013, p 303.

61. Weber, B.; Bauer, W.; Obel, J. *Angew. Chem., Int. Ed.* **2008**, *47*, 10098.

62. Boldog, I.; Gaspar, A. B.; Martínez, V.; Pardo-Ibañez, P.; Ksenofontov, V.; Bhattacharjee, A.; Gütlich, P.; Real, J. A. *Angew. Chem., Int. Ed.* **2008**, *47*, 6433.

63. Vieira, B. J. C.; Dias, J. C.; Santos, I. C.; Pereira, L. C. J.; da Gama, V.; Waerenborgh, J. C. *Inorg. Chem.* **2015**.

64. Klein, Y. M.; Sciortino, N. F.; Ragon, F.; Housecroft, C. E.; Kepert, C. J.; Neville, S. M. *Chem. Commun. (Cambridge, U. K.)* **2014**, *50*, 3838.

65. *Spin Crossover in Transition Metal Compounds I*; 1 ed.; Springer-Verlag Berlin Heidelberg, 2004.

66. *Spin Crossover in Transition Metal Compounds II*; 1 ed.; Springer-Verlag Berlin Heidelberg, 2004.

67. *Spin Crossover in Transition Metal Compounds III*; 1 ed.; Springer-Verlag Berlin Heidelberg, 2004.

68. Gütlich, P.; Garcia, Y.; Spiering, H. In *Magnetism: Molecules to Materials IV*; Wiley-VCH Verlag GmbH & Co. KGaA: 2003, p 271.

69. *Spin-Crossover Materials. Properties and Applications*; WILEY-VCH Verlag, 2013.

70. Aguila, D.; Prado, Y.; Koumousi, E. S.; Mathoniere, C.; Clerac, R. *Chem. Soc. Rev.* **2015**.

71. Bousseksou, A.; Molnar, G.; Salmon, L.; Nicolazzi, W. *Chem. Soc. Rev.* **2011**, *40*, 3313.

72. Gutlich, P.; Garcia, Y.; Goodwin, H. A. *Chem. Soc. Rev.* **2000**, *29*, 419.

73. Halcrow, M. A. *Chem. Soc. Rev.* **2011**, *40*, 4119.

74. Harding, D. J.; Harding, P.; Phonsri, W. *Coord. Chem. Rev.* **2016**, *313*, 38.

75. Muñoz, M. C.; Real, J. A. *Coord. Chem. Rev.* **2011**, *255*, 2068.

76. Shatruk, M.; Phan, H.; Chrisostomo, B. A.; Suleimenova, A. *Coord. Chem. Rev.* **2015**, *289–290*, 62.

77. Brooker, S. *Chem. Soc. Rev.* **2015**, *44*, 2880.

78. Cambi, L.; Szegö, L. *Berichte der deutschen chemischen Gesellschaft (A and B Series)* **1931**, *64*, 2591.

79. Gispert, J. R. *Coordination Chemistry*; Wiley–VCH, 2008.

80. Garcia, Y.; Gütlich, P. In *Spin Crossover in Transition Metal Compounds II*; Springer Berlin Heidelberg: Berlin, Heidelberg, 2004, p 49.

81. Lejay, J.; Jansen, A. G. M.; Wyder, P.; Bronger, W.; Kläui, W. *Physical Review B* **1991**, *43*, 8196.

82. Guionneau, P.; Marchivie, M.; Bravic, G.; Létard, J.-F.; Chasseau, D. In *Spin Crossover in Transition Metal Compounds II*; Gütlich, P., Goodwin, H. A., Eds.; Springer Berlin / Heidelberg: Berlin, Heidelberg, 2004; Vol. 234, p 97.

83. Gütlich, P.; Gaspar, A. B.; Garcia, Y. *Beilstein J. Org. Chem.* **2013**, *9*, 342.

84. Gütlich, P.; Eckhard, B.; Trautwein, A. X. *Mössbauer Spectroscopy and Transition Metal Chemistry: Fundamentals and Applications*; Springer Berlin Heidelberg, 2011.

85. Gütlich, P.; Goodwin, H. A. In *Spin Crossover in Transition Metal Compounds I*; Gütlich, P., Goodwin, H. A., Eds.; Springer Berlin Heidelberg: Berlin, Heidelberg, 2004, p 1.

86. Gütlich, P. *Z. Anorg. Allg. Chem.* **2012**, *638*, 15.

87. Gütlich, P. *Chemical Mössbauer Spectroscopy*; Springer US, 1984.

88. Gütlich, P. *Eur. J. Inorg. Chem.* **2013**, *2013*, 581.

89. Barrett, S. A.; Halcrow, M. A. *RSC Advances* **2014**, *4*, 11240.

90. Halcrow, M. A. *Chem. Commun. (Cambridge, U. K.)* **2013**, *49*, 10890.

91. Roberts, T. D.; Little, M. A.; Tuna, F.; Kilner, C. A.; Halcrow, M. A. *Chem. Commun. (Cambridge, U. K.)* **2013**, *49*, 6280.

92. Vela, S.; Gourlaouen, C.; Fumanal, M.; Ribas-Arino, J. *Magnetochemistry* **2016**, *2*, 6.

93. Wannarit, N.; Nassirinia, N.; Amani, S.; Masciocchi, N.; Youngme, S.; Roubeau, O.; Teat, S. J.; Gamez, P. *Inorg. Chem.* **2014**, *53*, 9827.

94. Barrett, S. A.; Kilner, C. A.; Halcrow, M. A. *Dalton Trans.* **2011**, *40*, 12021.

95. Salitros, I.; Pavlik, J.; Boca, R.; Fuhr, O.; Rajadurai, C.; Ruben, M. *CrystEngComm* **2010**, *12*, 2361.

96. Cook, L. J. K.; Kulmaczewski, R.; Cespedes, O.; Halcrow, M. A. *Chemistry – A European Journal* **2016**, *22*, 1789.

97. Murray, K. S.; Kepert, C. J. In *Spin Crossover in Transition Metal Compounds I*; Gütlich, P., Goodwin, H. A., Eds.; Springer Berlin Heidelberg: Berlin, Heidelberg, 2004, p 195.

98. Vela, S.; Novoa, J. J.; Ribas-Arino, J. *Phys. Chem. Chem. Phys.* **2014**, *16*, 27012.

99. Kulmaczewski, R.; Shepherd, H. J.; Cespedes, O.; Halcrow, M. A. *Inorg. Chem.* **2014**, *53*, 9809.

100. Dupouy, G.; Marchivie, M.; Triki, S.; Sala-Pala, J.; Salaün, J.-Y.; Gómez-García, C. J.; Guionneau, P. *Inorg. Chem.* **2008**, *47*, 8921.

101. Halcrow, M. A. In *Spin-Crossover Materials*; John Wiley & Sons Ltd: 2013, p 147.

102. Buchanan, R. M.; Pierpont, C. G. *J. Am. Chem. Soc.* **1980**, *102*, 4951.

103. Sato, O.; Iyoda, T.; Fujishima, A.; Hashimoto, K. *Science* **1996**, *272*, 704.

104. Sato, O.; Einaga, Y.; Iyoda, T.; Fujishima, A.; Hashimoto, K. *J. Electrochem. Soc.* **1997**, *144*, L11.

105. Zheng, C.; Xu, J.; Yang, Z.; Tao, J.; Li, D. *Inorg. Chem.* **2015**, *54*, 9687.

106. Koumousi, E. S.; Jeon, I.-R.; Gao, Q.; Dechambenoit, P.; Woodruff, D. N.; Merzeau, P.; Buisson, L.; Jia, X.; Li, D.; Volatron, F.; Mathoniere, C.; Clérac, R. *J. Am. Chem. Soc.* **2014**.

107. Jeon, I.-R.; Calancea, S.; Panja, A.; Pinero Cruz, D. M.; Koumousi, E. S.; Dechambenoit, P.; Coulon, C.; Wattiaux, A.; Rosa, P.; Mathoniere, C.; Clerac, R. *Chemical Science* **2013**, *4*, 2463.

108. Sato, O. *Proceedings of the Japan Academy. Series B, Physical and Biological Sciences* **2012**, *88*, 213.

109. Roman, M. A.; Reu, O. S.; Klokishner, S. I. *The Journal of Physical Chemistry A* **2012**, *116*, 9534.

110. Cafun, J.-D.; Lejeune, J.; Baudelet, F.; Dumas, P.; Itié, J.-P.; Bleuzen, A. *Angew. Chem., Int. Ed.* **2012**, n/a.

111. Funck, K. E.; Prosvirin, A. V.; Mathonière, C.; Clérac, R.; Dunbar, K. R. *Inorg. Chem.* **2011**, *50*, 2782.

112. Giorgetti, M.; Aquilanti, G.; Ciabocco, M.; Berrettoni, M. *Phys. Chem. Chem. Phys.* **2015**, *17*, 22519.

113. Liu, T.; Zhang, Y.-J.; Kanegawa, S.; Sato, O. *Angew. Chem., Int. Ed.* **2010**, *49*, 8645.

114. Liu, T.; Zhang, Y.-J.; Kanegawa, S.; Sato, O. *J. Am. Chem. Soc.* **2010**, *132*, 8250.

115. Avendano, C.; Hilfiger, M. G.; Prosvirin, A.; Sanders, C.; Stepien, D.; Dunbar, K. R. *J. Am. Chem. Soc.* **2010**, *132*, 13123.

116. Hilfiger, M. G.; Chen, M.; Brinzari, T. V.; Nocera, T. M.; Shatruk, M.; Petasis, D. T.; Musfeldt, J. L.; Achim, C.; Dunbar, K. R. *Angew. Chem. Int. Ed.* **2010**, *49*, 1410.

117. Dei, A. *Angew. Chem., Int. Ed.* **2005**, *44*, 1160.

118. Arimoto, Y.; Ohkoshi, S.-i.; Zhong, Z. J.; Seino, H.; Mizobe, Y.; Hashimoto, K. *J. Am. Chem. Soc.* **2003**, *125*, 9240.

119. Ohkoshi, S.; Hamada, Y.; Matsuda, T.; Tsunobuchi, Y.; Tokoro, H. *Chem. Mater.* **2008**, *20*, 3048.

120. Chorazy, S.; Stanek, J. J.; Nogaś, W.; Majcher, A. M.; Rams, M.; Kozieł, M.; Juszyńska-Gałązka, E.; Nakabayashi, K.; Ohkoshi, S.-i.; Sieklucka, B.; Podgajny, R. *J. Am. Chem. Soc.* **2016**, *138*, 1635.

121. Podgajny, R.; Chorazy, S.; Nitek, W.; Rams, M.; Majcher, A. M.; Marszałek, B.; Żukrowski, J.; Kapusta, C.; Sieklucka, B. *Angew. Chem., Int. Ed.* **2013**, *52*, 896.

122. Nakamoto, K. In *Infrared and Raman Spectra of Inorganic and Coordination Compounds*; John Wiley & Sons, Inc.: 2008, p 1.

123. In *The Organometallic Chemistry of the Transition Metals*; John Wiley & Sons, Inc.: 2014, p 98.

124. Woodward, J. *Philosophical Transactions (1683-1775)* **1724**, *33*, 15.

125. Brown, J. *Philosophical Transactions (1683-1775)* **1724**, *33*, 17.

126. Rossol, M. *Pigments and Dyes*, 1994.

127. Song, X.-X.; Liu, Z.-J.; Tang, Q. *J. Nanosci. Nanotechnol.* **2013**, *13*, 5233.

128. Mohammad, A.; Faustino, P. J.; Khan, M. A.; Yang, Y. *Int. J. Pharm.* **2014**, *477*, 122.

129. Mohammad, A.; Yang, Y.; Khan, M. A.; Faustino, P. J. *Clinical Toxicology* **2015**, *53*, 102.

130. Mohammad, A.; Yang, Y.; Khan, M. A.; Faustino, P. J. *J. Pharm. Biomed. Anal.* **2015**, *103*, 85.

131. Holden, A. N.; Matthias, B. T.; Anderson, P. W.; Lewis, H. W. *Phys. Rev.* **1956**, *102*, 1463.

132. Mayoh, B.; Day, P. *Journal of the Chemical Society, Dalton Transactions* **1976**, 1483.

133. Holmes, S. M.; Girolami, G. S. *J. Am. Chem. Soc.* **1999**, *121*, 5593.

134. Hatlevik, Ø.; Buschmann, W. E.; Zhang, J.; Manson, J. L.; Miller, J. S. *Adv. Mater. (Weinheim, Ger.)* **1999**, *11*, 914.

135. Dujardin, E.; Ferlay, S.; Phan, X.; Desplanches, C.; Moulin, C. C. D.; Sainctavit, P.; Baudelet, F.; Dartyge, E.; Veillet, P.; Verdaguer, M. *J. Am. Chem. Soc.* **1998**, *120*, 11347.

136. Entley, W. R.; Girolami, G. S. *Science* **1995**, *268*, 397.

137. Palii, A. V.; Ostrovsky, S. M.; Klokishner, S. I.; Tsukerblat, B. S.; Berlinguette, C. P.; Dunbar, K. R.; Galán-Mascarós, J. R. *J. Am. Chem. Soc.* **2004**, *126*, 16860.

138. Tsukerblat, B. S.; Palii, A. V.; Ostrovsky, S. M.; Kunitsky, S. V.; Klokishner, S. I.; Dunbar, K. R. *J. Chem. Theory Comput.* **2005**, *1*, 668.

139. Klokishner, S. I.; Ostrovsky, S. M.; Palii, A. V.; Dunbar, K. *J. Mol. Struct.* **2007**, *838*, 144.

140. Mironov, V. S. *Dokl. Phys. Chem.* **2007**, *415*, 199.

141. Palii, A. V.; Reu, O. S.; Ostrovsky, S. M.; Klokishner, S. I.; Tsukerblat, B. S.; Hilfiger, M.; Shatruk, M.; Prosvirin, A.; Dunbar, K. R. *J. Phys. Chem.* **2009**, *113*, 6886.

142. Klokishner, S.; Ostrovsky, S.; Palii, A.; Shatruk, M.; Funck, K.; Dunbar, K. R.; Tsukerblat, B. *J. Phys. Chem. C* **2011**, *115*, 21666.

143. Berlinguette, C. P.; Vaughn, D.; Cañada-Vilalta, C.; Galán-Mascarós, J. R.; Dunbar, K. R. *Angew. Chem. Int. Ed.* **2003**, *42*, 1523.

144. Pinkowicz, D.; Southerland, H.; Wang, X.-Y.; Dunbar, K. R. *J. Am. Chem. Soc.* **2014**, *136*, 9922.

145. Shatruk, M.; Dragulescu-Andrasi, A.; Chambers, K. E.; Stoian, S. A.; Bominaar, E. L.; Achim, C.; Dunbar, K. R. *J. Am. Chem. Soc.* **2007**, *129*, 6104.

146. Funck, K. E.; Hilfiger, M. G.; Berlinguette, C. P.; Shatruk, M.; Wernsdorfer, W.; Dunbar, K. R. *Inorg. Chem.* **2009**, *48*, 3438.

147. Berlinguette, C. P.; Dragulescu-Andrasi, A.; Sieber, A.; Galán-Mascarós, J. R.; Güdel, H.-U.; Achim, C.; Dunbar, K. R. *J. Am. Chem. Soc.* **2004**, *126*, 6222.

148. Berlinguette, C. P.; Dragulescu-Andrasi, A.; Sieber, A.; Güdel, H.-U.; Achim, C.; Dunbar, K. R. *J. Am. Chem. Soc.* **2005**, *127*, 6766.

149. Anderson, P. W. *Phys. Rev.* **1959**, *115*, 2.

150. Smith, J. A.; Galán-Mascarós, J.-R.; Clérac, R.; Sun, J.-S.; Ouyang, X.; Dunbar, K. R. *Polyhedron* **2001**, *20*, 1727.

151. Shatruk, M.; Avendaño, C.; Dunbar, K. R. In *Progress in Inorganic Chemistry, Vol 56*; John Wiley & Sons, Inc.: New York 2009; Vol. 56, p 155.

152. Waku, S.; Masuno, K.; Tanaka, T.; Iwasaki, H. *J. Phys. Soc. Jpn.* **1960**, *15*, 1185.

153. Jones, L. H. *Inorg. Chem.* **1963**, *2*, 777.

154. Tullber, A.; Vannerberg, N.-G. *Acta Chem. Scand.* **1974**, *28a*, 551.

155. Gentil, L. A.; Navaza, A.; Olabe, J. A.; Rigotti, G. E. *Inorg. Chim. Acta* **1991**, *179*, 89.

156. Desplanches, C.; Ruiz, E.; Alvarez, S. *Eur. J. Inorg. Chem.* **2003**, *2003*, 1756.

157. Dunn, T. M. *Transactions of the Faraday Society* **1961**, *57*, 1441.

158. Pedersen, K. S.; Dreiser, J.; Nehrkorn, J.; Gysler, M.; Schau-Magnussen, M.; Schnegg, A.; Holldack, K.; Bittl, R.; Piligkos, S.; Weihe, H.; Tregenna-Piggott, P.; Waldmann, O.; Bendix, J. *Chem. Commun. (Cambridge, U. K.)* **2011**, *47*, 6918.

159. Pedersen, K. S.; Schau-Magnussen, M.; Bendix, J.; Weihe, H.; Palii, A. V.; Klokishner, S. I.; Ostrovsky, S.; Reu, O. S.; Mutka, H.; Tregenna-Piggott, P. L. W. *Chemistry – A European Journal* **2010**, *16*, 13458.

160. Ruiz, E.; Rodríguez-Fortea, A.; Alvarez, S.; Verdaguer, M. *Chemistry – A European Journal* **2005**, *11*, 2135.

161. Deford, D. D.; Davidson, A. W. *J. Am. Chem. Soc.* **1951**, *73*, 1469.

162. Alexander, J. J.; Gray, H. B. *J. Am. Chem. Soc.* **1968**, *90*, 4260.

163. Eller, S.; Fischer, R. D. *Inorg. Chem.* **1990**, *29*, 1289.

164. Crean, F. M.; Schug, K. *Inorg. Chem.* **1983**, *23*, 853.

165. Hilfiger, M. G.; Shatruk, M.; Prosvirin, A.; Dunbar, K. R. *Chem. Commun.* **2008**, 5752.

166. Hoeke, V.; Stammler, A.; Bögge, H.; Schnack, J.; Glaser, T. *Inorg. Chem.* **2013**, *53*, 257.

167. Peresypkina, E. V.; Majcher, A. M.; Rams, M.; Vostrikova, K. E. *Chem. Commun. (Cambridge, U. K.)* **2014**, *50*, 7150.

168. Pinkowicz, D.; Southerland, H. I.; Avendaño, C.; Prosvirin, A.; Sanders, C.; Wernsdorfer, W.; Pedersen, K. S.; Dreiser, J.; Clérac, R.; Nehrkorn, J.; Simeoni, G. G.; Schnegg, A.; Holldack, K.; Dunbar, K. R. *J. Am. Chem. Soc.* **2015**, *137*, 14406.

169. Bendix, J.; Steenberg, P.; Søtofte, I. *Inorg. Chem.* **2003**, *42*, 4510.

170. Vostrikova, K. E.; Peresypkina, E. V. *Eur. J. Inorg. Chem.* **2011**, *2011*, 811.

171. Hydrogen Cyanide, United States Department of Labor, OSHA https://www.osha.gov/dts/chemicalsampling/data/CH_246400.html (accessed April 1, 2016).

172. Hilfiger, M. G. Dissertation, Incorporation of 4d and 5d Transition Metal Cyanometallates into Magnetic Clusters and Materials, Texas A&M University, 2010.

173. Krause, R. A.; Violette, C. *Inorg. Chim. Acta* **1986**, *113*, 161.

174. *Osmium Tetroxide*; MSDS No. 9926344 [Online]; Science Lab: Houston, TX, Oct 10, 2005. http://www.sciencelab.com/msds.php?msdsId=9926344 (accessed Nov 12, 2015).

175. Walum, E. *Environ. Health Perspect.* **1998**, *106*, 497.

176. Test No. 425: Acute Oral Toxicity: Up-and-Down Procedure DOI: http://dx.doi.org/10.1787/9789264071049-en.

177. *1,1,2,2-Tetrachloroethane*; MSDS No. 9925198 [Online]; Science Lab: Houston, TX, Oct 10, 2005. http://www.sciencelab.com/msds.php?msdsId=9925198 (accessed Dec 9, 2015).

178. Ruff, J. K.; Schlientz, W. J.; Dessy, R. E.; Malm, J. M.; Dobson, G. R.; Memering, M. N. In *Inorganic Syntheses*; Parshall, G. W., Ed.; John Wiley & Sons, Inc.: Hoboken, NJ, USA, 1974; Vol. 15, p 84.

179. Albores, P.; Slep, L. D.; Baraldo, L. M.; Baggio, R.; Garland, M. T.; Rentschler, E. *Inorg. Chem.* **2006**, *45*, 2361.

180. Cauzzi, D. A.; Mori, G.; Predieri, G.; Tiripicchio, A.; Cavatorta, F. *Inorg. Chim. Acta* **1993**, *204*, 181.

181. Buschmann, W. E.; Liable-Sands, L.; Rheingold, A. L.; Miller, J. S. *Inorg. Chim. Acta* **1999**, *284*, 175.

182. Wilson, R. D.; Bau, R. *J. Am. Chem. Soc.* **1974**, *96*, 7601.

183. Martinsen, A. *Acta chemica Scandinavica. Series A. Physical and inorganic chemistry* **1977**, *31*, 645.

184. Griffith, W. P.; Turner, G. T. *J. Chem. Soc. A* **1970**, 858.

185. Nakagawa, I.; Shimanouchi, T. *Spectrochim. Acta* **1962**, *18*, 101.

186. Figgis, B. N.; Hitchman, M. A. *Ligand field theory and its applications*; Wiley-VCH: New York :, 2000.

187. Dreiser, J.; Pedersen, K. S.; Schnegg, A.; Holldack, K.; Nehrkorn, J.; Sigrist, M.; Tregenna-Piggott, P.; Mutka, H.; Weihe, H.; Mironov, V. S.; Bendix, J.; Waldmann, O. *Chemistry – A European Journal* **2013**, *19*, 3693.

188. Miyasaka, H.; Matsumoto, N.; Re, N.; Gallo, E.; Floriani, C. *Inorg. Chem.* **1997**, *36*, 670.

189. Wang, X.-Y.; Avendano, C.; Dunbar, K. R. *Chem. Soc. Rev.* **2011**, *40*, 3213.

190. Spek, A. *Acta Crystallographica Section C* **2015**, *71*, 9.

191. Bernhardt, P. V.; Macpherson, B. P.; Martinez, M. *Journal of the Chemical Society, Dalton Transactions* **2002**, 1435.

192. Bernhardt, P. V.; Macpherson, B. P.; Martinez, M. *Inorg. Chem.* **2000**, *39*, 5203.

193. Bernhardt, P. V.; Martinez, M. *Inorg. Chem.* **1999**, *38*, 424.

194. Lescouëzec, R.; Vaissermann, J.; Ruiz-Pérez, C.; Lloret, F.; Carrasco, R.; Julve, M.; Verdaguer, M.; Dromzee, Y.; Gatteschi, D.; Wernsdorfer, W. *Angew. Chem., Int. Ed.* **2003**, *42*, 1483.

195. Sieber, R.; Decurtins, S.; Stoeckli-Evans, H.; Wilson, C.; Yufit, D.; Howard, J. A. K.; Capelli, S. C.; Hauser, A. *Chemistry – A European Journal* **2000**, *6*, 361.

196. Cotton, F. A. *Advanced Inorganic Chemistry*, 1998.

197. Eberspach, W.; Murr, N. E.; Kläui, W. *Angewandte Chemie International Edition in English* **1982**, *21*, 915.

198. Klaui, W. *J. Chem. Soc., Chem. Commun.* **1979**, 700.

199. Klaeui, W.; Eberspach, W.; Guetlich, P. *Inorg. Chem.* **1987**, *26*, 3977.

200. Dolomanov, O. V.; Bourhis, L. J.; Gildea, R. J.; Howard, J. A. K.; Puschmann, H. *J. Appl. Crystallogr.* **2009**, *42*, 339.

201. Janiak, C. *Journal of the Chemical Society, Dalton Transactions* **2000**, 3885.

202. Alvarez, S. *Dalton Trans.* **2013**, *42*, 8617.

203. Shatruk, M.; Chambers, K. E.; Prosvirin, A. V.; Dunbar, K. R. *Inorg. Chem.* **2007**, *46*, 5155.

204. Thuery, P.; Zarembowitch, J. *Inorg. Chem.* **1986**, *25*, 2001.

205. Hayami, S.; Nakaya, M.; Ohmagari, H.; Alao, A. S.; Nakamura, M.; Ohtani, R.; Yamaguchi, R.; Kuroda-Sowa, T.; Clegg, J. K. *Dalton Trans.* **2015**, *44*, 9345.

206. Chandrasekhar, V.; Dey, A.; Mota, A. J.; Colacio, E. *Inorg. Chem.* **2013**, *52*, 4554.

207. Diaz-Torres, R.; Menelaou, M.; Roubeau, O.; Sorrenti, A.; Brandariz-de-Pedro, G.; Sanudo, E. C.; Teat, S. J.; Fraxedas, J.; Ruiz, E.; Aliaga-Alcalde, N. *Chemical Science* **2016**, *7*, 2793.

208. Murray, K. S. In *Spin-Crossover Materials*; John Wiley & Sons Ltd: 2013, p1.

209. Toftlund, H.; McGarvey, J. J. In *Spin Crossover in Transition Metal Compounds I*; Gütlich, P., Goodwin, H. A., Eds.; Springer Berlin Heidelberg: Berlin, Heidelberg, 2004, p 151.

210. Olguín, J.; Brooker, S. In *Spin-Crossover Materials*; John Wiley & Sons Ltd: 2013, p 77.

211. Garcia, Y.; Niel, V.; Muñoz, M. C.; Real, J. A. In *Spin Crossover in Transition Metal Compounds I*; Gütlich, P., Goodwin, H. A., Eds.; Springer Berlin Heidelberg: Berlin, Heidelberg, 2004, p 229.

212. Real, J. A.; Gaspar, A. B.; Muñoz, M. C.; Gütlich, P.; Ksenofontov, V.; Spiering, H. In *Spin Crossover in Transition Metal Compounds I*; Gütlich, P., Goodwin, H. A., Eds.; Springer Berlin Heidelberg: Berlin, Heidelberg, 2004, p 167.

213. Liu, T.; Zheng, H.; Kang, S.; Shiota, Y.; Hayami, S.; Mito, M.; Sato, O.; Yoshizawa, K.; Kanegawa, S.; Duan, C. *Nat Commun* **2013**, *4*, 2826.

214. Shimamoto, N.; Ohkoshi, S.; Sato, O.; Hashimoto, K. *Inorg. Chem.* **2002**, *41*, 678.

215. Sessoli, R. *Nat Chem* **2010**, *2*, 346.

216. Dunbar, K. R.; Achim, C.; Shatruk, M. In *Spin-Crossover Materials*; John Wiley & Sons Ltd: 2013, p 171.

217. Zhao, H.; Clérac, R.; Sun, J. S.; Ouyang, X.; Clemente-Juan, J. M.; Gómez, G.; amp; x; a, C. J.; Coronado, E.; Dunbar, K. R. *J. Solid State Chem.* **2001**, *159*, 281.

218. Berlinguette, C. P.; Galán-Mascarós, J. R.; Dunbar, K. R. *Inorg. Chem.* **2003**, *42*, 3416.

219. Verdaguer, M.; Bleuzen, A.; Marvaud, V.; Vaissermann, J.; Seuleiman, M.; Desplanches, C.; Scuiller, A.; Train, C.; Garde, R.; Gelly, G.; Lomenech, C.; Rosenman, I.; Veillet, P.; Cartier, C.; Villain, F. *Coord. Chem. Rev.* **1999**, *190–192*, 1023.

220. Verdaguer, M.; Girolami, G. S. In *Magnetism: Molecules to Materials V*; Wiley-VCH Verlag GmbH & Co. KGaA: 2005, p 283.

221. Kettle, S. F. A.; Diana, E.; Boccaleri, E.; Stanghellini, P. L. *Inorg. Chem.* **2007**, *46*, 2409.

222. Kusz, J.; Gütlich, P.; Spiering, H. In *Spin Crossover in Transition Metal Compounds II*; Springer Berlin Heidelberg: Berlin, Heidelberg, 2004, p 129.

223. Guionneau, P. *Dalton Trans.* **2014**, *43*, 382.

224. Spek, A. *Acta Crystallographica Section D* **2009**, *65*, 148.

225. Pike, R. D. *Organometallics* **2012**, *31*, 7647.

226. *3,4-lutidine*; MSDS No. L03489 [Online]; Alfa Aesar: Ward Hill, MA, April 20, 2010. https://www.alfa.com/en/content/msds/USA/L03489.pdf (accessed Oct 9, 2015).

227. Patterson, B. T.; Keene, F. R. *Inorg. Chem.* **1998**, *37*, 645.

228. Sasse, W. H. F.; Whittle, C. P. *Journal of the Chemical Society (Resumed)* **1961**, 1347.

229. Della Ciana, L.; Dressick, W. J.; Sandrini, D.; Maestri, M.; Ciano, M. *Inorg. Chem.* **1990**, *29*, 2792.

230. Funck, K. E. Dissertation, Magnetic Properties and Reactivity Studies of Families of Trigonal Bipyramidal Cyanide Clusters and their Extended Structures, Texas A&M University, 2010.

231. Sheldrick, G. *University of Göttingen, Germany* **1996**.

232. Sheldrick, G. *Acta Crystallographica Section A* **2015**, *71*, 3.

233. Sheldrick, G. *Acta Crystallographica Section A* **2008**, *64*, 112.

234. Hübschle, C. B.; Sheldrick, G. M.; Dittrich, B. *J. Appl. Crystallogr.* **2011**, *44*, 1281.

APPENDIX A

Instrumentation and Physical Methods

Magnetic Measurements

With the exception of the Zn_3Os_2 TBP (5), magnetic measurements were collected on compounds 1 – 4 and 7 using a Quantum Design MPMS-XL SQUID magnetometer capable of helium temperature ranges of 1.8 – 400 K and equipped with a 7 Tesla magnet. The instrument utilizes the MPMS MultiVu software interface. For compounds 8 – 11 in chapter 5 and the Zn_3Os_2 TBP (5), magnetic measurements were collected using a Quantum Design MPMS®3 SQUID magnetometer equipped with a 7 Tesla magnet and an EverCool® system capable of a temperature range of 1.8 – 400 K. This instrument also utilizes the MPMS MultiVu software interface.

All measurements were made on crushed microcrystalline samples. Unless stated otherwise, samples were measured in a plastic bag constrained within a plastic straw attached to the instrument probe and prepared in air. The data were corrected for the diamagnetic contribution of the bag with the equation:

$$-7.0\times10^{-7} + \frac{4\times10^{-7}}{T + 4} \times \left(\frac{mg}{1000}\right) \qquad \textbf{Equation A-1}$$

where mg is the mass of the bag in milligrams and T is the temperature of the measurement. This equation was obtained by fitting magnetic measurements of the bags at multiple temperatures and fields. For compounds 7a-d in Chapter 4 (Fe_3Ru_2 TBPs), samples were put into a 100 MHz Quartz NMR tube under an anaerobic environment. The Fe_3Ru_2 TBP measured under MeCN (7a) had just enough solvent added to cover the top of the sample and then the tube was sealed. An inverted NMR tube was placed underneath the sample NMR tube in a plastic straw attached to the instrument probe. The straw was capped on the bottom to prevent the tubes from falling out of the straw and the straw was taped to the probe with a very small amount of duct tape to prevent the straw from falling off of the probe. Compound 7e (the humid Fe_3Ru_2 TBP) was prepared and measured in the same manner but was prepared in air. All Fe_3Co_2 TBP samples in chapter 5 (8 – 11) were measured using a Quantum Design VSM capsule constrained by a brass rod. The data were corrected by doing a point-by-point subtraction of the capsule from the raw data. All data were corrected for the diamagnetic contribution from solvent and Pascal's constants.[11] In order to account for all interstitial solvent as well as excess solvent, TGA were performed on all samples once they were removed from the SQUID. For samples that were measured in NMR tubes under excess solvent, the tubes were broken open and immediately put under vacuum to remove excess solvent before being weighed (to account for the solvent lost to vacuum) and immediately measured in the TGA.

Magnetic susceptibility measurements were performed in a DC applied field of 1000 Oe between 2 and 390 K. Low temperature magnetization measurements were carried out at 1.8 K at various fields up to 7 T. Room temperature magnetization measurements were made at 300 K at various fields up to 2 T in order to verify the purity of the samples. Reduced magnetization measurements were performed at various low temperatures at various fields up to 7 T.

Infrared (IR) Spectroscopy

Infrared (IR) spectral data were measured on a Nicolet 470 FT-IR spectrometer with a CsI beam splitter and analyzed with the OMNIC 5 or OMNIC 6.1 software package. All samples were prepared in air as Nujol mulls on KBr plates under a N_2 atmosphere between 4000 and 400 cm^{-1}.

Thermogravimetric Analysis (TGA)

Thermogravimetric analyses were performed on a Shimadzu TGA-50 Analyzer with a maximum temperature of 1,000 °C and a sample mass readability of 1 μg to 1 g. The analyzer is controlled by a TA-50WS thermal analysis workstation and software. All samples were prepared in air and analyzed in an aluminum sample pan under a N_2 atmosphere.

Elemental Analysis (EA)

Elemental analyses were performed off-site by Atlantic Microlab, Inc. Solid samples were sent by overnight express mail in closed vials. Duplicate analyses were performed on the same sample.

Cyclic Voltammetry (CV)

Electrochemical data were collected at room temperature using an HCH Electrochemical Analyzer model CH 1620A in dry MeCN. A BAS glassy carbon working electrode, Pt wire auxiliary electrode, Ag/AgCl (3M KCl(aq)) reference electrode and 0.1 M tetra-n-butylammonium hexafluorophosphate ($[^{n}Bu_4N][PF_6]$) as the supporting electrolyte were utilized to carry out the measurements. A scan rate of 0.2 V/s was used for all measurements.

Single Crystal X-Ray Diffractometry

The $(PPN)_3[Ru^{III}(CN)_6]$ (1), $(PPN)_3[Os^{III}(CN)_6]$, (2), Co_3Ru_2 (3), Co_3Os_2 (4) and Fe_3Co_2 5dmbpy (10) samples were collected on a Bruker APEXII (Mo Kα) diffractometer equipped with a CCD detector. The crystals were mounted in air using oil on a nylon loop and put into a $N_{2(g)}$ cold stream at 110 K.

All Fe_3Ru_2 (7a-e), the Fe_3Co_2 (8, 9, 11) structures, the Zn_3Os_2 TBP (5) and the Mn_2Ru_2 square (6) were collected using a synchrotron radiation source at the Advanced Light Source (ALS) at Lawrence Berkeley National Laboratory (LBNL). Experiments were done on beamline 11.3.1 using a beam energy of 16 keV

(λ = 0.7749) and a Bruker AXS APEXII CCD shutterless detector. Crystals were mounted in air using oil on a MiTeGen loop and collected at temperatures between 15 and 300 K using $He_{(g)}$ or $N_{2(g)}$.

Integration for all data sets were performed with the Bruker SAINT Software package and absorption corrections were empirically applied using SADABS.[231] The structures were initially solved using Direct Methods with the shelxt[232] structure solution program and refined using Least Squares minimization from the shelxl[233] refinement software. A combination of Olex2,[200] shelxle[234] and manual editing of the res file were used to refine, finalize and render images of the structures. All hydrogen atoms were placed in calculated positions. The final refinements were carried out with anisotropic thermal parameters for all non-hydrogen atoms unless otherwise noted within the chapter text. Thermal ellipsoids are drawn for all applicable structures at 50%.

Fe_3Ru_2 Solvated 7a

These crystals were placed into a tube that had been treated with Glassclad® 18 in an oxygen and water-free environment. The tube was sealed in an anaerobic manner and then shipped to the ALS. Upon opening the sealed tube in air, the crystals were immediately transferred to oil. A dark, purple/red prism was transferred from the oil and mounted to a MiTeGen loop. The crystal was placed into a He cold stream at 150 K and a data set was collected using synchrotron radiation at 16 eV (λ = 0.7749). Once the data collection was finished,

the crystal was cooled to 100 K at 20 K/minute and the structure was recollected. Cooling and data collection continued in this manner for both 50 K and 20 K data sets. The crystal was then warmed from 20 K to 200 K, again at a rate of 20 K/min, and another data set was collected. This continued for temperatures of 250 and 300 K as well. The crystal no longer diffracted well at 300 K so the data could not be used.

Fe_3Ru_2 24 Hours 7d

These crystals were put into a tube that had been treated with Glassclad® 18 in an oxygen and water-free environment. The tube was sealed in an anaerobic manner and then shipped to the ALS. Upon opening the sealed tube, crystals were immediately put into oil and then a dark, reddish-purple prism was quickly mounted on a MiTeGen loop and put into a He cold stream at 150 K. The crystal no longer diffracted well at 300 K so the data could not be used.

Fe_3Ru_2 Humid 7e

These crystals were shipped to the ALS in a sealed glass tube. The tube was opened and crystals were put into oil before a dark, reddish-purple prism was mounted on a MiTeGen loop and put into the He cold stream at 150 K. The crystal was cooled and warmed while data sets were being collected in the same manner as the solvated sample (7a). Again, the crystal no longer diffracted well at 300 K so the data could not be used.

^{57}Fe Mössbauer

^{57}Fe Mössbauer spectra were collected on constant acceleration instruments using cryostats that allowed the sample temperature to be varied between 1.5 and 300 K in external fields up to 8 T (Carnegie Mellon University). Spectral simulations were generated using WMOSS (WEB Research, Edina, MN), and isomeric shifts were reported relative to an Fe metal standard at room temperature. Mössbauer data were obtained on the same batch of Fe_3Ru_2 TBP crystals as all other characterization techniques. Except for the humid sample (7e), all samples (7a-d) were prepared in a water- and oxygen-free glove box under a N_2 atmosphere. Crystals were placed in Teflon® Mössbauer cups, capped and the junctions where the cup and cap meet were lined with vacuum grease. The sample under MeCN (7a) was NOT capped and greased but frozen in the cup with liquid N_2 instead. The cups were placed in vials covered with electrical tape and Parafilm® M and then shipped over night on dry ice to Dr. Catalina Achim at Carnegie Mellon University for Mössbauer measurements. At Carnegie Mellon University, the samples are stored under in an inert atmosphere when not being measured.